

①

DTIC
ELECTE
JAN 24 1995

C D



DISTRIBUTION STATEMENT A
Approved for public release;
Distribution Unlimited

**DESIGN, FABRICATION AND CHARACTERIZATION OF
MICRO OPTO-ELECTRO-MECHANICAL SYSTEMS**

THESIS

Darren E. Sene, MS HRM, BS EE
Captain, USAF

AFIT/GEO/ENG/95D-03

DEPARTMENT OF THE AIR FORCE
AIR UNIVERSITY
AIR FORCE INSTITUTE OF TECHNOLOGY

Wright-Patterson Air Force Base, Ohio

DTIC QUALITY INSPECTED 1

AFIT/GEO/ENG/95D-03

**DESIGN, FABRICATION AND CHARACTERIZATION OF
MICRO OPTO-ELECTRO-MECHANICAL SYSTEMS**

THESIS

Darren E. Sene, MS HRM, BS EE
Captain, USAF

AFIT/GEO/ENG/95D-03

19960119 016

Approved for public release; distribution unlimited.

The views expressed in this thesis are those of the author and do not reflect the official policy or position of the Department of Defense or the U. S. Government.

DESIGN, FABRICATION AND CHARACTERIZATION OF MICRO OPTO-ELECTRO-MECHANICAL SYSTEMS

THESIS

Presented to the Faculty of the Graduate School of Engineering
of the Air Force Institute of Technology
Air University (AU)
Air Education and Training Command (AETC)

In Partial Fulfillment of the
Requirements for the Degree of
Master of Science in Electrical Engineering

Darren E. Sene, MS HRM, BS EE
Captain, USAF
December 1995

Accession For	
NTIS CS&I	<input checked="" type="checkbox"/>
DTIC TAB	<input type="checkbox"/>
Unannounced	<input type="checkbox"/>
Justification	
By _____	
Distribution/	
Availability Codes	
Dist	Avail and/or Special
A-1	

Approved for public release; distribution unlimited.

Acknowledgements

Any effort of this magnitude requires the recognition of numerous contributing individuals, not the least of which is my family. My wife Mikki, daughter Ashlyn, and soon to be second child (name not yet decided) are my soul inspiration and guiding light. Without the understanding and support of Mikki this thesis would never have been completed. She deserves the greatest portion of my appreciation.

At AFIT I would like to thank my thesis advisor, Dr. Victor Bright, for his fortitude and excellent ability to critique documents. Without his expert penmanship this thesis would have lacked completeness. Secondly, I want to recognize the MEMS group, for providing a sense of camaraderie that helped enhance the late night pleasures of completing a MUMPS layout. Specifically, I bow to the king of MEMS, Maj. John Comtois, and extend my sincere thanks for providing numerous thought provoking discussions and email attachments.

Mr. Robert Conkle deserves my recognition for always being available to discuss circuit design and providing me with components from the AFIT archives. Without the rapid responsiveness of Capt. Gary Mauersberger parts of the testing in this thesis would not have been possible and I deeply appreciate his assistance. A special thanks goes to Mr. Charlie Powers who kept me stocked with supplies and was instrumental in my success. I also want to recognize Mr. Chris O'Brien and Mr. Bill Trop for putting up with the day-to-day questions that arose from operating equipment in the cooperative microelectronics laboratory. Finally, I would like to thank everyone else that contributed, in whatever capacity, to the success of this thesis.

Table of Contents

	Page
Acknowledgements.....	ii
List of Figures.....	viii
List of Tables.....	xiv
Abstract.....	xv
1. Introduction.....	1-1
1.1. Background.....	1-1
1.2. Problem Statement.....	1-4
1.3. Scope.....	1-5
1.4. Approach.....	1-6
1.4.1. Components.....	1-7
1.4.2. Systems.....	1-8
1.4.3. Thermal Testing.....	1-9
1.5. Sequence of Presentation.....	1-9
2. Literature Review.....	2-1
2.1. Historical Perspective.....	2-1
2.2. Architecture and Fabrication.....	2-2
2.2.1. Polycrystalline Silicon and Light Properties.....	2-2
2.2.2. Electrostatic versus Thermal Structures.....	2-6
2.2.3. Flip-up versus Surface Structures.....	2-9
2.2.4. Device Design and Processing.....	2-13

2.3. Micro-Optical Devices	2-15
2.3.1. Micromirrors	2-15
2.3.2. Diffraction Gratings.....	2-17
2.3.3. Fresnel Lenses	2-20
2.4. Micro-Optical Systems	2-20
2.4.1. Interferometers	2-20
2.4.2. Optical Switches.....	2-23
2.4.3. Fiber Optic Couplers	2-24
2.4.4. Fabry-Perot Etalons	2-25
2.5. Summary.....	2-26
3. Theoretical Review	3-1
3.1. Microscope-Based Laser Probe Interferometer Theory	3-1
3.2. Component Theory	3-3
3.2.1. The Flexure Beam Micro-Mirror Device	3-3
3.2.1.1. Mechanical Force of Electric Origin	3-4
3.2.1.2. The Ideal FBMD Model.....	3-6
3.2.1.3. FBMD as a Single Degree-of-Freedom System.....	3-7
3.2.2. Heat Actuator	3-11
3.2.3. Fresnel Lens.....	3-12
3.2.4. Diffraction Grating.....	3-14
3.2.4.1. Geometric Modeling	3-14
3.2.4.2. Fourier Modeling.....	3-15

3.2.4.3. Variable Grating Example.....	3-21
3.3. Micro-Interferometer	3-24
3.4. Thermal Testing.....	3-25
3.5. Summary.....	3-31
4. Experimental Setups, Procedures, and Design Descriptions	4-1
4.1. MUMPS Process	4-1
4.1.1. Design Considerations.....	4-2
4.1.2. Post Processing Procedures	4-6
4.2. Experimental Setups.....	4-7
4.2.1. Optical Device Experiments.....	4-7
4.2.2. Probe Station Device Experiments.....	4-9
4.2.3. Thermal Experiments	4-10
4.2.3.1. Thermal Testing Procedures.....	4-13
4.2.3.2. Frequency Testing Procedure	4-17
4.2.4. Testing and Characterization Equipment	4-19
4.4. Device Descriptions.....	4-24
4.4.1. Flip-up Optical Devices.....	4-24
4.4.2. Heat Actuators	4-34
4.4.3. Surface Mirrors.....	4-37
4.4.4. Variable Gratings.....	4-40
4.4.5. Fiber Optic Couplers	4-42
4.4.6. Micro Interferometers.....	4-46

4.4.7. Other Devices	4-48
4.5. Summary.....	4-48
5. Results and Discussion	5-1
5.1. Fabrication Results	5-1
5.2. Grating Pixel Results.....	5-6
5.3. Fresnel Lens Results.....	5-15
5.4. Flip-up Structure Results.....	5-17
5.5. FBMD Hidden Hinge Results.....	5-21
5.6. Resonant Frequency Results.....	5-22
5.7. Thermal Testing Results.....	5-28
5.7.1. Test Setup Difficulties.....	5-28
5.7.2. Resonant Frequency Results.....	5-30
5.7.3. Resistivity Results	5-31
5.8. Micro-Interferometer Results	5-32
5.9. Heat Actuator Results.....	5-37
5.10. Summary.....	5-39
6. Conclusions and Recommendations	6-1
6.1. Conclusions	6-1
6.2. Recommendations	6-3
6.2.1. Continued Thermal Testing.....	6-3
6.2.1.1. Material Parameter Measurements.....	6-4
6.2.2. Variable Grating Testing	6-5

6.2.3. Fiber Optic Coupler Testing	6-7
6.2.3. Optimized Flip-up Locking Mechanism	6-8
6.2.5. Rotating Flip-up Structures	6-8
Appendix A: Matlab Diffraction Grating M-files.....	A-1
Appendix B: MUMPS Die Layouts from Cadence	B-1
Appendix C: Cadence Layouts not shown in Chapter 4	C-1
Appendix D: Scanning Electron Micrographs not shown in Chapters 4 or 5.....	D-1
Bibliography	BIB-1
Vita	VITA-1

List of Figures

	Page
Figure 1-1. Overlapping of the three major fields	1-3
Figure 1-2. Concept drawing of a micro-optical bench.....	1-4
Figure 1-3. Schematic of how a structure can be fabricated using planar technologies and later “flipped-up” to create 3-Dimensional objects.....	1-8
Figure 2-1. Characteristics of bulk silicon as a function of optical wavelength.....	2-3
Figure 2-2. Scanning electron micrograph of a square Flexure Beam Micromirror Device array	2-7
Figure 2-3. Schematic of a Flexure Beam Micromirror Device	2-8
Figure 2-4. Schematic of a thermally driven actuator	2-8
Figure 2-5. Scanning electron micrograph of thermally driven actuators	2-9
Figure 2-6. Two basic hinge types for flip-up structures.....	2-11
Figure 2-7. Cross section of a substrate hinge.....	2-12
Figure 2-8. Proportional cross-section of the MCNC MUMPS Process.....	2-15
Figure 2-9. Scanning electron micrograph of a hexagonal micromirror array	2-17
Figure 2-10. Schematic of microscope-based laser probe interferometer	2-18
Figure 2-11. 2-D rectangular sinc function.....	2-19
Figure 2-12. Example of a grating array.....	2-21
Figure 2-13. Sample Fresnel lens with precision locks	2-22
Figure 2-14. Schematic of a micro-fabricated optical chopper	2-23
Figure 2-15. 1x2 fiber optic coupler.....	2-25
Figure 2-16. Cross section of the Fabry-Perot modulator	2-26

Figure 3-1.	Phasor representation of the summation for the reference and object beams of the microscope-based laser probe interferometer	3-2
Figure 3-2.	Pictorial representation of the computation of mechanical force of electric origin.....	3-5
Figure 3-3.	Uniform electric field for a parallel plate capacitor.....	3-6
Figure 3-4.	Single degree-of-freedom system with viscous damping	3-8
Figure 3-5.	Zone-plate geometry	3-13
Figure 3-6.	Variation of allowed incoming light angle ($\theta_m - \theta_i$) versus grating period width.....	3-16
Figure 3-7.	Binary versus blazed gratings	3-17
Figure 3-8.	Diffraction by an aperture	3-17
Figure 3-9.	Diffraction model. Method for calculating diffraction pattern for Young's slits	3-20
Figure 3-10.	Diffraction model. Method for calculating diffraction pattern for a blazed grating	3-20
Figure 3-11.	Diffraction model with introduction of noise and the production of ghosts.....	3-21
Figure 3-12.	Grating period development for the variable diffraction grating with a $2 \times 6 \mu\text{m}$ line/spacing setup	3-23
Figure 3-13.	Output from grating model for a $2 \mu\text{m} \times 2 \mu\text{m}$ grating.....	3-24
Figure 3-14.	Schematic of a micro-interferometer design.....	3-26
Figure 3-15.	Four types of spring constants	3-27
Figure 3-16.	Pictorial representation of a two sided hinge	3-27
Figure 3-17.	Representation of the spring system for a square FBMD	3-28
Figure 4-1.	Typical Cadence layout editor screen	4-2
Figure 4-2.	Conformal effect of polysilicon layering in MUMPS	4-4

Figure 4-3.	Flip-helper layouts in Cadence	4-5
Figure 4-4.	Setup used for characterization of optical components and systems	4-8
Figure 4-5.	Interface schematic for equipment used in thermal testing.....	4-11
Figure 4-6.	Photograph of thermal testing station	4-11
Figure 4-7.	MMR technologies thermal test setup	4-12
Figure 4-8.	Schematic diagram of device input drive signal generator	4-13
Figure 4-9.	Schematic diagram of gas manifold for low temperature microprobe	4-16
Figure 4-10.	Side view of low temperature micro probe.....	4-18
Figure 4-11.	Schematic of electrical connections from the HP4195A network/spectrum analyzer	4-19
Figure 4-12.	Cadence layout of ver. 3 flip-up mirror with ratchet	4-26
Figure 4-13.	Cadence layout of heat drive actuated ratcheting adjustable mirror	4-26
Figure 4-14.	Scanning electron micrograph of ver. 1 flip-up mirror with ratchet.....	4-27
Figure 4-15.	Cadence layout and scanning electron micrograph of ver. 11 tilt adjustable flip-up mirror.....	4-28
Figure 4-16.	Cadence layout and scanning electron micrograph of ver. 2 rotating flip-up grating.....	4-30
Figure 4-17.	Cadence layout and scanning electron micrograph of 360 degree rotating flip-up mirror	4-31
Figure 4-18.	Angled scanning electron micrograph of locking mechanism and pivot point for rotating flip-up structures.....	4-32
Figure 4-19.	Cadence layout and scanning electron micrograph of ver. 7 rotating ratchet mirror	4-33
Figure 4-20.	Cadence layout and scanning electron micrograph of circular heat actuator.....	4-35

Figure 4-21.	Cadence layout and scanning electron micrograph of vertical heat actuators	4-36
Figure 4-22.	Cadence layout and scanning electron micrograph of vertical heat actuated surface mirror	4-38
Figure 4-23.	Shaped mirrors for testing electric field fringing effects	4-39
Figure 4-24.	Scanning electron micrograph of square mirror for testing electric field fringing effects	4-40
Figure 4-25.	Cadence layout of heat actuated grating	4-43
Figure 4-26.	Scanning electron micrographs of ver. 4 variable grating	4-44
Figure 4-27.	Cadence layout of 1x2 fiber optic coupler	4-45
Figure 4-28.	Cadence layout of the small micro interferometer	4-47
Figure 5-1.	Scanning electron micrograph of "stuck" hinge on MUMPS 7 due to fabrication problem	5-5
Figure 5-2.	Schematic of MUMPS layering process indicating the connection between Poly 1 and Poly 2 which immobilizes the hinge pins	5-5
Figure 5-3.	Image of diffraction patterns for three different variable diffraction gratings	5-7
Figure 5-4.	Image of diffraction patterns for a $\omega_1 = 6 \mu\text{m}$ & $\omega_2 = 2 \mu\text{m}$ variable diffraction grating with and without hold downs	5-9
Figure 5-5.	Scanning electron micrograph of ver. 7 (MUMPS 9) variable grating with hold downs	5-9
Figure 5-6.	Diffraction pattern for the original generation (MUMPS 8) variable grating versus theory	5-10
Figure 5-7.	Images of diffraction patterns for a $\omega_1 = 6 \mu\text{m}$ & $\omega_2 = 2 \mu\text{m}$ variable grating, ver. 8, for different applied currents	5-13
Figure 5-8.	Theoretical peak amplitude for the $m=0$ and first two diffracted orders as a function of lateral displacement of the Poly 2 grating	5-14

Figure 5-9.	Second generation variable grating, ver. 8 (MUMPS 9), experimentally obtained profiles for the change in intensity of the $m=0$ and first two diffracted orders versus applied current to the heat drive actuators	5-14
Figure 5-10.	Scanning electron micrograph of 8 element flip-up Fresnel lens array (MUMPS 9)	5-16
Figure 5-11.	View of intensity pattern obtained using a Helium Neon laser to illuminate the lens	5-16
Figure 5-12.	Scanning electron micrograph of 45 degree nominal flip-up 150 x 150 μm mirror with smaller 50 x 50 μm mirror attached (MUMPS 9)	5-19
Figure 5-13.	Scanning electron micrograph of scissor hinge section for flip-up mirror shown in Fig. 5-12 (MUMPS 9)	5-20
Figure 5-14.	Scanning electron micrograph of two flip-up mirrors like the one shown in Fig. 5-12 indicating how various angles are achieved by the ratchet and flexure lock mechanism.....	5-21
Figure 5-15.	Scanning electron micrograph of ver. 2 (MUMPS 8) of the hidden hinge mirrors	5-22
Figure 5-16.	Transfer function plotted for three different values of the fraction of critical damping.....	5-23
Figure 5-17.	Experimental and theoretical resonant frequency curves for a square, 65x65 μm , FBMD.....	5-24
Figure 5-18.	Resonance profile for a single fringe test array containing 36 mirrors with 4 different geometry's.....	5-26
Figure 5-19.	Theoretical frequency profile for a fringe test array	5-26
Figure 5-20.	Experimentally obtained resonance profiles for all four of the fringe test arrays	5-27
Figure 5-21.	Results of thermal testing of a square FBMD from MUMPS 6	5-31
Figure 5-22.	Results of resistivity versus temperature of the three polysilicon layers of the MUMPS process	5-32

Figure 5-23.	Scanning electron micrographs of a 172 x 400 μm small interferometer (MUMPS 9)	5-35
Figure 5-24.	Scanning electron micrograph of 250 x 1500 μm large interferometer designed with optical fiber couplers for the input and output	5-36
Figure 5-25.	Optical modulation calculated for the micro-interferometer as a function of the object mirrors deflection distance	5-37
Figure 6-1.	Cadence layout of simple resonator from array designed for fabrication on MUMPS 10.....	6-4
Figure 6-2.	Cadence layout of transfer length resistor from MUMPS 10	6-5
Figure 6-3.	Cadence layout of large, 500x500 μm , variable diffraction grating designed for fabrication on MUMPS 10.....	6-6

List of Tables

	Page
Table 2-1. Selected Mechanical Properties of Silicon	2-6
Table 4-1. Release Procedure for MUMPS Fabricated Die	4-7
Table 4-2. Low Temperature Microprobe Start-up Procedure	4-14
Table 4-3. Low Temperature Microprobe Backfill Procedure	4-15
Table 4-4. Versions of Flip-up Rail Guided Ratcheting Mirrors	4-25
Table 4-5. Versions of Rotating Optical Structures with Characteristic Dimensions	4-29
Table 4-6. Versions of Variable Diffraction Grating	4-42
Table 5-1. MCNC Process Statistics for MUMPS 4, 6, 7, 8, and 9	5-2

Abstract

Several micro-opto-electro-mechanical structures were designed using the Multi-User MEMS Process (MUMPS). Specific design techniques were investigated for improving the capabilities of elevating flip-up structures. The integration of several flip-up micro-optical structures into a micro-optical system was explored with primary emphasis on the development of a micro-interferometer. The thermal effects on the Modulus of Elasticity were determined by detecting the resonant frequency for a single square Flexure Beam Micromirror Device. The resonance of the device was found to match theory to within 0.1 % and the Modulus of Elasticity was found to decrease by 0.041 GPa/K from 290 to 450 K. Thermal testing on each of the polysilicon MUMPS layers yielded a linear increase in resistivity of 1×10^{-6} to 2×10^{-6} Ω -cm/K from 290 to 450 K. Thermal testing down to 77 K was desired but could not be performed due to water condensation within the evacuation chamber which impedes the operation of MEMS devices. Several designs of a surface micro-optical structure known as a variable grating were developed and characterized. This device was found to yield a diffraction pattern with multiple orders that could switch intensities by swapping energy. The device yielded modulation intensities of up to 6.4 and 9.0 dB for the first two diffracted orders, respectively. The original devices utilized a single heat drive actuator to deflect a Poly 2 grating laterally, up to 2 μ m, over a Poly 1 stationary grating which yielded a change in the period dimensions of the composite grating. Later versions of the device used two heat drive actuators to increase the lateral deflection up to the full deflection requirement of 4 μ m. This device can be effectively used for multi-channel optical switching.

DESIGN, FABRICATION AND CHARACTERIZATION OF MICRO OPTO-ELECTRO-MECHANICAL SYSTEMS

1. Introduction

1.1. Background

When the laser was first introduced, the standard comment was: “the laser is a solution in search of a problem” [1]. Now the laser takes on such diverse roles as steel cutting, communication, and even eye surgery. It can be argued that Micro-Electro-Mechanical Systems (MEMS) are also a solution in search of a problem. Are there applications for this technology? Can it be used to solve real engineering problems?

Presently MEMS technology is searching for applications. Micro-mirrors are being studied to determine if they can be used to correct a communication laser beam affected by atmospheric turbulence [2] and are already a prime candidate for use in High Definition Television Systems (HDTV) [3,4]. Furthermore, inkjet nozzles fabricated from bulk etched silicon are already in use [5] and other devices are currently in the development stage such as micromachined accelerometers and micro-electro-mechanical resonators for use in aerospace navigation [6]. These are just some examples of applications for micromachining. Only through continued testing and research will the ability to miniaturize “macro” applications be demonstrated and the technologies unique approach exploited to provide potential solutions for a myriad of problems. Even Richard Feynman was amazed at the possibilities for MEMS and went as far as to offer a \$1000 prize in 1959 to the first individual who could develop a micromotor 1/64th of an inch

cube. This prize was presented only a year later to William McLellan for developing an electric motor the size of a speck of dust [7,8].

A recent extension of ongoing MEMS research includes the development of micro-optical devices. The concept of marrying electrical, mechanical and optical components together to form an integrated Micro Opto-Electro-Mechanical System (MOEMS) was envisioned by Motamedi [9]. This integration of three major engineering fields is shown pictorially in Figure 1-1 and indicates that each of the three fields have been coupled together to provide bi-field disciplines such as electro-optics, but have never been shown completely grouped together into a single field. It is conceivable that MOEMS will eventually lead to commercial applications of MEMS technology for everything from micro-optical communication to imaging systems. This thesis explores both a component and systems approach to utilizing MOEMS by building a so called Micro-Optical Bench (MOB) as shown with a schematic in Figure 1-2.

The MOB takes advantage of a number of structural components to perform a specific function utilizing light as the information carrier. Optical devices that are currently being used on macro-optical benches, such as spectrometers and interferometers, are ideal candidates for miniaturization onto a MOB. This thesis explores the possibility of a working micro-interferometer and 1x2 fiber optic coupler as two potential systems that can benefit from the advances in MEMS technology. In both systems there are electrically driven MEMS devices that provide the mechanical motions

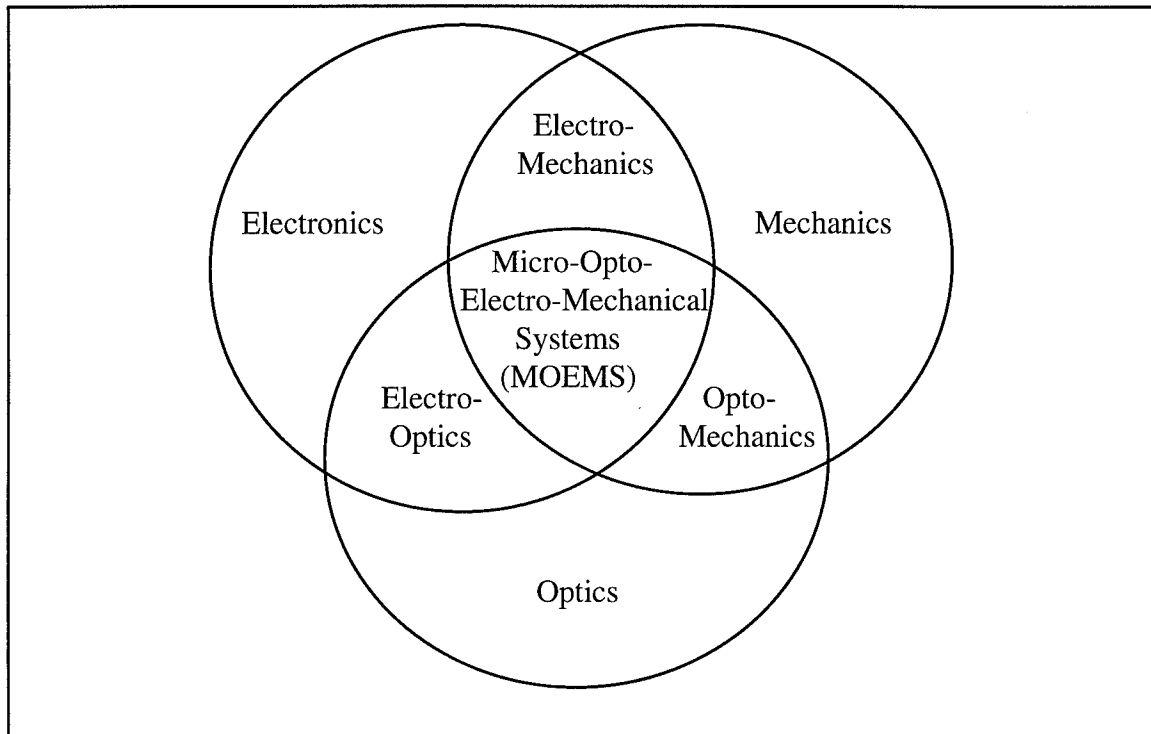


Figure 1-1. Overlapping of the three major fields. Micro-electro-mechanical systems technology is based on electromechanics. Micro-opto-electro-mechanical systems technology is based on the interaction of all three [9].

required to operate the systems. These devices have already been developed and extensively tested at the Air Force Institute of Technology (AFIT) during prior research efforts [10,11]. These existing MEMS devices and their operating principles are discussed later in Chapters 2 & 3. Further devices that perform optical functions, such as beam splitters and micro-mirrors, must also be developed in order to build the MOB systems. These optical devices and others were initially explored at the onset of this research in order to solidify their designs prior to incorporating them into systems. In some cases fabrication problems precluded testing of the optical devices required in the MOB systems and testing was performed first hand as the devices were being prepared for evaluation.

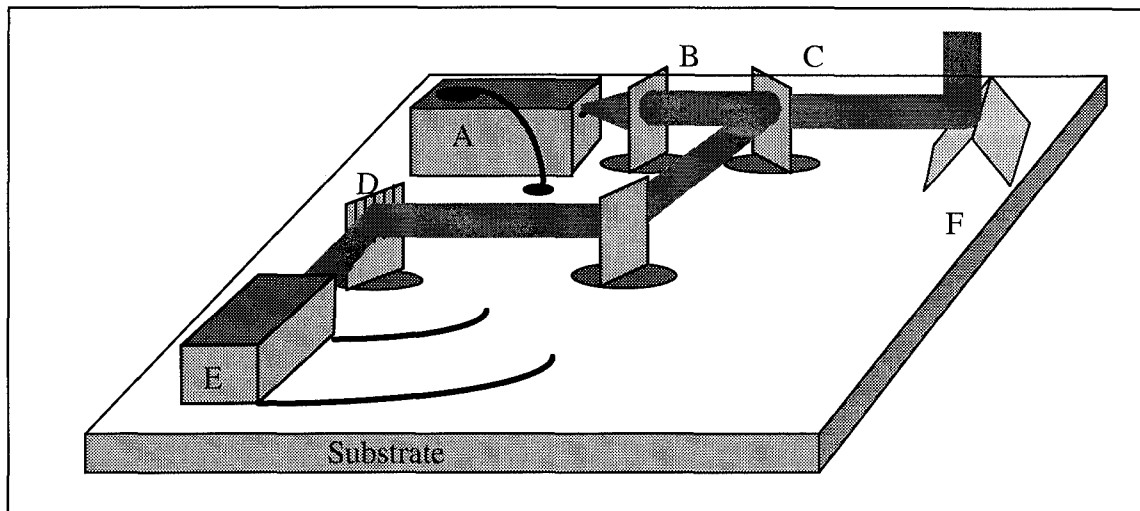


Figure 1-2. Concept drawing of a micro-optical bench (MOB). A: Edge emitting laser; B: Collimating lens; C: Beam splitter; D: Diffraction grating; E: Detector; F: 45° mirror [12].

1.2. Problem Statement

The Air Force is rapidly becoming more interested in the increasing capabilities of MEMS. The work contained in this thesis is part of an ongoing effort to identify potential military applications for MEMS and MOEMS technology. Current optical components and systems are often bulky and do not lend themselves well to the decreasing size and weight of some military systems. Furthermore, bulky macro-optical devices often have difficulties meeting the severe environmental performance requirements which are required of military hardware. These downfalls of the macro-optical bench are where MOEMS devices have the potential to provide the greatest benefits. Newly developed systems should be able to deliver significant advantages in these areas without excessive degradation of performance. The objective of this thesis was two-fold: first, to demonstrate the ability to use commercial fabrication facilities in the manufacture of micro-optical components and to test these components for various

operational characteristics; and second, to fabricate and test complete optical systems utilizing the MOB concept by integrating two or more micro-optical components.

The goal of this thesis was to explore the design and testing of various MOEMS components and how they might be integrated into a known optical system. Verification of fundamental optical concepts, based on the application of selected micro-optical components, was a critical step toward integrating the selected optical components into various micro-optical systems.

1.3. Scope

The research conducted in support of this thesis included the design, fabrication and testing of numerous MOEMS devices. The design work was conducted using the Cadence[®] drawing tool available at the Air Force Institute of Technology [13]. The Multi-User MEMS ProcesS (MUMPS), which is provided through the Microelectronics Corporation of North Carolina (MCNC), has proven to be the most accessible commercial fabrication facility available to AFIT for this specific type of research [14]. The details of the MUMPS fabrication process are reviewed in Chapter 2.

There are some existing MEMS components that are potential candidates for assisting in designing the particular optical devices of interest. They include: the heat-drive actuator, *flip-jack* and *microhinge*. Although there are numerous optical components and systems that could be miniaturized using MEMS principles, a few specific ones have been selected in order to provide a level of scope for this thesis. The optical devices investigated included: the Flexure Beam Micromirror Device (FBMD), the micro-diffraction grating (static and dynamic), a 1x2 fiber optic coupler, and a micro-

interferometer. These basic devices and their operating principles are described in Chapter 2.

The testing of individual components was device dependent. For example, the micromirror and heat-drive actuator characteristics could be tested using the microscope-based laser probe interferometer setup, whereas the fiber optic and grating devices require the use of a laser source, fiber optic equipment, an energy meter and oscilloscope. The test setups and procedures utilized for all devices covered in this thesis are discussed in Chapter 4.

1.4. Approach

The time span of this thesis covered approximately 3 complete MUMPS runs which allowed for the design and testing of devices from three different die (each design run yields 15 duplicate 1 cm x 1 cm die). The last die was received just prior to the thesis completion and only partial testing was performed on that die for inclusion in this thesis. The original plan was to develop designs for basic optical components on the first MUMPS fabrication run (MUMPS 7) and to incorporate component modifications into system level designs for the second design run (MUMPS 8). The last fabrication run (MUMPS 9) was to be used for further research and improvements. As will be discussed further in Chapter 5, problems in the fabrication of MUMPS 7 & 8 resulted in failure of all flip-up style devices on these runs. This forced more extensive use of MUMPS 9 in order to produce devices and systems in support of this thesis. Although this was a major setback, the additional time allowed for more extensive testing of the planar optical devices as will be described in Chapter 5.

The work performed in support of this thesis breaks down into three major areas that cover the progression of a sound engineering development process. To provide an overview of what is covered in later chapters, the three areas are briefly discussed below:

1.4.1. Components

Of all the various optical components that could be selected for miniaturization only a handful have been chosen for this thesis. The first and probably most prevalent of these is the diffraction grating. As will be discussed in Chapter 2, the diffraction grating shall be fabricated on both planar and flip-up devices. A pictorial representation of how a flip-up plate can be developed is shown in Figure 1-3. A diffraction grating can be used to separate out the spectral content of a light beam or steer a selected wavelength in a particular direction. Another component of interest to this research is an optical mirror. Mirrors shall be made on flip-up devices in order to direct light beams around the chip, parallel to the substrate surface. Modifications to the FBMD shall be made in order to investigate the possibility of “hiding” the flexures under the mirror surface to increase their packing densities when used in arrays. Fresnel lenses shall be developed on flip-up devices to help collimate a beam with a set wavelength and therefore aid in coupling the light beam to certain optical systems. Finally, in order to design systems that require fiber optic cables, flip-up fiber holders shall be developed that lock down the fiber onto the substrate. These lock down devices allow for fiber mounting to the substrate without having to use bulk etched v-grooves.

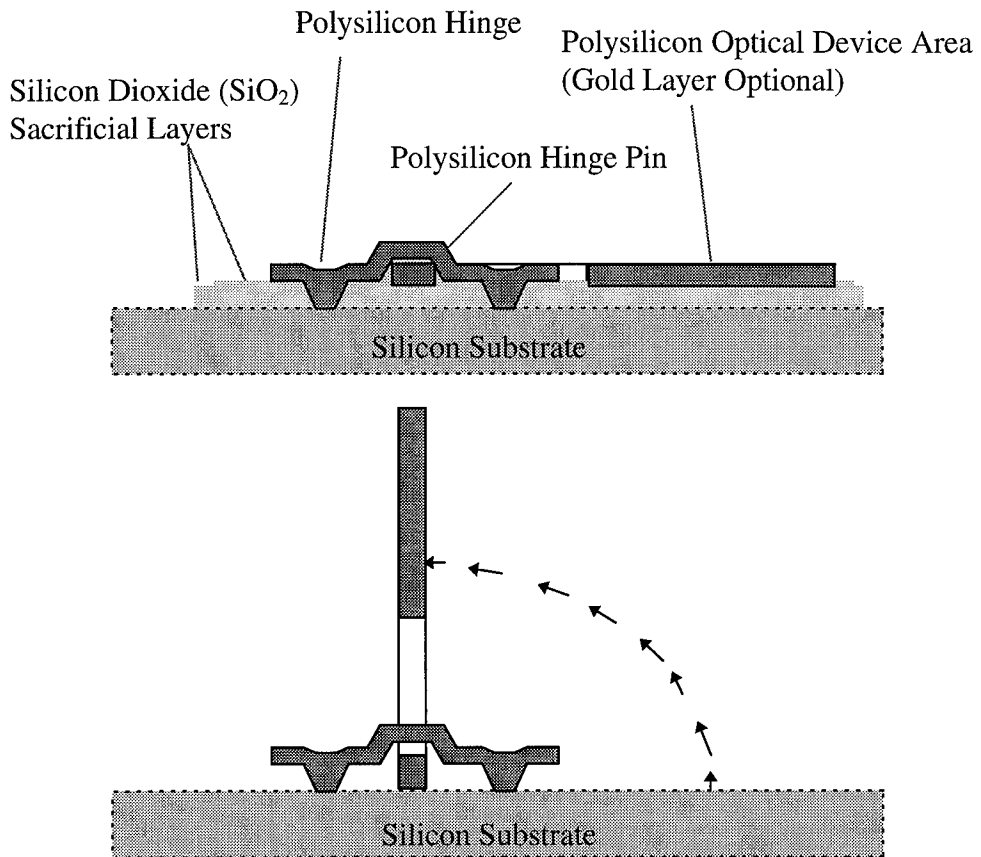


Figure 1-3. Schematic of how a structure can be fabricated using planar technologies and later “flipped-up” to create 3-Dimensional objects.

1.4.2. Systems

Two selected systems shall be studied utilizing established component designs. One of the systems shall be a micro-interferometer for use in optically modulating the amplitude of a light source. This system could be used with light sources that are coupled to a fiber, operate in free space, or emanate from a laser diode directly on the chip. The other system is a 1x2 fiber optic coupler for performing selective coupling between a single source fiber and two output fibers. This system may prove useful since coupling of single mode fibers is extremely sensitive to alignment.

1.4.3. Thermal Testing

Although MEMS testing has been performed on selected devices at various pressures, namely atmospheric to vacuum, current literature does not provide test results of devices operated at various temperatures. Temperature testing is important for understanding how certain devices will operate in severe environments. Of specific interest is the operation of FBMD's in a space environment when used for optical communication. Three devices have been selected for testing at temperatures above and below room temperature. The details of this testing are covered in Chapter 4.

1.5. Sequence of Presentation

This thesis is broken down into 6 distinct chapters in order to facilitate the coverage of what was accomplished. Chapter 2 begins with an investigation of the origins of micro optics and its application to the field of MEMS. Next, Chapter 2 takes an in-depth look at the particular MEMS fabrication process used for this research and highlights the key implications for its use in developing optical components. Chapter 2 concludes with a literature review of selected optical components, discusses what work in the field has already been accomplished and where the state of the art currently resides. Chapter 3 begins by covering well known MEMS devices that are of use in building MOEMS and describes their mathematical models. Next, the associated mathematical theory for each of the optical devices covered in this thesis is developed and discussed. Chapter 4 contains descriptions of the experimental setups and procedures used to test each optical device. This chapter further keys on the development of a variable temperature microscope-based laser probe interferometer for use in testing MEMS devices where sub micrometer measurements are required. Chapter 5 outlines the results

obtained from the numerous test setups discussed in Chapter 4. The results are broken down on a component by component basis with each device being described based on what was expected from theory versus what was observed by the experiment.

Conclusions and recommendations are discussed in Chapter 6 with emphasis on where further research can contribute and expand on the accomplishments of this thesis.

2. Literature Review

2.1. Historical Perspective

The idea for a MOB has been around since at least 1974 when work was performed to couple optical fibers to photodetectors using anisotropically etched v-grooves [15]. Recent work at the University of California, Los Angeles (UCLA) has demonstrated the ability to design and fabricate flip-up structures on a MOB, thereby expanding the realm of potential applications for this technology [12]. A representation of some of the possibilities for this work was shown in Figure 1-2. Since the advent of the laser, the macro optical bench has been used for numerous applications, both in the laboratory and in working systems. The optical bench utilizes a number of components such as: light sources - uncollimated/collimated, polarized/unpolarized, broadband or narrowband (one example is the laser); beam splitters - to separate the energy of a beam into two or more paths; mirrors - to redirect the beam along a different path; polarizers - to establish a set polarization of a beam; and waveplates - to change the polarization of a beam (linear, circular, or elliptical). Other components include: filters - to select a specific spectral band or component; nonlinear crystals - to change the spectral content of a beam; lenses - to modify a beam, by focusing or collimating; and diffraction gratings used to separate out the spectral components of a beam [16]. This is an overview of some of the primary optical elements that can be considered for potential miniaturization.

2.2. Architecture and Fabrication

2.2.1. Polycrystalline Silicon and Light Properties

In surface micromachining, the released structures are allowed to move freely according to the established design. One type of material often used for the released layers is polycrystalline silicon (polysilicon), pure silicon which contains numerous grain boundaries and is not of a single crystal form. The polysilicon material is typically heavily doped p-type, for reasons that shall be explained in Section 2.2.4, with a resistivity in the range of $1.84 - 2.72 \times 10^{-3} \Omega\text{-cm}$ [17]. In utilizing this material to build MOEMS it is important to look at some of its optical characteristics. Figure 2-1 shows a few of the important parameters as a function of optical wavelength in the visible region. The data is not for polysilicon but rather for bulk silicon. Although the data for polysilicon may be slightly different, this information provides at least a fundamental understanding of the trends for these important parameters. Ching, *et al.*, found that the reflectance of polysilicon was approximately 30 % at 500 nm and increased only slightly for longer wavelengths [18]. From Figure 2-1 it is observed that the reflectance, for bulk silicon, is approximately 34 % at 632.8 nm. These numbers, although at different wavelengths, appear to be in the same range. Since silicon has a room temperature bandgap of approximately (\sim) 1.12 eV, any radiation with a wavelength less than $\sim 1.1 \mu\text{m}$ is severely attenuated due to absorption [19]. This fact creates limitations for use of silicon micromachined devices in the infrared (IR) spectral region. One way to overcome this problem is to plate the surfaces of the devices with a metal such as aluminum or gold to increase the reflectance of the device. As will be discussed later, the MUMPS process

provides for a gold coating on the upper polysilicon layer and has been used effectively for making probe contacts, wiring, and mirrors.

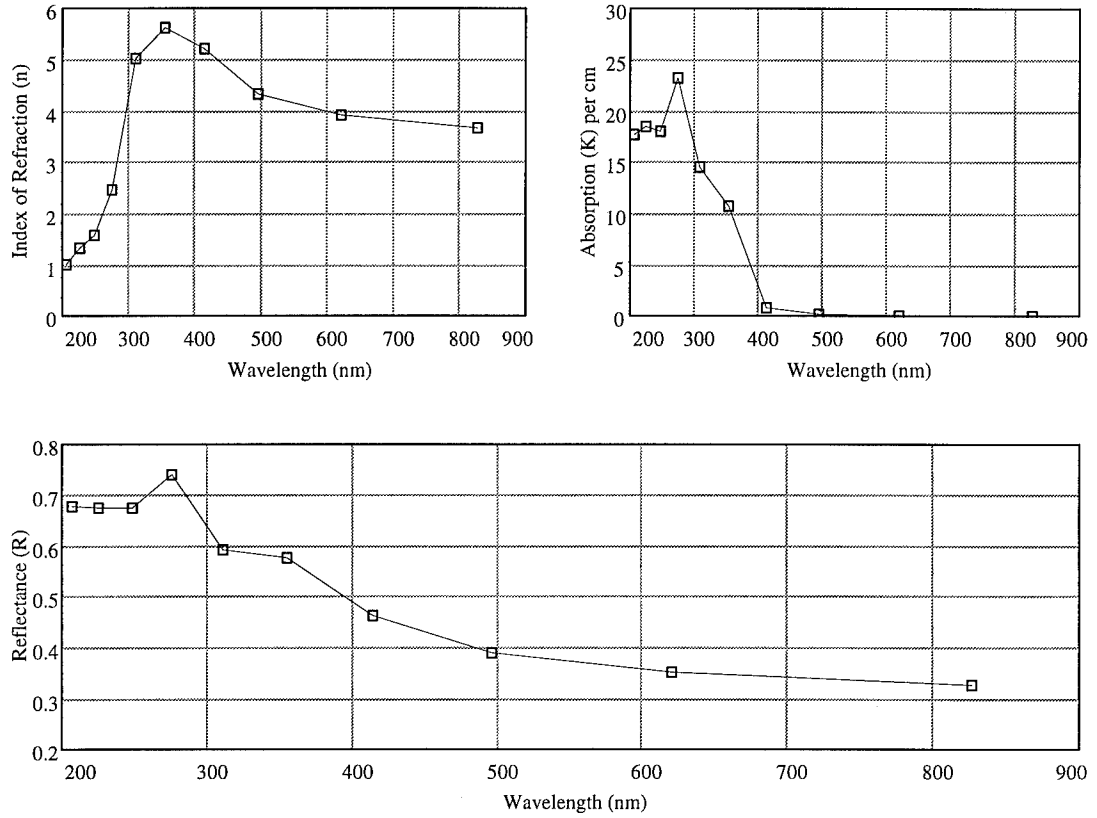


Figure 2-1. Characteristics of bulk silicon as a function of optical wavelength [20].

The index of refraction, n , of a material is also wavelength dependent and provides an indication of how electromagnetic waves are affected by different media.

Ignoring the wavelength dependence, n can be calculated as follows [16]:

$$n = \frac{c}{v} = \sqrt{\frac{\epsilon\mu}{\epsilon_o\mu_o}} \quad (2.1)$$

where:

c = the speed of light in free space;

v = the phase velocity of the wave in the medium;

ϵ = the relative permittivity of the medium;

μ = the relative permeability of the medium;

ϵ_0 = the permittivity of free space;

μ_0 = the permeability of free space.

This approach, using Maxwell's theory, treats matter as continuous by representing its electric and magnetic responses to applied E- and B-fields in terms of constants, ϵ and μ . Consequently, n is unrealistically independent of frequency. The fact that n is dependent on frequency is known as dispersion and to develop equations that relate the two requires incorporating some frequency dependent aspect of the atomic nature of matter. Using an atomic model and Newton's second law (sum of the forces equals the mass times acceleration) one can develop a second order differential equation that describes the effect on an atom due to an applied oscillating electromagnetic field [16]:

$$q_e E_o \cos \omega t - m_e \omega_o^2 x - m_e \gamma \frac{dx}{dt} = m_e \frac{d^2 x}{dt^2} \quad (2.2)$$

where: the first term is the driving force;

the second term is the opposing restoring force;

the third term is the damping force;

m_e = mass of the electron affected by the field;

q_e = charge of an electron;

ω_o = resonant frequency of the atom (ω is the frequency of the harmonic wave);

γ = damping constant;

E_o = the applied electric field;

x = displacement of the atom;

t = time.

From Eq. (2.2), the index of refraction is complex. In otherwords, it has both a real and imaginary part and can be described as [16]:

$$n^2(\omega) = 1 + \frac{q^2 N [(\omega_o^2 - \omega^2) + i\gamma\omega]}{E_o m_e [(\omega_o^2 - \omega^2)^2 + \gamma^2 \omega^2]} \quad (2.3)$$
$$n = \Re e(n) + \text{Im}(n)$$

where: N = number of contributing electrons per unit volume;

The complex part of the index of refraction is known as absorption. Absorption has an associated wavelength dependence and units of inverse length. In terms of its effect on a propagating electric field, the absorption is described as a decaying exponential of the electromagnetic wave [16].

All of these terms are important to consider when evaluating a material for use in an optical instrument. The primary driver for material selection might be the device manufacturability, but the wavelength of interest might require, for example, coatings to increase the reflectance or minimize the absorption.

Table 2-1 demonstrates the incredible mechanical strength of silicon which makes it an ideal candidate for MOEMS. Although brittle like a ceramic, silicon displays a hardness and yield strength greater than steel yet has 1/3 the density. This allows for rather large plates to be fabricated that can be self supporting with minimal deformation due to weight. Furthermore, *microhinges*, like those shown in Figure 1-3

can be made to hold rather large structures down onto the substrate with a minimal length of hinge material.

Micromachining of GaAs has recently been demonstrated [21] and would be an ideal candidate for MOEMS. The direct bandgap of GaAs based compounds is used extensively for solid state optical components such as the Light Emitting Diode (LED) and the laser diode [19]. Coupling MEMS with these optical components would provide numerous MOEMS applications. Although mentioned in this review, no exploration of GaAs based MEMS devices is conducted for this thesis.

Table 2-1. Selected Mechanical Properties of Silicon [5,22].

Material	Yield Strength	Knoop Hardness	Young's Modulus	Density
	(10^{-10} dyne/cm ²)	(Kg/mm ²)	(10^{12} dyne/cm ²)	(grams/cm ³)
Diamond†	53	7000	10.35	3.5
Silicon (Si) †	7.0	850	1.9	2.3
Stainless Steel	2.1	660	2.0	7.9

† Single Crystal

2.2.2. *Electrostatic versus Thermal Structures*

The electrostatic driven systems work much like a capacitor in which the two plates are attracted to each other relative to the voltage applied. This is the primary drive mechanism utilized in the micromirror arrays and the comb-drive actuators. In the case of micromirrors, the lower plate of the capacitor is attached to the substrate and does not move. The upper polysilicon surface, that is metal plated in order to act as the mirror surface, forms the movable capacitor plate [23]. The mirror is suspended above the lower plate by springs (very thin polysilicon runners) that flex to allow the mirror to move. The spacing between the two plates is on the order of 0.5-2.5 μm which allows for greater

than 2π of phase movement in the visible spectrum (400-800 nm) [23]. A typical mirror of this design is known as a Flexure Beam Micromirror Device (FBMD) and is shown with a Scanning Electron Microscope (SEM) micrograph in Figure 2-2. A schematic of what the device looks like in both the static and actuated states is outlined in Figure 2-3.

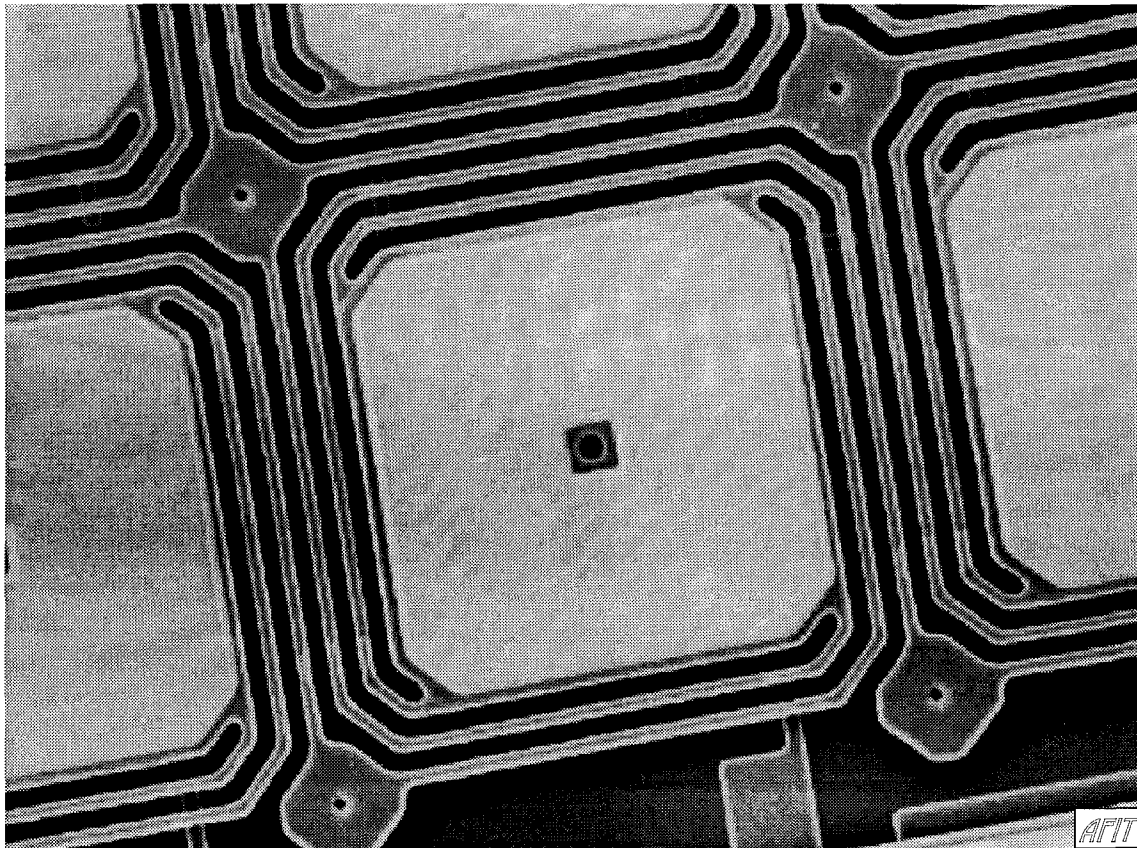


Figure 2-2. Scanning electron micrograph of a square Flexure Beam Micromirror Device array [23].

Thermally driven structures utilize the coefficient of thermal expansion for the material, in this case polysilicon, to force a change in displacement. This device can be mounted to designs in various configurations to achieve the desired movement. AFIT has built thermal actuators as shown in Figure 2-5 that can be deflected up to $12\ \mu\text{m}$ [11].

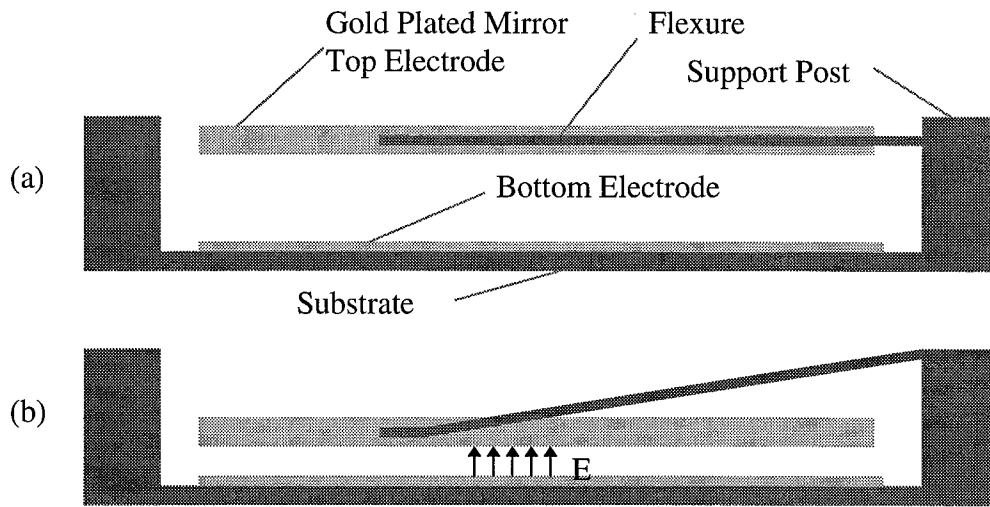


Figure 2-3. Schematic of a Flexure Beam Micromirror Device in the (a) resting and (b) activated modes.

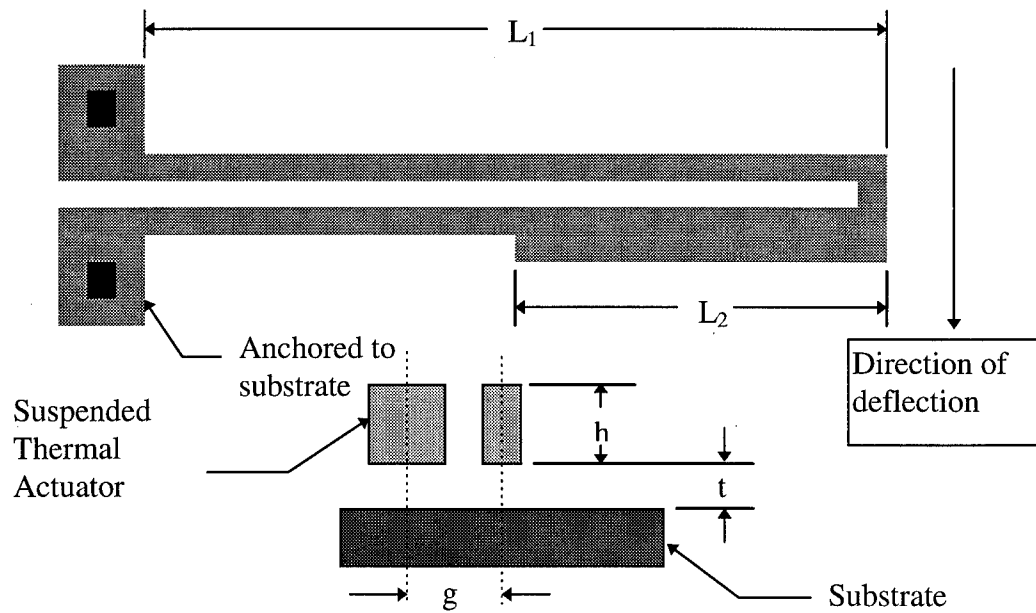


Figure 2-4. Schematic of a thermally driven actuator. Pictorial concept from [24].

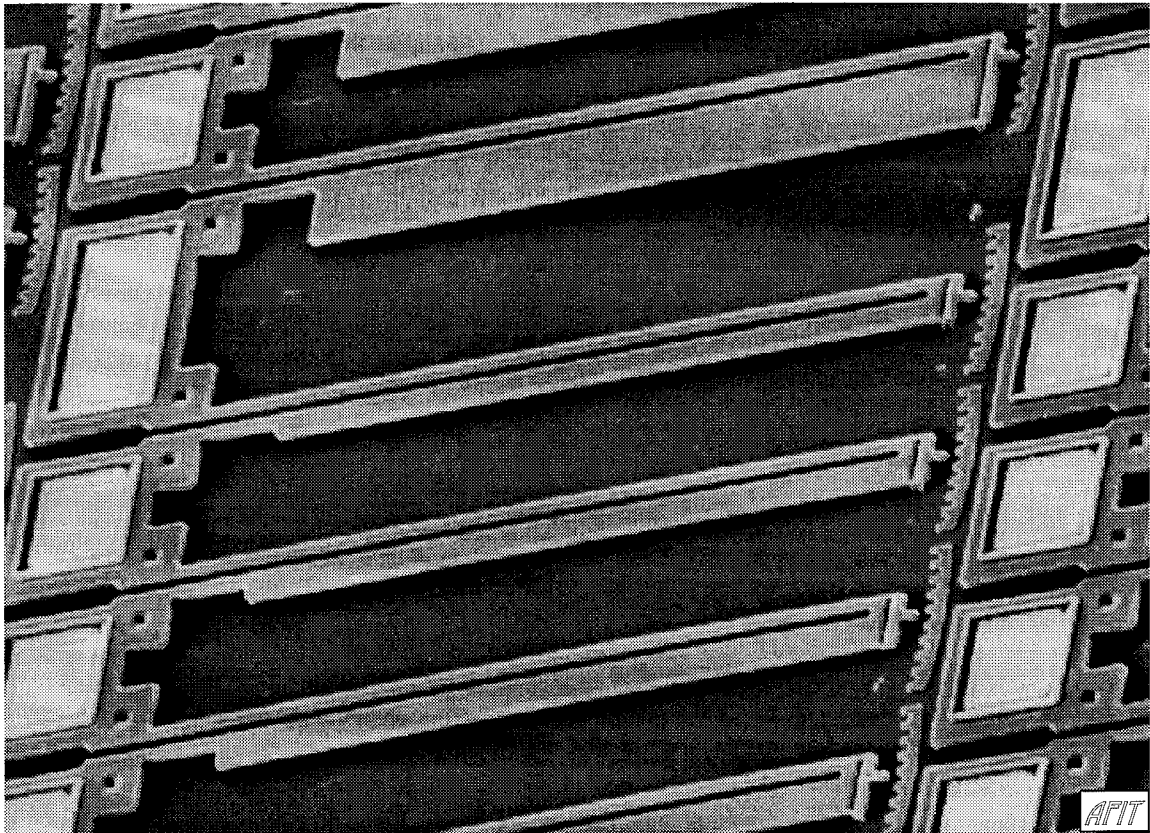


Figure 2-5. Scanning electron micrograph of thermally driven actuators from MUMPS 6.

The basic layout of the device is shown in Figure 2-4. Making one leg of the device thicker causes the other leg to grow due to thermal expansion and the device to deflect in the direction shown [24].

2.2.3. Flip-up versus Surface Structures

Surface structures can be either electrostatically or thermally driven. The diffraction grating array principle, a surface structure that is electrostatically driven, has been used to perform spectral separation in an attempt to develop a high definition display [25]. This device shall be discussed in Section 2.3.2 since it has the potential for spin-offs in other applications and variations of this device have been designed in support

of this thesis.

The flip-up structures, like those shown pictorially in Figures 1-2 and 1-3, offer the ability to develop vertically integrated devices such as spectrometers, spatial filters, and beam deflectors. Crucial to the design and development of flip-up structures is the concept of a *microhinge* [26]. *Microhinges* have been designed for connecting polysilicon plates to the substrate and for hinging two plates completely off of the surface of the substrate. The layout of both of these types of hinges is shown in Figure 2-6. A 3-dimensional view of how the layers come together to form a substrate hinge is shown in Figure 2-7. *Microhinges* provide the primary mechanical connections that allow for the development of structures in the 3rd dimension away from the plane of the chip.

Although the layout of *microhinges* has been well established, the true difficulty in utilizing 3-dimensional structures rests in the post fabrication process of assembly. Post fabrication assembly has so far proven to be a delicate operation that requires a micromanipulator probe station, a set of clean probes, and a patient operator with a delicate hand. Some relief for this operation may soon be on the way as devices begin to be designed to assist the assembler. Slider devices and springs that can be used to erect flip-up structures have already been demonstrated and provide some of the initial ideas for the "assembly helper" designs used in this thesis [27]. So far the published devices have all been mechanically flipped-up with no known reporting of flip-up structures that are electrically or thermally activated. A sound approach to flipping-up vertical structures using electrostatic and/or thermal techniques has not yet been shown in the literature. One proposed mechanical lifting technique is the use of a *flip-Jack*, where a probe tip is

assisted in the lifting process by a released stringer made from one of the polysilicon layers [28].

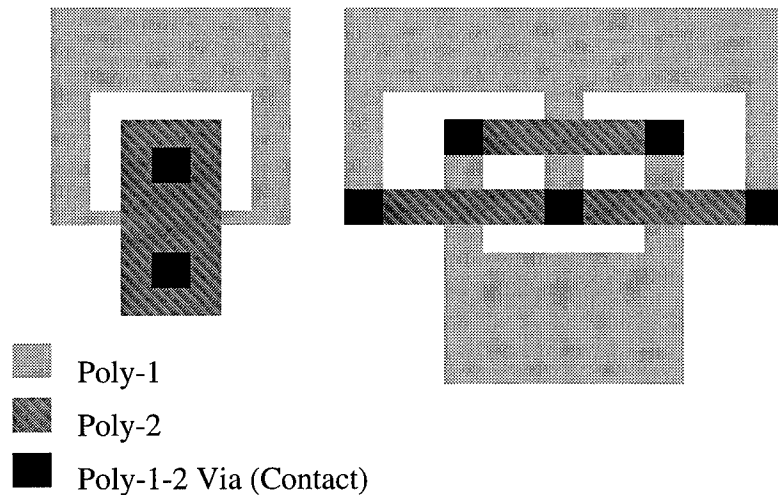


Figure 2-6. Two basic hinge types for flip-up structures. (A) A substrate hinge, which anchors flip-up structures to the substrate. (B) A scissor hinge, which allows attachment of two or more flip-up structures above the substrate [26].

Since the polysilicon is extremely flexible, on such a small scale, it has been observed to bend upwards of $50\ \mu\text{m}$ into the air for a stringer $200\ \mu\text{m}$ long, $5\ \mu\text{m}$ wide and $2\ \mu\text{m}$ thick. This allows for the lifting of the selected device enough to allow another probe to be inserted under the device to lift it into place. The *flip-Jack* can even be made with a lock, in order to free up the probe tip for use in other operations. Another reported technique for assisting in assembling flip-up structures is the use of hydrodynamic forces in a water rinse to drive the structures into the upright and locked position. This technique has been labeled *Water Assembled MicroStructures (WAMS)* and has been demonstrated at the UCLA with some limited degree of success [29]. The use of *WAMS*

appears to be more relevant when the geometry of the devices is large since the hydrodynamic forces have not been strong enough to flip-up $\sim 50 \mu\text{m}$ square structures tested at AFIT.

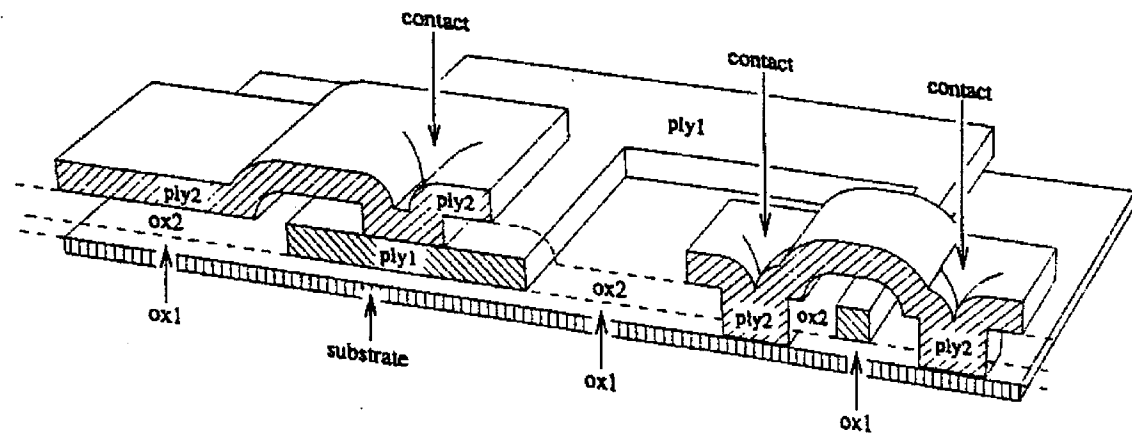


Figure 2-7. Cross section of a substrate hinge. Fabricated as follows: First, the lower sacrificial layer (ox1) is deposited, then polysilicon (ply1) is deposited and patterned into the desired shapes. The second sacrificial layer (ox2) follows on top and finally the last polysilicon layer (ply2) is deposited and patterned. The sacrificial layers are removed using release etchant [29].

Another extension for flip-up structures is the development of articulated micro-robots. These devices have been proposed for development with multiple degrees of freedom, workspaces on the order of a cubic millimeter, and payloads on the order of a milligram. Devices of this nature utilize similar flip-up system techniques such as microhinged polysilicon plates and scissor hinges that are completely released from the substrate. The paper by Yeh, *et al.*, discusses micro-robots and additional concepts for providing assembly of structures that move out of the plane of the substrate [30].

2.2.4. Device Design and Processing

As mentioned in Chapter 1, MOEMS devices are laid out at AFIT using the Cadence® design tool. Devices are specifically designed for fabrication at MCNC using MUMPS and its associated design rules [14]. This process is supported by the Advanced Research Projects Agency (ARPA) as part of an effort to build a MEMS infrastructure program to provide easy access to advanced MEMS technology and a standard fabrication process [31]. A cross-section of the MUMPS layers is outlined in Figure 2-8 along with the corresponding descriptions and nominal thicknesses. This fabrication process was adapted specifically for producing MEMS devices. It consists primarily of two polysilicon releasable surface layers (Poly1 & Poly2), which form the actual devices of interest, and 2 sacrificial layers (1st Oxide & 2nd Oxide), also known as phosphosilicate glass (PSG) 1 & 2, which are etched away in order to release the Poly1 & Poly2 structures. The other layers provide electrical contact paths, mounting to the substrate and passivation of the silicon surface. Limitations of this fabrication process include: only two releasable structural layers and no control over the process parameters (i.e. layer thickness, conductivity, and materials used).

MCNC deposits MUMPS polysilicon layers using Low Pressure Chemical Vapor Deposition (LPCVD) at temperatures greater than 600 °C. Polysilicon thin films can be deposited in either a doped or undoped state which helps determine the mechanical properties of the layer. Typical LPCVD grown polysilicon layers contain large amounts of residual stress (~ 175 MPa) which can cause deformation of the released structures and therefore require some amount of thermal annealing. Doped polysilicon can be thermally

annealed at a lower temperature than undoped polysilicon and is therefore preferred for use in the fabrication of MEMS devices.

Chips fabricated at MCNC are encased in SiO₂ sacrificial layers and coated with photoresist which helps to protect the die during shipment. Upon receipt of the chips, the photoresist must be removed prior to etching away the sacrificial layers which releases the MEMS devices. A 3-5 minute rinse in acetone has proven to be sufficient in removing the photoresist coating. Afterwards, the sacrificial layers of SiO₂ must be removed utilizing some type of etchant. Etchants come in two primary classes, dry and wet. Wet etching is the traditional method, and the method most often used since dry etching usually involves high temperatures or use of RF energy that may damage the MEMS devices. The typical etchant for silicon dioxide is a buffered oxide etchant (BOE) consisting of HF and NH₄F (with a volume ratio of 1:8). Caution must be taken when utilizing BOE since it will attack aluminum films and cause bonding problems in the packaging process [32]. If aluminum pads exist then the preferred etchant is a solution of NH₄F and CH₃COOH (1:2) [33]. At AFIT, straight 49% HF is used to etch away the sacrificial layers of the MUMPS die.

Material parameters from each of the fabrication runs are provided by the manufacturer and are often required in the device models that will be discussed in Chapter 3. The material parameter results for die used in this thesis research are included in Chapter 5.

AFIT students and faculty have used MUMPS to develop over 25 die in the last two years. Design techniques specific to the process have been developed that were used

as common practice in designing devices for this thesis [35].

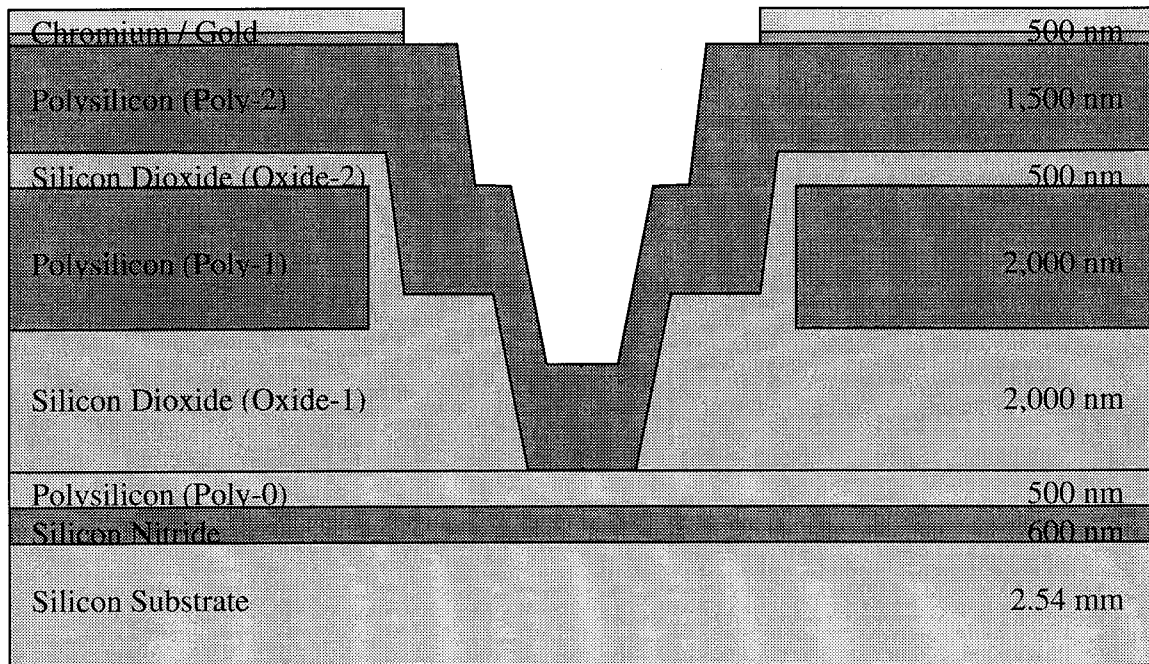


Figure 2-8. Proportional cross-section of the MCNC MUMPs Process [14].

2.3. *Micro-Optical Devices*

2.3.1. *Micromirrors*

Configurations for this device have been demonstrated in both flip-up and surface structures. The surface devices typically utilize polysilicon springs and electrostatically driven plates to change the phase characteristics of a light beam.

Light can be described in many different ways and special types of light have nice mathematical descriptions. In the case of a communication beam, the light source is usually a laser, from which light is coherent, collimated and polarized. There are

different types of polarization, and by observing the spatial change of the electric or magnetic field of the light one can determine its polarization. But, of greater importance in communication is the fact that the light is collimated (i.e. all the rays are parallel) and spatially coherent (i.e. the phase is constant for every lateral slice across the beam). In this case the field can be described by a plane wave as [16, 34]:

$$\psi(x, y, z, t) = Ae^{i[k(\alpha x + \beta y + \gamma z) - \omega t]} \quad (2.4)$$

where: A = amplitude;
 k = wave number ($2\pi/\lambda$);
 α, β, γ = directional cosines.

When communicating through the atmosphere, this perfect plane wave is distorted by turbulence in the air. It is a well known fact that this atmospheric turbulence effects the communication beam's phase front and AFIT has built array's of micromirrors in hopes of utilizing their small size and rapid response characteristics to correct the distorted phase front. The latest device is a hexagonal micromirror array with 127 elements as partially shown in Figure 2-9. These devices can be characterized with the microscope-based laser probe interferometer set-up which was originally designed by Rhoadarmer, *et al.*, and further refined by Michalick [36,23]. The interferometer set-up, as shown in Figure 2-10, allows for the characterization of individual mirror elements for such characteristics as: frequency response, deflection vs. voltage, and nonuniformities in the deflection vs. element location. Extensive work has been performed at AFIT and other locations on modeling these devices [23,36-41].

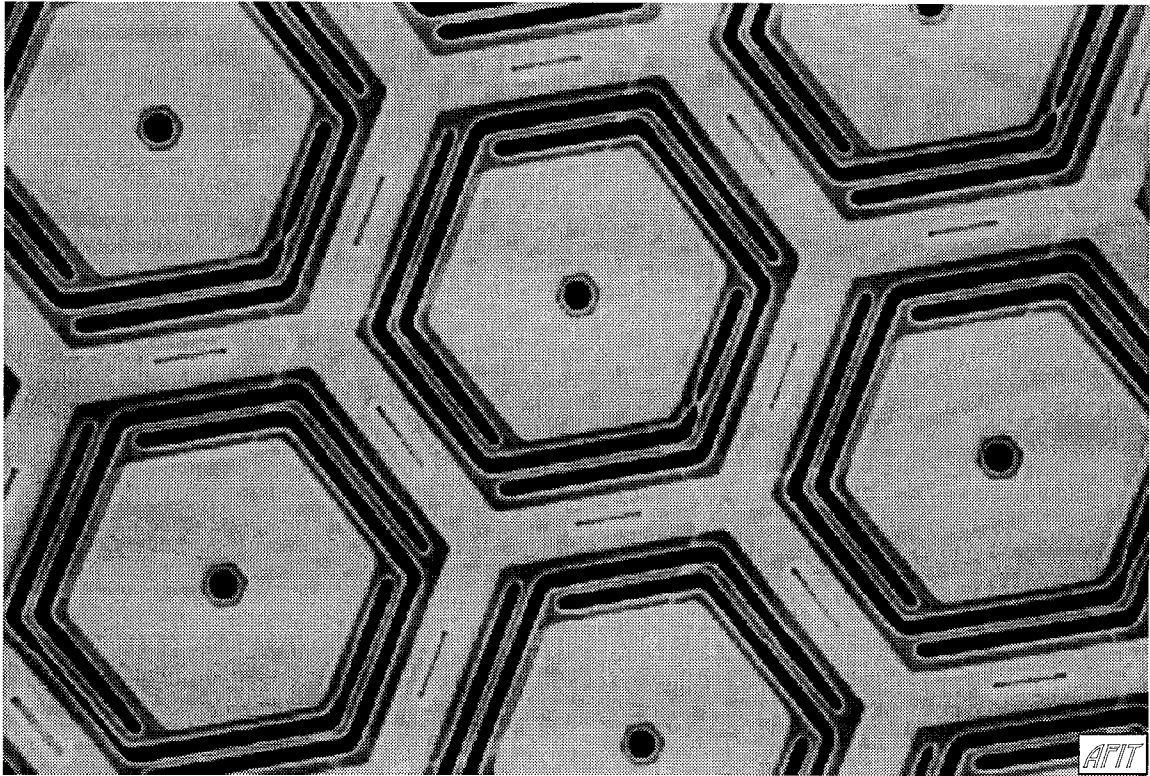


Figure 2-9. Scanning electron micrograph of a hexagonal micromirror array [23].

2.3.2. *Diffraction Gratings*

A diffraction grating can also be utilized to perform spectral selection, yet it utilizes a different physical principle. Diffraction was defined by Sommerfeld as “any deviation of light rays from rectilinear paths which cannot be interpreted as reflection or refraction” [34]. One would initially expect that light that passed through a square aperture would project a square pattern of proportional dimensions on a screen placed in the far field. But due to the effects of diffraction, the intensity observed in the far field exhibits some edging effects that “blur” the square pattern. A representation of this far field intensity pattern for a square aperture is shown in Figure 2-11.

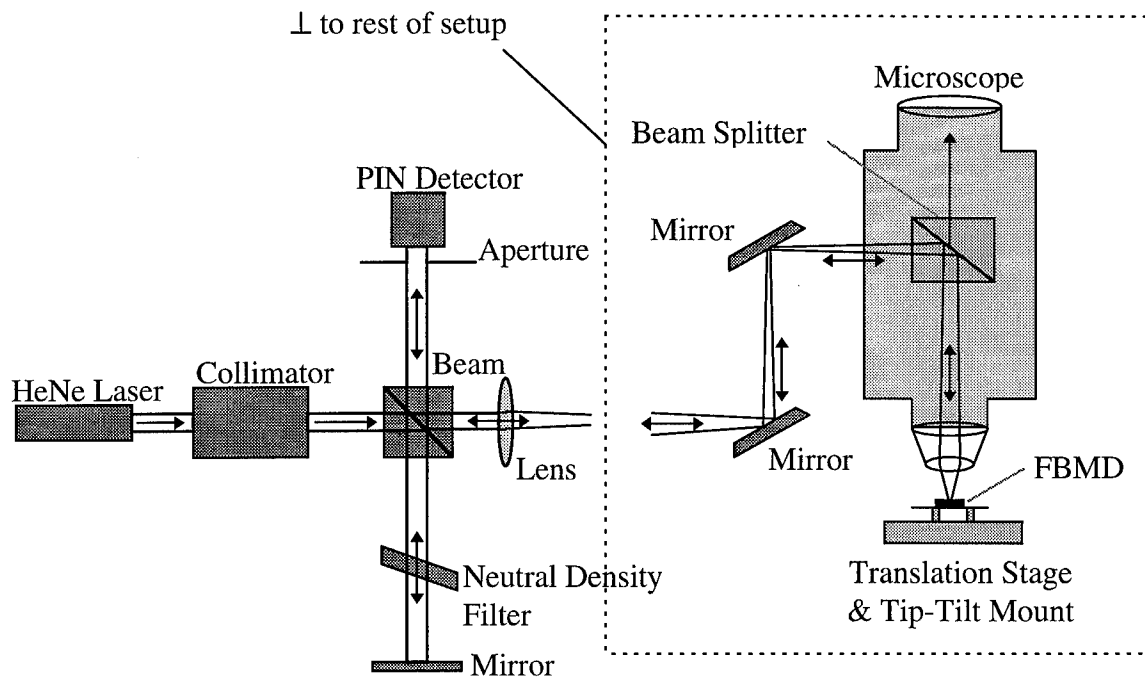


Figure 2-10. Schematic of microscope-based laser probe interferometer setup used to measure deflection of devices that move out of the plane of the substrate [36].

As mentioned previously, a diffraction grating array can be used as a high definition display. Each array element is considered a grating light valve since it turns on/off one of the primary spectral colors (i.e. red, green, or blue) as will be discussed later in Chapter 3. This thesis explores the development of grating pixels that could be used to steer a light beam of set wavelength into different angles using mechanical actuation from a thermally driven actuator. Furthermore, these pixels could be used to replace the function of the three grating light valves required to produce the primary spectral colors. In this case the desired modulation could be obtained at the desired angle by adjusting the mechanical mechanism of the grating pixel.

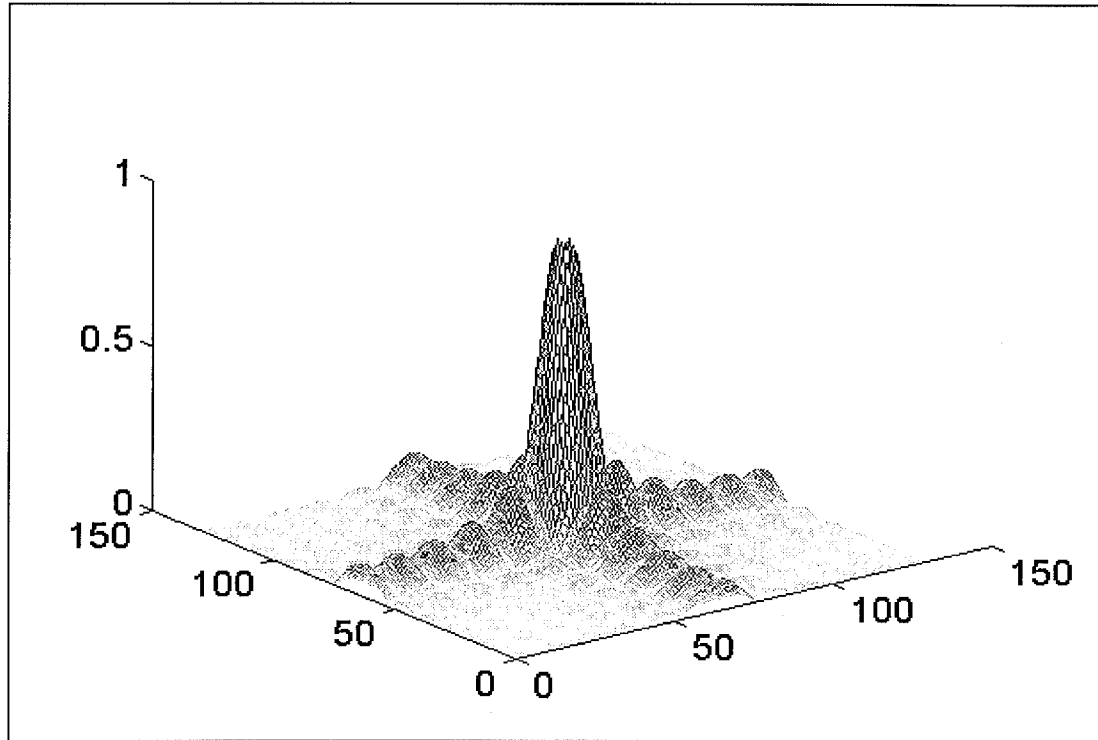


Figure 2-11. 2-D rectangular sinc function. Normalized Fraunhofer diffraction pattern from a 10x10 rectangular aperture in a 128x128 array.

A pictorial representation of the diffraction grating array is shown in Figure 2-12. The suspended grating can be electrostatically pulled down to adjust the amount of diffraction. Diffraction gratings are the basic elements used in monochromators and spectrometers to perform spectral separation. A micro-spectrometer has been fabricated using LIGA, an acronym for lithography, electroforming, and micromolding (the acronym came from the German process names: lithographe, galvanofornung, and abformung) [24,42], but no record exists of an attempt to use micromachined flip-up surface structures.

More elaborate gratings can be created using the MCNC process in which the grating period is allowed to change or have more than two surfaces for diffraction. Using the actuation techniques already discussed, moveable gratings can be developed in order to vary the period dimensions. These more detailed types of gratings require special analysis that is beyond the simple grating equation.

2.3.3. *Fresnel Lenses*

The Fresnel zone plate (or Fresnel lens) appears to have been invented by Lord Rayleigh in 1871 [16]. Since that time Fresnel lenses have been developed for use in everything from overhead projectors to stop lights.

Micro-Fresnel lenses have been fabricated on a MOB and effectively utilized to collimate the light from an edge emitting laser diode as shown in Figure 2-13 [12]. Furthermore, Fresnel lens arrays have been used to perform beam steering for micro-optical scanners by moving one array relative to the other in a sandwich arrangement [43]. These 200 μm x 200 μm Fresnel lenses were fabricated out of fused quartz with greater accuracy than is achievable with polysilicon surface micromachining. Fresnel lenses can be utilized to focus collimated light of a narrow bandwidth.

2.4. *Micro-Optical Systems*

2.4.1. *Interferometers*

The basic concept of an interferometer is based on detecting the optical path difference (OPD) between two light paths. Utilizing flip-up structures it should be possible, in principle, to design a micro-interferometer. Utilizing a beam splitter, a single light source would be split into two paths of equal energy. One leg of the interferometer

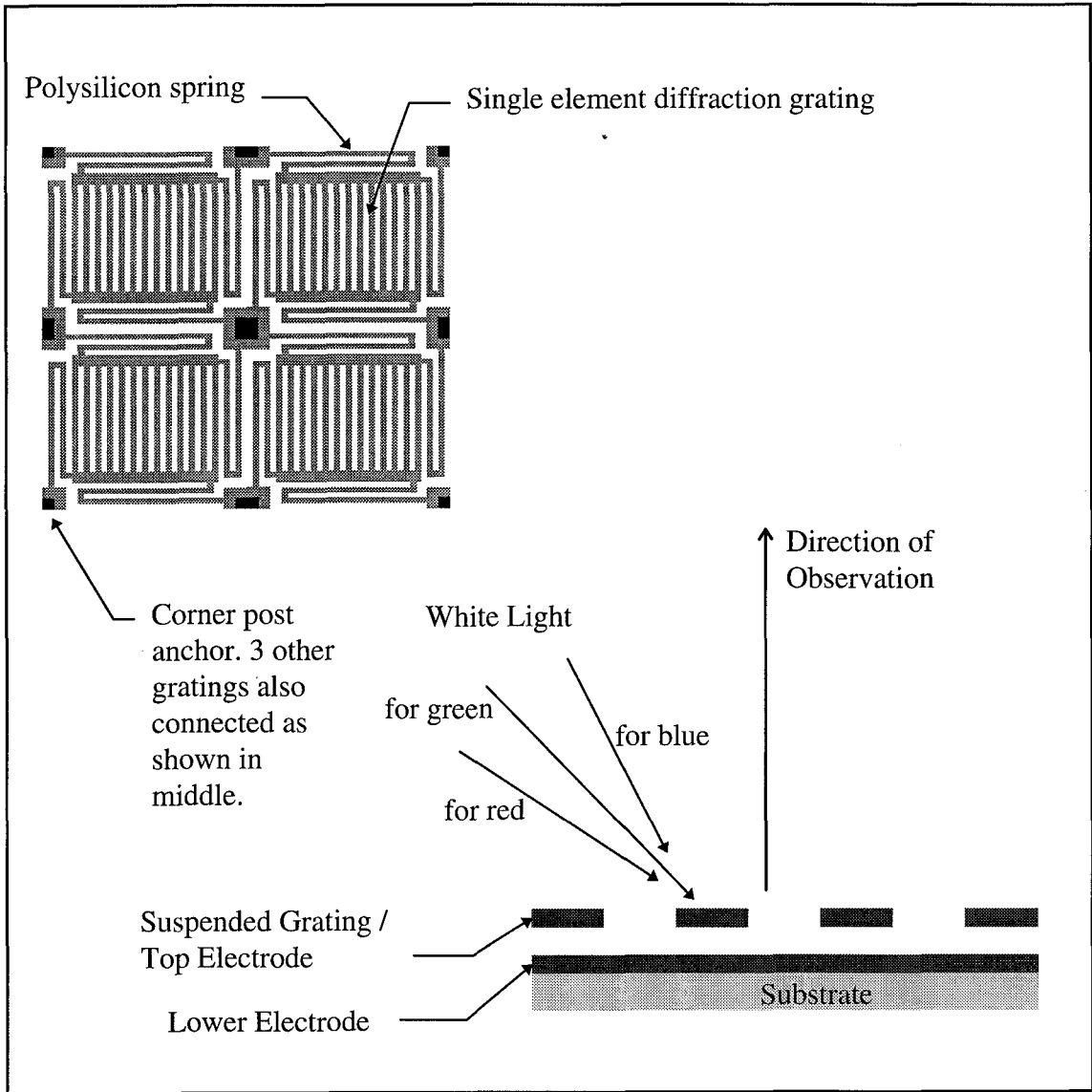


Figure 2-12. Example of a grating array.

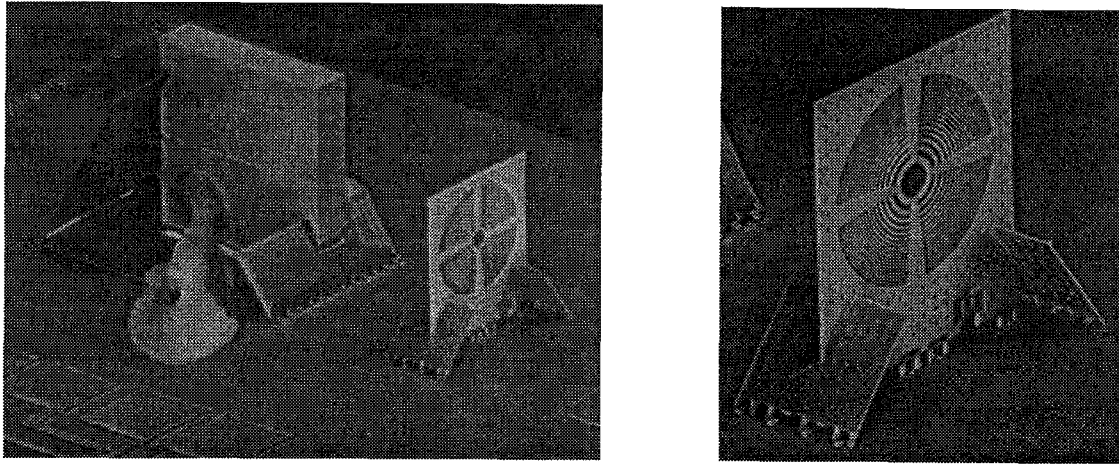


Figure 2-13. Sample Fresnel lens with precision locks. From work performed at the University of California, Los Angeles [12].

would have a stationary mirror while the other leg would contain a location for test samples and an adjustable mirror. The beams are brought back together to form an interference pattern. At an observation screen the interference is characterized by a fringe pattern. The coherence length of a source, the refractive index of a substance, and other measurements can be made with this type of device. The difficulty arises in trying to develop a micro beam splitter out of polysilicon since half of the energy of the beam has to be transmitted and the other half reflected in order to create the two beam paths. On a macro-optical table the beam splitter is usually a piece of glass that is coated with a partially reflecting material in which a portion of the energy of the oncoming beam is passed and the other portion is reflected. In the case of micro-optics, a piece of glass is not available on the surface of the chip, but a diffraction grating should work as a beam splitter by passing equal amounts of energy into the same order (i.e. $m = +1$ and $m = -1$). This idea has already been conceptually proven in the LIGA interferometer research that was mentioned earlier [42].

2.4.2. Optical Switches

Modulating the amplitude of an optical beam is essential in fiber optic communication. Recently, a micro-optical chopper was fabricated using surface and bulk micromachining (Fig. 2-14). This device had an etched channel for interfacing with an optical fiber and used a electrostatic comb drive actuator to cycle a shutter across the aperture achieving greater than 2 KHz of output modulation. The device was further operated under vacuum and displayed increased movement ($400\ \mu\text{m}$ versus $30\ \mu\text{m}$) with a decrease in drive voltage ($5\ \text{VDC}$ & $3.8\ \text{VAC}_{\text{p-p}}$ versus $50\ \text{VDC}$ & $20\ \text{VAC}_{\text{p-p}}$) [18]. Etched channels and flip-up micromirrors have also been considered for coupling a semiconductor laser and a fiber optic cable [44]. This technique could be used to perform amplitude modulation by rapidly adjusting the flip-up mirror. Although this type of device is not investigated explicitly in this thesis, it provides another example of the use of MEMS in optical applications.

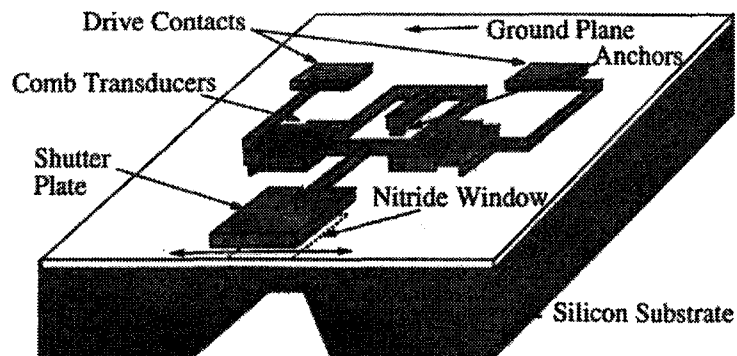


Figure 2-14. Schematic of a micro-fabricated optical chopper [18].

2.4.3. Fiber Optic Couplers

Hewlett-Packard has developed a 1x2 thermally actuated optical fiber switch that utilizes both bulk and surface micromachining techniques [45]. The switch included a thick (25-50 μm) electroplated nickel actuator to move a single-mode optical fiber and a 37.5 μm deep trench that was anisotropically etched in the silicon for alignment of send and receive optical fibers. The switch allows for coupling without the use of waveguides or lenses in order to achieve a low-loss switching function. The switches used the edges of the anisotropically etched grooves for fiber alignment and thermal isolation trenches on the "hot" side of the actuators to increase deflection capability. In order to couple the one fiber to both of the other stationary fibers movement of $>125 \mu\text{m}$ was required out of the actuators. Such a large deflection distance was achieved by making the actuators extremely long and narrow ($\sim 1 \text{ cm} \times 900 \mu\text{m}$). The devices were fabricated on 4 inch diameter $\langle 100 \rangle$ Si wafers. Figure 2-15 provides a schematic representation of the layout used for this device.

An extension to this type of work is the idea of utilizing surface micromachined mirrors for laser-beam positioning [46]. In this case the mirror is flipped up and then used to align the output of a surface emitting laser to a wafer bonded fiber. A flip-up mirror can also be used to create a fiber data distribution interface (FDDI) by directing the light beam for coupling between selected fibers. This technique has been demonstrated at UCLA using an X-shaped, four fiber pattern with a mechanically operated sliding flip-up mirror [47].

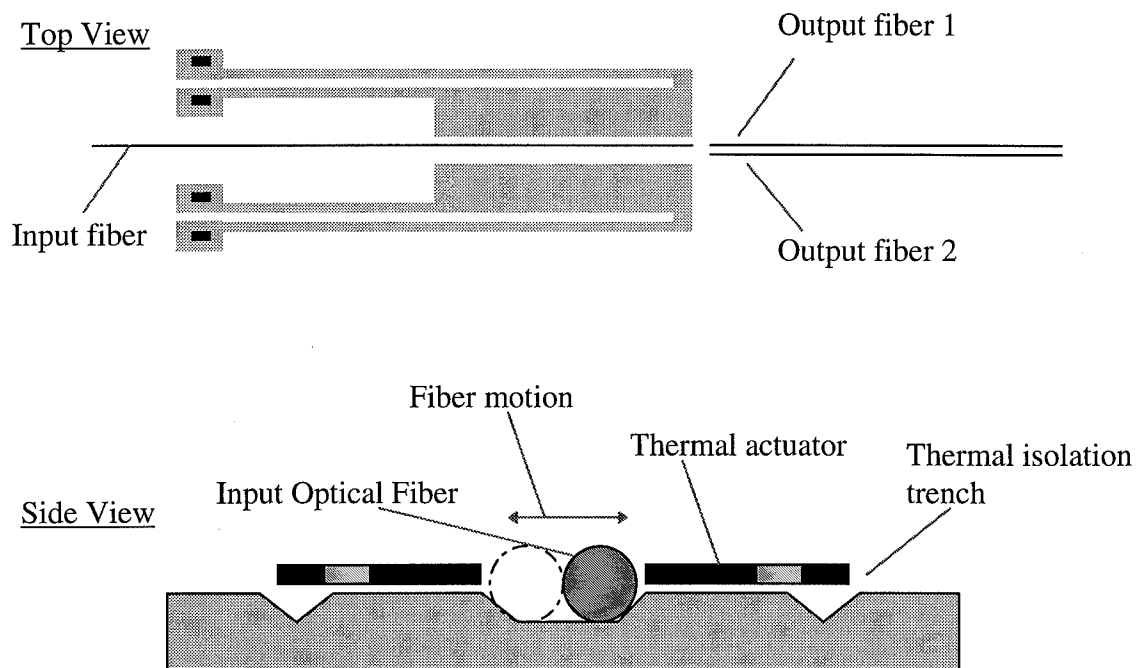


Figure 2-15. 1x2 fiber optic coupler [45].

2.4.4. Fabry-Perot Etalons

Three-dimensional tunable Fabry-Perot etalons have been fabricated and reported in the literature [48,49]. A paper by UCLA reports on using both rotating and translating flip-up mirrors for tuning [48]. Transmission peak wavelength shifts of 32 nm for the rotating mirror and 103 nm for the translational mirror have been observed. In both cases the translation was performed by mechanical probing. These devices still need to be integrated with some form of drive mechanism. The ability to cascade the flip-up mirrors in order to decrease the full-width-at-half-maximum (FWHM) yet maintain the free-spectral-range (FSR) was also investigated. Devices were tested with 1.3 μm light to minimize the absorption from the polysilicon.

A surface micromachined Fabry-Perot modulator has been proposed by using a two layer process similar to MUMPS [49]. In this case the air gap is provided between the polysilicon first and second layers as shown in Fig. 2-16. The modulator was optimized for 1.3 μm and intended for fiber-in-the-loop applications. By moving the upper polysilicon plate electrostatically, the air gap distance is changed which modulates the reflected light through interference from the two polysilicon surfaces.

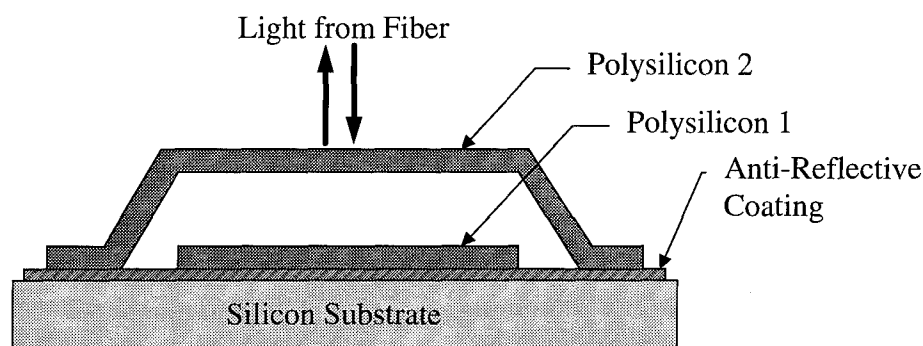


Figure 2-16. Cross section of the Fabry-Perot modulator, where the fixed mirror is formed by the polysilicon 1 layer and the movable mirror by the polysilicon 2 layer [49].

2.5. Summary

This chapter has covered in detail a number of the relevant developments in the field of MOEMS. Specifically covered were the concepts of hinged structures and their use in the development of a MOB. The fabrication process to be used for this thesis was reviewed and the post processing steps that are taken at AFIT were explained. Finally, some key optical devices and systems that are well suited to miniaturization using MOEMS concepts were examined, such as the Grating Light Valve, the Optical Switch, and the 1x2 Fiber Optic Coupler.

3. Theoretical Review

This chapter develops in detail the mathematical descriptions for the operation of devices investigated in this thesis. These derived models provide the theoretical results for comparison with the experimental data in Chapter 5. In using the microscope-based laser probe interferometer the experimental data required mathematical manipulation in order to evaluate the output. The manipulation of the experimental data from this setup is described in Section 3.1. Component and system theory follow in Sections 3.2 and 3.3. Theoretical data, developed from these models, was generated using both Mathcad and Matlab software packages [50,51].

3.1. Microscope-Based Laser Probe Interferometer Theory

An interferometer operates by utilizing a split coherent laser beam that recombines either constructively or destructively due to phase interference. Referring to Fig. 2-10, one leg of the interferometer is known as the reference leg since it has a fixed length and therefore the light travels a set distance before being recombined with the light from the object beam at the detector. The object beams path length is modulated by the device under test and therefore the phase of the beam at the detector changes proportional to the modulation. Using a phasor representation of the reference and object beams, the detector output can be equated to a change in phase. The light intensity at the detector is described by:

$$I = |\vec{S}|^2 = |\vec{R} + \vec{D}|^2 \quad (3.1)$$

where \vec{R} is the reference phasor and \vec{D} is the object phasor from the two legs of the

interferometer. As shown in Fig. 3-1, choosing set directions for the two phasors in an orthogonal plane allows for the following descriptions for the two phasors:

$$\vec{R} = R\hat{x} \quad (3.2)$$

$$\vec{D} = D \cos\theta\hat{x} + D \sin\theta\hat{y} \quad (3.3)$$

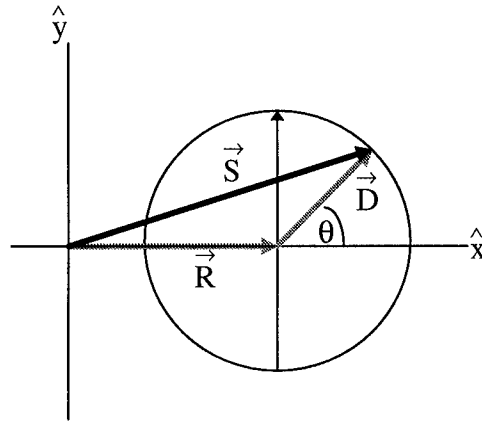


Figure 3-1. Phasor representation of the summation for the reference and object beams of the microscope-based laser probe interferometer [36].

Substituting Eq. (3.2) and (3.3) into Eq. (3.1) yields:

$$I = R^2 + 2RD \cos\theta + D^2 \quad (3.4)$$

As the detector output is modulated, the maximum (I_{max}) and minimum (I_{min}) intensity values obtained correspond to the sum and difference of the magnitudes for \vec{R} and \vec{D} .

From Fig. 3-1 it follows that:

$$\begin{aligned} \sqrt{I_{max}} &= \vec{R} + \vec{D} \\ \sqrt{I_{min}} &= \vec{R} - \vec{D} \end{aligned} \quad (3.5)$$

Combining with Eq. (3.4) yields a relationship for the phase of the output with respect to an arbitrary intensity value between I_{max} and I_{min} [36].

$$\theta = \cos^{-1} \left(\frac{2I - I_{\max} - I_{\min}}{I_{\max} - I_{\min}} \right) \quad (3.6)$$

When using the laser probe interferometer to measure deflections of micro-optical devices it is necessary to sweep through at least π radians in phase in order to use Eq.

(3.6) since both the maximum and minimum intensity values must be known.

Furthermore, Eq. (3.6) only generates data between 0 and π radians (with a π ambiguity)

which requires the output to be pieced together to form the complete phase change

profile. This analysis is conducted using a program written by Michalicek [23] in which

device deflection versus voltage is calculated using

$$d = \frac{\lambda}{2} \left(\frac{\theta}{2\pi} \right) \quad (3.7)$$

where d is the amount of deflection for a known voltage and λ is the wavelength of the

laser used in the microscope-based laser probe interferometer (in this case $\lambda=632.82$ nm).

Adjustments are made for the π ambiguity plus any signal shift that exists due to

capacitive losses in the instrumentation [23].

3.2. Component Theory

3.2.1. The Flexure Beam Micro-Mirror Device

Recent work at AFIT has generated an advanced model for the operation of this particular device which takes into account fringing losses by utilizing a Schwartz-Christoffel transformation [23]. This thesis, however, investigates devices which have surface areas that are larger than those where fringing losses are a factor. For this reason, the ideal micro-mirror model is utilized in this thesis as a sufficient descriptor of the devices behavior. The ideal model is then modified to take into account the parameters

that are to be varied through testing.

3.2.1.1. Mechanical Force of Electric Origin

The computation of the mechanical force, F_{ex} , of electric origin follows from the consideration of energy balance associated with an electromechanical system. The energy balance can be expressed as shown in Fig. 3-2. To simplify the equation, the system is considered to be lossless so that the last term on the right side of Fig. 3-2 is zero. To find an expression for F_{ex} assume that an external force of magnitude $-F_{ex}$ is applied to the movable plate of the system shown in Fig. 3-3(b). The force has a negative sign since it acts in the downward (-x) direction. Assume that this force displaces the plate an infinitesimal distance in the direction of the force so that no change in stored mechanical energy occurs. This eliminates the first term on the right side of Fig. 3-2. Therefore the equation which describes the electrical-to-mechanical interaction is

$$-F_{ex}dx + VIdt = dW_e \quad (3.8)$$

where dx is the displacement of the movable plate, I is the current drawn from the voltage source, V , and W_e is the electric stored energy in the capacitor. Substituting $I=dQ/dt$ from the law of conservation of charge, Eq. (3.8) can be rewritten as:

$$F_{ex} = -\frac{dW_e}{dx} + V \frac{dQ}{dx} \quad (3.9)$$

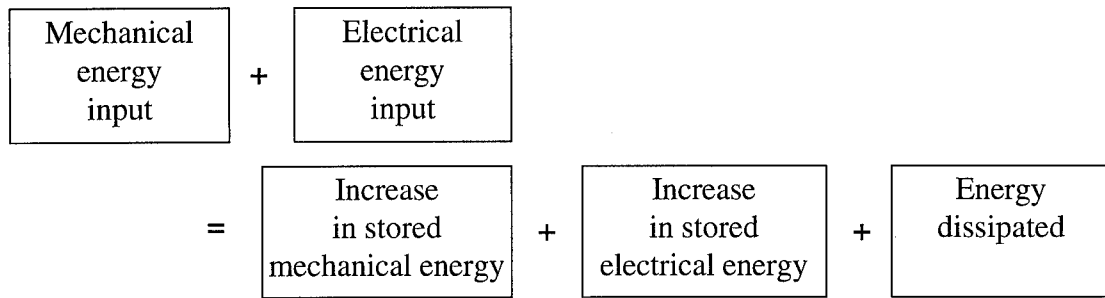


Figure 3-2. Pictorial representation of the computation of mechanical force of electric origin [52].

Neglecting any fringing of the electric field at the edges of the capacitor plates such that the charges on the plates, and the electric field between the plates, are uniformly distributed allows W_e to be written as

$$W_e = \frac{1}{2} \epsilon_o E^2 Ax = \frac{1}{2} \epsilon_o \left(\frac{V}{x} \right)^2 Ax = \frac{\epsilon_o V^2 A}{2x} \quad (3.10)$$

where ϵ_o is the permittivity of free space and A is the area of each capacitor plate.

Differentiating Eq. (3.10) results in

$$\frac{dW_e}{dx} = -\frac{\epsilon_o V^2 A}{2x^2} \quad (3.11)$$

Also, since the charge Q is related to the capacitance and voltage applied it can be written as

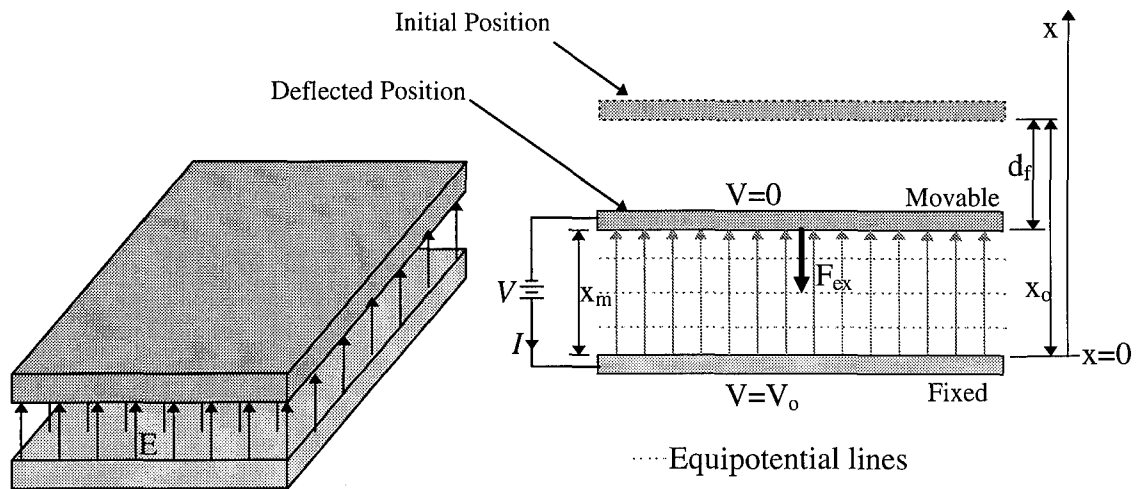
$$Q = CV = \frac{\epsilon_o AV}{x} \quad (3.12)$$

$$\frac{dQ}{dx} = -\frac{\epsilon_o AV}{x^2}$$

Therefore, combining Eq's. (3.9), (3.11), and (3.12), results in an equation that relates the voltage and displacement to the applied force as [52]

$$F_{ex} = \frac{\epsilon_o V^2 A}{2x^2} - \frac{\epsilon_o AV^2}{x^2} \quad (3.13)$$

$$F_{ex} = -\frac{1}{2} \frac{\epsilon_o AV^2}{x^2}$$



(a) Uniform field within micromirror device [23] (b) Side view of micromirror system [52].

Figure 3-3. Uniform electric field for a parallel plate capacitor.

3.2.1.2. The Ideal FBMD Model

Now that the force imparted on the system by the movable capacitor is known it is possible to find an equation that relates the voltage applied to a set deflection distance.

The other force acting upon the movable plate in Fig. 3-3 is the restoring force imparted by the flexure springs. The four flexure springs of a square FBMD can be seen in the

SEM image of Fig. 2-2. From Hooke's law the force imparted by a spring is known to be

$$F_s = k_{sys}x \quad (3.14)$$

where the force is in the +x direction and therefore positive. The system equation is then found by summing the forces, Eqs. (3.13) and (3.14), which equals zero by definition. As shown in Fig. 3-3, the positions of the mirror at rest and deflection are related to each other by

$$x_m = x_o - d_f \quad (3.15)$$

Therefore, the resulting equation which determines the required voltage, V , needed to displace the mirror a desired distance, d_f , is

$$V(d_f) = (x_o - d_f) \sqrt{\frac{2k_{sys}d_f}{\epsilon_o A}} \quad (3.16)$$

where x_o is fixed based on the initial resting position of the mirror due to its weight and any material stress induced deflection. The resting position is typically assumed to be the thickness of the sacrificial layer since the deflection due to weight & stress can be considered to be negligible for small mirror devices. Equation (3.15) neglects any deformation of the mirror (i.e. bending) due to a non linear applied field.

The spring constant of the flexures can be determined from beam theory by knowing the material properties and dimensions of the flexures. This development is covered in Section 3.4 since the accuracy of the spring constant equation is critical to the extraction of the elastic modulus, as a function of temperature, from thermal testing.

3.2.1.3. FBMD as a Single Degree-of-Freedom System

The FBMD can be modeled as a single degree-of-freedom (SDOF) system since

the operational movement can be considered to be primarily in one direction.

Furthermore, the mirror undergoes forced vibration due to an applied voltage (mechanical force of electrical origin) and experiences viscous damping (or squeeze film damping) from the air film layer between the capacitor plates. These conditions and components are shown schematically in Fig. 3-4.

The application of modal analysis theory utilizes an understanding of how the structural parameters of mass, damping, and stiffness relate to the frequency-response function (Fourier domain) for a SDOF system. Modal analysis can also relate the structural parameters to the time domain and Laplace domain but are not considered here since the goal of this section is the frequency characteristics of the device.

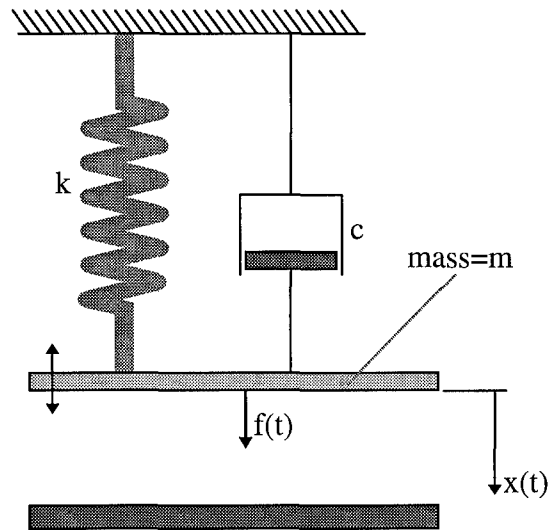


Figure 3-4. Single degree-of-freedom system with viscous damping, excited in forced vibration by force acting on the movable plate (mirror) of the capacitor [53].

The general mathematical representation of a SDOF system is given by [53]

$$m\ddot{x} + c\dot{x} + kx = f(t) \quad (3.17)$$

where: \ddot{x} represents the 2nd derivative wrt time;

\dot{x} represents the 1st derivative wrt time;

m = mass constant;

c = damping constant;

k = spring constant;

$f(t)$ = force applied to mass m ;

and is represented schematically in Fig. 3-4. By setting $f(t)=0$, the homogeneous form of Eq. (3.17) can be solved. The general solution is

$$x(t) = A \exp(p_1 t) + B \exp(p_2 t) \quad (3.18)$$

where A and B are constants and the values of p_1 and p_2 , for an underdamped system, are given by

$$p_r = \sigma_r + j\omega_r \quad (3.19)$$

where σ_r is the damping factor in radians per second and ω_r is the damped natural frequency in radians per second. For most real structures, unless active damping systems are present, the fraction of critical damping is rarely greater than 10 %. Therefore, the two roots p_1 and p_2 , are always complex conjugates and are referred to as the poles of the system. A and B are also complex conjugates of each other.

An equivalent equation of motion may be determined for the Fourier or frequency domain. The frequency response characteristics of the SDOF is obtained by taking the Fourier transform of the time domain representation, Eq. (3.17), of the system. By knowing that [54]

$$\mathfrak{F}\{f^n(t)\} = (j\omega)^n F(\omega) \quad (3.20)$$

the resultant frequency representation is found to be

$$\left[-m\omega^2 + jc\omega + k\right]X(\omega) = F(\omega) \quad (3.21)$$

This equation has the advantage of converting a differential equation to an algebraic equation. By letting $B(\omega)$ equal the term in the brackets, Eq. (3.21) can be written as

$$X(\omega) = \frac{F(\omega)}{B(\omega)} = H(\omega)F(\omega) \quad (3.22)$$

where $H(\omega) = 1/B(\omega)$ and is known as the frequency response function of the system. A frequency response function relates the Fourier transform of the system input to the Fourier transform of the system response. From Eq. (3.21), the frequency response function can be written as [53]

$$H(\omega) = \frac{1/m}{-\omega^2 + j(c/m)\omega + (k/m)} \quad (3.23)$$

The denominator of Eq. (3.23) is known as the characteristic equation of the system. The characteristic values of this equation are typically complex even though the equation is a function of a real valued independent variable, ω . The characteristic values are known as the complex poles of the system. Plotting the real part of Eq. (3.23) as a function of frequency provides for a representation of the shape of the resonance profile for a given m, k, c system. The damping constant is often written in terms of the fraction of critical damping ($\zeta = c/c_c$) where c_c is the critical damping coefficient and can be calculated as [53]

$$c_c = 2\sqrt{km} \quad (3.24)$$

Therefore the damping coefficient, c , in Eq. (3.23) can be replaced by

$$c = 2\zeta\sqrt{km} \quad (3.25)$$

For $\zeta < 1$ the system is said to be less than critically damped, $\zeta = 1$ critically damped, and $\zeta > 1$ greater than critically damped. The quality factor, Q , is a measure of the maximum response at resonance and is defined for a mechanical system as $Q = 1/2\zeta$. Finally, the undamped natural frequency, ω_n , in radians per second is given as [53]

$$\omega_n = \sqrt{\frac{k}{m}} \quad (3.26)$$

where the mass, m , is taken to be the mass of the movable mirror since the mass of the spring flexures is considered to be negligible. As damping becomes a factor (i.e. ζ increases), the damped natural frequency is found to be

$$\omega_{damped} = \omega_n \sqrt{1 - \zeta^2} \quad (3.27)$$

The developments of this section shall be used in a comparison of the experimental frequency data taken from mirrors off of MUMPS 6. Furthermore, the SDOF model developed in this section provides for an estimation of the resonant frequency of MEMS devices by knowing their mass and spring constant. Conversely, the spring constant can be calculated by experimentally determining the resonance frequency and knowing the mass of the structure.

3.2.2. Heat Actuator

The heat actuator is used to control the movement of numerous devices developed for this thesis. Previous studies at AFIT have yielded an empirical equation for relating the deflection, d , for an applied current, I , in a heat actuator with known geometry [10,

11]. The data was taken from a heat actuator array on MUMPS 6 and yielded the following exponential fitting equation

$$d = A \exp(BI) \quad (3.28)$$

where A and B are fitting constants. These heat actuators contained no load and therefore the empirical equation may not represent the deflection of heat actuators used in this research. The starting point for application of heat actuators as driving mechanisms was to utilize actuator dimensions that were found to provide the greatest deflection (up to 12 μm) with a current of ~ 5 mA. Referring to Fig. 2-4, the “best” dimensions were $g = 4$ μm , $L_1 = 200$ μm and $L_2 = 160$ μm with a width of 14 μm . For larger mass devices and those which required restoring springs, the optimum heat actuator was arrayed (from 2 up to 24) in order to provide more actuating force.

3.2.3. *Fresnel Lens*

A Fresnel lens can be constructed by utilizing the fact that successive Fresnel zones tend to nullify each other. The basic physical mechanism of a Fresnel lens is constructive interference utilizing the phase of the optical rays originating from the source. Referring to Fig. 3-5, the radii of successive zones can be calculated by noting that a wave traveling the path S-A_m-P must arrive out of phase by $m\lambda/2$, where m = zone number, with a wave that travels the path A-O-P, such that [16]:

$$\frac{1}{\rho_o} + \frac{1}{r_o} = \frac{m\lambda}{R_m^2} \quad (3.29)$$

This is a first order approximation obtained by utilizing a binomial expansion and is valid for R_m small compared to ρ_o and r_o . The primary focal length can be found from

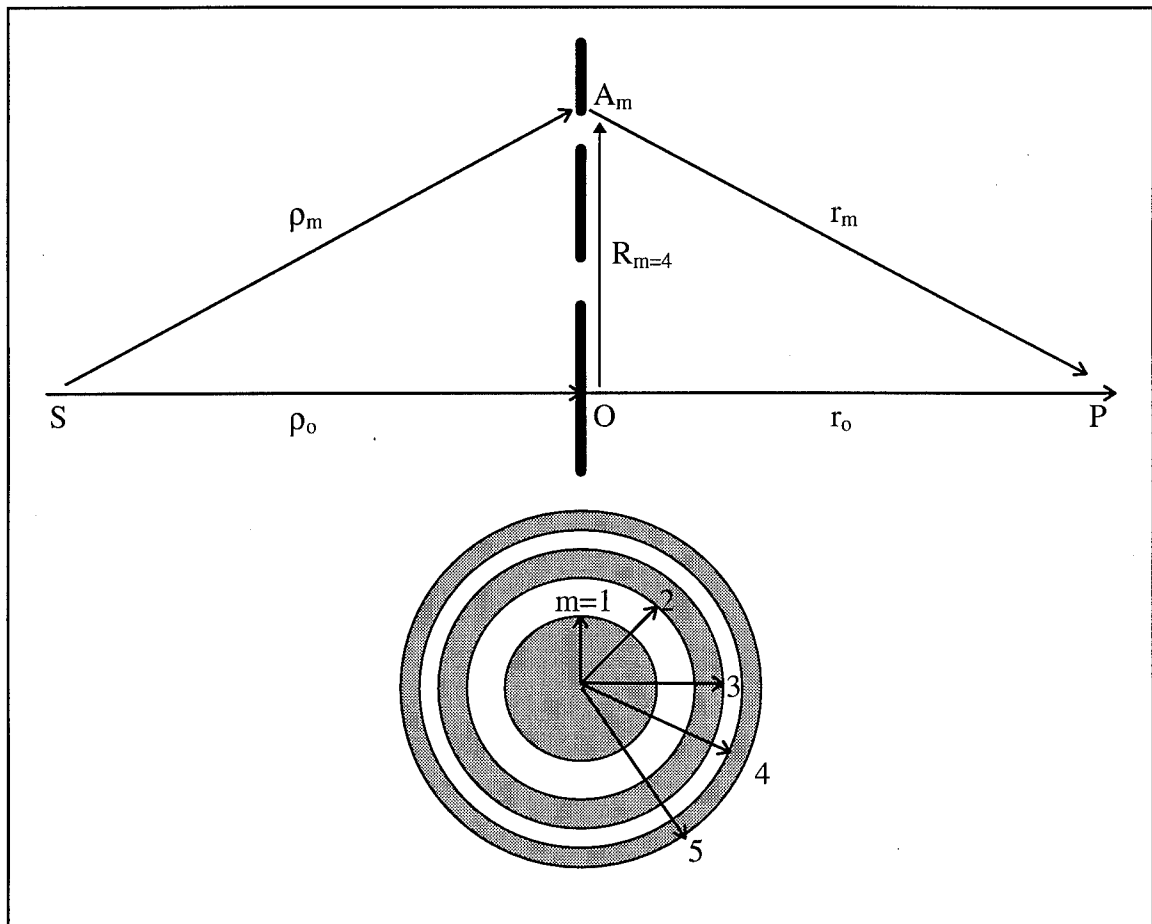


Figure 3-5. Zone-plate geometry. Top sketch is a cross-section of the lens with dimensions labeled for the equations. Bottom sketch shows how the orders correspond to the radii [16].

Eq. (3.29) by setting $r_o = \infty$ and $\rho_o = f$ such that a point source at S is collimated by the lens. The resultant equation is

$$f = \frac{R_m^2}{m\lambda} \quad (3.30)$$

Therefore, the Fresnel lens displays extensive chromatic aberration since the focal point is a function of the optical wavelength. Also, the area of each Fresnel zone is approximately equal, with only a slight increase being observed.

3.2.4. Diffraction Grating

Two primary types of diffraction theory exist: one is vectoral in nature and relies on the use of Maxwell's equations (with established boundary conditions), the other is a scalar approach that utilizes Fourier theory [34]. The scalar approach to diffraction problems is often utilized since it is much easier to solve with existing techniques. Scalar theory is based on the works of Huygen, Kirchoff, Rayleigh and Sommerfeld [34,55]. In order to use the scalar approach, the Fourier transform must be utilized.

3.2.4.1. Geometric Modeling

For simple gratings with periods that contain only two levels and have equal width spacings of the layers there exists a simplified equation to describe the diffraction that occurs. The equation is derived by using a scalar approach to the light rays or wavelets that emanate from the slits or valleys. Based on constructive interference, the angles for the diffracted orders for a particular wavelength can be determined. All that is required is to know the grating period dimensions, light wavelength, and diffracted order of interest. The MCNC surface micromachining process has a minimum feature size of 2 μm [14]. By using the grating equation [16]

$$\sin \theta_m + \sin \theta_i = \frac{m\lambda}{a} \quad (3.31)$$

where: θ_m = angle from surface normal to the mth order;

θ_i = angle from incident light to surface normal;

λ = wavelength of light used;

a = grating period width;

the maximum achievable separation angle is defined for a set period width a . For the

m=1 order, reflection at normal incidence ($\theta_m=0$) and a grating period of $a=4 \mu\text{m}$, $\theta_i = 5.74$ -to- 10.08 degrees when $\lambda = 400$ -to- 700 nm.

To use this type of grating to generate images, as mentioned in Chapter 2, all three of the primary colors are required for a display and therefore three angles must be used for the incoming white light source with a fixed slit width grating. An alternative solution is to vary the slit widths in order to maintain a set value of θ_i for the incoming white light source. At period widths greater than $2 \mu\text{m}$ the incoming light ray is so close to the direction of observation that it creates interference problems (see Fig. 3-6). Improvements in the lithography of the MCNC process would allow for grating spaces of less than $2 \mu\text{m}$ and therefore greater incident light angles.

Another difficulty is that most of the light on a standard binary grating is diffracted into the zero order, therefore decreasing the intensity of the image. Figure 3-7 demonstrates how gratings are typically blazed to alleviate this problem. To date, no method has been developed to generate continuous blazed (versus binary blazed) surfaces with planar surface micromachining processes.

3.2.4.2. Fourier Modeling

One scalar method that has proven very useful for modeling the diffraction pattern produced by a particular diffraction grating is based on the Fourier transform. For the particular case shown in Fig. 3-8 the expression which describes the sum in the image plane of the amplitude components due to contributions from the entire aperture may be written in integral form as [55]:

$$G(\xi) = \int_{-\infty}^{+\infty} \rho(x) \exp\{2\pi i \xi x\} dx \quad (3.32)$$

where $G(\xi)$ is the resultant one-dimensional amplitude at a point s in the plane of the focused diffraction pattern defined by $(\sin\theta/\lambda)=\xi$ and $\rho(x)$ is the function describing the amplitude of the wavefront at a position x in the plane of the aperture (see Fig. 3-8). This operation of multiplying a function $\rho(x)$ by an appropriate phase factor and integrating over the result is known as a Fourier transformation. In optical terms, $G(\xi)$ is simply the

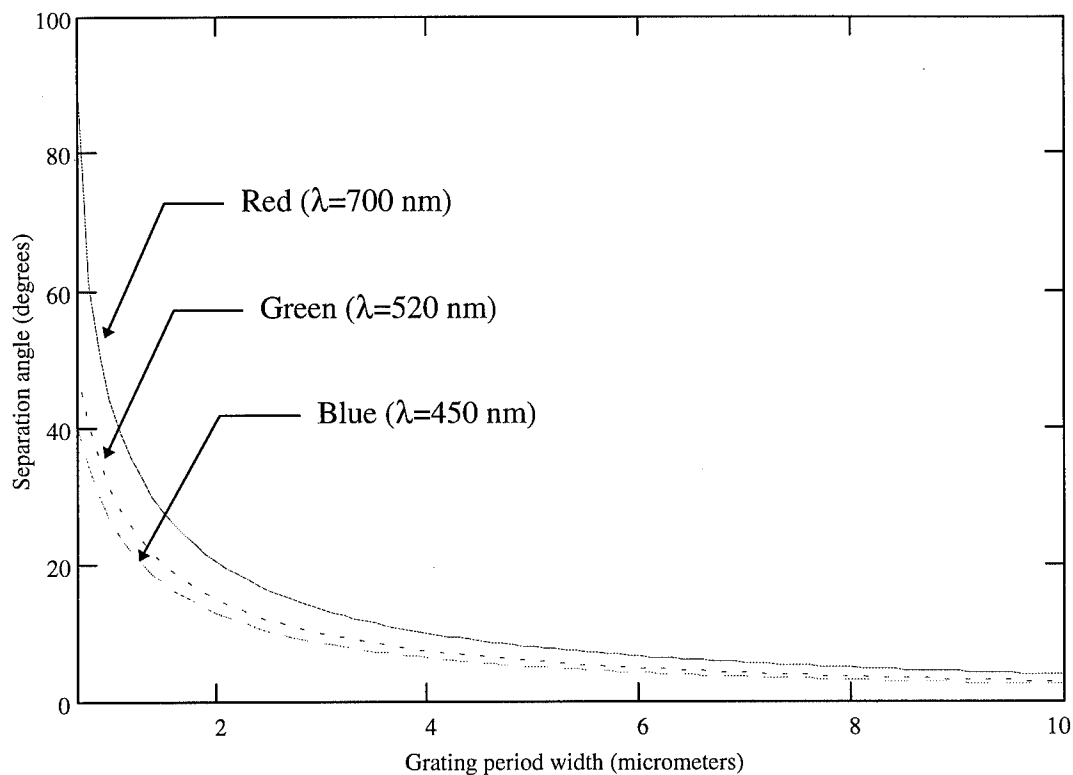


Figure 3-6. Variation of allowed incoming light angle ($\theta_m - \theta_i$) versus grating period width (a) for three wavelengths.

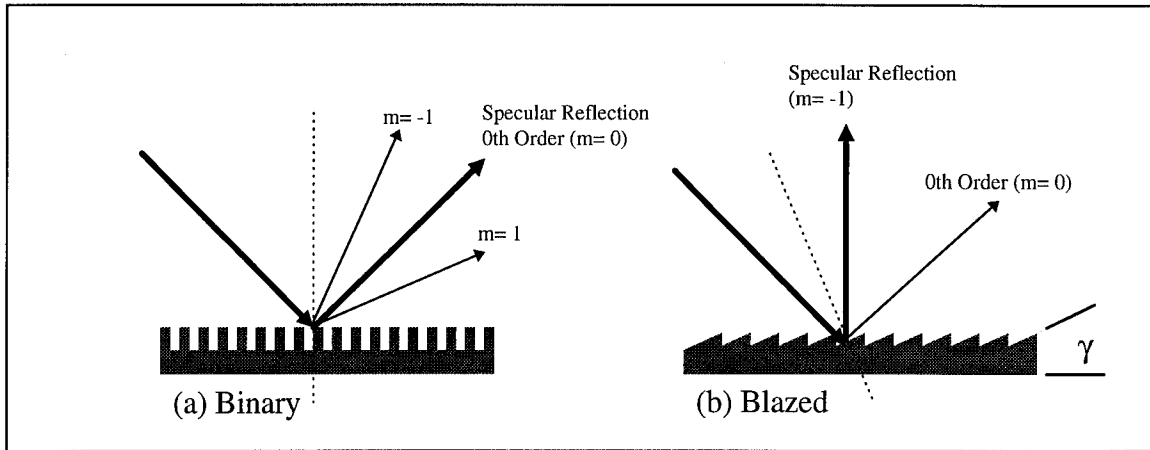


Figure 3-7. Binary versus blazed gratings. γ is the blaze angle [15].

Fraunhofer diffraction pattern of the object represented by $\rho(x)$. By using the results of this theory a very succinct description of a selected diffraction grating can be obtained in order to provide insight into how given features will affect its performance.

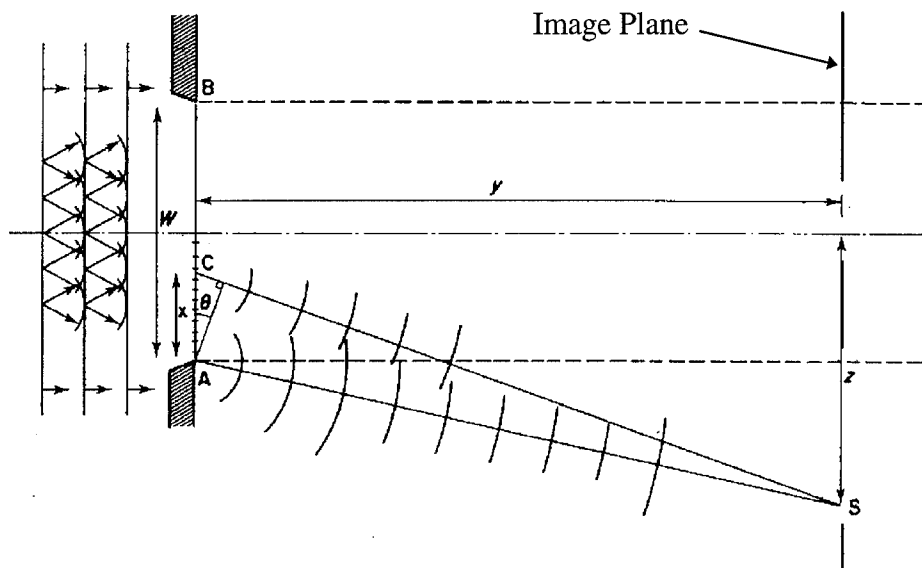


Figure 3-8. Diffraction by an aperture [55].

A grating is composed of three basic functions. First is the rectangle that describes the opening or aperture for the entire grating. A 2-D rectangular apertures

Fourier transform is shown in Fig. 2-11. Next is the period of the grating, in other words its physical shape, which describes the phase shift that the light encounters as a function of the thickness of the grating. The Fourier transform of this function is unique to its shape. Finally, there is a function that describes the frequency of occurrence for the period, this is usually described by a comb function (a series of delta functions with a set period).

A simplified way to describe how the developed model works for analyzing diffraction gratings designed using the MCNC process is to consider, as an example, the analysis of Young's slits. In order to evaluate the double slit, two transforms must be utilized. The first one is the Dirac delta function $\delta(x)$ and the second is the $rect(x)$. The Dirac delta can be described optically as a point source, or slit source in 2-dimensions, and is described mathematically as [54]

$$\delta(x) = \begin{cases} \infty & x = x_0 \\ 0 & x \neq x_0 \end{cases} \quad (3.33)$$

the integrated amplitude is defined to be equal to unity and the Fourier transform of a Delta function at a position x is given to be [54]

$$G(\xi) = \int_{-\infty}^{+\infty} \delta(x) \exp\{2\pi i \xi x\} dx = \exp\{2\pi i \xi x\} \quad (3.34)$$

Likewise, for an infinite set of Dirac delta functions separated by a distance d (known as a *comb* function) the Fourier transform is [54]

$$\sum_{n=-\infty}^{n=\infty} \exp\{2\pi i n d \xi\} \quad (3.35)$$

The *rect* function (or top hat function) is unity between some limits and zero elsewhere. This function represents a uniformly illuminated aperture. For a *rect* with width (a), symmetrically positioned with respect to the origin, the mathematical description of the Fourier transform follows [54]

$$G(\xi) = \int_{-a/2}^{a/2} \exp\{2\pi i \xi x\} dx = \left[\frac{\exp\{2\pi i \xi x\}}{2\pi i \xi} \right]_{-a/2}^{a/2} = \frac{\sin(\pi a \xi)}{\pi \xi} = a[\text{sinc}(a\xi)] \quad (3.36)$$

The convolution of the period function with the comb function results in a copy of the period function being positioned at each *delta* (δ) of the *comb* function. After multiplication with the rectangular aperture function the grating is defined. This entire process is shown in Figs. 3-8 and 3-9, where Fig. 3-8 shows the aperture in which the grating function from Fig. 3-9 is placed. It is important to point out that a multiplication (\times) in space is a convolution (\otimes) in inverse space and likewise a convolution in space is a multiplication in inverse space, as shown in Figs. 3-9 and 3-10. After Fourier transforming each function and performing the associated mathematical manipulation the resulting diffraction pattern is generated [55]. The only mathematical step required to determine the angle of diffraction for the different orders is to use the relationship [34]

$$\xi = \frac{\cos(\phi)}{\lambda} \quad (3.37)$$

where: $\phi = 90 - \theta =$ angle of diffraction measured from the surface;

$\lambda =$ the diffracted wavelength.

Additional model parameters must be added to account for long-term periodic errors in the grating, such as the surface roughness of the substrate, which creates what are known

as Rowland ghosts in the diffraction pattern. These ghosts are seen to be close to the diffracted orders. Furthermore, short-term periodic errors in groove position, such as imperfections in the grating line edges, effect the resulting diffraction pattern by creating what are known as Lyman ghosts. Ghosts of this type are widely separated from the diffracted order lines. These effects are shown in Fig. 3-11. Modeling of devices in this thesis have shown that these effects do not need to be included for an engineering evaluation.

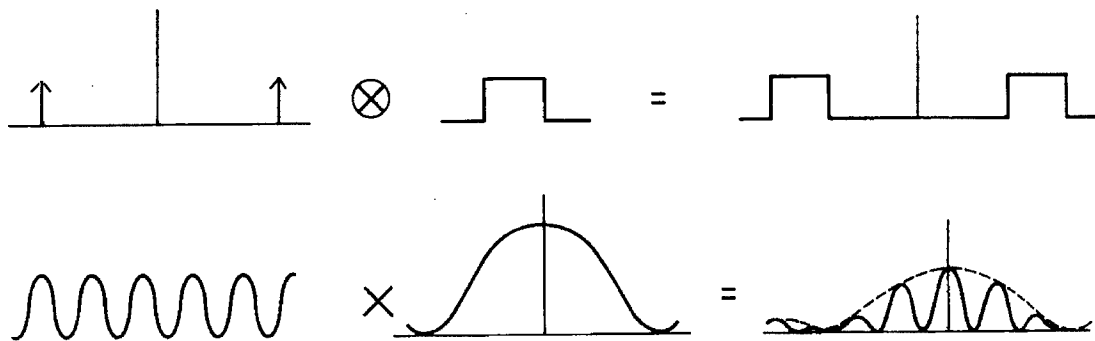


Figure 3-9. Diffraction model. Method for calculating diffraction pattern for Young's slits [55].

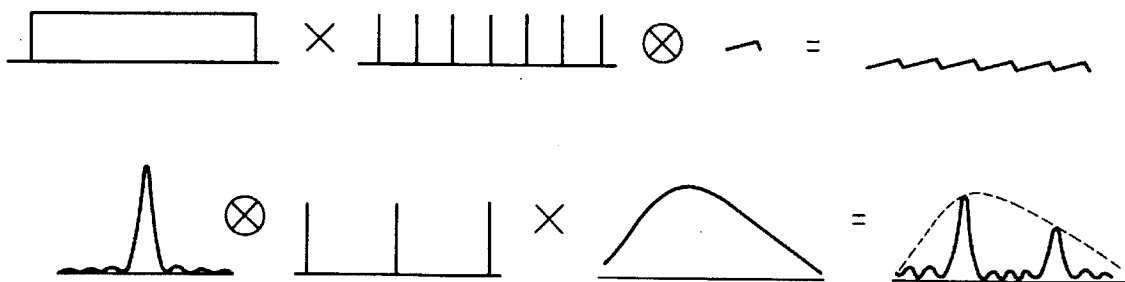


Figure 3-10. Diffraction model. Method for calculating diffraction pattern for a blazed grating [55].

3.2.4.3. Variable Grating Example

Using the theory that was outlined in Section 3.2.4.2, a mathematical description can be derived for a grating of any set dimensions. This section goes through the development of an expression for the Fraunhofer diffraction pattern of a three level variable grating as shown in Fig. 3-12. The relative heights correspond to complex amplitudes and are described in the equations as complex exponentials which account for the phase shift that the light experiences when reflecting off of the different surfaces.

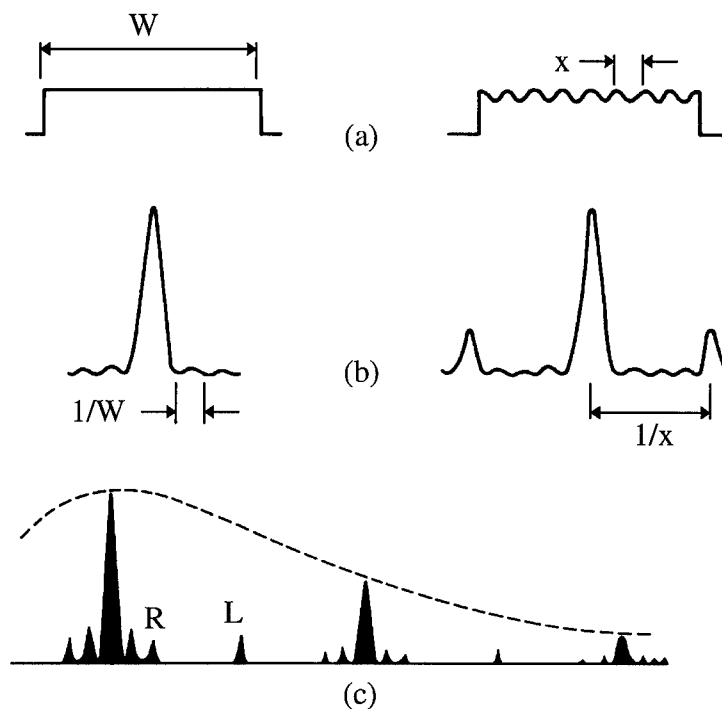


Figure 3-11. Diffraction model with introduction of noise and the production of ghosts. (a) real space rectangular aperture with and without noise; (b) reciprocal space patterns for functions in (a), notice the formation of satellite peaks in the right-side image; (c) representation of where ghosts “appear” in the diffraction pattern [55].

The real space expression for the grating in Fig. 3-12, for $\gamma=0-2 \mu\text{m}$, would therefore be

$$g(x) = \left[\sum_{n=-\infty}^{\infty} \left\{ \text{rect} \left(\frac{x - \Lambda_p n - \Lambda_p / 2}{\omega_2} \right) + e^{i \left(\frac{4\pi}{\lambda} \alpha \right)} \text{rect} \left(\frac{x - \Lambda_p n}{\omega_1} \right) + e^{i \left(\frac{4\pi}{\lambda} \beta \right)} \text{rect} \left(\frac{x - \Lambda_p n - \gamma}{\omega_2} \right) \right\} \right] \text{rect} \left(\frac{x}{W} \right) \quad (3.38)$$

where the rect outside the summation defines the number of periods that make up the grating and W is the width of the aperture. The terms α , β , γ , Λ_p , ω_1 , and ω_2 , are defined in Fig. 3-12 and will vary depending on the grating design or deflection position during operation. By taking the Fourier transform of Eq. (3.38) we obtain the complete description of the diffraction pattern:

$$G(\xi) = \sum_{n=-\infty}^{\infty} \left[e^{i(\pi \Lambda_p \xi)} \frac{\omega_2}{\Lambda_p} \text{sinc} \left(\frac{\omega_2 n}{\Lambda_p} \right) \delta \left(\xi - \frac{n}{\Lambda_p} \right) + e^{i \left(\frac{4\pi}{\lambda} \alpha \right)} \frac{\omega_1}{\Lambda_p} \text{sinc} \left(\frac{\omega_1 n}{\Lambda_p} \right) \delta \left(\xi - \frac{n}{\Lambda_p} \right) + e^{i \left(\frac{4\pi}{\lambda} \beta \right)} e^{i(2\pi \gamma \xi)} \frac{\omega_2}{\Lambda_p} \text{sinc} \left(\frac{\omega_2 n}{\Lambda_p} \right) \delta \left(\xi - \frac{n}{\Lambda_p} \right) \right] \otimes W \text{sinc}(W\xi) \quad (3.39)$$

The amplitude as a function of angle can now be found by taking the absolute value of Eq. (3.39) and using Eq. (3.37) to correlate the reciprocal space location, ξ , to an angle with respect to the normal of the grating. Equation (3.38) can be modified to yield an equation for $\gamma=2-4 \mu\text{m}$ by adding an additional *rect* term since the Poly 2 grating will partially overlap the Poly 0 surface.

Application of a Fast Fourier Transform (FFT) algorithm in Matlab allows for Eq. (3.38) to be calculated for any designed grating period. Matlab m-files have been written to obtain diffraction pattern data for a given grating design. These m-files are included in Appendix A. The generic output for a specified set of input conditions resembling a 2

μm grating (i.e. $4 \mu\text{m}$ period) is shown in Fig. 3-13. The model sets up a discrete vector that represents the phase height of each portion of the grating like that accounted for by the complex exponentials in Eq. (3.37). As shown in Fig. 3-13, the grating had 10 periods each $4 \mu\text{m}$ wide for a total width of $40 \mu\text{m}$. The model uses a resolution of 1000 pixels per μm (i.e. one pixel per nm). The model then uses the FFT to achieve the discrete result of Eq. (3.38). The vector must be increased in size to a value equal to a power of two, since the FFT algorithm used by Matlab differs depending on the size of the vector. After the diffraction pattern is obtained, the angles for the first three diffraction peaks past normal incidence are calculated from Eq. (3.36). The angle of

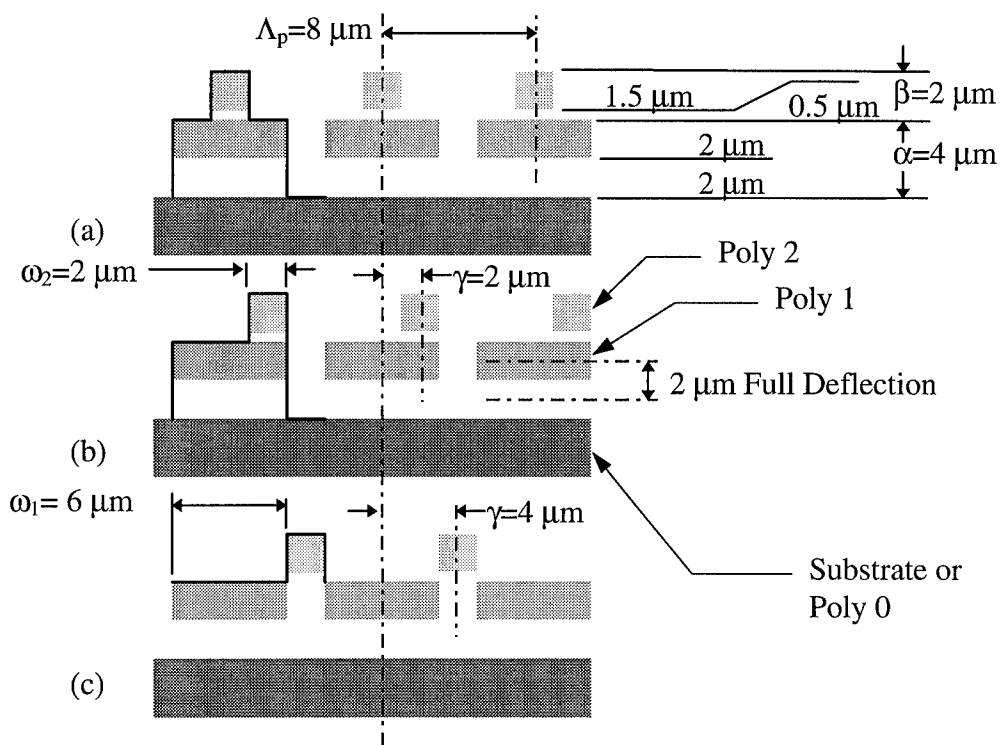


Figure 3-12. Grating period development for the variable diffraction grating with a $2 \times 6 \mu\text{m}$ line/spacing setup. (a) indicates the zero deflection position ($\gamma=0 \mu\text{m}$), (b) is for $\gamma=2 \mu\text{m}$ deflection position and (c) is for $\gamma=4 \mu\text{m}$ deflection position. The period is shown for each position by the black line.

incidence can also be varied and a second layer with a different period can be added (i.e. the Poly 2 layer). Additional m-files allow for data to be extracted over a range of positions, both for lateral deflection of the poly 2 grating and up-down deflection of the poly 1 grating. This data will be compared to the experimental results in Chapter 5.

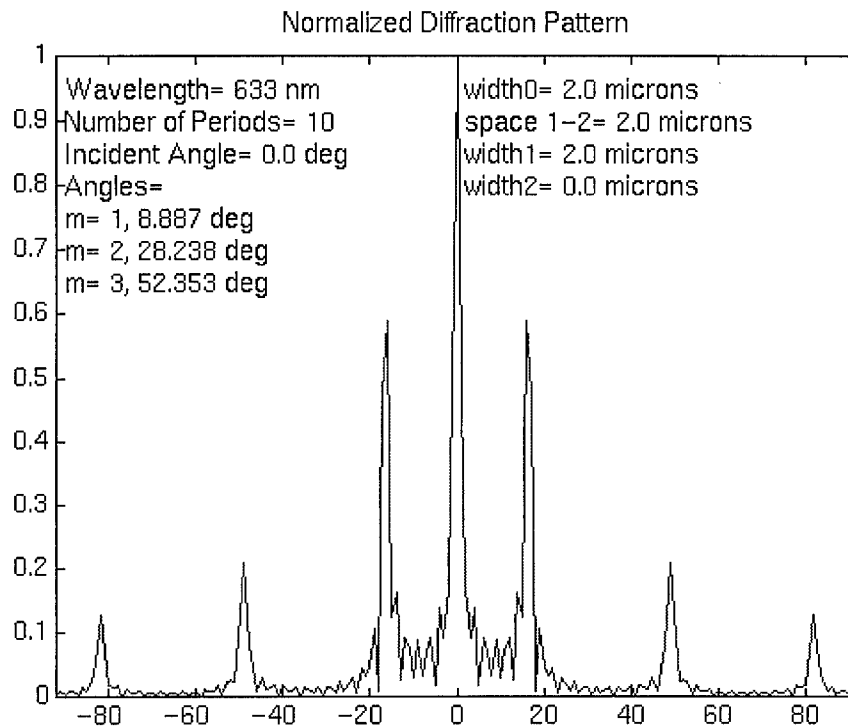


Figure 3-13. Output from grating model for a 2 μm x 2 μm grating illuminated by a HeNe laser ($\lambda=632.82$ nm) at normal incidence.

3.3. Micro-Interferometer

From Fig. 3-14 the change in distance traveled for the light on the object path $\text{BS}_1\text{-M}_1\text{-BS}_2$ relative to a set displacement x_o of mirror M_1 is found to be

$$2d = \frac{2x_o}{\sin(\varphi)} \quad (3.40)$$

where φ is the angle of the first diffracted order ($m=1$) for the beam splitter (BS_1), as calculated from Eq. (3.30). Therefore, since $\lambda/2\pi$ is the number of $\mu\text{m}/\text{rad}$, the change in

phase can be calculated and substituted into Eq. (3.6) to obtain a relationship for I as a function of the displacement x_o . The resulting equation describing the micro-interferometer operation is

$$I = \frac{(I_{\max} - I_{\min}) \cos \left[\left(\frac{2x_o}{\sin(\varphi)} \right) \left(\frac{2\pi}{\lambda} \right) \right] + I_{\max} + I_{\min}}{2} \quad (3.41)$$

3.4. Thermal Testing

The primary goal of thermal testing was to characterize the change in the Elastic Modulus (Young's Modulus) as a function of temperature. The FBMD was the main device selected for this characterization. In order to obtain the modulus as a function of temperature an accurate model for the spring constant, k_{sys} , of the device must be developed. The accuracy of the Young's Modulus versus temperature curve that is generated will be limited by the equation that describes the spring constant of the flexures.

A spring, as shown in Fig. 3-16, can exhibit 4 independent spring constants from lateral loading, bending, stress, and torque [46]. Since the FBMD can move at most 2.75 μm in the vertical direction (for MUMPS 9 devices where Poly 2 forms the flexure), the spring constant due to beam elongation is negligible compared to the other three terms. Stress is considered an axial term since it depends on the cross-section of the beam and is included in the total spring constant. Beam bending is taken into account by the lateral spring constant since the beam is anchored at one end to the substrate. Figure 3-16 shows the forces that act upon one of the square FBMD flexures. Since springs can be treated as inductors, and the three spring constants are in parallel, they sum to provide the spring

constant, k_{flex} , that describes the flexure. This model is shown in Fig. 3-17.

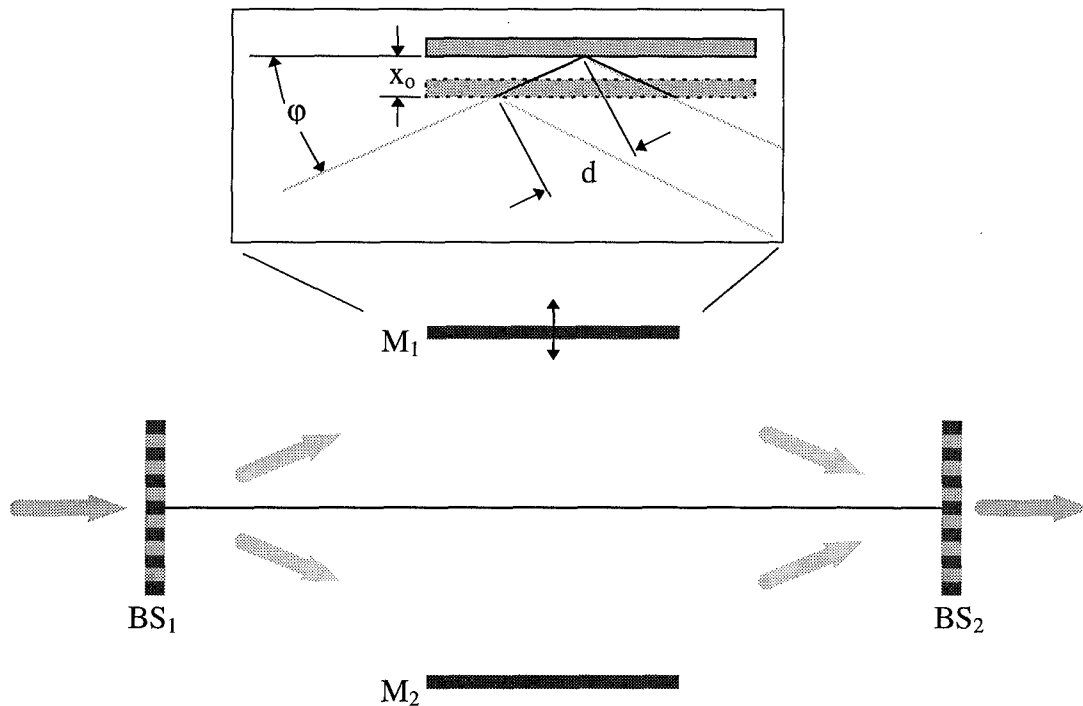


Figure 3-14. Schematic of a micro-interferometer design. BS = beam splitter and M = mirror. M_1 is the mirror that moves to provide the optical modulation.

The lateral deflection of a rectangular beam can be described by [53]

$$k_l = \frac{3\alpha EI}{L^3} \quad (3.42)$$

where $\alpha=1$ -to-4 depending on whether the flexure is considered to be hinged at both ends ($\alpha=1$) or fixed at both ends ($\alpha=4$). Selection of an intermediate value for α can be used to account for the bending within the plate which causes the flexure-to-plate interface to be semi-fixed/semi-hinged. E is Young's Modulus of elasticity, I is the moment of inertia for the cross-section of the beam, and L is the length of the beam.

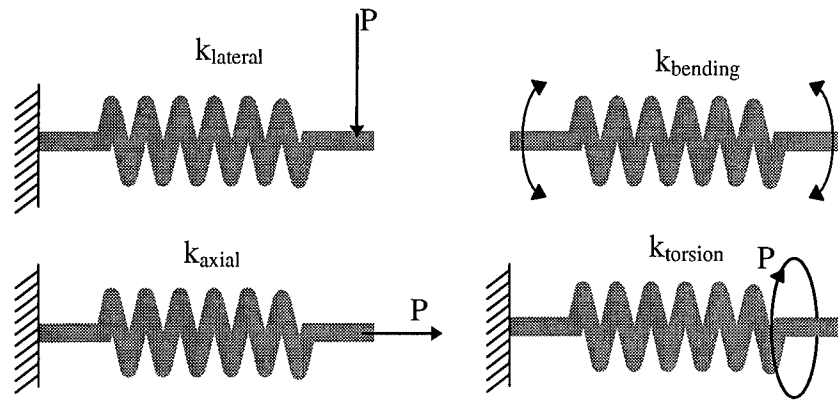


Figure 3-15. Four types of spring constants where P is the applied force. In model, the thin film stress is accounted for as an axial spring constant term [46].

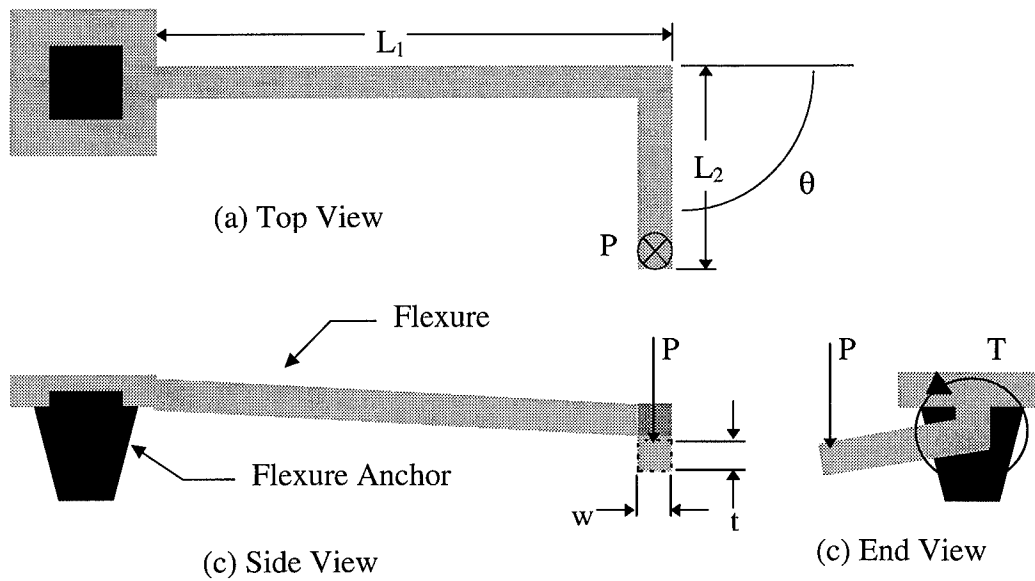


Figure 3-16. Pictorial representation of a two sided hinge, like that used on the square FBMD, with the forces (P and T due to P) acting upon the flexure shown.

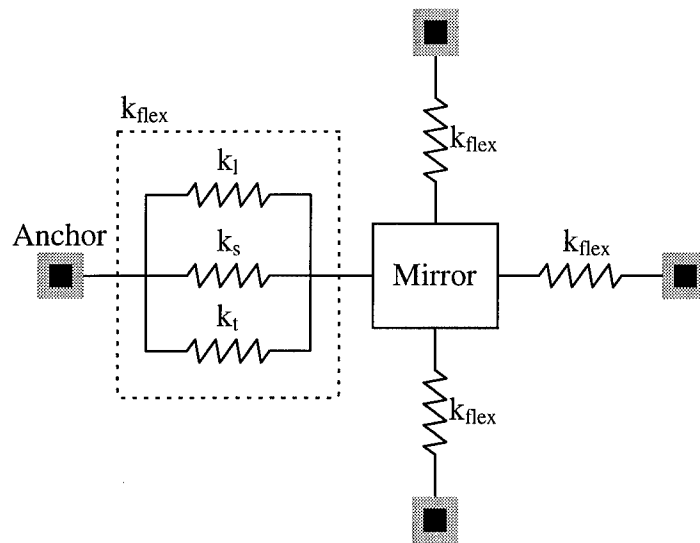


Figure 3-17. Representation of the spring system for a square FBMD where: k_l is the lateral spring constant, k_s is the axial spring constant due to material stress, and k_t is the torsional spring constant.

For a rectangular beam with dimensions as in Fig. 3-16, the inertia is given as [56]

$$I = \frac{wt^3}{12} \quad (3.43)$$

Therefore, the spring constant due to bending is found to be [56]

$$k_l = \frac{E\alpha wt^3}{4L^3} \quad (3.44)$$

The residual stress in the beam contributes an additional spring constant term. The force imparted on the beam in the downward direction can be related to the force in the axial direction which is proportional to the stress within the material. The residual stress spring constant is therefore calculated as follows

$$k_s = \frac{P}{L} \quad (3.45)$$

$$P = \sigma_r A = \sigma_r wt \quad (3.46)$$

$$k_s = \frac{\sigma_r wt}{L} \quad (3.47)$$

where σ_r is the residual stress of the material and $L = L_1 + L_2$. Finally, the torsional spring constant of the flexure is calculated by knowing the force that acts upon the second length of the flexure (L_2) which imparts a torque on the first length (L_1). The angle of rotation (ϕ) that is observed due to the torque is known to follow the relationship [57]

$$\phi = \frac{TL_1}{KG} \quad (3.48)$$

where T is the observed torque and equals the force (P) times the perpendicular distance from the first leg ($L_2 \sin(\theta)$), where θ is defined as shown in Fig. 3-16. The shear modulus of the material (G) can be related to the elastic modulus by knowing the Poisson ratio (ν), such that [58]

$$G = \frac{E}{2(1+\nu)} \quad (3.49)$$

and K is a constant that depends on the cross-sectional geometry of the material. For a rectangular cross-section K is [57]

$$K = ab^3 \left[\frac{16}{3} - \left(\frac{3.36b}{a} \right) \left(1 - \frac{b^4}{12a^4} \right) \right] \quad (3.50)$$

where $a=w/2$ and $b=t/2$. Since ϕ is small for the deflection, d , being considered, it can be approximated as $d/(2L_2)$ where the 1/2 factor accounts for the corner only being deflected half of the distance d , therefore decreasing the amount of torque on the flexure.

Substituting this relationship for ϕ and Eq. (3.49) into Eq. (3.48) and solving for the force-deflection ratio yields the torsional spring constant.

$$k_t = \frac{P}{d} = \frac{KE}{4L_2^2 L_1 (1+\nu) \sin(\theta)} \quad (3.51)$$

For the square FBMD flexure θ is 90 degrees and the sine term equals unity in the equation, but for mirrors like those in the hexagonal array this term can be other than unity. The total spring constant for the mirror is the flexure spring constant times the number of flexures, which yields

$$k_{sys} = Nk_{flex} = N(k_l + k_s + k_t) \quad (3.52)$$

The modulus of elasticity can now be derived by knowing the experimentally determined spring constant at a particular temperature. The application of a finite element code would allow for the determination of a spring constant, while in the design phase. This would allow for model characterization of the device and prediction of its performance. For example, the spring constant directly effects the resonant frequency of the device as shown in Eq. (3.25). The deflection as a function of voltage will also depend on the spring constant of the flexure system. The fact that the spring constant directly affects the performance parameters makes it a very important design factor for any device.

Another method for obtaining spring constants of MEMS devices is known as the Rayleigh method and was used to calculate the spring constant for a microresonators meander spring [58]. This method equates the maximum strain energy to the maximum kinetic energy for the given meander. In all cases the maximum strain energy is known to be when the beam is fully deflected and the maximum kinetic energy occurs at the resting position [53]. This method will yield an approximation for the natural frequency of the meander from which the spring constant can be calculated by Eq. (3.26). If the deflection

of the beam is known exactly then this method will give the true natural frequency.

When the classical method used to derive Eq. (3.52) becomes excessively difficult due to the number of moments (i.e. corners and bends) then the Rayleigh method can be used to obtain a satisfactory result.

3.5. Summary

This chapter has discussed the key mathematical concepts used to analyze the devices and systems designed for this thesis. As discussed in Chapter 2, MOEMS embodies the three fields of optical, mechanical and electrical engineering. The interferometer, diffraction grating, and Fresnel lens concepts embody the optical work of this thesis. The flexure spring constants, material strength parameters, and mechanical work of electrical origin are the mechanical aspects of the selected MOEMS devices. Finally, the electrical parameters are evident in the analysis of drive mechanisms such as the parallel plate capacitor and the heat drive actuator.

4. Experimental Setups, Procedures, and Design Descriptions

This chapter covers the MUMPS design process, specific design considerations, characterization setups, testing procedures, and device descriptions. Several test setups, requiring various pieces of test equipment, were required to conduct this research. This chapter discusses those setups, procedures and test equipment. The later section of this chapter describes the major classifications of devices that were designed for study. Each classification is described based on intended function, operational characteristics, and where appropriate, design variations.

4.1. MUMPS Process

The devices studied in this thesis were designed in the Very Large Scale Integration (VLSI) Laboratory, bldg. 640, at AFIT using the Cadence layout editor. The Cadence layout editor has been customized with a MUMPS technology file that describes the specific process used by MCNC. Each layer that is drawn represents a specific process mask that is used to fabricate the MEMS devices. The designer draws the mask layers as required to form the desired design. Figure 4-1 is a representative example of the Cadence screen layout observed during the design phase. After layout of designs is accomplished using Cadence, the mask layers are digitized in the form of Caltech Intermediate Files (CIF). This format is acceptable to MCNC and is sent via electronic mail (email) or File Transfer Protocol (FTP). Provided in Appendix B is the complete Cadence layout for each die designed during this thesis.

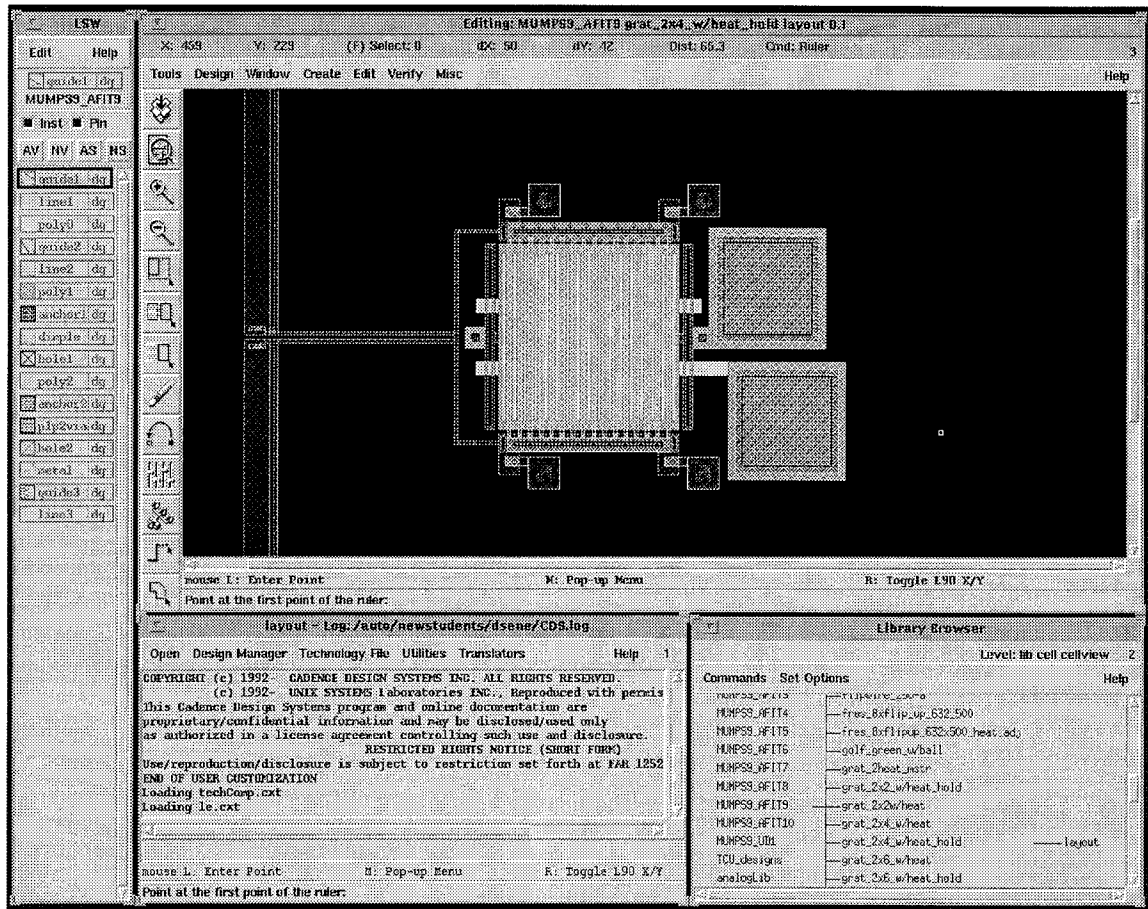


Figure 4-1. Typical Cadence layout editor screen with heat actuated grating pixel shown.

4.1.1. Design Considerations

Numerous design considerations must be taken into account that are specific to the fabrication of thin film surface micromachined devices. One consideration involves the layout of electrical contacts and wiring of devices which can be designed in a variety of orientations. If devices are to be integrated with fibers or will require an optical interface that would be obstructed by electrical probes then wiring must be provided to external pads on the device. External bond pads on the edge of the die allow for wire bonding of the chip into standard integrated circuit packages. Electrical connections can

subsequently be made to the device through the pins on the package. Surface wiring can also be used to array numerous devices together in order to provide a common electrical interface which reduces the amount of probing required. The majority of wiring is drawn with the gold layer on top of Poly 2 to reduce the series resistance, but can be drawn with any of the layers (Poly 0,1 or 2) if the resistance is not a factor in the design.

Another design consideration is the effect of surface topology on the thin film layers. During fabrication each successive layer conforms to the topology that is defined by the masking steps already performed in the fabrication. This results in a conformal effect as shown in Fig. 4-2. This effect must be considered during the design phase and can be used to constrain movement or guide mechanical operation of the device.

Conformance can also cause detrimental effects such as nonuniformity in surface layers and change in the physical properties of a spring flexure. For mirror surfaces these nonuniformities will lead to loss in reflected intensity at the desired angle. Furthermore, conformance can contribute to fabrication problems if the sacrificial layer is too thin since the structural layers can come into contact and stick.

For flip-up structures it is important to consider how the devices will be elevated and locked into the desired position. As was mentioned in Chapter 2, *flip-helpers* have been constructed to assist in this process. Locks in the structure must be high enough off of the substrate to provide adequate restraining force yet not too high that they impede the flip-up procedure. The *flip-helper* must be designed such that it prevents shearing of the hinge pins yet allows for a probe to be inserted under the elevating structure or

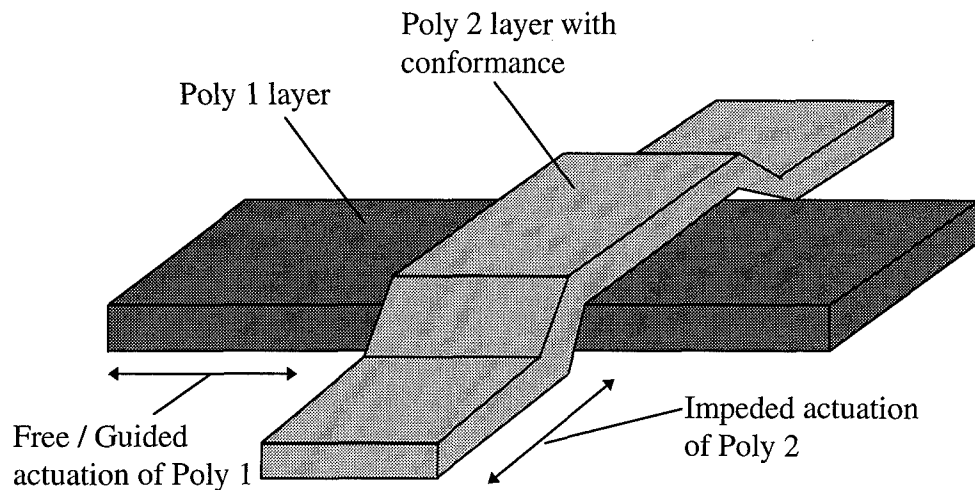


Figure 4-2. Conformal effect of polysilicon layering in MUMPS.

completely performs the elevation process. Initial flip-up designs, both on MUMPS 7 and MUMPS 8 did not include *flip-helpers* and indicated that such devices were needed. Preferably, different design variables would be altered in order to determine the optimum design for these devices. Since this thesis is looking at systems with numerous flip-up elements, a *flip-helper* had to be used that would work with a high degree of confidence. The chosen *flip-helper* utilizes both a flip-jack and pyramid elevating arm to increase the chance that the flip-up procedure will be successful. The layout of this device is shown in Fig. 4-3. Selection of a lock point on the flip-up structure relative to the hinge pins was also made based on a desire to ensure device success. In order to minimize the force imparted on the hinge pins and structure by the lock mechanisms, the hinge pin-to-lock point distance was made very short ($\sim 10\text{-}15\ \mu\text{m}$). Future work should look at improving the design of the *flip-helper* and lock mechanisms.

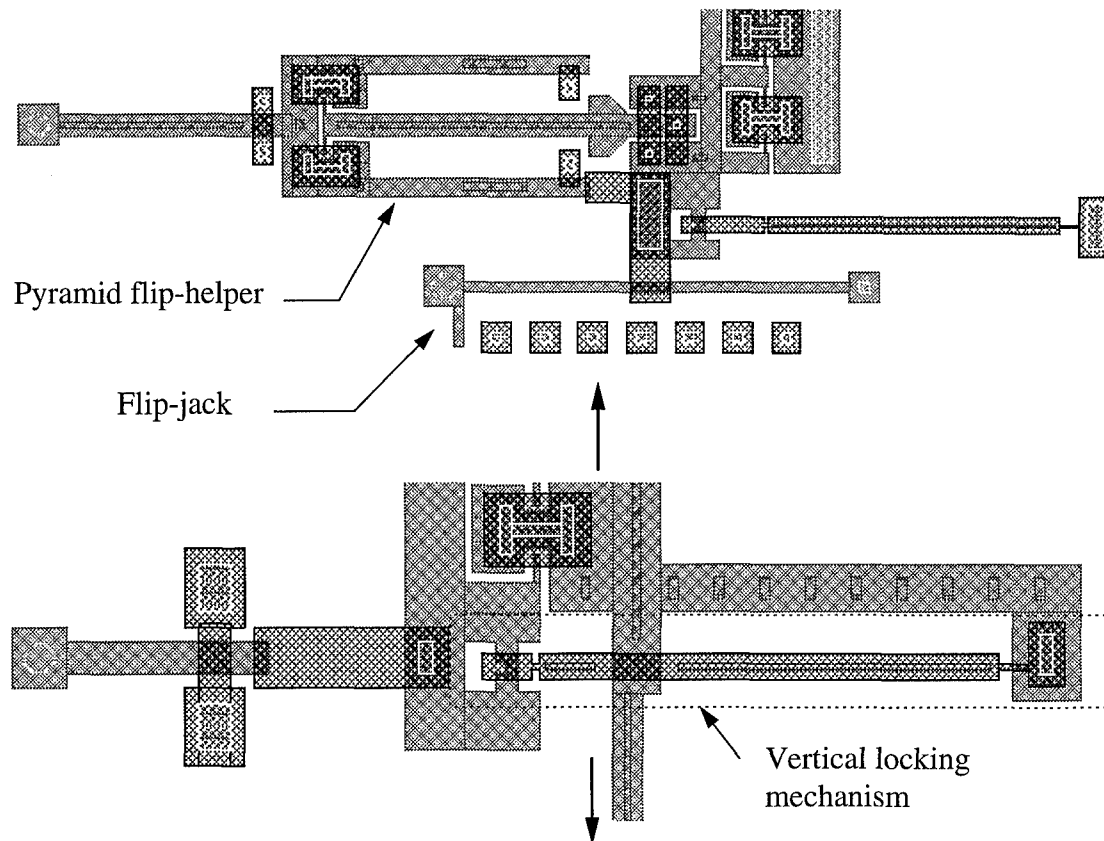


Figure 4-3. Flip-helper layouts in Cadence. Top view is the standard flip-helper with pyramid lock and flip-jack. Bottom view is modified flip-helper used on structure that must move in the direction shown after elevating. In both views the standard vertical locking mechanism is shown.

Design guidelines from MCNC recommend that a etch hole be provided in large plates at $30\ \mu\text{m}$ centers [14]. If the plate is to be used as a mirror then these etch holes introduce diffraction effects into the beam. Plates have recently been fabricated with $\sim 100\ \mu\text{m}$ separation between centers of etch holes and are successfully released during etching. Flip-up mirrors on MUMPS 8 and MUMPS 9 used etch holes at every $50\ \mu\text{m}$ in order to minimize their effect on the optical beam.

The minimum design snapgrid, based on MCNC lithography, is $0.25\ \mu\text{m}$. For this reason it is futile to snap to dimensions less than $0.25\ \mu\text{m}$ when using Cadence to layout

devices. For large structures this poses no problems, but for dimensionally precise structures such as Fresnel lenses it limits the accuracy of the device dimensions and requires rounding in the calculation of the orders from Eq. (3.30). Furthermore, the minimum feature size in MUMPS is 2 μm , which sets a limit on how small the period can be for a diffraction grating. The minimum feature size also establishes a threshold for the spring constant since it defines the minimum cross-sectional area possible by design.

Finally, adequate space on the surface of the die must be allowed for operation and probing of the flip-up devices. It was discovered throughout this thesis that the desire to make die density large degraded the efficiency of testing by causing interference between devices and difficulty in probing (both electrical and mechanical). If possible, probe pads should be made at least 100 μm square. In a research effort support structures should not impede the characterization of devices and making probe pads too small with devices packed too close together may limit successful testing.

4.1.2. Post Processing Procedures

After devices are received from MCNC, it is necessary to perform some post processing steps to release the devices and prepare them for characterization. Individual die are shipped from MCNC in an unreleased state, with a layer of protective photoresist coating to protect them during shipment. The MUMPS release procedure developed at AFIT is summarized in Table 4-1. An overview of the typical post processing steps was given in Chapter 2.

Table 4-1. Release Procedure for MUMPS Fabricated Die.

Step	Solution	Time	Notes
1	Acetone	5-20 min.	Removes Photoresist
2	Deionized water	5 min.	Rinse off acetone
3	HF(49%)	2-2.5 min.	Etch sacrificial layers
4	Deionized water	5 min.	Rinse off etchant
5	HF:HNO ₃ :CH ₃ COOH(Glacial) (2:2:30)	~20 sec.	Polish etch polysilicon [†]
6	Deionized water	5 min.	If step 5 is included
7	2-Propanol	5 min.	Displace water
8	Hot Plate at ~100°C	~30 sec.	Evaporate 2-propanol

[†] Used for MUMPS 7 and 8 die to attempt releasing hinge pins on flip-up structures.

4.2. Experimental Setups

After devices have been fabricated and released they must be characterized using one of the testing locations available at AFIT. For electrical testing and mechanical probing of devices the micromanipulator probe station in the AFIT Cooperative Microelectronics Laboratory, bldg. 125, was utilized. For optical characterization of such devices as the grating pixels and arrays, as well as the interferometers, the photonics lab in bldg. 194 was required. Finally, thermal device testing and deflection measurements were obtained using the MMR refrigerator and laser probe interferometer located in bldg. 640. Each setup is reviewed in the sections that follow.

4.2.1. Optical Device Experiments

Depending on the device to be tested, the setup in Fig. 4-4 was modified to obtain the appropriate data. Most of the work on this station involved characterization of the variable diffraction gratings. The far field intensity pattern was obtained by placing a screen at position 2. By measuring the distance from the device to the screen, and the separation between diffracted orders, the respective diffraction angles could be calculated.

The zero diffraction order was directed away from the incoming beam by tilting beam splitter (B) enough to place the zero order on the screen for measurement. With the room lights dimmed, the far-field intensity pattern could be recorded using the far-field CCD camera and Image-Pro™ software [60]. Frequency response measurements were taken using the FND-100 detector and a LeCroy digital oscilloscope. The order to be modulated was directed onto the detector by using a mirror at position 1. The same mirror setup was also used to feed a Coherent Fieldmaster optical power meter to determine relative static intensity values as a function of the voltage applied to the device. Imaging of the device with this setup can be obtained by sliding the 10x objective into the beam path and using the near-field CCD camera.

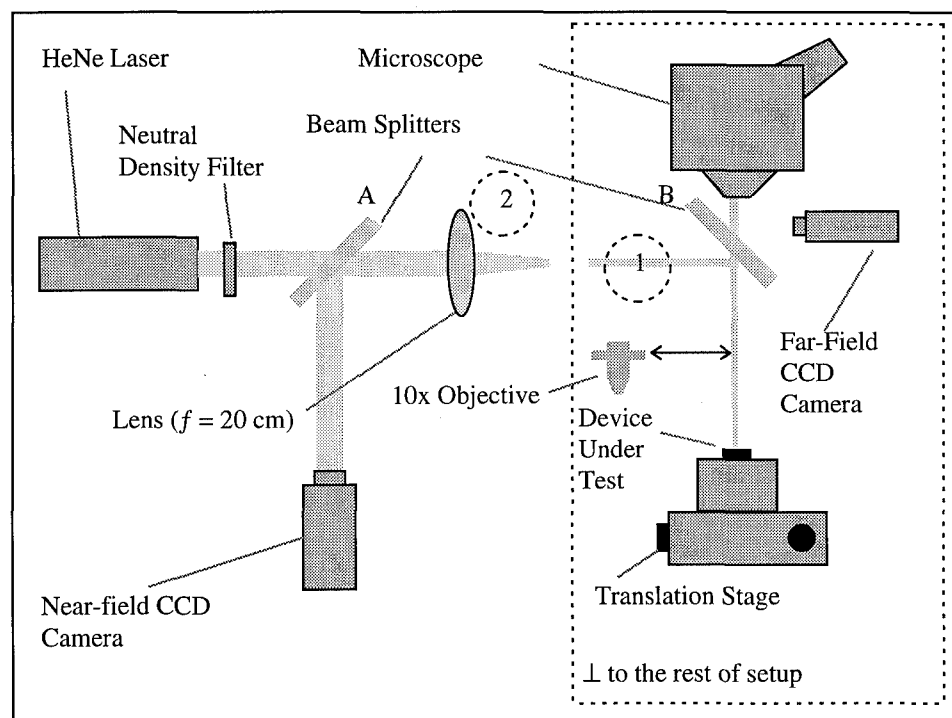


Figure 4-4. Setup used for characterization of optical components and systems.

For testing of the micro interferometer, the incoming beam is directed at one of the 45 degree mirrors that are located at the ends of the micro interferometer on the die being tested (see Section 4.4.6) and the output from the system is angled away from the input using beam splitter B. Optical modulation as a function of drive signal to the heat drive actuators can be measured using the FND-100 and LeCroy oscilloscope as was done for the variable gratings. The maximum and minimum output intensity can also be determined by using the Fieldmaster and mirror arrangement. This data can then be used to calibrate the intensity data from the modulation measurements.

Fresnel lenses were not tested in a flipped up state using this set up, but their effectiveness can be determined by observing the screen pattern achieved during illumination. By measuring the separation distances between the rings created on the screen and knowing the distance from the DUT to the screen, the focal point can be estimated and compared to the designed value. The screen patterns can be captured using the far-field CCD camera and the frame grabber software. Using this method it is difficult to determine the amount of power incident upon the Fresnel lens that would be focused down at the focal point since the reflected pattern on the screen is larger than the detectors available and would require the use of another focusing lens.

4.2.2. Probe Station Device Experiments

A probe station was used for the mechanical probing operations of all flip-up style devices. Furthermore, the probe station provided for basic electrical parameter characterization. After releasing the die, it was secured in a holding block and placed on the micromanipulator probe station. Flip-up optical components and systems were adjusted into their operational configuration using the mechanical probes with the

assistance of the flip helpers described in Section 4.1.1. After mechanical adjustments were made, electrical devices that provide device movement, usually heat drive actuators, were tested using a function generator or voltage/current source. At this time any electrical parameters requiring measurement were taken. After removal from the micromanipulator probe station, die with optical components were characterized using optical testing as explained in Section 4.2.1.

4.2.3. Thermal Experiments

Performance of thermal testing requires the interface of three sets of components: the microscope-based laser probe interferometer; the Low Temperature Micro Probe (LTMP); and various pieces of electrical testing equipment. The interface is shown schematically in Fig. 4-5 with a photograph of the operational setup shown in Fig. 4-6. Prior research work has described in detail the operation of the microscope-based laser probe interferometer [23] which works off of the mathematical principle described in Chapter 3. The original setup dimensions for this device were modified in order to maintain a small laser spot size on the device under test (DUT). Modification also required changing the microscope objective to facilitate a longer focal length in order to reach the DUT within the LTMP. The LTMP was first used at AFIT by Merkel to study the thermal effects on Heterostructure Field Effect Transistors [68].

The LTMP, model #LTMP-4, is manufactured by MMR Technologies and is composed of four major components: the LTMP; the Joule-Thomson refrigerator; the gas manifold and Nitrogen supply tanks; and the K-20 programmable temperature controller.

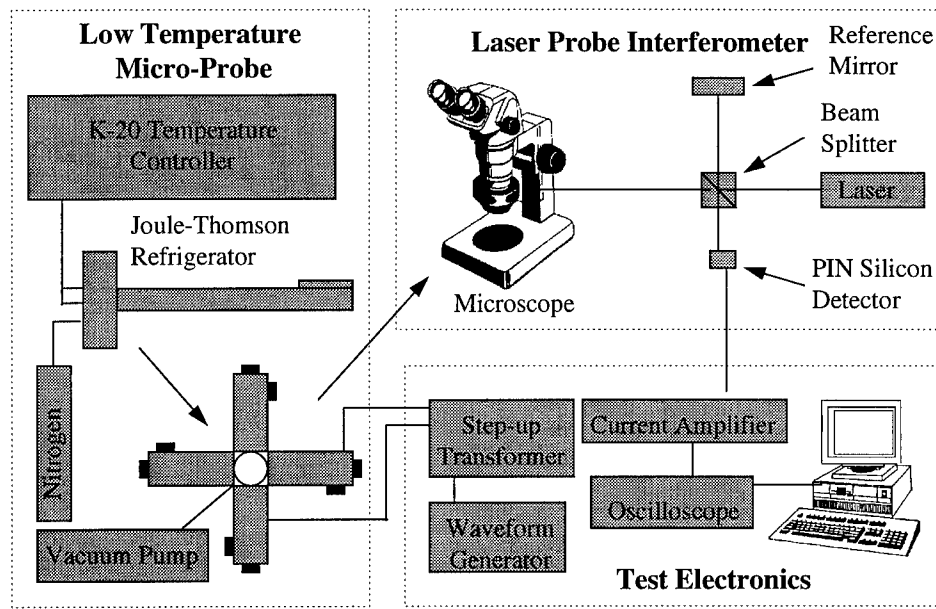


Figure 4-5. Interface schematic for equipment used in thermal testing.

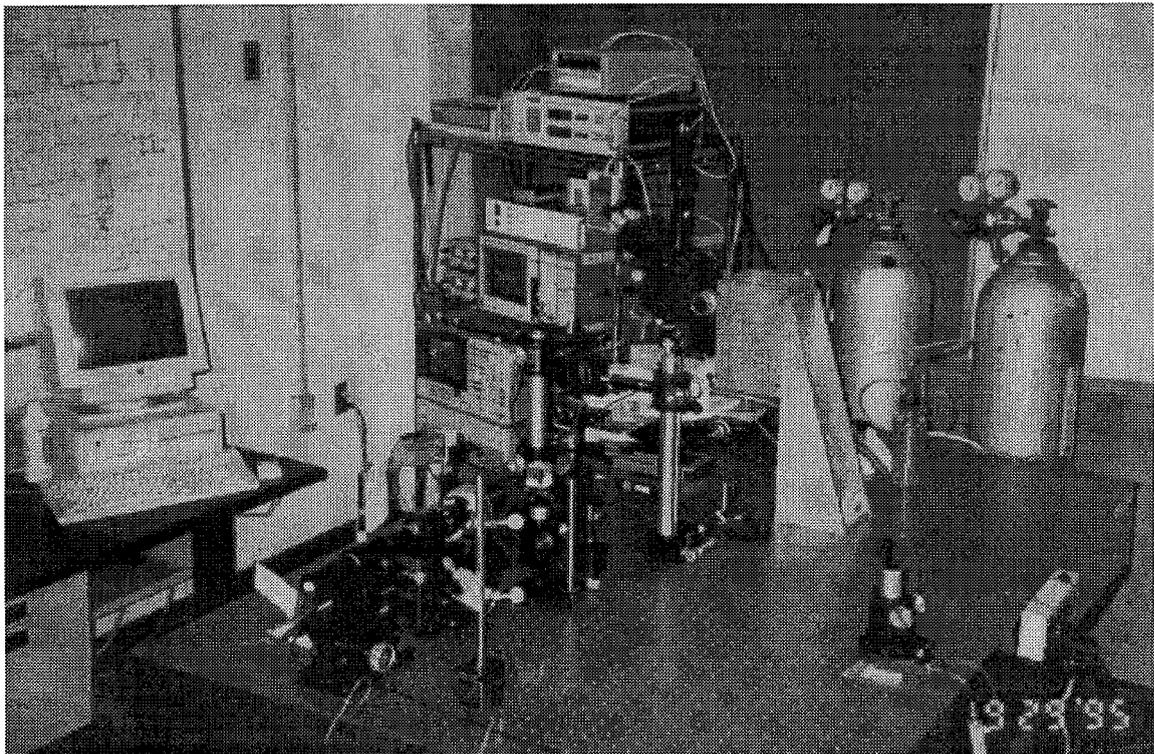


Figure 4-6. Photograph of thermal testing station. Electrical test equipment is contained on the rack behind the air table. Microscope-based laser probe interferometer with low temperature microprobe positioned below the microscope is shown on the air table. Nitrogen tanks are for the Joule-Thomson refrigerator and backfill system.

A model similar to the one used is shown schematically in Fig. 4-7. The procedure for operation of this device is described in Section 4.2.3.1. The physical principle of how it operates is described in Section 4.2.4.

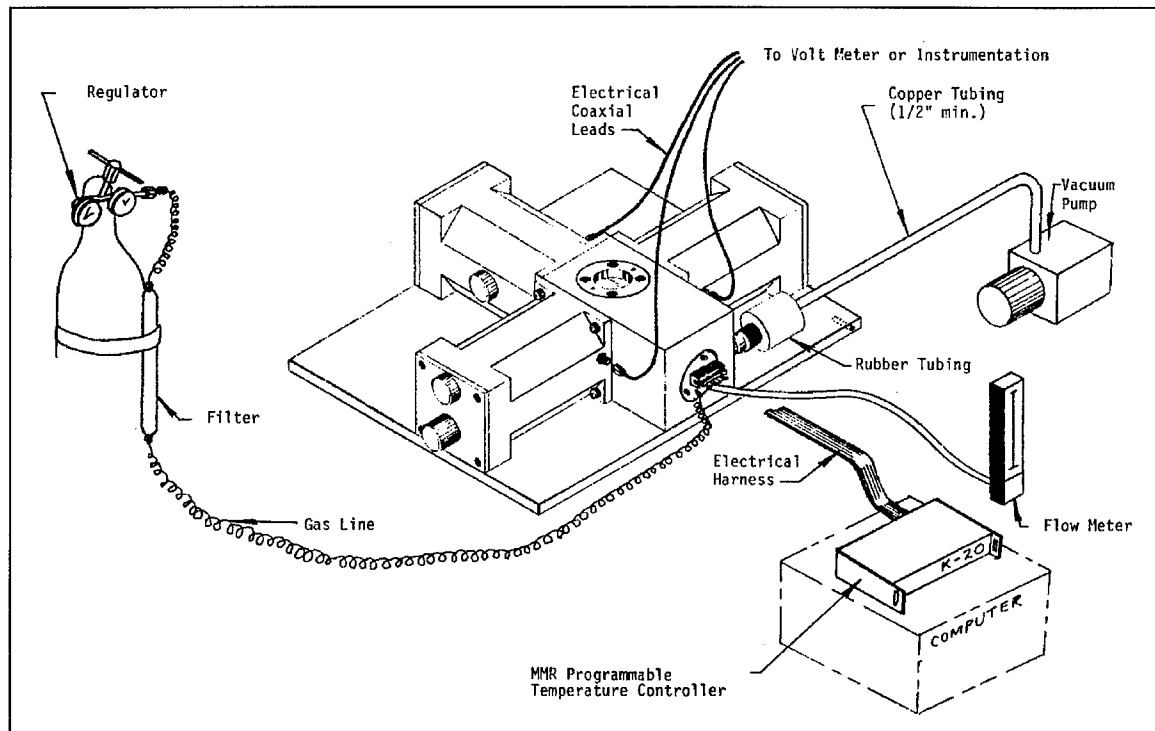


Figure 4-7. MMR technologies thermal test setup. Low temperature micro probe shown is a 3 probe chamber unit (versus the 4 probe used in experiments) [63].

Continued testing of micromirrors for voltage versus deflection required the development of a new drive signal generator. Prior thesis students were testing mirrors which could be sufficiently driven with available function generators or used a signal generator which continually failed due to design deficiencies. Function generators at AFIT are limited to 15 V sinusoidal peak-to-peak with a maximum offset bias of 7.5 V. This is often insufficient to drive the micromirror devices depending on design of the spring flexures and area of the mirror.

Acquisition of 1:5 step up transformers designed with an input impedance of $50\ \Omega$ (North Hills Electronics, model #0904LB [69]) allowed for the design of a signal generator, as shown in Fig. 4-8, that could reliably provide a drive signal of 75 V sinusoidal peak-to-peak with up to 50 V bias. Available transformers with a 1:5 turns ratio can be used from 1 kHz to 100 MHz. If required, 1:2 step up transformers that operate down to 50 Hz are available from the same manufacturer. For the drive signal generator to interface with the 7200 LeCroy Oscilloscope, 10:1 and 100:1 voltage dividers are provided in the design [61]. Tuning potentiometers were used to calibrate this part of the circuit. The bias is provided by an external power supply (HP 6236B). The allowed bias of 50 V is limited by the specifications of the transformer. The $500\ \mu\text{F}$ capacitor provides protection for the transformer from the bias. The circuit was verified using a Spice[®] simulation software package [61].

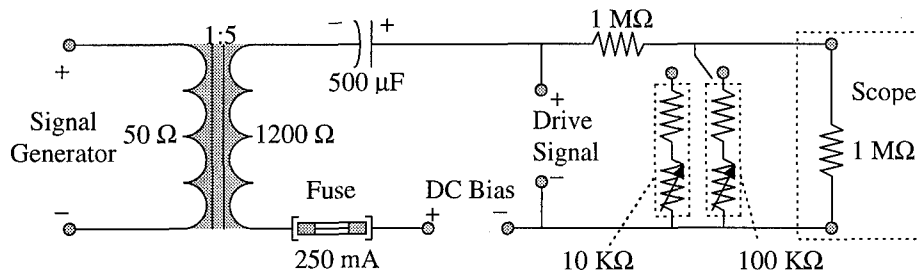


Figure 4-8. Schematic diagram of device input drive signal generator.

4.2.3.1. Thermal Testing Procedures

Specific procedures exist for accurate operation of the MMR refrigerator assembly [63-67]. In order to heat or cool devices using the LTMP, a start-up procedure must first

be carried out as discussed in Table 4-2. All manifold operations refer to the valves as labelled in Fig. 4-9.

Table 4-2. Low Temperature Microprobe Start-up Procedure.

Step	Operation
1	Make sure all valves are in the closed position (turned clockwise)
2	Turn on the vacuum pump. If the pump does not transition from initial noisy to subsequent quiet operation, turn pump off and check all vacuum line connections to ensure they are tight.
3	Turn on power to Convectron vacuum gauge. Check power light on front panel (red). Observe that the pressure indicated is 760 Torr or greater.
4	Open vacuum isolation valve (V_1). Chamber pressure can now be monitored from the vacuum gauge.
5	Initial pump down times to 5 mTorr could be 10-to-24 hours. 20 mTorr or less is sufficient to operate the refrigerator. If this pressure is not achieved in the time period specified, close V_1 and monitor the vacuum pressure rise. If the pressure increases to atmospheric in a few minutes, there is a leak in the system.

The rapid recycling of a MMR cryogenic system from atmospheric pressure to below 5 mTorr and room temperature to 80 K requires the use of a dry gas backfill system. The backfill gas selected for use is the same prepurified grade Nitrogen (99.998% pure) used for the MMR refrigerator. After the new high pressure tanks (~2500 pounds per square inch gauge (psig)) drop below the required operating pressure of the refrigerator (~1800 psig) then the tank is used for the backfill operation. Backfill is performed at a pressure of 15 psig or less and is regulated by R and VR in Fig. 4-9. The backfill operation is outlined in Table 4-3 and is performed whenever the LTMP will not be used for extensive periods of time. During this thesis, backfill was performed every night after testing since maintaining vacuum overnight risked contamination of the chamber in the event of a power failure.

Table 4-3. Low Temperature Microprobe Backfill Procedure.

Step	Operation
1	Allow the vacuum chamber pressure to increase above 5 mTorr when operation of the MMR refrigerator has terminated and have warmed the refrigerator to room temperature (300 K).
2	Close the vacuum isolation valve (V_1).
3	Regulate the pressure from the backfill tank to 15 psig or less. [†]
4	Open backfill isolation valve (V_4). If gas pressure exceeds atmospheric by more than 1 psi the pressure relief valve (V_R) will open and allow some of the backfill gas to escape. Gas hissing may therefore be evident.
5	Open the vacuum chamber valve (V_3). The flow restrictor (R) will limit gas flow so that the pressure will increase to atmospheric slowly. When the vacuum gauge (VG) indicates atmospheric pressure, proceed to step 6.
6	Close vacuum chamber backfill valve (V_3).
7	Turn off the vacuum pump (VP).
8	Open the pump line backfill valve (V_2). Wait until the pressure relief valve (V_R) starts venting. Will hear gas hissing.
9	Close the pump line backfill valve (V_2).
10	Close the backfill gas isolation valve (V_4).
11	Close the main valve on the backfill tank.

[†] Do not change the low pressure gas setting of the regulator on the backfill gas tank.

Prior to performing the setup procedure outlined in Table 4-2, the die containing the Devices Under Test (DUT) is mounted onto the tip of the refrigerator. In order to facilitate the optical interface of devices through the Sapphire window of the LTMP a ~1/8 inch thick copper block has been mounted onto the end of the refrigerator using the same silicon-based conductive grease used for mounting of the chip. This positions the focal length of the selected microscope objective at the surface of the chip with enough clearance above the sapphire window such that the translation stage can be adjusted while maintaining focus. Due to the limited size of the sapphire window, interference with the microscope objective prevents viewing of the entire chip without repositioning the chip on the refrigerator. In order to mount the chip onto the refrigerator it must first be

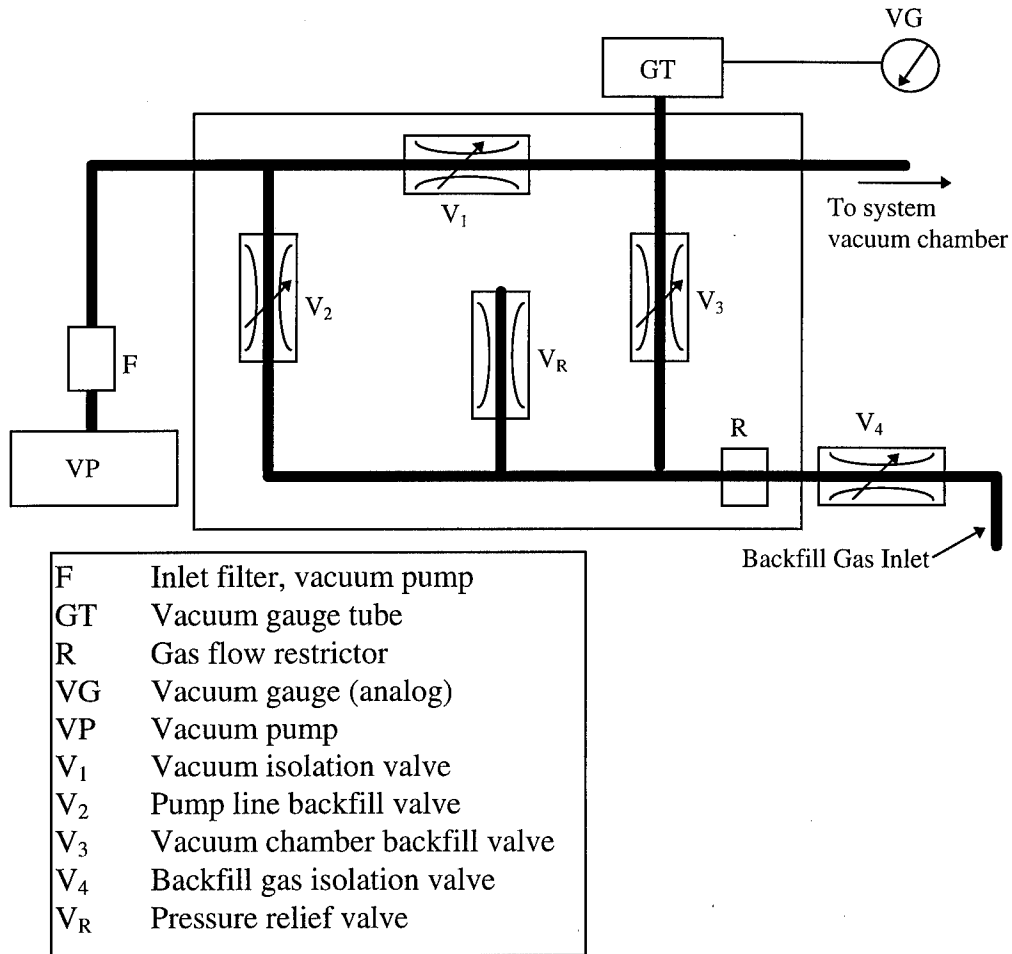


Figure 4-9. Schematic diagram of gas manifold for low temperature microprobe [65].

removed from the LTMP vacuum chamber. To prevent contamination, the chamber is first pressurized by performing steps 1-5 of Table 4-3. Prior to removal of the refrigerator care must be taken to ensure that the probe tips are raised to their highest position so they are out of the way of the refrigerator and DUT. After removal from the chamber the new chip with DUT is mounted onto the copper block using the conductive silicon grease provided by MMR (see Fig. 4-10). After mounting, the refrigerator assembly is reinserted into the vacuum chamber. A hose is connected to the external flange of the refrigerator which is mounted to a flow meter to monitor nitrogen flow through the

refrigerator. If it is desired to obtain 70 K, the output of the flow meter is subsequently connected to a vacuum assist vacuum pump. This was not done in any of these experiments. The stainless steel capillary gas line is also connected to a fitting on the flange of the refrigerator along with the ribbon cable of the K-20 Programmable temperature controller. At this time the start-up procedure in Table 4-2 is performed. After reaching the desired vacuum level (~20 mTorr or less) the high pressure Nitrogen regulator is adjusted to 500 psi. Gas at this pressure is run through the refrigerator for 3 minutes to purge out any moisture in the system. During this operation the K-20 is programmed to maintain the refrigerator temperature at 325 K. After the purge is completed, the High pressure Nitrogen regulator is adjusted to 1800 psi, probes are lowered to the desired position for testing and the K-20 is programmed to obtain the desired temperature. Temperatures from 80 K to 450 K can be achieved with this setup. After testing has been concluded the high pressure gas supply is turned off and the refrigerator is allowed to warm up (above 0°C) prior to performing the backfill procedure outlined in Table 4-3. The specification on the silicon conductive grease limits the upper temperature to ~450 K. Above this temperature it is unknown what will happen to the grease. Use of an epoxy can allow for testing at temperatures above this value up to the limit of the refrigerator (580 K).

4.2.3.2. Frequency Testing Procedure

The LTMP test setup was also modified to include a spectrum analyzer for measuring frequency characteristics of MEMS devices. Since the LTMP can be used to

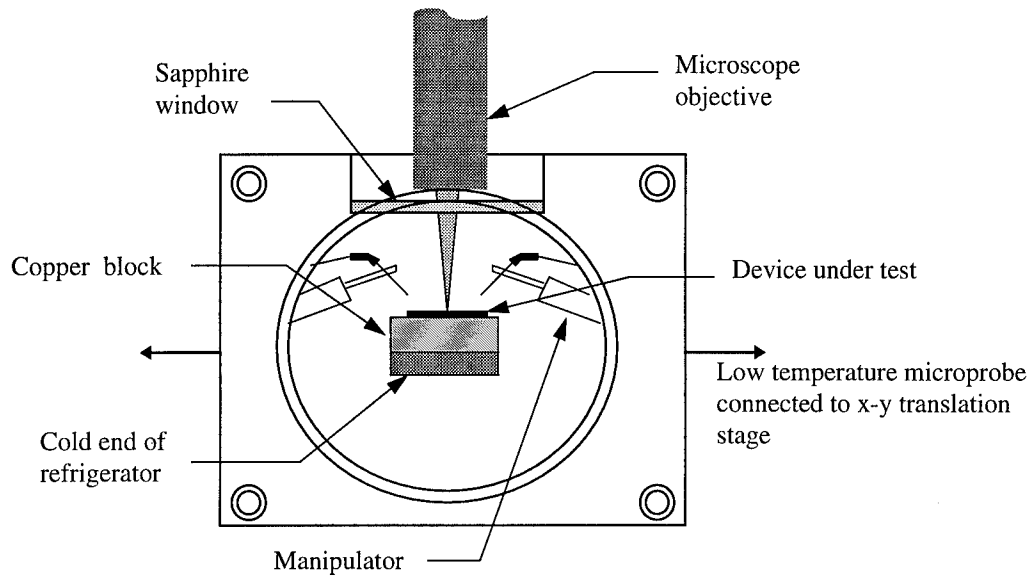


Figure 4-10. Side view of low temperature micro probe with two manipulators shown. Copper block is inserted to allow focus of laser spot onto device under test and to provide for imaging of the chip.

create a vacuum environment, the viscous damping of FBMD devices can be essentially eliminated allowing for detection of the devices resonance frequency. The setup used to interface the HP 4195A Network/Spectrum Analyzer to the LTMP for testing is shown in Fig. 5-11. The bias voltage can be adjusted from 0 to 40 V and the source (S1) can provide 1.26 V peak-to-peak. After connecting to the device, the chamber is pumped down (see Section 4.2.3.1) and the spectrum analyzer is adjusted to output T1/R1 which is the transmission coefficient. This value can also be considered the relative mirror displacement as a function of frequency. Reflection measurements would typically yield cleaner output signals than transmission, but require the use of a bidirectional bridge. The bridge available at AFIT is only good for frequencies greater than 100 kHz which is too high for the devices being tested.

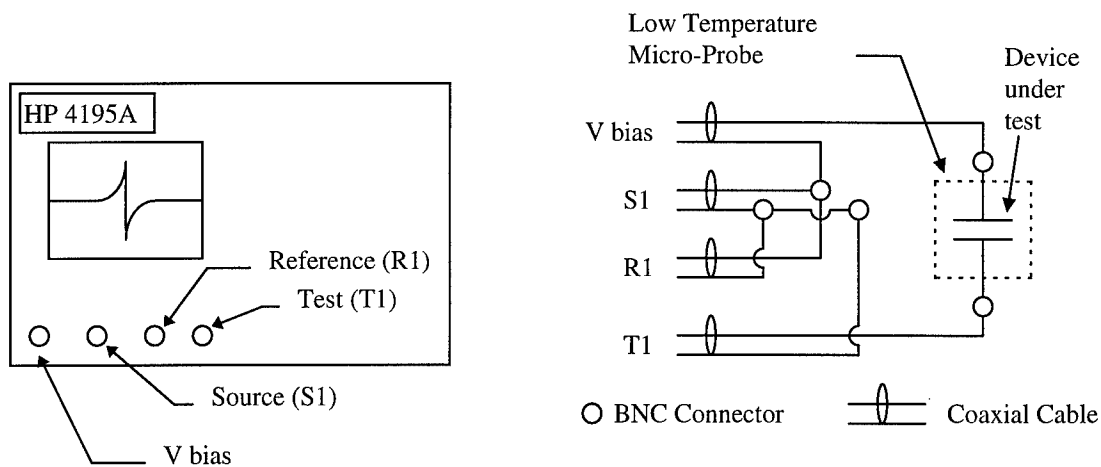


Figure 4-11. Schematic of electrical connections from the HP 4195A network/spectrum analyzer to the device under test.

4.2.4. Testing and Characterization Equipment

The following list describes the major equipment utilized in the post-processing and characterization of devices.

Micromanipulator table - The micromanipulator Company, Model #6200

The micromanipulator allows for the testing of 1 cm square die by placement in a vacuum chuck. The station can handle up to eight probes for providing voltage or current sources to the Device Under Test (DUT). Probe tips used in this research are between 10 to 20 μm in diameter which is sufficiently small to contact the device probe pads which have been designed at 20 to 50 μm square. The probe station has been customized for MEMS device testing with electrical interfaces provided for use of a function generator, voltage sources, multimeters, and a digital oscilloscope. Videos of movable devices can be taken through the use of a video camera mounted on top of the microscope.

Dual Power Supplies (2) - 1. Hewlett Packard, Model #HP 6236B, 2. Powertec, Model #6C3000

The HP is an analog controlled supply for providing two independent voltage or current sources. Voltages of +/- 20 V and currents of +/- 2.5 A are achievable if connected independently or the two sources may be wired together to provide up to +/- 40 volts or +/- 2.5 amps. The Powertec can supply 0 to 36 V DC at 1 A.

Multimeters - Fluke, Model #77/BN, #77/AN, and #8600A

The multimeter is the primary device used to measure currents, voltages, and resistances of devices under static loads. The Fluke is capable of measuring voltages from 0 to 1000 VDC or 750 VAC and currents up to 10 A. Resistance measurements can be made up to 32 M Ω .

Function Generators (3) - 1.Wavetek, Model #148, 2.Hewlett Packard, Model #3314A, 3. Hewlett Packard, Model #33120A

The Wavetek is a 20 MHz AM/FM/PM generator with one output at 50 Ω . It can supply a 15 V peak-to-peak sinusoidal voltage with up to 7.5 V bias. The Wavetek is used as the signal source for the Microscope-based Laser Probe Interferometer. The HP 3314A is able to provide a square, sinusoidal, or sawtooth waveform at frequencies from 10 Hz to 20 MHz. The peak-to-peak voltage can be varied from 0.1 to 10 V with a DC bias of up to 10 V. This generator is used in conjunction with the probe station. The last generator, HP 33120A is a 15 MHz Function/Arbitrary waveform generator capable of supplying up to 20 V peak-to-peak with a 10 V bias. This generator is used with the optical test setup for grating measurements.

Ball Bonder - Kulicke and Soffa Industries, Inc., Model #4124

This device is utilized when numerous electrical contacts of devices are required, such as in the micromirror arrays. The device uses temperature, pressure, and ultrasound

to bond a 25 μm diameter gold wire to the die bond pad and selected IC package.

Scanning Electron Microscope - International Scientific Instruments, Model #WB-6

This piece of equipment is used exclusively at AFIT to photograph the micro details of the MEMS devices since it has a resolution capability of ~ 4 nm. Photography is essential for recording device performance and qualitatively evaluating the fabrication and design of devices. The three dimensional features of MEMS devices are best seen using this evaluation tool. In order to improve viewing of devices, a thin film of gold (~ 300 Å) is sputtered on to the die using a Ladd bench top sputter coater, model #30800. The gold layer prevents charging of the polysilicon which degrades the image quality.

Thermal Testing Station - MMR Technologies, Inc., Model #K20P4-4

1. Low Temperature Micro Probe, Model #LTMP-4
2. Programmable Temperature Controller, Model #K-20
3. Joule-Thomson Refrigerator, Model #R2400-22
4. Vacuum Accessory Kit, Model #C1805/6

The Low Temperature Micro Probe (LTMP) is designed to make thermal material and device characterization a simple operation without the use of a bulky liquid nitrogen apparatus. The LTMP has four manipulator assemblies for electrical probing with external Sub Miniature Adaptor (SMA) connectors provided for interface with test equipment. Each manipulator assembly is housed in it's own vacuum chamber which is attached to the main chamber where the refrigerator is housed. Each manipulator is capable of X, Y, and Z movement over a 1.0 x 1.0 x 0.25 inch volume with high precision. The main chamber contains a Sapphire window for viewing and optical interface of the device. Vacuum (for pumping down the main chamber to ~ 20 mTorr)

and backfill (with Nitrogen at ~760 Torr) is provided through a gas manifold which contains a pressure gauge for monitoring chamber pressure. A three probe LTMP is shown in Fig. 4-7. The K-20 provides controlled temperature and cycling measurements over a temperature range from 70 K (-203 °C) to 580 K (307 °C) which are the limits of the supplied refrigerator. The K-20 provides electrical signals to the refrigerator for heating and driving devices (if die is wire bonded to refrigerator) and receives signals from the refrigerator for monitoring temperature and electrical signals from devices. The MMR refrigerators operate using the Joule-Thomson effect. When a gas is allowed to expand through a porous plug or fine capillary tube at high pressure, the gas cools. The refrigerator uses a counter-current heat exchanger to magnify this effect by precooling the incoming high pressure gas. The process can be further improved by hooking the atmospheric (atm) side of the capillary to a vacuum pump in order to achieve ~70 K operation. The high pressure gas source is 1800 psi, 99.998% prepurified grade Nitrogen.

Digital Oscilloscopes - LeCroy, Model #7200 with #7242B plug-in & 9400A

These LeCroy scopes can monitor 2 independent channels of data with voltages up to +/- 5 VDC into 50 Ω or 250 V (DC + peak AC) into 1 M Ω . The allowed 50 Ω voltage can be increased with the use of probe attenuators. The scopes are capable of measuring frequencies from 10 MHz-250 MHz at 1 M Ω AC. Both LeCroy's are setup with an HP-IB interface to a personal computer in order to capture waveforms for analysis.

Current amplifier - Kiethley, Model #427

This piece of test equipment replaces the transimpedance amplifier that was designed by prior researchers for use in the microscope-based laser probe interferometer

[23]. Gain up to 10^{11} volts/ampere is achievable. This amplifier allows for resolution of the modulation of intensity measured by the PIN photodetector.

Network/Spectrum Analyzer - Hewlett-Packard, Model #HP 4195A

This analyzer is capable of performing measurements from 10 Hz -to- 500 MHz with the ability to measure the transmission coefficient over this entire range and the reflection coefficient for values ≥ 100 kHz with the use of a separate directional bridge.

Programmable Stepping Motor Controller with Translation Stages - Klinger Scientific, Model #CC1.2

Used for precise positioning of the laser spot from the microscope-based laser probe interferometer. The stepper can move in two dimensions with a step size of $0.1 \mu\text{m}$ and can be programmed with a personal computer through a HP-IB interface.

Optical Detectors (2) - 1. Newport, Model #818-BB-21 2. EG&G, Model #FND-100

The Newport is a battery biased Silicon PIN detector with a risetime of < 1 nsec and an output impedance of 50Ω . Responsivity is 0.4 A/W @ 830 nm with a saturation level of 10 mA (25 mW). The EG&G Salem detector has the same risetime, with a responsivity of 0.62 A/W @ 900 nm .

Optical Power Meter - Coherent Fieldmaster, Model #FM

The Fieldmaster is a digital device that allows for calibrated measurement of optical power up to $\sim 20 \text{ mW}$ without an attenuator.

4.4. Device Descriptions

This section outlines in detail the major classes of devices designed for this thesis. In each case a representative layout from Cadence is provided along with a Scanning Electron Microscope (SEM) micrograph of the device after fabrication. Where appropriate, the main components of the device are labeled in the Cadence layout.

4.4.1. Flip-up Optical Devices

Device Name: Flip-up Mirror
Actuation Method: Mechanical and Heat drive actuator

This device is designed primarily to provide single direction / adjustable angle control of a light beam. All of these devices (see Table 4-4) have a nominal size of 171 x 745 μm with an active mirror area of 150 x 150 μm (see Fig. 4-12). For use with the small interferometers, discussed in Section 4.4.6, a 50 x 50 μm mirror is attached to one side as shown in Fig. 4-14. The original designs of this device (ver. 1-6) included etch holes in the mirror at every 30 μm which led to a total of 30 etch holes per mirror. Versions 7-10 include only 4 etch holes for the entire mirror. The original rail formers included a 20 x 20 μm square hole for using the probe to remove them from the device. The rails are 20 μm wide with a 4 μm wide anchor section. There are two substrate and one scissor hinge used to elevate the mirror.

Versions 7, 8 and 10 modify the original design for a 45 and 90 degree mirror by stiffening the mirror elevating arm and connecting the removable rail formers to the ratchets. The stiffening of the mirror elevating arm is done by utilizing the conformance of different layers to emboss the arm. Alternating rows, along the entire length of the arm, of 2 μm dimple and Poly 0 layers provides the necessary embossing.

Versions 9 and 10 are both a 90 degree mirror with two sets of heat drive actuator arrays attached to the ratchet locks in order to provide the final mirror angle mechanical adjustment (see Fig. 4-13). The Poly 1 lines running from the heat drive actuator arrays, to the ratchets, are 2 μm wide and the lock is dimpled to reduce the surface area contacting the substrate. This minimizes the possibility of stiction during the sacrificial layer release or operation of the device. A single heat drive actuator is used to engage the ratchet lock into the ratchet. Versions 1-10 are all initially adjusted for the desired or starting angle using mechanical probing at the probe point shown in Fig. 4-12.

Table 4-4. Versions of Flip-up Rail Guided Ratcheting Mirrors.

Version #	Description	MUMPS
1	Nominal 45 degree with 200 μm long lock	7,8
2	Nominal 45 degree with 100 μm short lock	7,8
3	Nominal 90 degree with 200 μm long lock	7,8
4	Nominal 90 degree with 100 μm short lock	7,8
5	Fixed 45 degree with 200 μm long lock	7,8
6	Fixed 90 degree with 200 μm long lock	7,8
7	Modified ver. #1	9
8	Modified ver. #3	9
9	Modified ver. #3 with heat actuated ratchets	8
10	Modified ver. #9	8,9
11	Adj. tilt mirror with Heat actuator array	8,9
12	ver. #11 with different lock former	8,9

For ver. 11 and 12 (see Fig. 4-15), pieces of Poly 1 are used to form lock positions for the elevated plate. Versions 11 and 12 are designed to hold the flip-up plate vertical after elevation by using the depression caused by conformance of the layers. Version 12 uses a Poly 1, 2 μm wide line that is longer than one on ver. 11 to form the locking mechanism. After being locked into place, the heat drive actuators are used to tilt the mirror for angle adjustment relative to the substrate.

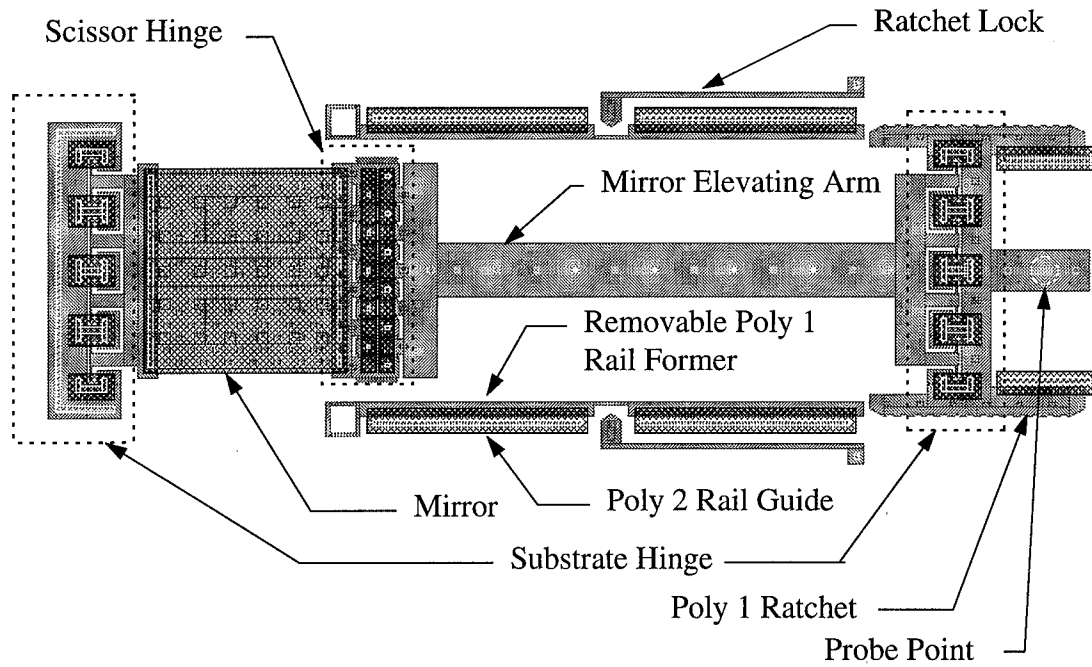


Figure 4-12. Cadence layout of ver. 3 flip-up mirror with ratchet for 45 degree nominal angle relative to substrate.

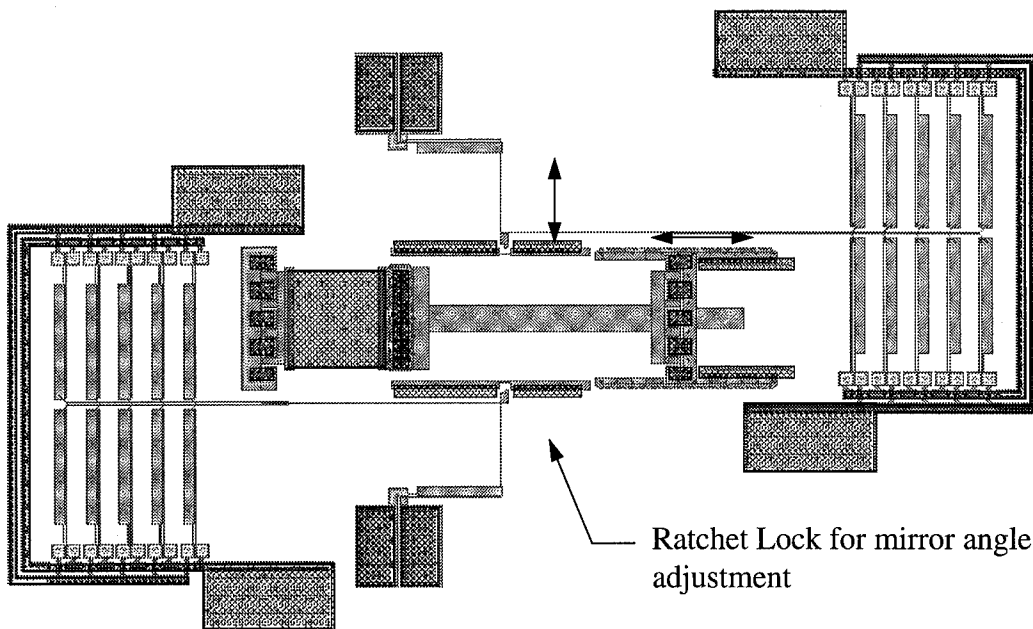


Figure 4-13. Cadence layout of heat drive actuated ratcheting adjustable mirror from MUMPS 8. The arrows indicate directions of movement for one side of the ratchet mechanism.

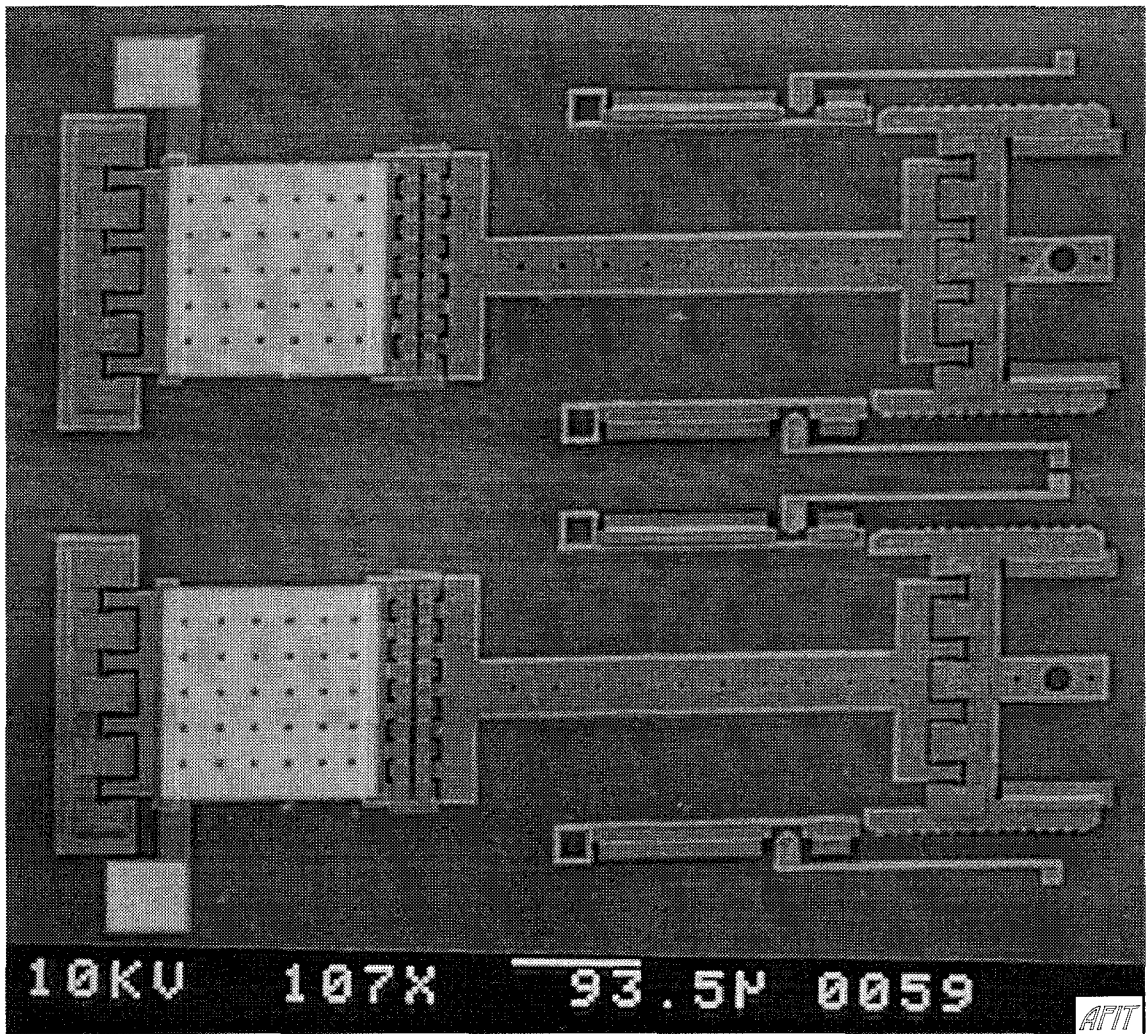


Figure 4-14. Scanning electron micrograph of ver. 1 flip-up mirror with ratchet for 45 degree nominal angle relative to substrate.

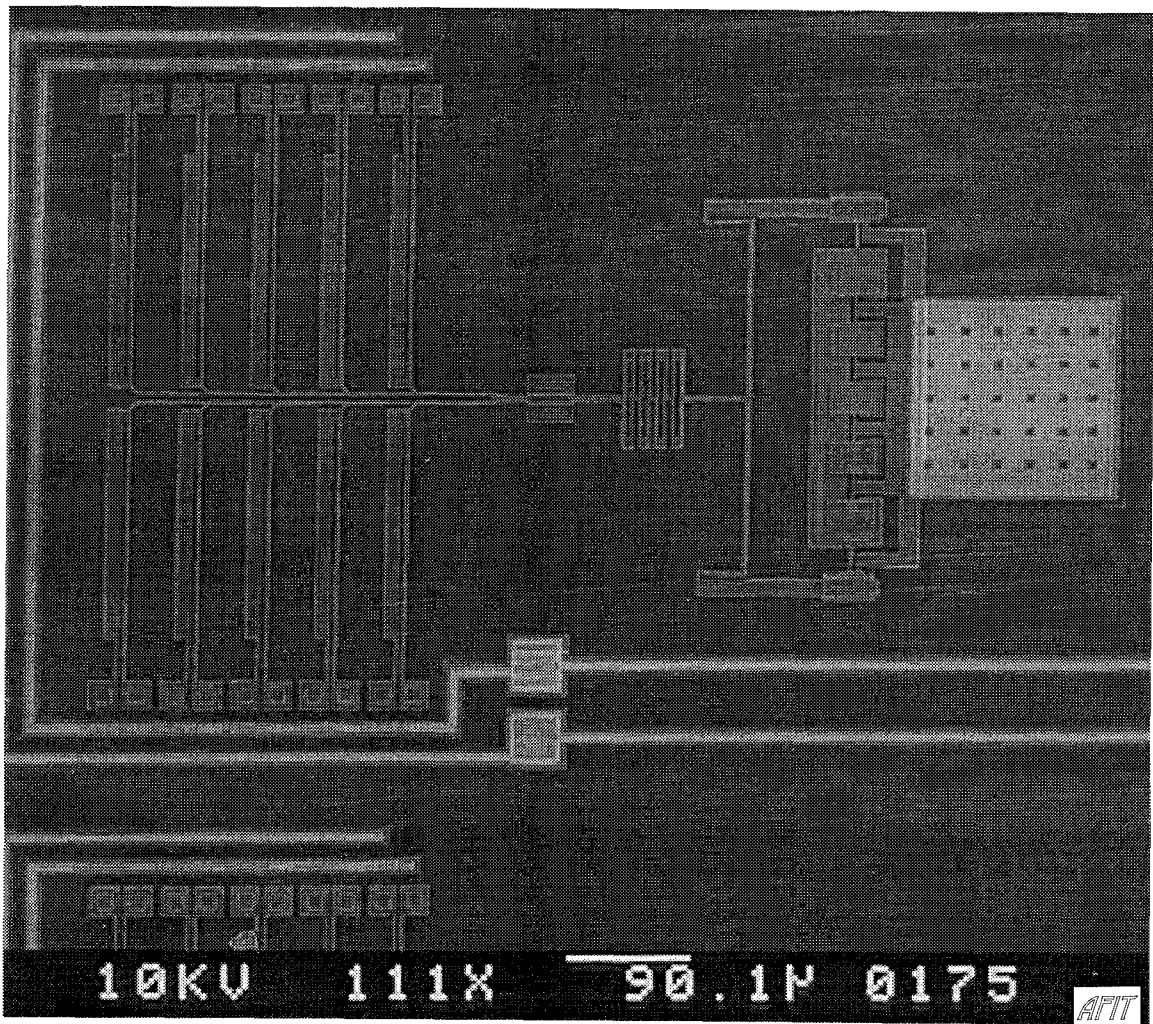
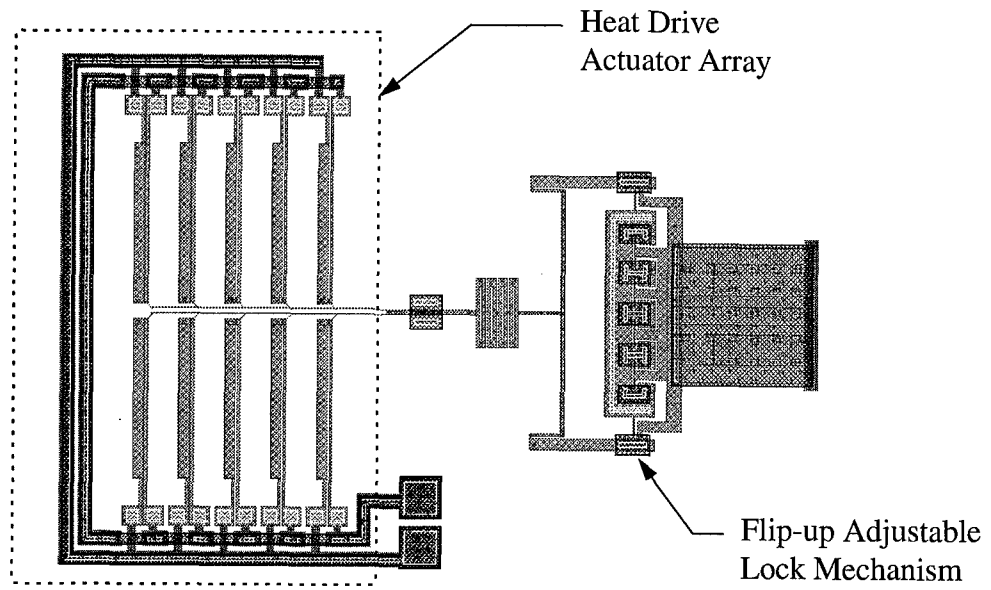


Figure 4-15. Cadence layout and scanning electron micrograph of ver. 11 tilt adjustable flip-up mirror from MUMPS 7.

Device Name: Rotating Flip-up Optical Parts
Actuation Method: Mechanical and Heat drive actuator

Numerous designs have been drawn using a rotating, pinned to the substrate, plate as the steering mechanism (see Table 4-5). Devices included Fresnel lenses, gratings, and mirrors. All appear similar to the Cadence layout shown in Fig. 4-16 with the exception of ver. 5 and 6 which looks like the device shown in Fig. 4-17. A micrograph of the center structure of ver. 1-4 is shown in Fig. 4-18. Version 6 modifies ver. 5 by replacing the numerous rail formers with a continuous (~ 320 degree) rail former which stays in the rail guide during operation. The locks for ver. 1-4 extend from the sides of the rotating plate and are one sided to provide precise alignment. The lock idea was first presented by UCLA [11].

Version 7 is a ver. 3 mirror with heat drive actuators positioned for ratcheting the lower plate to provide rotation of the device as shown in Fig. 4-19. The rotation is limited to one direction since the teeth of the ratchet are only in one direction and only over ~ 150 degrees of the circumference.

Table 4-5. Versions of Rotating Optical Structures with Characteristic Dimensions.

Version #	Description	Length (μm)	Width (μm)	MUMPS
1	Rotating Fresnel Lens with 500 μm focal length for 632 nm wavelength.	489	625	7, 8
2	Rotating Grating with 4 μm period and 2 μm spaces.	489	625	7,8
3	Mirror made of Poly 1	489	625	7,8
4	Mirror made of Poly 2	489	625	7,8
5	90 degree mirror with 360 degree rotation	972	1,249	7,8
6	Modified 90 degree mirror with 360 degree rotation	972	1,249	9
7	Rotating Ratchet Mirror	489	625	7,8

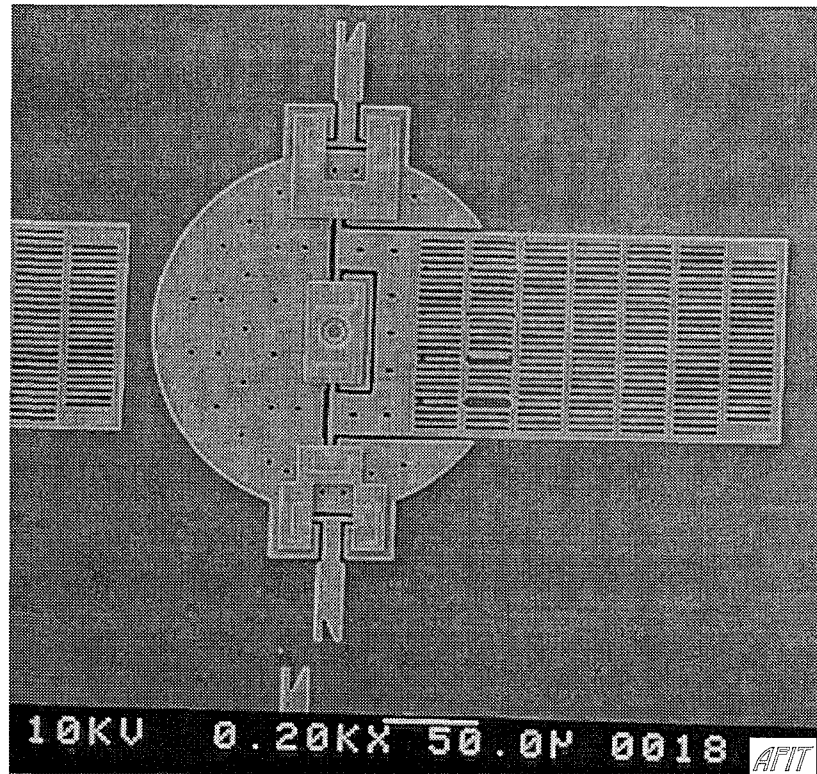
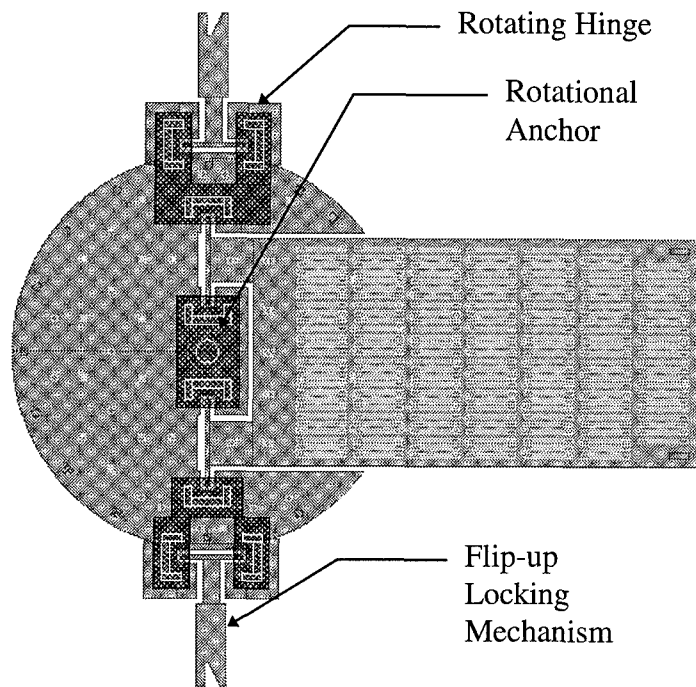


Figure 4-16. Cadence layout and scanning electron micrograph of ver. 2 rotating flip-up grating.

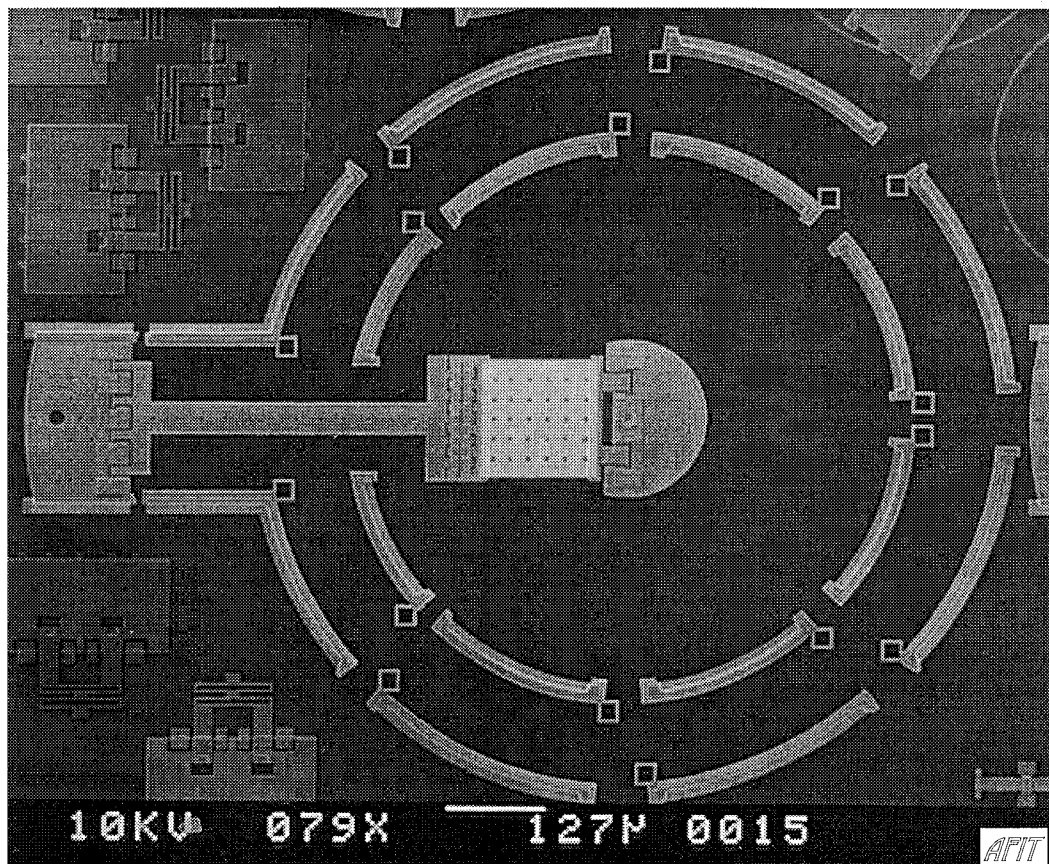
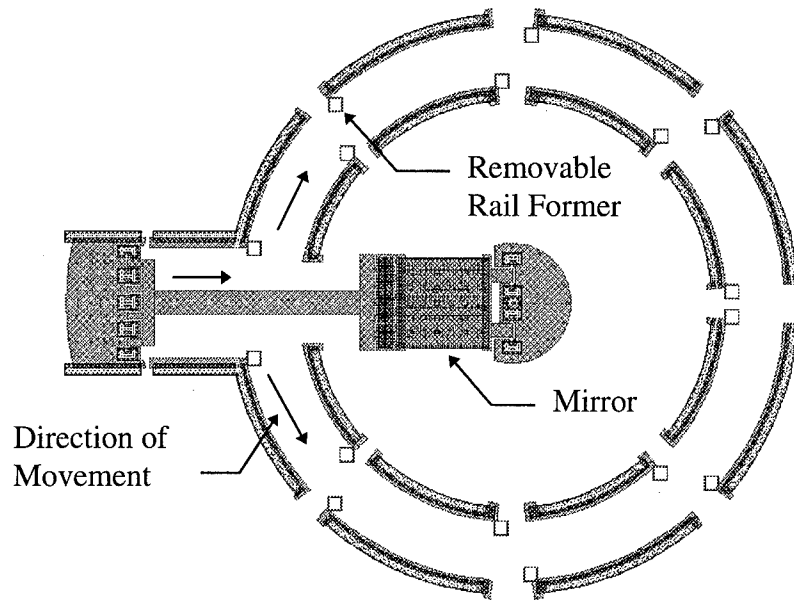


Figure 4-17. Cadence layout and scanning electron micrograph of 360 degree rotating flip-up mirror from MUMPS 7.

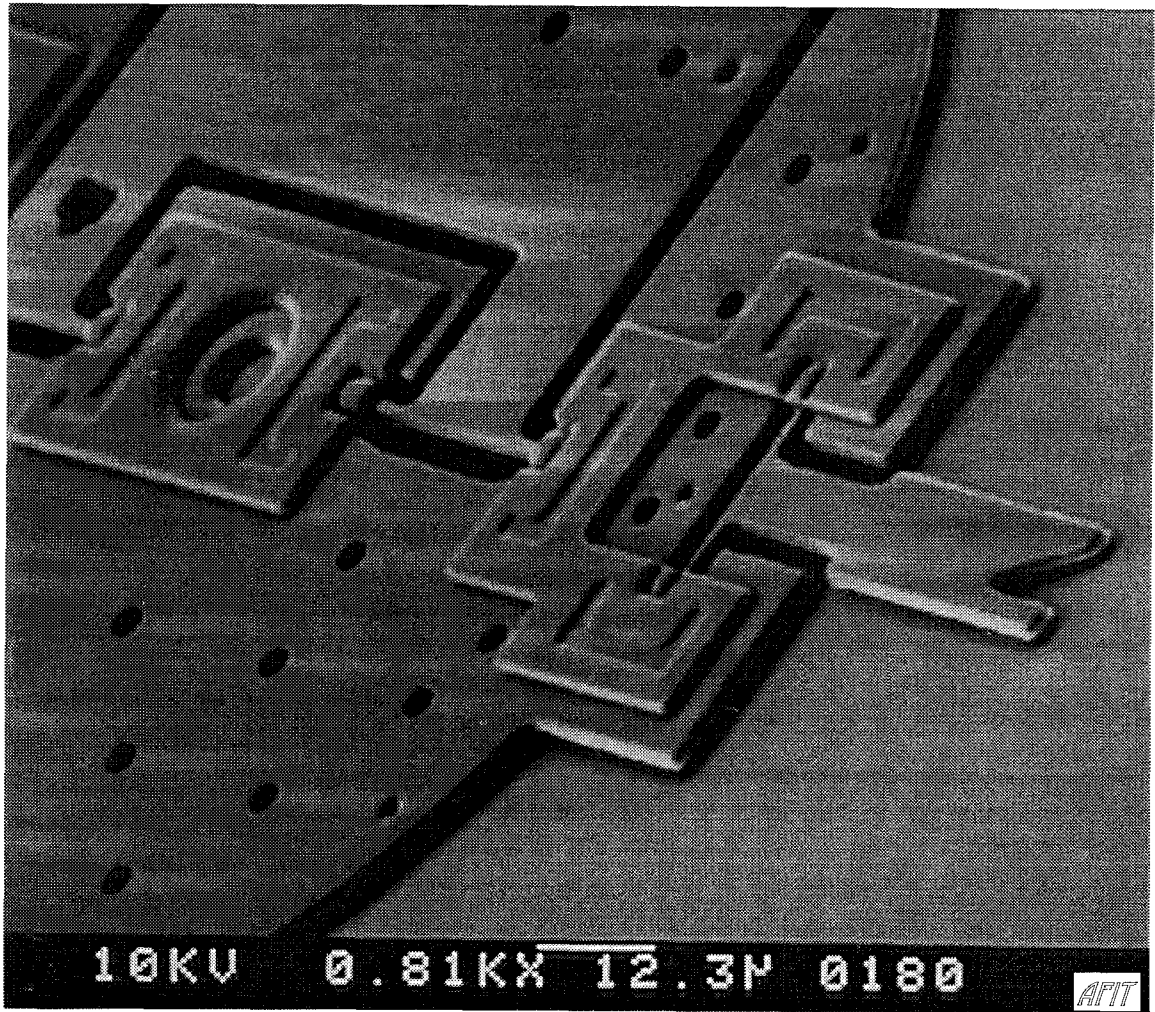


Figure 4-18. Angled scanning electron micrograph of locking mechanism and pivot point for rotating flip-up structures.

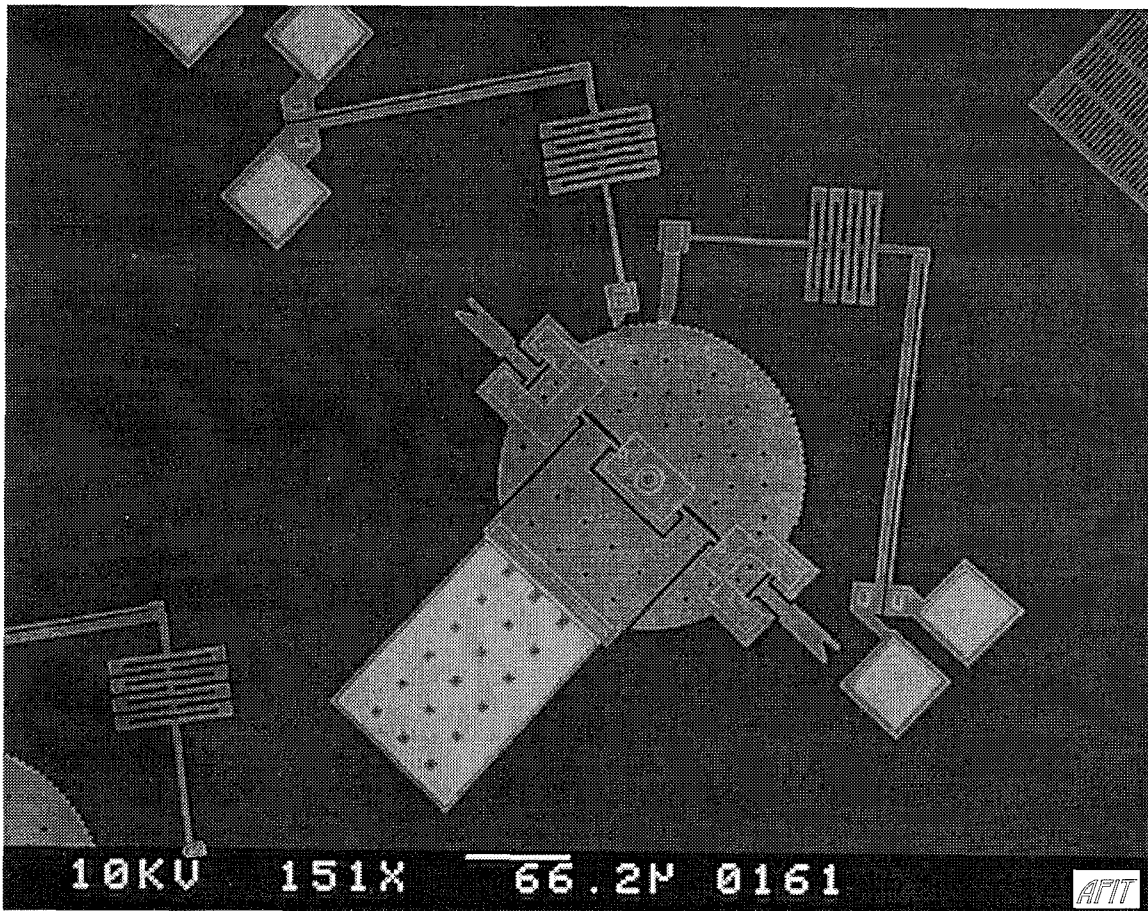
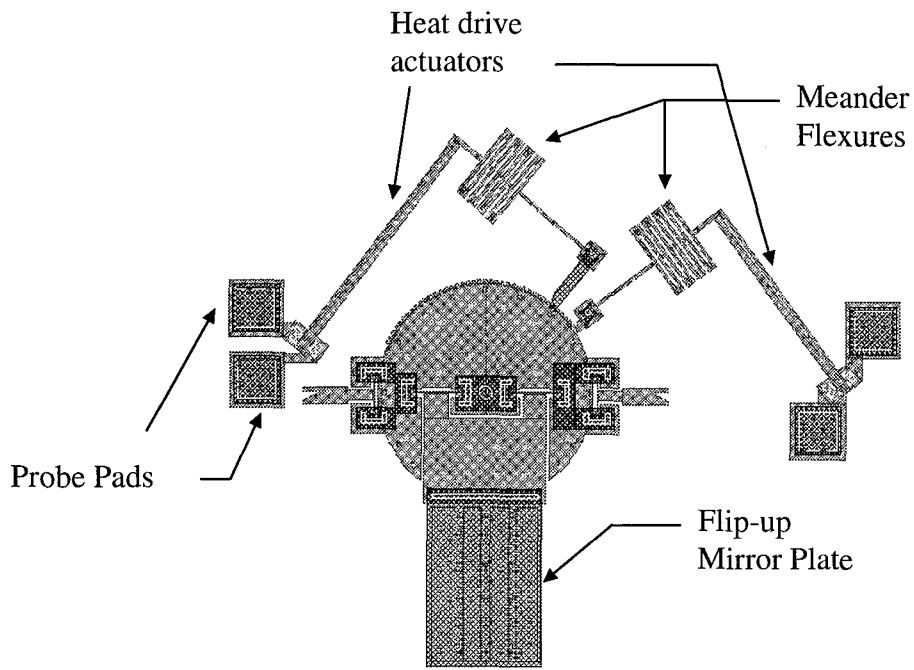


Figure 4-19. Cadence layout and scanning electron micrograph of ver. 7 rotating ratchet mirror.

4.4.2. Heat Actuators

Device Name: **Circular Heat Actuator**
Actuation Method: **Heat drive actuator**

This device is drawn with three different arc lengths of 180, 270, and 285 degrees (see Fig. 4-20). Similar to the straight heat drive actuator described in Chapter 2, this device expands outward by applying a current through the two legs. The outer leg is thicker for half of its length in order to cause the inner leg to heat up and expand. Dimples are provided at the 180 degree point and at the end of the arc in order to prevent the device from sticking to the substrate. For all three devices, the legs were drawn in Poly 1 since it is thicker and can handle a larger current as well as provide more force when used to actuate a device.

Device Name: **Vertical Heat Actuator Test Arrays**
Actuation Method: **Heat drive actuator**

Two versions of these actuators were designed for testing. Version 1 uses a Poly 1-2 via (2 μm diameter) to connect Poly 1 and Poly 2 thin runners together at 90 degrees with respect to each other (see Fig. 4-21). By applying a current between the pads, the thinner 2 μm wide Poly 1 runner should expand more than the thicker 6 μm wide Poly 2 runner. The net result should be an upward and outward movement of the device at the anchor corner. Runners were drawn with four different lengths (50, 70, 90, and 105 μm). Version 2 of this device uses the same layer (Poly 1) for both runners. Both runners on this version have the same width of 2 μm and thermal expansion should cause the corner to move outward.

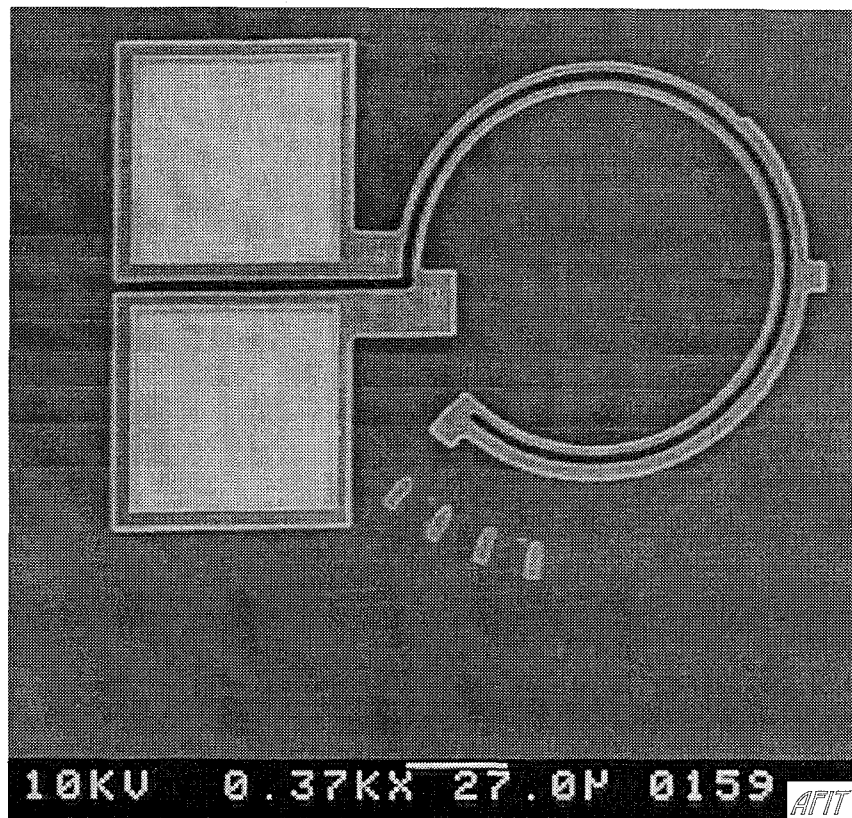
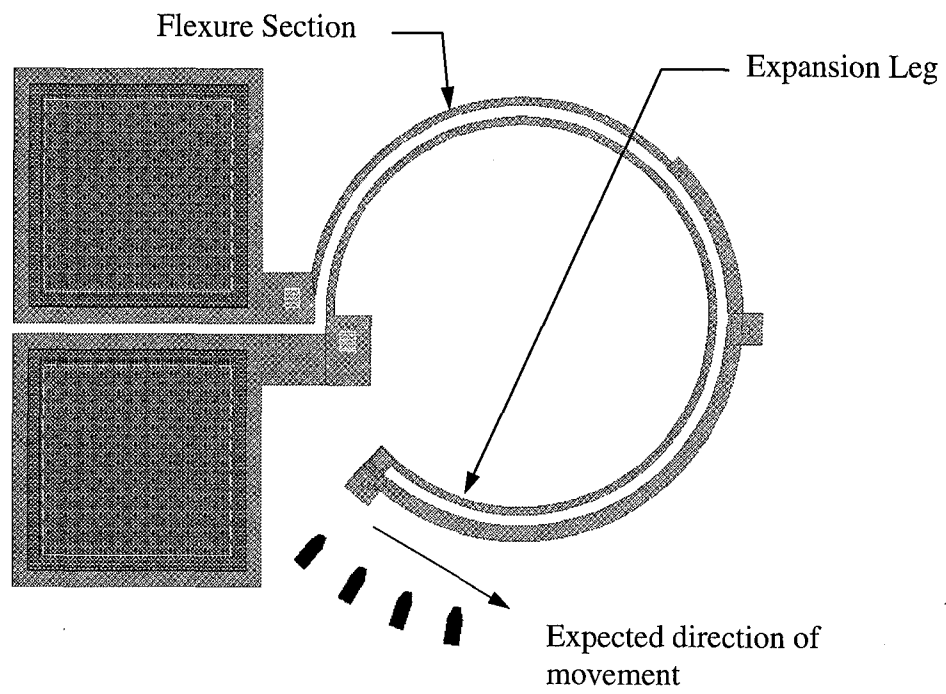


Figure 4-20. Cadence layout and scanning electron micrograph of circular heat actuator from MUMPS 7 (arc length of 285 degrees).

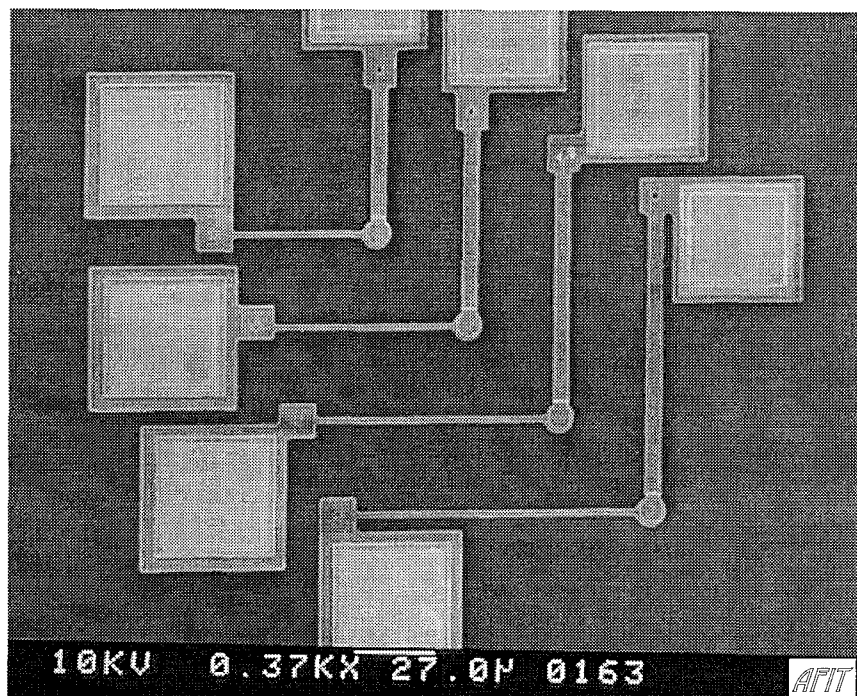
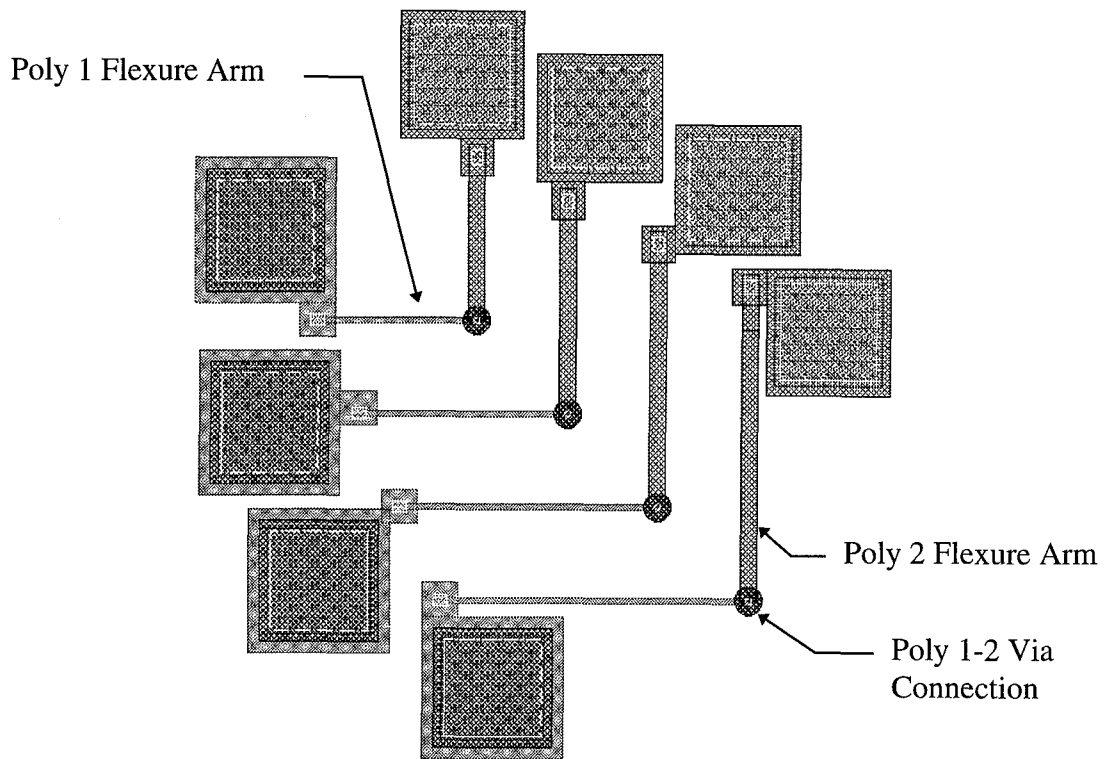


Figure 4-21. Cadence layout and scanning electron micrograph of vertical heat actuators from MUMPS 7.

4.4.3. *Surface Mirrors*

Device Name: Vertical Heat Actuated Mirror
Actuation Method: Mechanical and Heat drive actuator

This device uses four copies of ver. 2 of the vertical heat drive actuator, with 2 μm wide poly1 extension arms, to move a Poly 2 mirror normal to the substrate (see Fig. 4-23). The lengths of the extension arms are only 30 μm and the four sets of actuators are wired in parallel. Series wiring would prevent testing of the device once a single actuator was burned out and therefore a parallel scheme is preferred for characterization of the device. The mirror is gold plated and connected at the corners to the vertical heat actuators using Poly 1-2 via's. It is expected that the current through the mirror should be restricted since the Poly 1-2 via's are small and the primary current path is through the vertical heat drive actuators.

Device Name: Fringe Test Array
Actuation Method: Electrostatic

Four Poly 2 and Gold mirrors with equal surface areas ($\sim 1,240 \mu\text{m}^2$) have been drawn with different circumferential lengths to test for the effects of fringing in the electric field. The different circumferential lengths are obtained by using different geometries: a circle, square, hexagon, and octagon (see Fig. 4-24). Each device is supported with the same spring flexure setup, with 4 springs connected to the mirror at 90 degrees apart from each other. Each flexure is 73 μm in length (L) and 2 μm wide as shown in Fig. 4-24. A SEM micrograph of the square fringe test mirror is shown in Fig. 4-25.

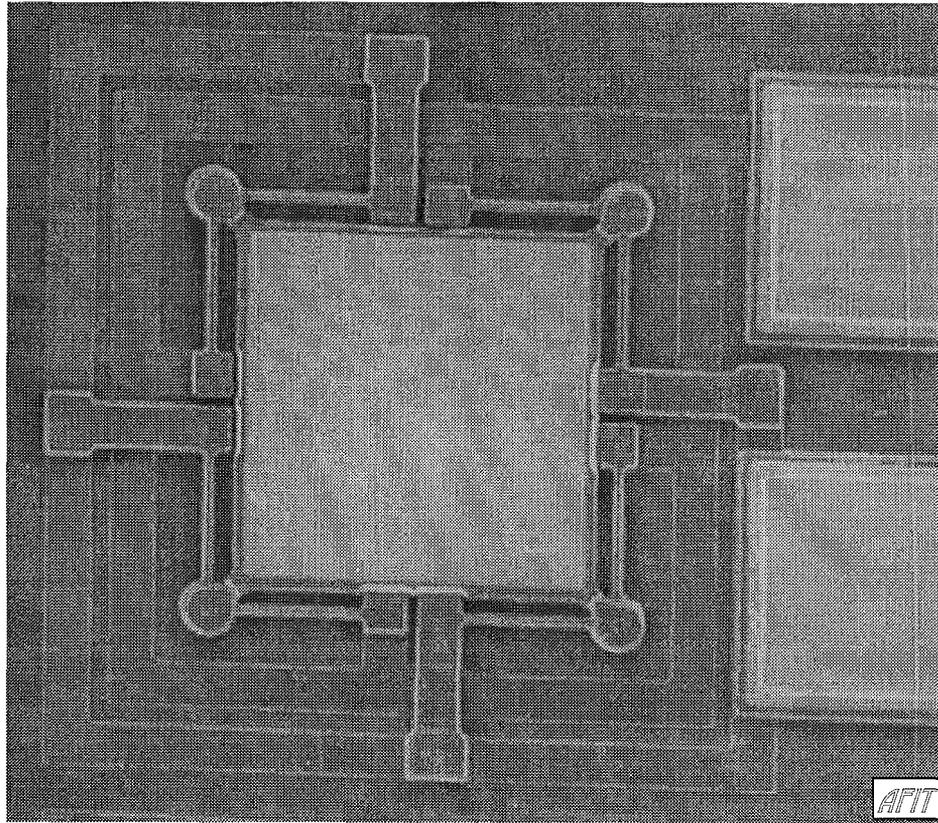
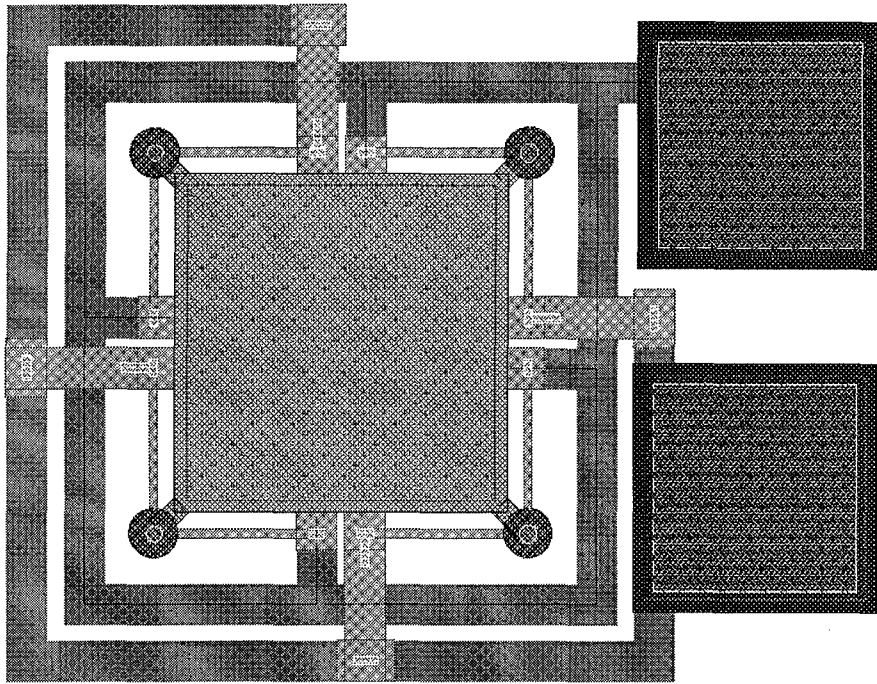


Figure 4-22. Cadence layout and scanning electron micrograph of vertical heat actuated surface mirror from MUMPS 7.

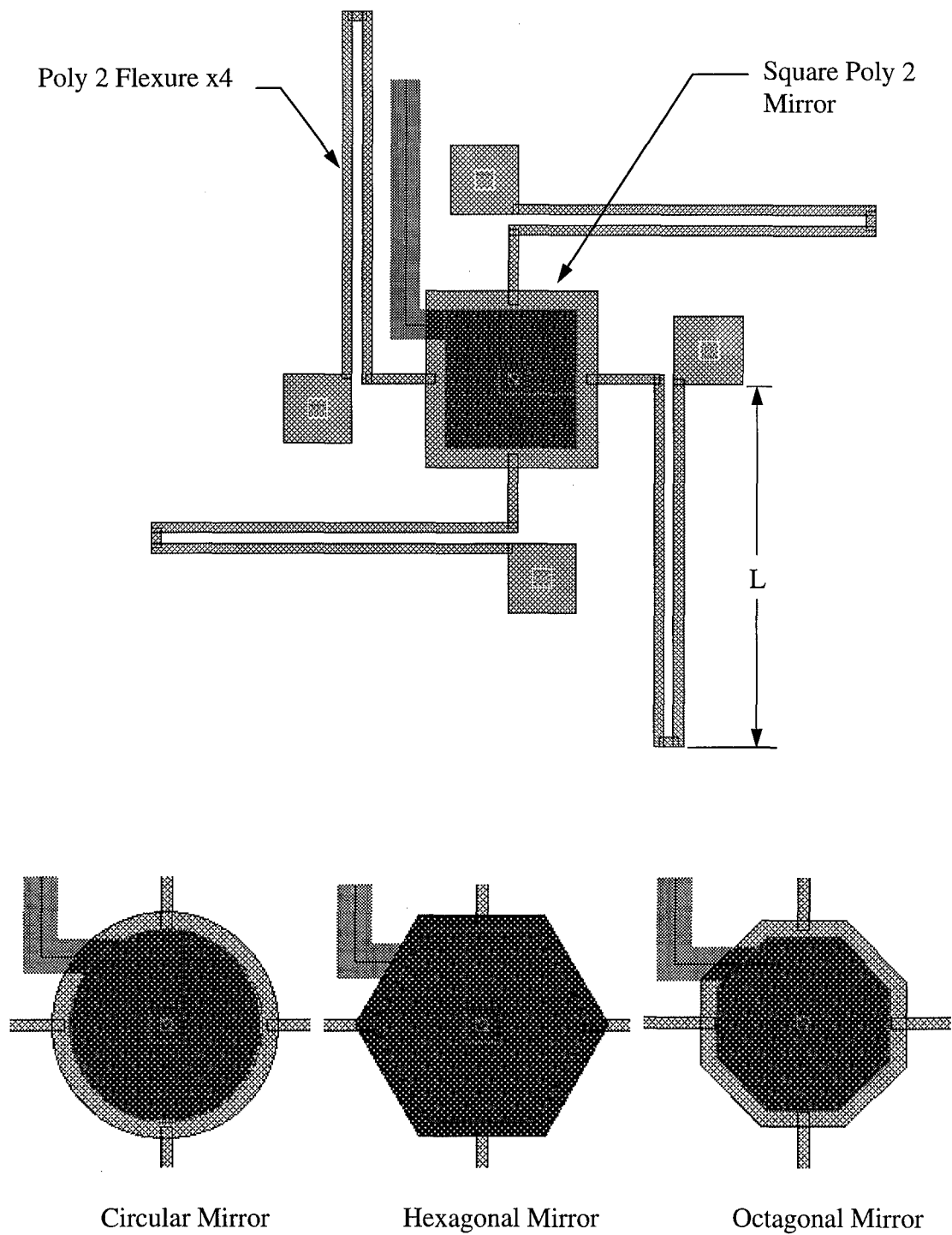


Figure 4-23. Shaped mirrors for testing electric field fringing effects from MUMPS 7.

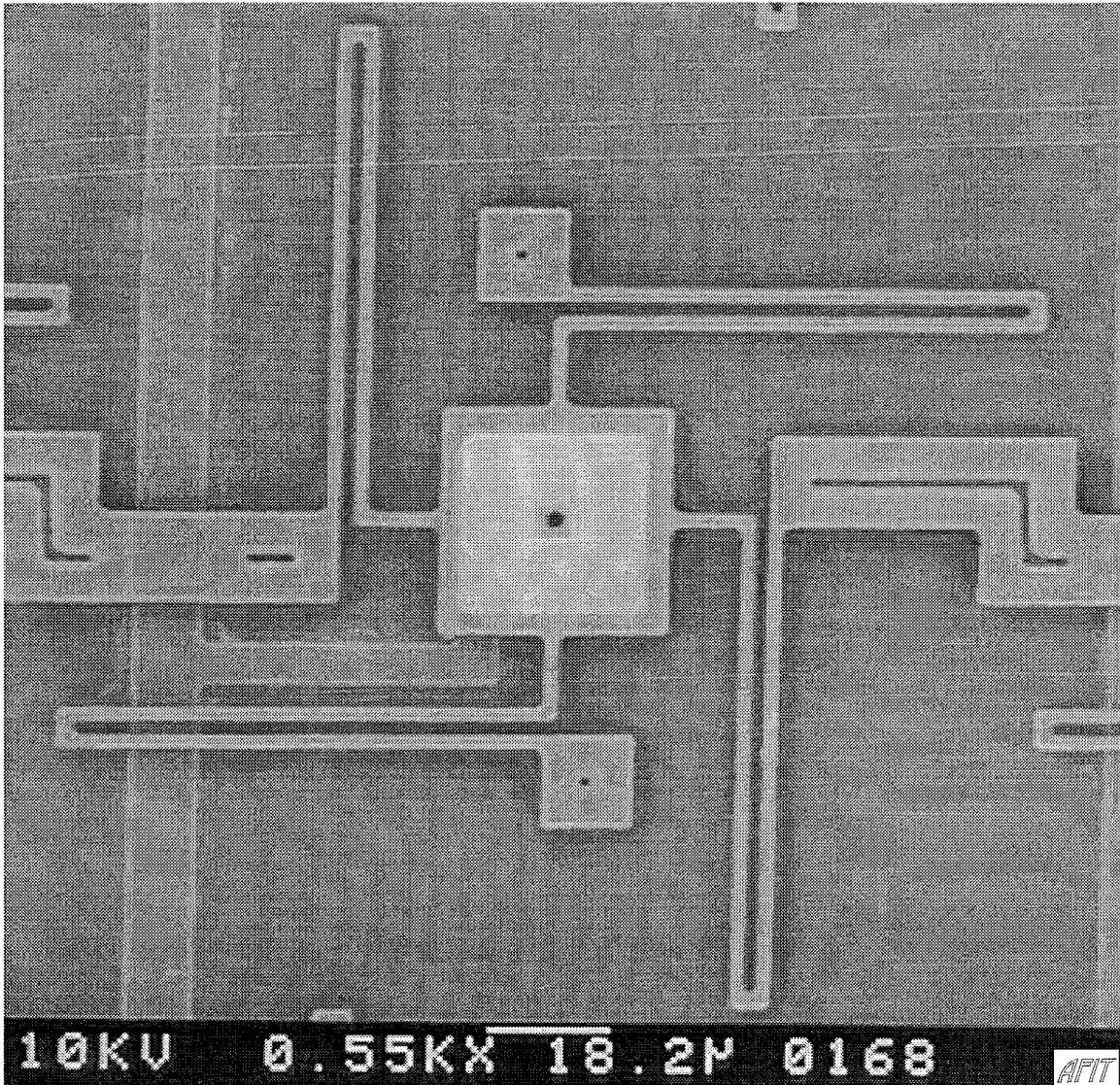


Figure 4-24. Scanning electron micrograph of square mirror for testing electric field fringing effects from MUMPS 7.

4.4.4. Variable Gratings

Device Name: Variable Diffraction Gratings
Actuation Method: Electrostatic and Heat drive actuator

Numerous variable diffraction gratings have been designed for fabrication with different dimensions. All of these gratings have the same basic structure, as shown in

Fig. 4-26, which includes: an electrostatic Poly 1 actuated grating; Poly 1 and Poly 2 formed rails; and a Poly 2 laterally deflected heat actuator driven grating. Important period dimensions include: the width of the Poly 1 runners; the width of the Poly 2 runners; the spacing between the Poly 1 runners; and the number of periods in the grating as outlined for the various devices in Table 4-6. In all cases, the spacing between the Poly 2 runners is fixed (2-6 μm) since the Poly 2 runners are centered above the Poly 1 runners before actuation. All devices except ver. 1 and 9 have a nominal Poly 1 runner length of 50 μm . Versions 1 and 9 have a runner length of 30 μm . Versions 10-12 are different in that the rail guides were redesigned to prevent sticking by extending the Poly 2 runners over the edge of the Poly 1. This allows for more holes through which the low surface tension solution (2-propanol) can displace the dionized water to prevent stiction during the chip release procedure. These versions also differ in that the number of heat actuators has been increased to ensure that the Poly 2 plate will be deflected. Versions 10-12 have been designed in two configurations, with and without four Poly 2 hold downs which are located at the corners of the grating plate. The hold downs should keep the Poly 2 plate from lifting or twisting after release and during actuation. Versions 10-12 do not include spring flexures in order to minimize the force required to deflect the plate. Furthermore, these versions have two heat drive actuators in order to increase the force applied to the plate and make it symmetrical to prevent twisting since the device may lock up if it twists. Heat actuators were replaced by 5, 16 and 20 finger electrostatic combs for ver. 2, 3, 5 and 6 to test the ability to move these gratings with other types of actuators. For either drive mechanism, the Poly 2 plate only has to be deflected 1/2 of the

period of the lower plate (a+c from Table 4-6) in order to sweep through the entire diffraction change possible using lateral deflection. Two scanning electron micrographs of the original style variable grating, ver. 4, is shown in Fig. 4-27.

Table 4-6. Versions of the Variable Diffraction Grating. (a) Poly 1 runner width; (b) Poly 2 runner width; (c) spacing between Poly 1 runners; (d) number of periods; (e) drive mechanism: H for heat drive actuator and C for comb drive actuator; and (f) number of heat drive actuators or fingers for the electrostatic combs.

Version #	a (μm)	b (μm)	c (μm)	d	e	f	MUMPS
1	2	2	2	14	H	1	8,9
2	2	2	2	14	C	5	8,9
3	2	2	2	14	C	16	8,9
4	4	2	2	16	H	1	8,9
5	6	2	2	12	H	1	8,9
6	6	2	2	12	C	5	8,9
7	6	2	2	12	C	20	8,9
8	6	2	2	40	H	1	8,9
9	2	2	2	64	H	1	8,9
10	2	2	2	14	H	2	9
11	4	2	2	16	H	2	9
12	6	2	2	12	H	2	9
13	3.5	1.5	1.5	12	H	2	9
14	1.5	1.5	1.5	12	H	2	9

4.4.5. Fiber Optic Couplers

Device Name: 1x2 Fiber Optic Couplers
Actuation Method: Mechanical and Heat drive actuator

There are 3 versions of fiber optic 1x2 couplers that have been designed for fabrication on MUMPS 9. All fiber locks are of two diameters. Some couplers were

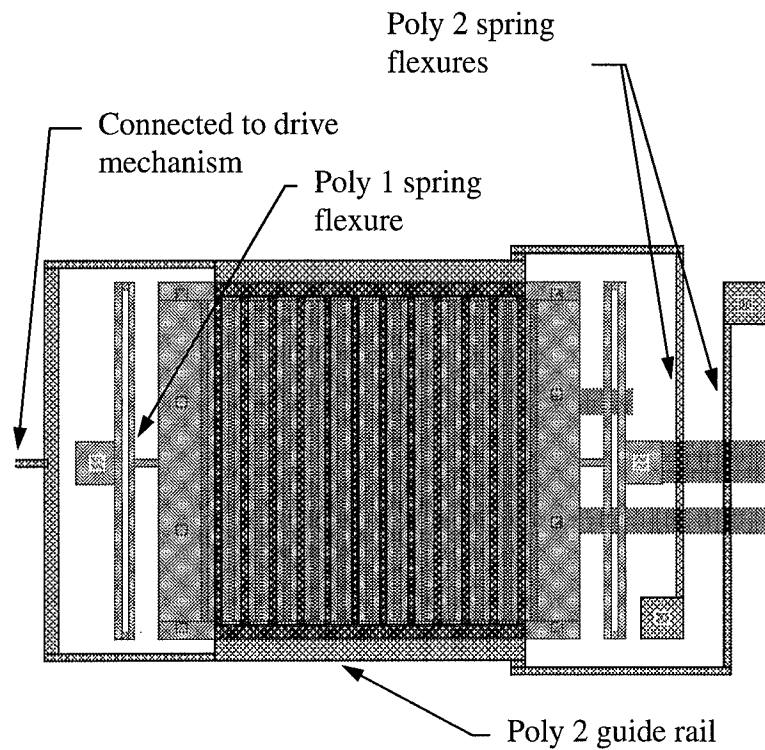


Figure 4-25. Cadence layout of heat actuated grating with 6 micron period and 2 micron poly2 runners.

drawn with a 125 μm diameter which matches the cladding diameter of the single mode fiber selected for characterization of the device. Larger (250 μm) diameter holders were drawn separately in order to test the ability to lock down fibers without stripping the protective barrier layer. The three designs include two with mechanical adjustment only and one with large heat drive actuator arrays to move the single fiber for coupling. Of the two mechanical designs, one is for probing only with no alignment marks, and the other includes simple locks that indicate alignment as shown in Fig. 4-28.

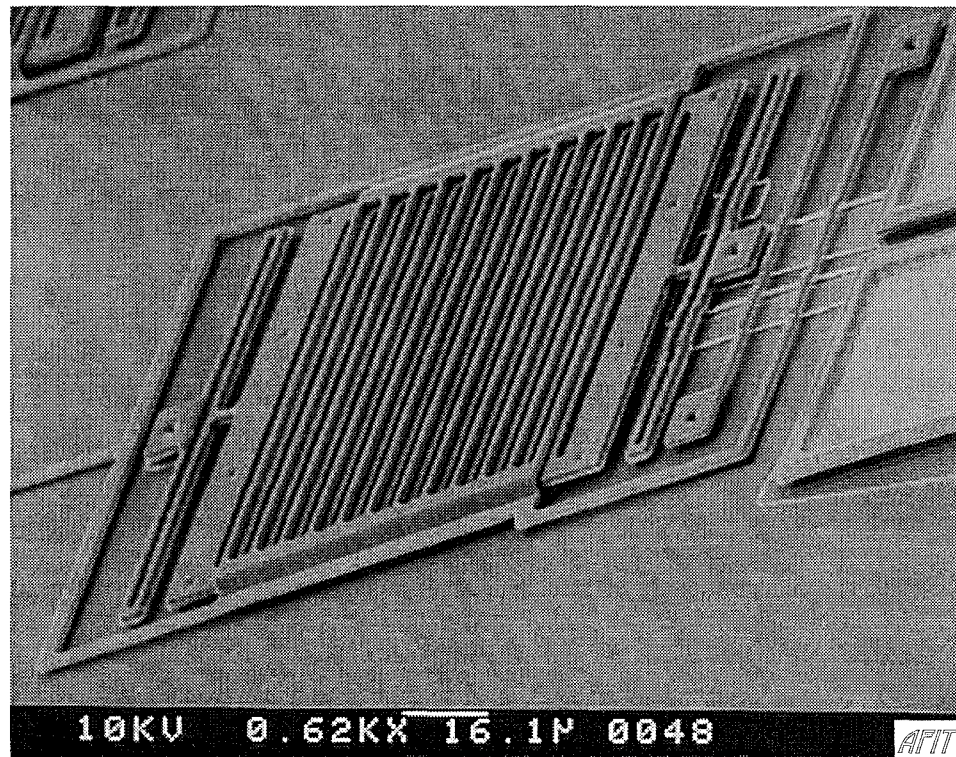
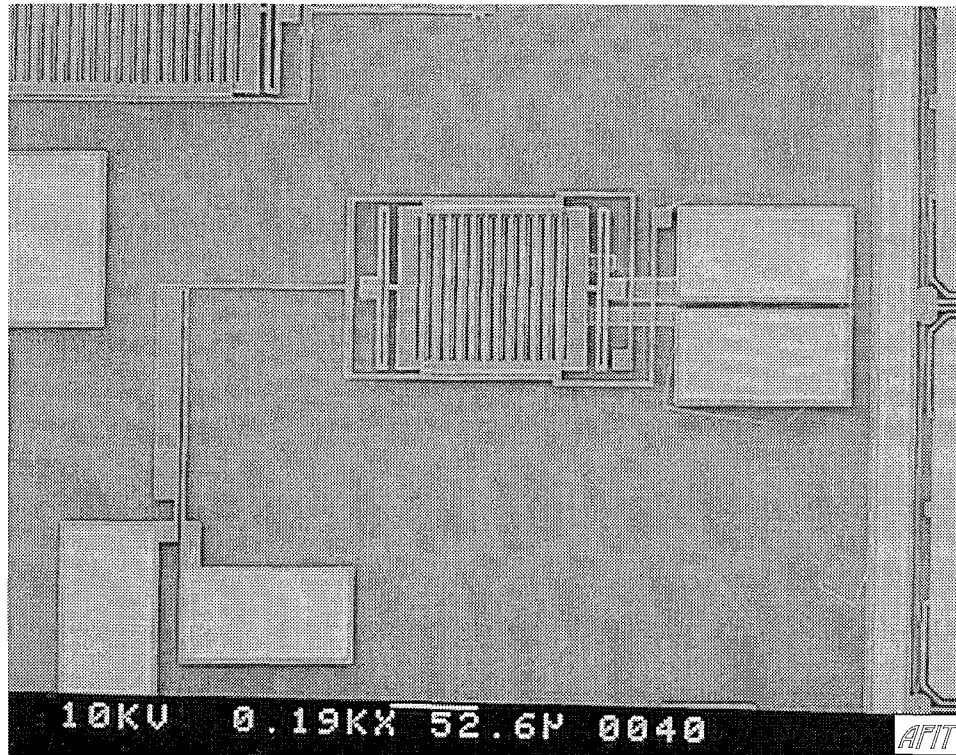


Figure 4-26. Scanning electron micrographs of ver. 4 variable grating from MUMPS 8. Lower Polysilicon plate (Poly1) has 6 μm stringers with 2 μm spaces. Top polysilicon plate (Poly2) has 2 μm stringers with 6 μm spaces.

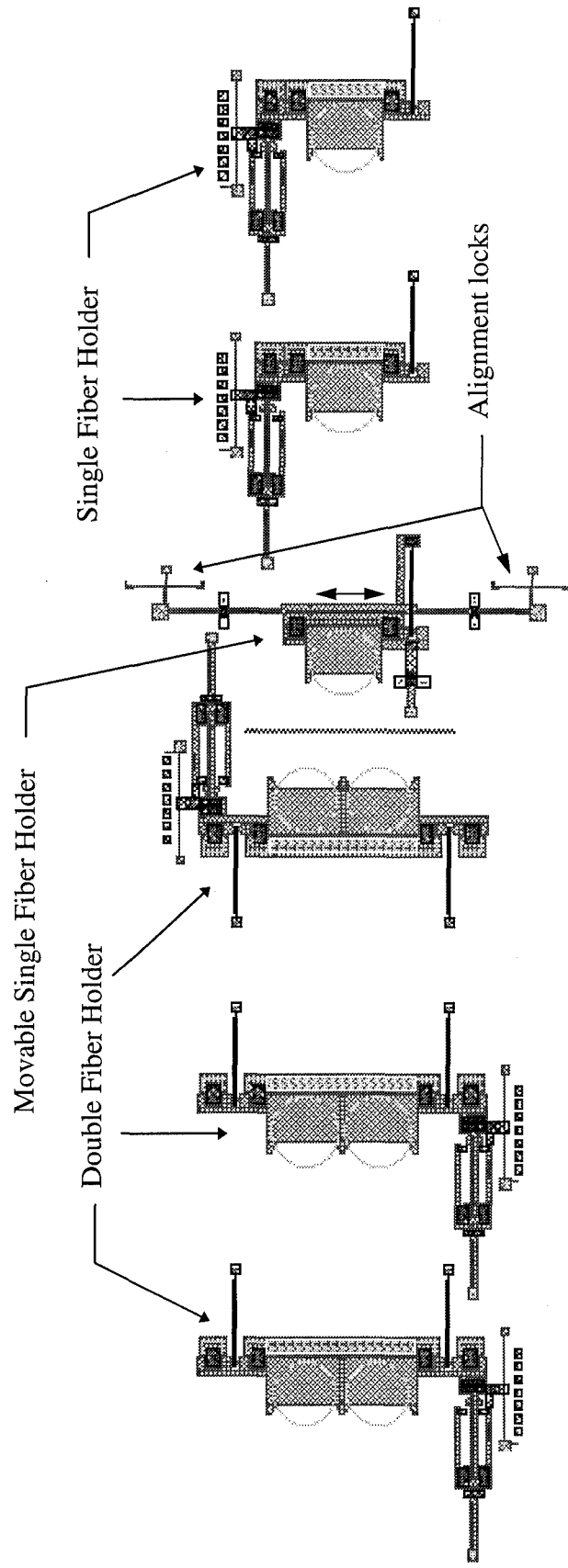


Figure 4-27. Cadence Layout of 1x2 fiber optic coupler from MUMPS 9. This particular coupler is driven mechanically with a probe and provides alignment locks for positioning. Arrow indicates single fiber holder that moves laterally to provide alignment.

4.4.6. Micro Interferometers

Device Name: Micro Interferometer
Actuation Method: Mechanical and Heat drive actuator

There are four versions of the micro interferometer all of which were drawn for fabrication on MUMPS 9. The interferometer operates by utilizing two flip-up gratings (2 μm runners and spacers = 4 μm period) which act as beam splitters and two flip-up mirrors. The light enters one of the diffraction gratings and is diffracted into numerous orders. The $m = \pm 1$ orders are directed to the two mirrors, one of which can be modulated by driving a set of heat drive actuators. The light reflected off of these mirrors is recombined at the second grating. Light interface on all but one of the interferometers is provided by two 45 degree flip-up adjustable mirrors as discussed in Section 4.4.1. One mirror is placed to direct the incoming light into the first beam splitter and the other is placed after the second beam splitter to direct the light back off of the substrate. This configuration is shown in Fig. 4-29.

Version 1 has been designed with fiber locks for providing the incoming/outgoing light paths (see Appendix C). The fiber lock style is 1500 μm between beam splitters and 400 μm between mirrors, with an overall size of 2,868 x 6,434 μm . The mirrors and beam splitters are 150 x 150 μm square. The other three versions are configured as shown in Fig. 4-29. Version 2 has the same dimensions as ver. 1, the other two versions are 400 μm between beam splitters, 172 μm between mirrors, and have active device areas of 50 x 50 μm square. These smaller interferometers differ in that ver. 3 does not include a flip-up DC ($m=0$) block plate like ver. 4. The block is provided in one of the

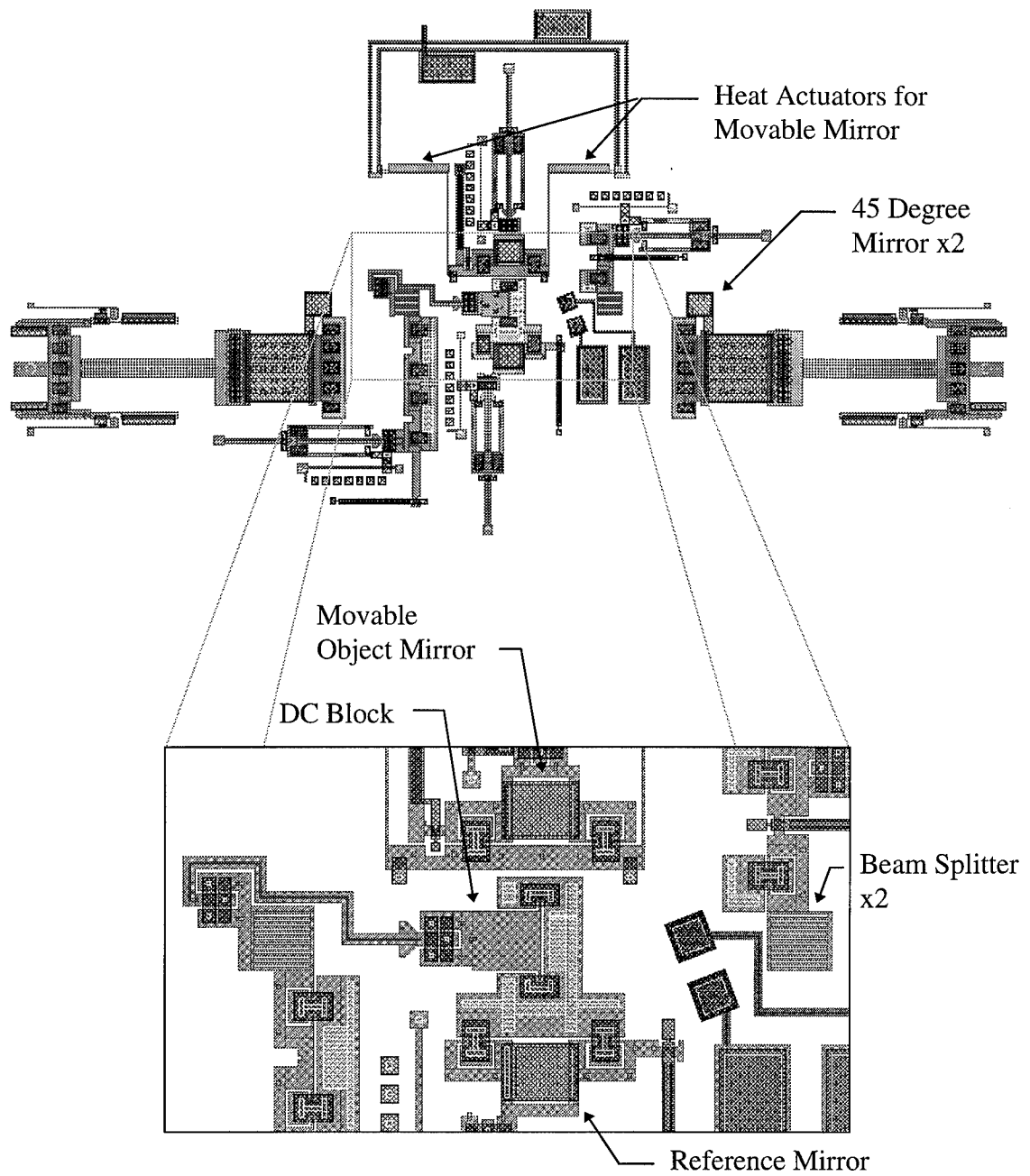


Figure 4-28. Cadence layout of the small micro interferometer, ver. 4, from MUMPS 9.

versions to increase the contrast between maximum and minimum output intensity during modulation since the DC order carries a majority of the diffracted energy. All micro interferometers were designed for use at 632.82 nm (HeNe wavelength) which simplifies the testing procedure. Using this wavelength requires consideration of the absorption of the 1.5-2.0 μm flip-up layers. If the absorption is significant, then the device will still work but will rely on mostly amplitude constructive interference instead of phase constructive interference. The amount of light lost due to absorption from passing through the two beam splitters and reflection from the surfaces of each flip-up directly reduces the maximum intensity achievable at the output. If absorption is significant, then the interferometers would work better if designed for wavelengths greater than $\sim 1.1 \mu\text{m}$, but testing would require a source at that wavelength.

4.4.7. Other Devices

Also designed and fabricated on MUMPS 7,8, and 9 were various other structures not shown pictorially in this section of Chapter 4. Additional Cadence layout schematics and scanning electron micrographs of devices are included in Appendix C and D. These additional devices include: hidden flexure micromirrors; a flip-up Fresnel lens array (with 8 lenses); a flip-up Fresnel lens plate (with 4 lenses); circular comb drive resonators; and a 10 x 10 element grating array.

4.5. Summary

This chapter reviewed the key concepts that must be considered when designing MOEMS devices for fabrication at MCNC. This thesis effort utilized three test stations in order to collect data on selected devices. Each of these setups was described along

with the associated testing procedures that were developed. Operation of the Low Temperature Micro-Probe for testing thermal and frequency characteristics was covered in detail. The last half of the chapter reviews the major devices that were designed over the span of three MUMPS (7,8 and 9) runs. The intended function of the devices and a discussion of the design variations between versions were included for each group of devices.

5. Results and Discussion

This chapter describes the results of the fabrication and testing procedures for each device category covered in Chapter 4. Where devices were found to be limited or inoperable due to design, suggested improvements have been made. Work that was planned, yet unable to be performed due to time constraints, is also discussed.

5.1. Fabrication Results

The three fabrication runs (MUMPS 7, 8 and 9) used to design devices in support of this thesis yielded mixed results. Material parameters supplied by the foundry are indicated in Table 5-1. The residual stress in each layer is a figure-of-merit which can be used to judge the success of a given run. This parameter alone indicates that MUMPS 9 was substantially better than MUMPS 7 or 8. Device testing later substantiated this claim to be true. MUMPS 4 material parameters are included since resistivity measurements versus temperature were taken on a device from this run (see Section 5.7). Both MUMPS 7 and 8 exhibited spots of residue after release. Originally the cause of the residue spots was unknown and was believed to be a result of the release procedure or contamination of the release chemicals. Because of this, extra steps were taken to improve the cleanliness of the lab station and procedures. Containers were individually marked for each chemical, cleaned before each use with dionized (DI) water and blown dry with Nitrogen. Chip containers were always new from the box and were also blown clean with Nitrogen. Fresh chemicals were used for each batch that was being released and then discarded in appropriate containers. The DI water was kept covered during the

Table 5-1. MCNC Process Statistics for MUMPS 4, 6, 7, 8, and 9.

Film	Thickness (Å)	Stress (MPa)	Resistivity (Ω-cm)
MUMPS 4			
POLY0	5207	14 (C)	1.74E-3
POLY1	18755	4 (C)	2.95E-3
POLY2	14800	9 (C)	2.74E-3
Cr/Au	5200	73 (T)	2.08E-6
Si ₃ N ₄	5169	63 (T)	---
MUMPS 6			
POLY0	5200	19.7 (C)	1.84E-3
POLY1	20220	5.1 (C)	2.58E-3
POLY2	15650	5.1 (C)	2.72E-3
Cr/Au	5540	30 (T)	3.39E-6
Si ₃ N ₄	6213	19.2 (T)	---
OXIDE1	20151	---	---
OXIDE2	5230	---	---
MUMPS 7			
POLY0	4880	---	~2E-3
POLY1	20100	8.0 (C)	1.65E-3
POLY2	14706	11.1 (C)	1.54E-3
Cr/Au	5318	21 (T)	3.30E-3
Si ₃ N ₄	6049	41.0 (T)	---
OXIDE1	20400	---	---
OXIDE2	5281	---	---
MUMPS 8			
POLY0	4696	8.0 (C)	1.5E-3
POLY1	19780	14.1 (C)	1.6E-3
POLY2	15450	10.3 (C)	2.5E-3
Cr/Au	5200	166 (T)	3.50E-6
Si ₃ N ₄	5580	133 (T)	---
OXIDE1	20362	---	---
OXIDE2	6133	---	---
MUMPS 9			
POLY0	5122	3 (C)	1.5E-3
POLY1	19948	3 (C)	2.2E-3
POLY2	15048	6 (C)	3.0E-3
Cr/Au	4923	5 (T)	3.0E-6
Si ₃ N ₄	6243	67 (T)	---
OXIDE1	20008	---	---
OXIDE2	7598	---	---

notes: C = Compressive stress, T = Tensile stress.

release procedure and chips were immediately placed in containers after the release. Although these added measures reduced the introduction of foreign matter on the die, such as dust particles, it did not eliminate the spots that were present on the substrate. The other suspected cause of the spotting was an incomplete removal of the photoresist on one of the layers, most likely the one used to pattern Poly 0. MUMPS 9 did not exhibit any of the spotting problems apparent on MUMPS 7 and 8. Since the chemicals used in the release procedure were not replaced, the cleanliness of MUMPS 9 confirms that the spotting was due to a fabrication problem and not the release procedure or chemicals.

Flip-up devices rely on the fabrication of the substrate and scissor hinges discussed in Chapter 2. Mumps 7 and MUMPS 8 both experienced fabrication difficulties which yielded almost all flip-up devices inoperable. As shown in Fig. 5-1 and Fig. 5-2, the incomplete reactive ion etch of Poly 1 along with the thin second oxide and conformance of Poly 2 caused the two releasable layers to connect. This effect was seen on any device which had Poly 2 running over Poly 1. The connection of the two layers is approximately 0.2-0.4 μm thick as observed using the SEM. As was discussed in Chapter 4, an additional polishing etch step was added to the release procedure in an attempt to break this rather thin connection by etching away the polysilicon. After a couple of calibration runs to determine the time required to etch away $\sim 0.5 \mu\text{m}$, die were released and polish etched. On all of the Flip-up devices this procedure yielded limited results. The hinge pins were often thinned too much to be effective or the polish etch did not completely alleviate the problem. The polish etch caused the surfaces to become rough and the time required to reach the necessary amount of polish became unpredictable. It

was found that the mixed solution for performing the polish etch was very sensitive to concentration ratios. Initial mixes of the polish etch took ~20 seconds to completely etch away the polysilicon layers and further modifications were found to require ~16 minutes to etch away ~1 μm of polysilicon. The 16 minute etchant allowed for evaluation of how the etched surfaces changed with time. From these evaluations it was apparent that the polish etch would thin the structures but make them very rough and non-uniform in thickness. The polish etch did sufficiently release some structures that exhibited this fabrication problem. For example, the grating pixels from MUMPS 8 have slide rails on each side that are formed by allowing Poly 2 to conform over Poly 1. At this interface the layers were stuck and mechanical probing was required to break the Poly 1-2 connection. Even after the probe break, the device would stick during operation on a frequent basis. Devices that were polish etched were much easier to break free with a probe and exhibited less sticking during operation. Stringers of Poly 1 were evident on MUMPS 8 due to the incomplete reactive ion etch (RIE) of the layer (see Fig. 4-26). The stringers are free to move on the substrate after release and are therefore undesirable. MCNC started using a new RIE machine on Poly 2 of MUMPS 8 which had smoother edges and no stringers.

Dimensions of the layers for all three runs were found to be as drawn in Cadence. Gratings with 2 μm lines were drawn on MUMPS 7 and MUMPS 8 which yielded diffraction patterns that verified the dimensions to be as drawn. Measurements were compared to those taken with the SEM and it was found that the reference scale provided

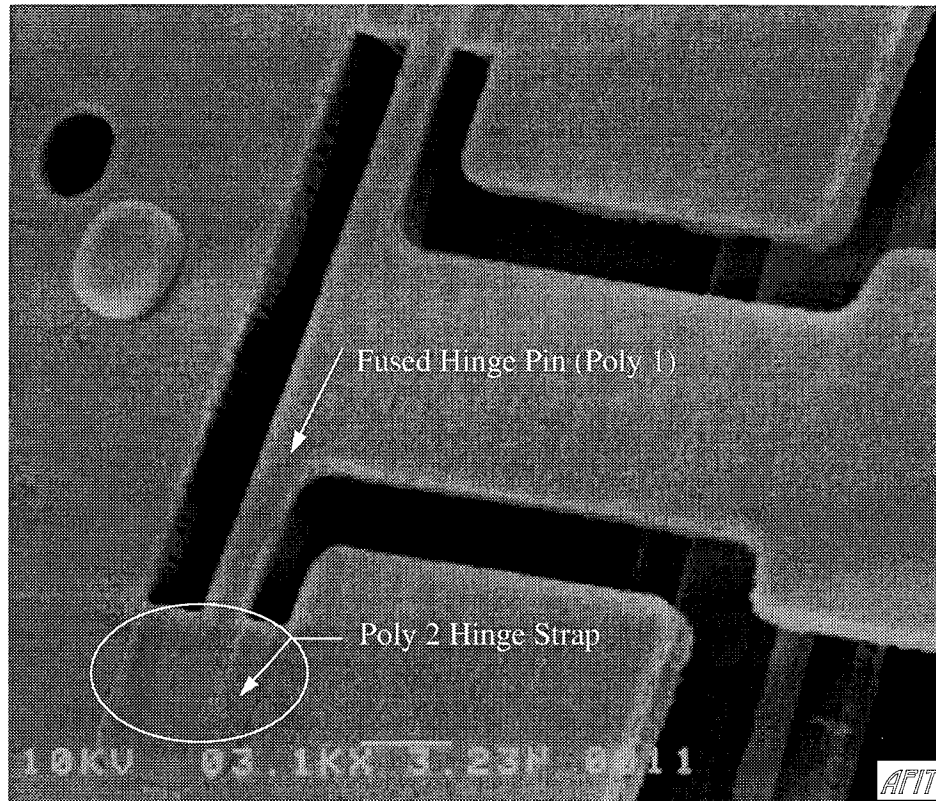


Figure 5-1. Scanning electron micrograph of “stuck” hinge on MUMPS 7 due to fabrication problem. This micrograph is of the backside of a device.

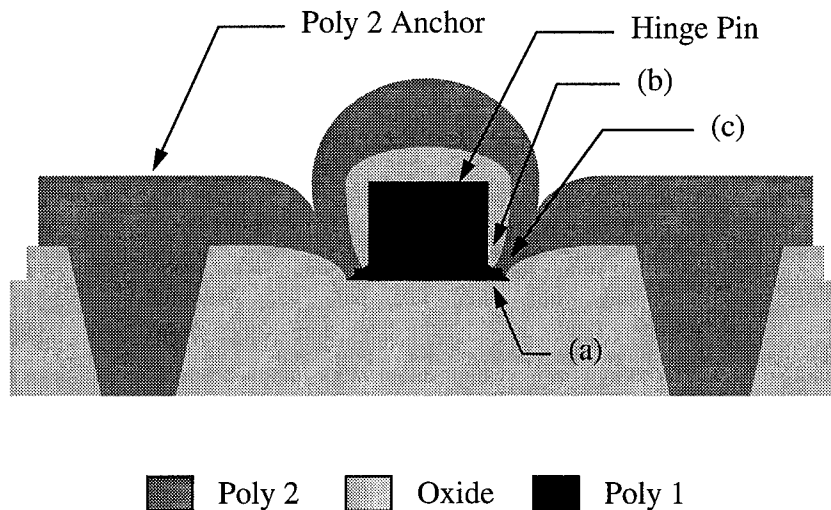


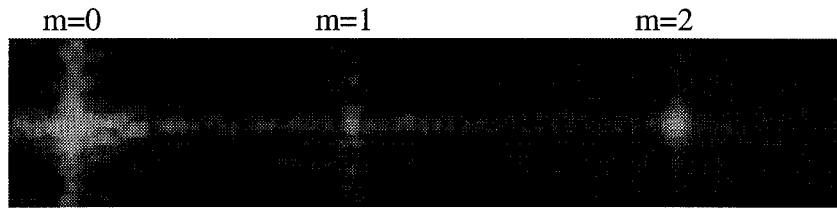
Figure 5-2. Schematic of MUMPS layering process indicating the connection between Poly 1 and Poly 2 which immobilizes the hinge pins. (a) Indicates the rough edge of Poly 1 caused by the reactive ion etch process. (b) Shows how the 0.5 μm thick second oxide layer is broken at the interface. (c) Identifies where the Poly 2 layer conforms to the surface topology, flows into the oxide gap and connects with Poly 1.

on the scanning electron micrographs needs to be recalibrated by . Additional verification of the dimensions was obtained using an Olympus microscope, model #BH2 UMA.

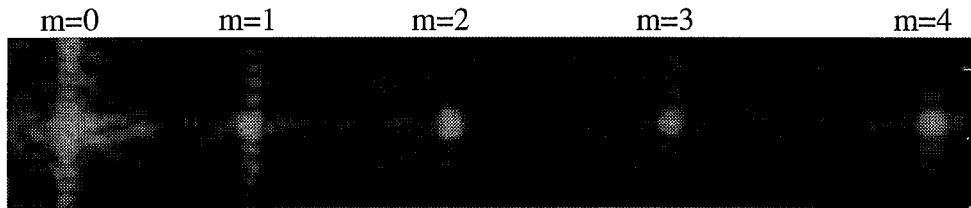
5.2. *Grating Pixel Results*

The initial grating design used for testing was from MUMPS 8 and included only one heat actuator for lateral deflection of the Poly 2 grating (see Fig. 4-20). Due to the fabrication problem, discussed in Section 5.1, the devices would not operate without additional post processing. This included performing the polishing etch discussed in Chapter 4 and using the probe station to slide the Poly 2 plate, breaking free the Poly 1-to-Poly 2 connection along the guide rails. Even with these additional process steps, the device exhibited limited movement of $\sim 1.5 \mu\text{m}$ which is less than half of the full period movement desired of $4 \mu\text{m}$. In an effort to increase the deflection distance, the two spring flexures attached to the other end of the plate (see Fig. 4-20 and Fig. 4-21) were broken using a probe. Devices that were tested with the spring flexures broken exhibited the largest deflection ($\sim 3 \mu\text{m}$) for this generation of the device.

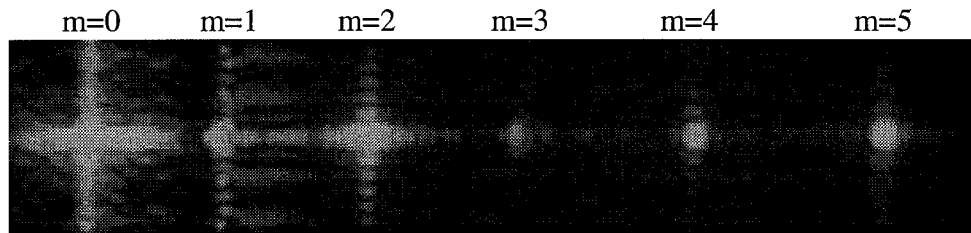
Three primary period variations were investigated with $\omega_1 = 2, 4, \text{ and } 6 \mu\text{m}$ and $\omega_2 = 2 \mu\text{m}$, as shown in Fig. 3-12. The $\omega_1 = 6 \mu\text{m}$ is the only version that conforms to the MCNC MUMPS design rules [14] and exhibited the best movement for the first generation of devices (MUMPS 8). By observing the operation of the device it appeared that the smaller ω_1 gratings would stick due to overlapping of the Poly 1 and Poly 2 layers. A comparison of the images for each of the period dimensions is shown in Fig. 5-3. Notice that the angles between the diffracted orders increases as ω_1 decreases. This is expected from standard diffraction theory where the diffracted angles increase as the



(a) $\omega_1=2 \mu\text{m}$ & $\omega_2=2 \mu\text{m}$



(b) $\omega_1=4 \mu\text{m}$ & $\omega_2=2 \mu\text{m}$



(c) $\omega_1=6 \mu\text{m}$ & $\omega_2=2 \mu\text{m}$

Figure 5-3. Image of diffraction patterns for three different variable diffraction gratings. Patterns were taken under static (0 mA) conditions.

period width of the grating decreases. The measured angles for all three gratings agree within 5 % with the values taken from the diffraction model. Also apparent in Fig. 5-3 is the increase in separation distance between successive orders as the order number increases. This is due to the fact that the camera used to image the diffraction pattern had to be oriented at a slight angle (~5.5 degrees) to obtain the pattern which was also spatially angled (~5 degrees) away from the incoming laser beam of the setup in order to image the m=0 diffracted order.

The second generation of gratings, fabricated on MUMPS 9, did not exhibit the

fabrication problem seen with the MUMPS 8 gratings. These devices were easily moved through a full period of deflection (up to 4 μm) for 6 mA of applied current. The pair of heat actuators ensured that the Poly 2 plate was deflected uniformly versus the angle that was exhibited in the first generation of devices when the spring flexures were broken. If the Poly 2 grating is not uniformly supported it can exhibit differences in vertical position from end-to-end. This effect creates a splitting in the diffraction pattern along the direction of the diffracted orders. Furthermore, if the plate can twist by some amount, then the pattern can shift perpendicular to the diffraction pattern. A combined effect of these two shifts is shown in Fig. 5-4. Variable gratings with hold downs, as shown in Fig. 5-5, appeared to prevent the splitting of the diffraction pattern in either the x or y direction as shown in Fig. 5-4.

A complete evaluation of the optical properties of the $\omega_1 = 6 \mu\text{m}$ and $\omega_2 = 2 \mu\text{m}$ diffraction grating was performed for both the original design on MUMPS 8 and the newer design on MUMPS 9. The MUMPS 8 devices, although exhibiting less deflection, matched theory extremely well for both the diffracted angle values (within a tenth of a degree) and the change in intensity of the diffracted orders versus grating deflection. A comparison of the theoretical and experimental line intensity profiles is shown in Fig. 5-6. The theoretical data is for the zero and full deflection (4 μm) conditions and the experimental data was for both 0 mA (no deflection) and 2 mA (~1.75 μm of deflection) of applied current which was the safety threshold established to ensure that the heat drive actuator was not burned-out.

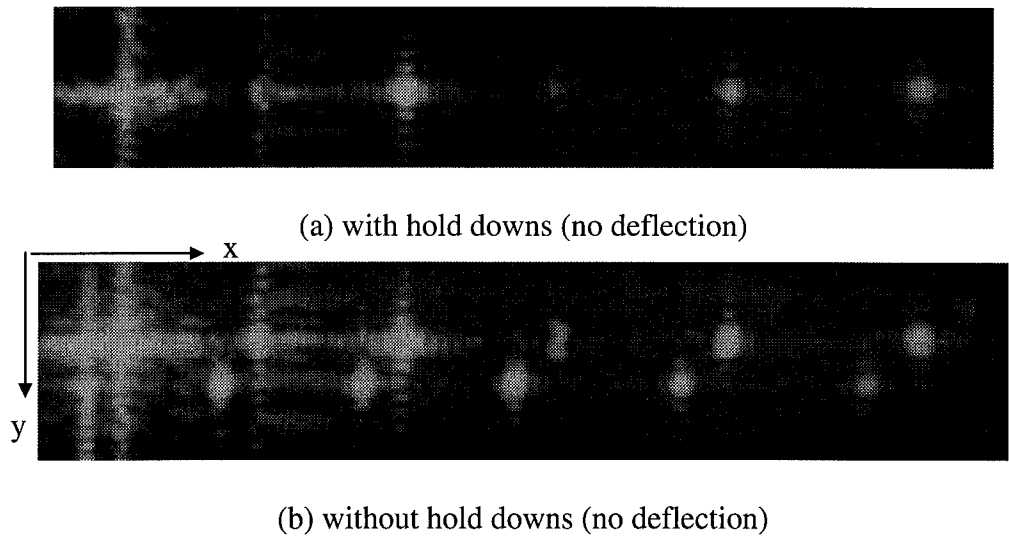


Figure 5-4. Image of diffraction patterns for a $\omega_1=6 \mu\text{m}$ & $\omega_2=2 \mu\text{m}$ variable diffraction grating with and without hold downs as indicated. Notice that the grating without hold downs exhibits a secondary diffraction pattern.

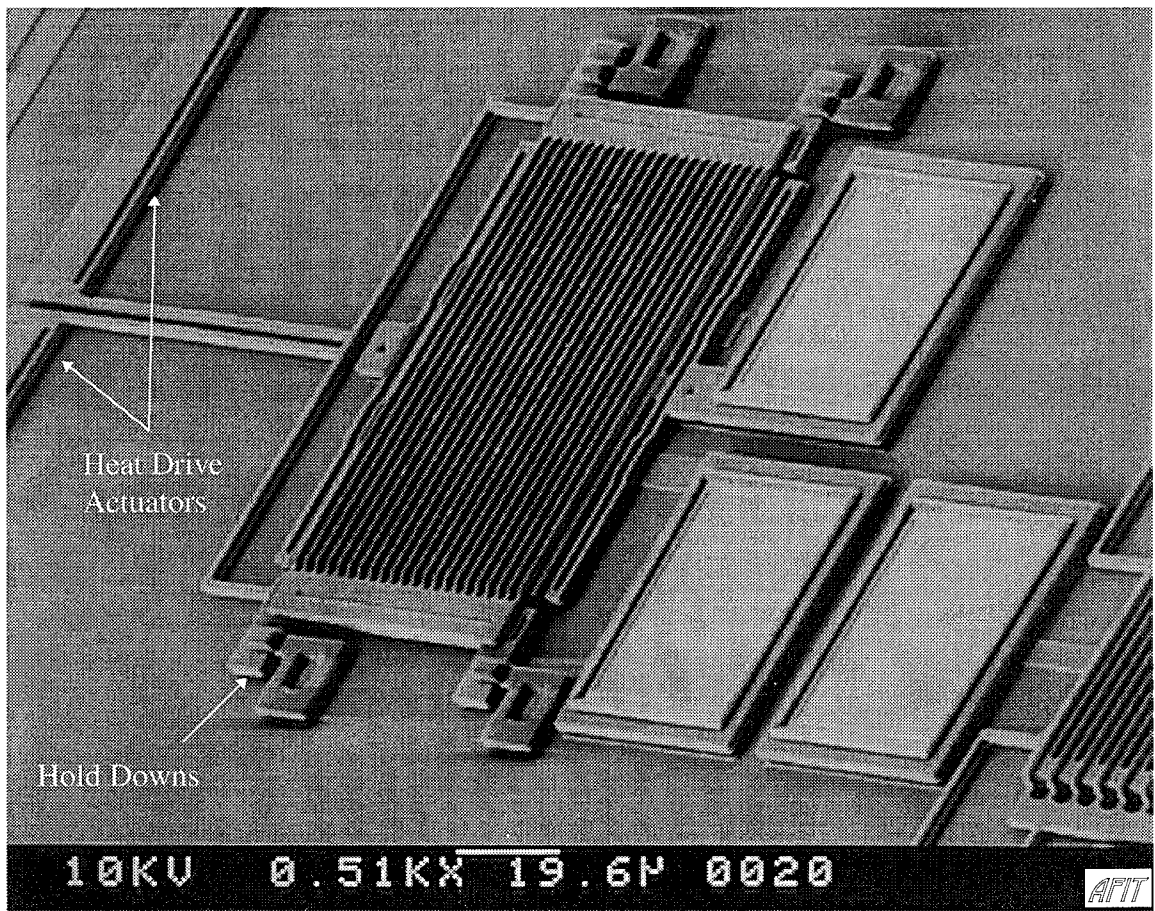


Figure 5-5. Scanning electron micrograph of ver. 7 (MUMPS 9) variable grating with hold downs.

The deflection value for the maximum current applied (2 mA) was obtained from the mechanical probe station as $\sim 1.75 \mu\text{m}$. The change in intensity for the two levels matches the trend predicted by the model, but the difference is not as significant since the movement is not sufficient to obtain the maximum and minimum values for the orders. Altering the drive current from 0 to 2 mA yielded intensity modulation values of 1.2 dB for the $m=1$ order and 3.8 dB for the $m=2$ order. Measurable modulation up to 10 kHz was achieved yet significant roll off in the amount of modulation occurred at approximately 1 kHz. The sticking of the rails on this device made it impossible to accurately determine a 3dB roll off point.

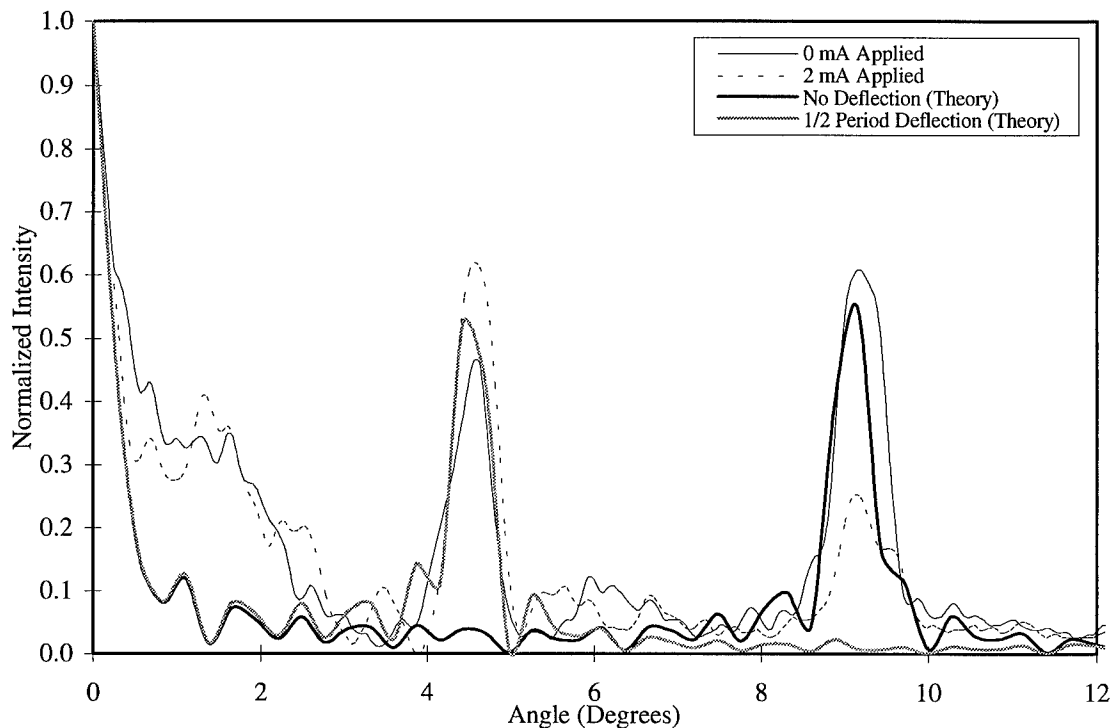


Figure 5-6. Diffraction pattern for the original generation (MUMPS 8) variable grating versus theory.

As was evident from the MUMPS 8 devices, a single heat actuator was insufficient and yielded non-uniform deflection characteristics. The addition of a second heat drive actuator improved the design by providing sufficient symmetrical deflection. As discussed in Chapter 6, the next step in the design process is to increase the size of the grating to prevent overfilling by the illuminating light source.

Operation of a two heat drive actuator grating with hold downs yielded the diffraction patterns shown in Fig. 5-7 as a function of applied current. The model predicts a change in the intensity for the first two diffracted orders as shown in Fig. 5-8. The change of intensity for the first two diffracted orders as a function of applied current to the heat drive actuators is shown in Fig. 5-9. The maximum intensities for the first two diffracted orders is different since the separation between the two polysilicon layers was assumed to be $0.5 \mu\text{m}$ in the model. The model found that the intensity of each diffracted order had different maximum values depending on the lateral position of the Poly 2 diffraction grating. Depending on the separation distance between the two suspended gratings and the substrate the intensity would modulate between the maximum value and zero. From the obtained intensities it is apparent that the separation distance is less than $0.5 \mu\text{m}$ and after review of the Cadence layout it appears that the top grating in this design might be resting on the lower grating with no separation. From Fig. 5-9 it can be seen that the heat drive actuators do not initially deflect at the onset of an applied current. Chapter 3 showed that the deflection obtained for the heat drive actuators can be modeled by an exponential which indicates minimum deflection is achieved for small currents. Deflection was observed for these devices when the current increased above approximately 2.5 mA. If the horizontal axis of Fig. 5-9 was readjusted to start at 2.5 mA

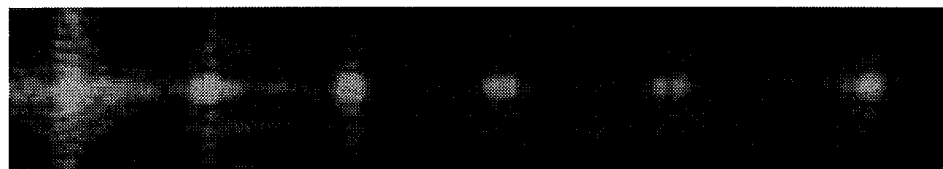
then the curves would look very similar to the ones obtained from the model as shown in Fig. 5-8.

Since the amount of lateral deflection was greater for this device, the change in intensity values of the orders was also greater. Specifically, intensity modulation of 6.4 dB for $m=1$ and 9.0 dB for $m=2$ was achieved. Modulation values were not obtained since the device appeared to either snap free from the hold downs or break them as the frequency increased, which caused the diffraction pattern to be altered as previously discussed. Without a consistent diffraction pattern the point at which the reduction in intensity occurs cannot be accurately determined. On future designs the hold downs need to be made larger to prevent breakage, allow for more deflection and prevent the release of the Poly 2 plate from the hold downs.

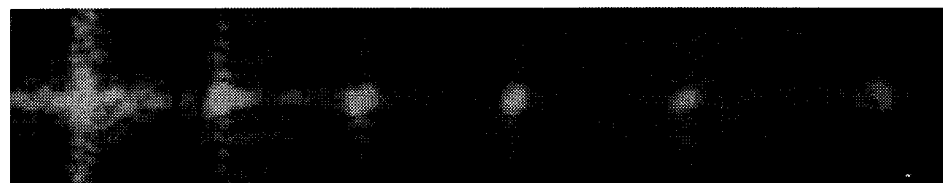
All of the designs tested exhibited a loss in energy to the sinc function that is apparent in the intensity profile at each order from the external dimensions of the device. If the device was made large enough to eliminate the overflow condition then the sinc patterns would not be present in the diffracted orders and the diffracted orders would contain all of the diffracted energy. Original designs of this device were made with a small active area ($\sim 70 \times 70 \mu\text{m}$) to ensure success of the deflection operation. It was originally unknown how much load could be applied to the heat drive actuator, and the grating was therefore made as small as possible, with the design constraint that there be at least ten periods in the grating to ensure a clean diffraction pattern.



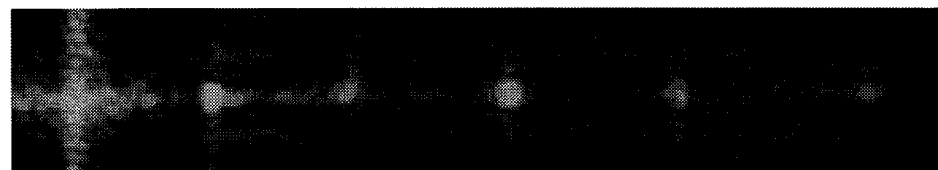
(a) 0 mA



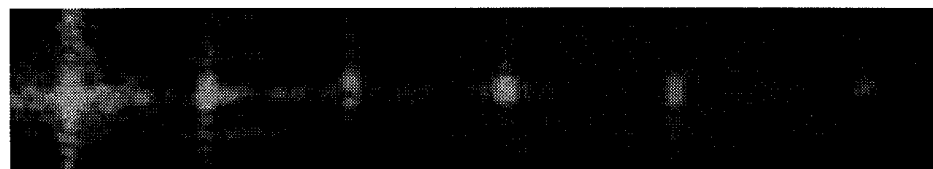
(b) 3 mA



(c) 4 mA



(d) 5.5 mA



(e) 6 mA

Figure 5-7. Images of diffraction patterns for a $\omega_1=6 \mu\text{m}$ & $\omega_2=2 \mu\text{m}$ variable grating, ver. 8, for different applied currents.

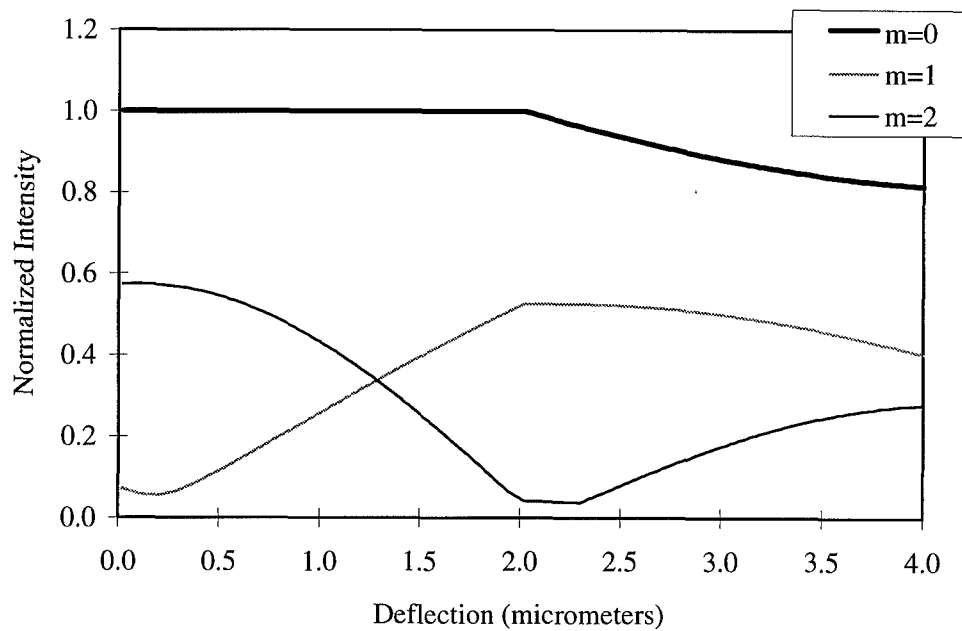


Figure 5-8. Theoretical peak amplitude for the $m=0$ and first two diffracted orders as a function of lateral displacement of the Poly 2 grating.

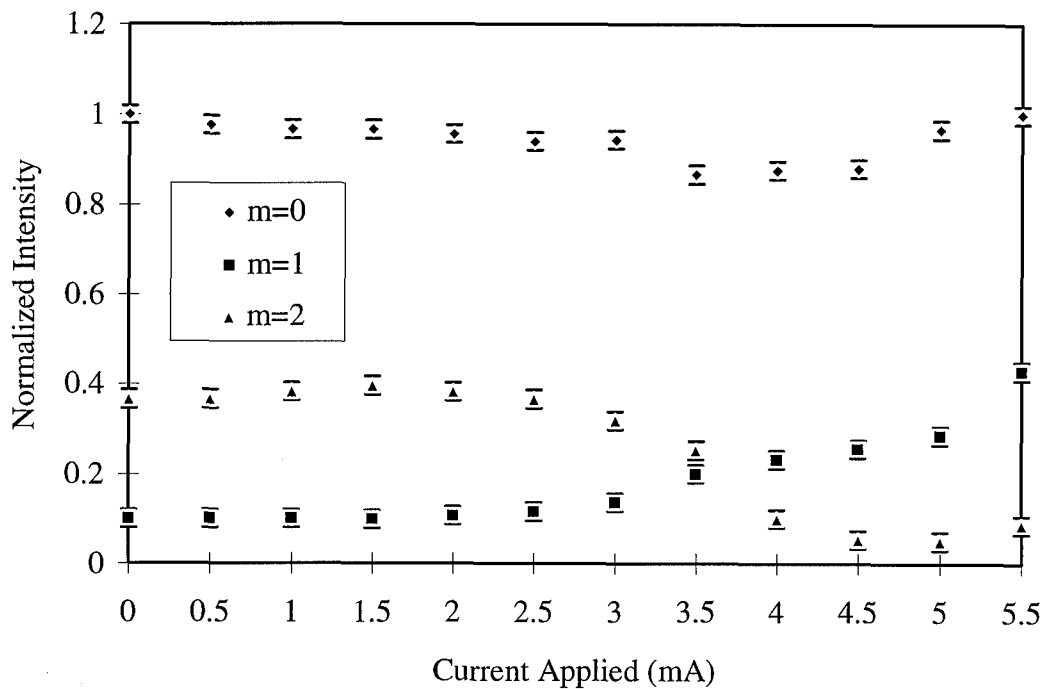


Figure 5-9. Second generation variable grating, ver. 8 (MUMPS 9), experimentally obtained profiles for the change in intensity of the $m=0$ and first two diffracted orders versus applied current to the heat drive actuators.

5.3. Fresnel Lens Results

The large 8 element Fresnel lens arrays from MUMPS 9 were found to flip-up during the die release procedure about 50 % of the time (see Fig. 5-10). The *WAMS* technique discussed in Chapter 2 appears to work for structures that have large areas (in this case 200x1600 μm). Approximately 90 % of the lens arrays flipped-up during release were also effectively locked into the desired position with the designed flip lock mechanisms. The Fresnel lenses designed as part of the fiber optic coupled interferometer were not elevated during the release procedure, but were effectively flipped-up with probing.

No Fresnel lens was tested in its elevated operational position. However, reflection patterns from a MUMPS 8, ver. 1, Fresnel lens (see Fig. 5-11) allowed for a quick examination of the resultant focal point versus the design value of 1000 μm . Using the measurements taken at the observation screen from the centroid of the reflected Fresnel lens pattern to the edges of the successive orders, a resultant focal point for each order can be obtained. The Fresnel lens measured was composed of 7 orders. The mean focal length obtained for the measured lens was 1,277 μm with a standard deviation of 275 μm . Using this simple technique, the resultant focal length was found to be very close to the design goal and indicates that Fresnel lenses can be evaluated before they are flipped-up for operation. The Fresnel lenses designed as part of the fiber optic coupled interferometer also exhibited the same reflection pattern but had more light rings since the lens was designed with a 500 μm focal length and can therefore have more orders before reaching the 2 μm spacing design limit.

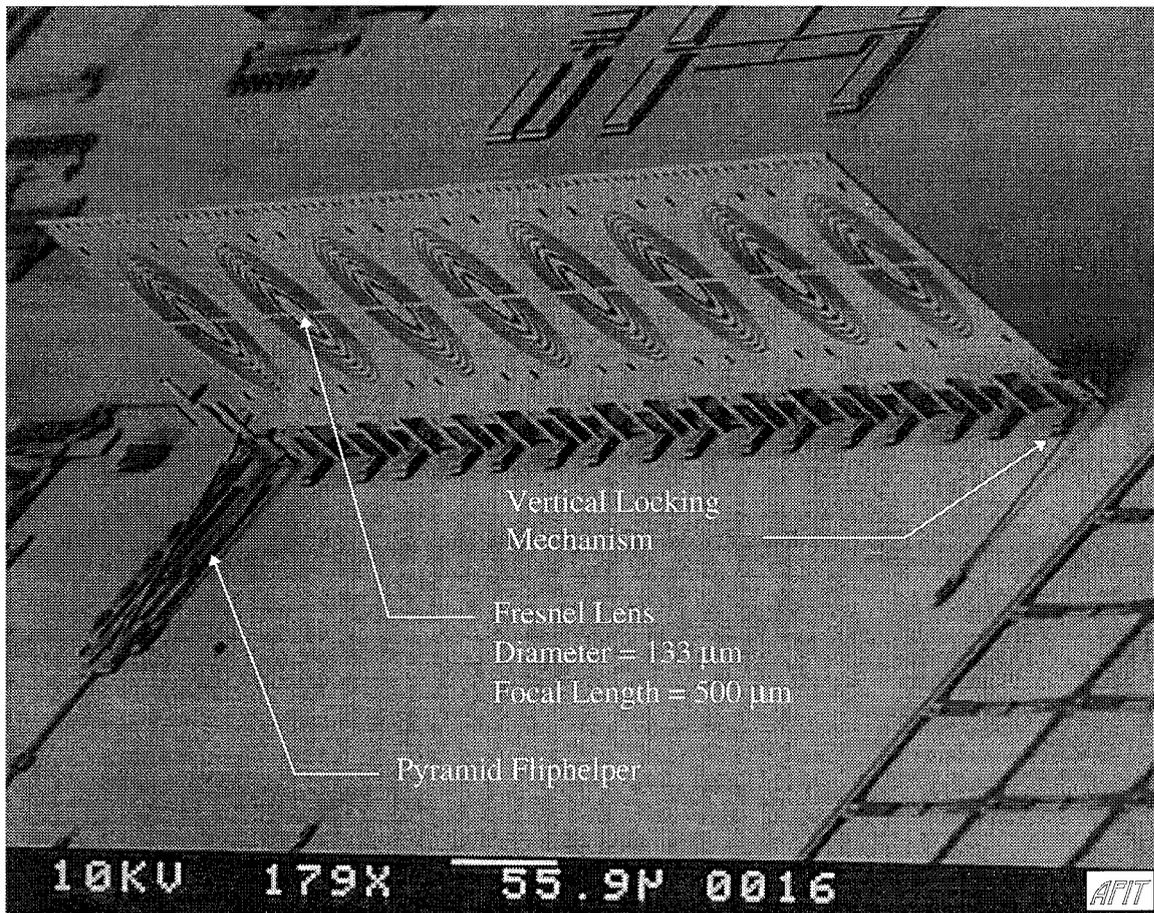


Figure 5-10. Scanning electron micrograph of 8 element flip-up Fresnel lens array (MUMPS 9). Plate is $200\ \mu\text{m}$ in height and is locked into place with only two vertical locking mechanisms. The pyramid flip-helper is shown in the upper left of the micrograph.

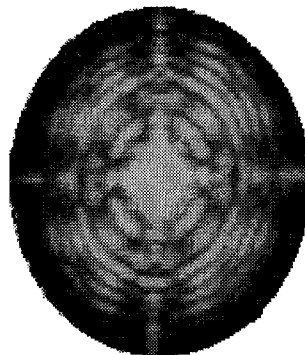


Figure 5-11. View of intensity pattern obtained using a Helium Neon laser to illuminate the lens. Ring diameters allow for the focal length to be calculated and compared to the designed value.

5.4. Flip-up Structure Results

The MUMPS 9 run was the first successful fabrication of flip-up structures designed for this thesis. Since the chips arrived at AFIT on 23 Oct. 95, only two weeks was allowed for testing of devices from this run. The mechanical probe station was used to flip-up the structures and evaluate the *fliphelper* and mechanical locking mechanisms.

The pyramid *fliphelper* was found to work extremely well with greater than 90% success. If used along with the *flip-jack*, every device was successfully flipped-up. The *flip-jack* would be lightly tapped with the probe tip to provide an initial lift to the device. The initial lift would often cause the device to stick in a temporarily elevated state. From this position, the end of the pyramid arm could be slid under the device plate extension. Once the pyramid shaped portion of the pyramid *fliphelper* was positioned under the plate, elevation of the device was accomplished by probing the sliding mechanism. In some cases the guide rails of the pyramid *fliphelper* were too long and connected with the hinge of the elevating structure. Also, in some cases the probe hole on the sliding rail was found to connect with the anchor strap prior to complete elevation. Shown in Fig. 5-24 is a pyramid *fliphelper* and *flip-jack* after having been used to elevate a grating beam splitter. The interference between the guide rails of the pyramid *fliphelper* and elevated structure is apparent in the top micrograph of Fig. 5-23. After elevation, the locking mechanism of the device is designed to drop down into the notch in the flipped-up structure (as also shown in Fig. 5-23). In approximately 50% of the devices tested the mechanical lock worked as designed with the pyramid *fliphelper* performing the entire flip-up and lock operation. The devices that failed to lock exhibited interference between the pyramid *fliphelper* and the elevated structure which prevented sufficient elevation to

allow the lock mechanism to catch. Furthermore, it was found that additional extension is required from the pyramid *fliphelper* since during the elevation procedure the hinge pin slides under the hinge pin strap until it connects with the poly 2 anchor of the hinge strap (this movement is $\sim 5 \mu\text{m}$). The fact that the hinge pin can move from its initial drawn position was not accounted for in the pyramid *fliphelper* design. Future designs should add approximately $10 \mu\text{m}$ to the sliding rail to safely account for the hinge pin movement. Devices which were not locked after probing of the pyramid *fliphelper* could be subsequently locked by probing the surface of the elevated structure. Extension of the probe at a position approximately $20\text{-}40 \mu\text{m}$ above the hinge pins would make contact with the elevated structure and allow it to be rotated about the hinge pins. By extending and retracting the probe tip the device would obtain a position to allow the lock mechanism to catch. Mechanical probing of the elevated structure is undesirable since it can lead to damage and should be avoided where possible. Furthermore, the goal is to achieve a *fliphelper* that minimizes the probing required to elevate and lock the structure, with a single probe operation preferred. Future designs should modify the pyramid *fliphelper* to eliminate the need to mechanically probe the elevated structures.

Version 7 of the 45 degree flip-up mirror is shown in Fig. 5-12. The extension arm embossing and scissor hinge of this device are shown in Fig. 5-13. For these devices no *fliphelper* is required. Probing at the probe hole allows for complete elevation of this device to the required angle. The ratchets would maintain the elevated position of the structure if the device was probed from the exterior edge of the probe hole extension.

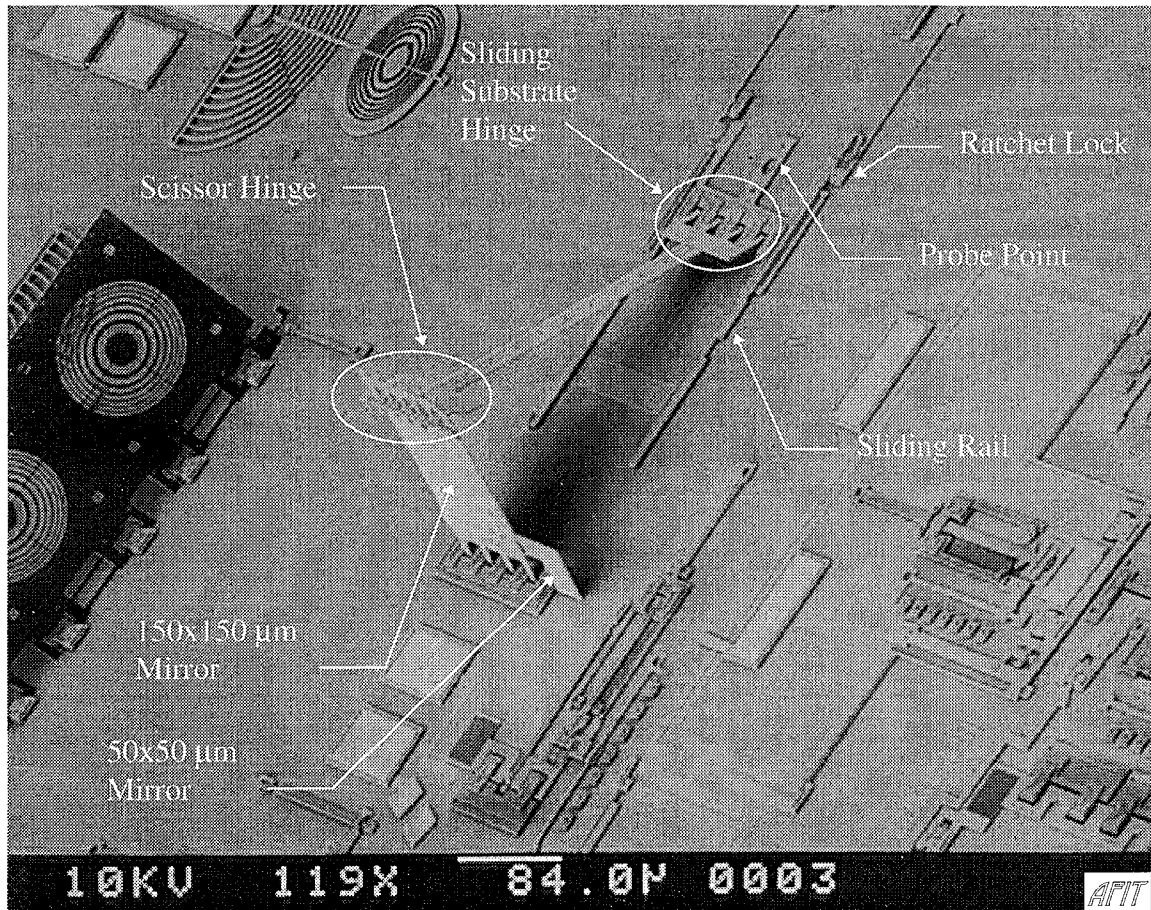


Figure 5-12. Scanning electron micrograph of 45 degree nominal flip-up 150 x 150 μm mirror with smaller 50 x 50 μm mirror attached (MUMPS 9).

When the probe was placed in the probe hole the device would often move during retraction of the probe tip since it slides along the surface before being elevated. A T-shaped probing point would be an improvement on the current design by preventing interference during probe tip retraction yet still allowing for the device to be adjusted since movement may be required in both directions for angle adjustment. Figure 5-13 shows how various angles can be achieved by adjusting the sliding ratchet to the desired position. Various ratchet locking arm lengths need to still be evaluated to ensure that the device maintains the set angle during operation. On devices that were gold plated for

evaluation using the SEM, the angle was observed to have changed from the probe set point. This is likely due too the gold sputter operation and indicates that the holding force of the ratchet lock might be insufficient for operational devices. The length of the ratchet locking arm on the MUMPS 9 ratcheting mirrors was 200 μm , but could be drawn any length as long as it allowed for movement of the ratchet rail.

The number of hinge pins on the two substrate hinge sections appears to be adequate to hold the device. The Poly 0 lines that were drawn to emboss the elevation arm do not appear to cause any interference and in fact may help ensure that the ratchet lock and rail make contact since the sliding plate rides along the top of the emboss lines.

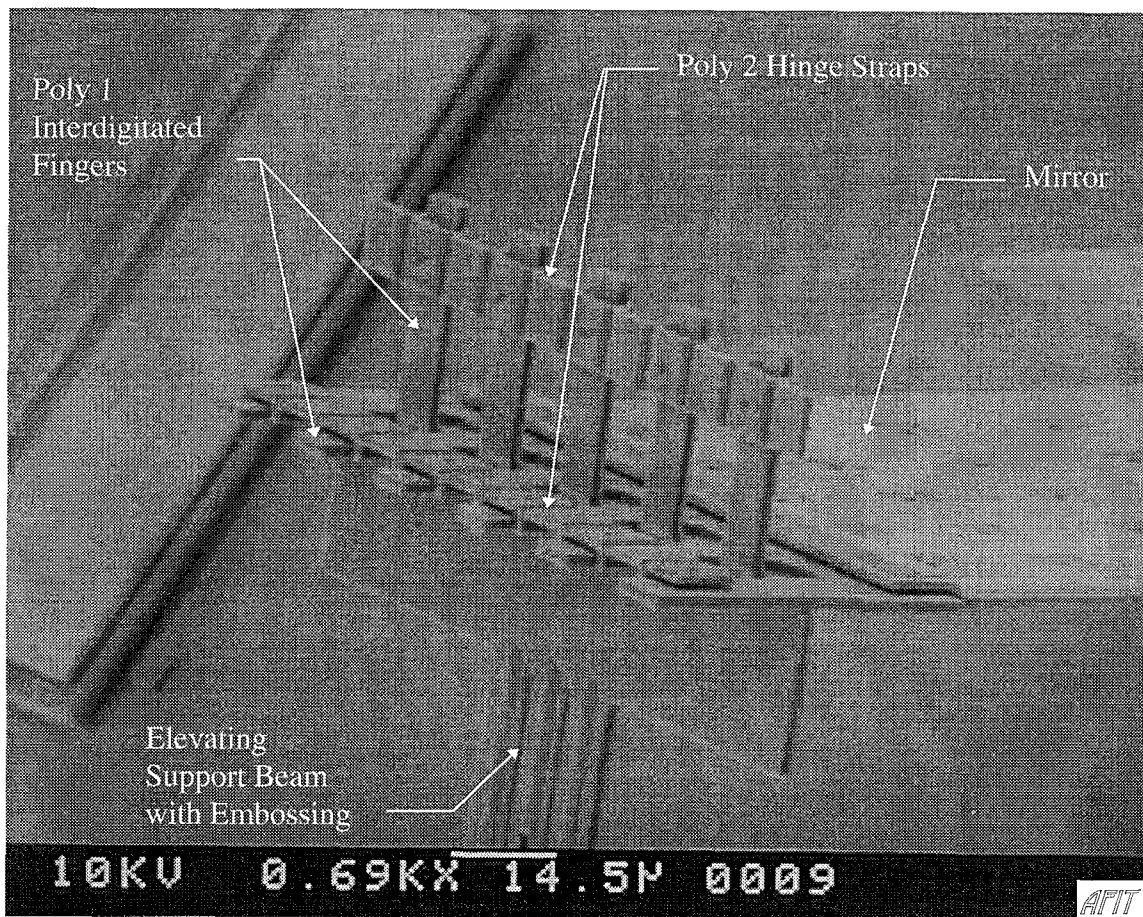


Figure 5-13. Scanning electron micrograph of scissor hinge section of flip-up mirror shown in Fig. 5-12 (MUMPS 9).

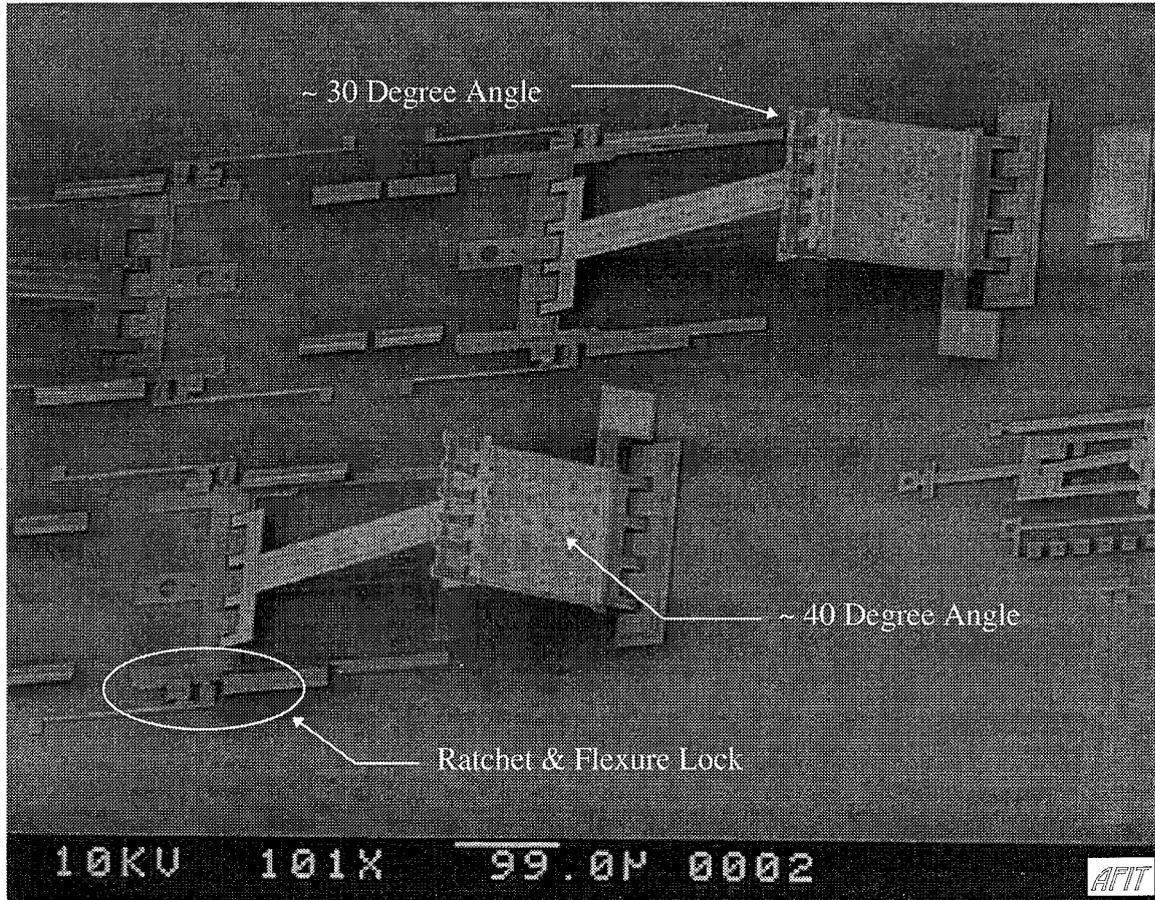


Figure 5-14. Scanning electron micrograph of two flip-up mirrors like the one shown in Fig. 5-12 indicating how various angles are achieved by the ratchet and flexure lock mechanism.

5.5. FBMD Hidden Hinge Results

Three versions of hidden hinge flexures were fabricated on both MUMPS 8 and MUMPS 9. It was expected that the fabrication problem on MUMPS 8 would yield those devices inoperable and therefore the layout was copied onto a MUMPS 9 die. Testing was therefore delayed until receipt of MUMPS 9. A representative micrograph of one of the versions is shown in Fig. 5-15. From the micrograph it is evident that the hidden flexures will effect the topology of the mirror surface but the packing density can be increased since the separation between mirrors can be reduced to the minimum design

guide line for Poly 2 separation (currently 2 μm).

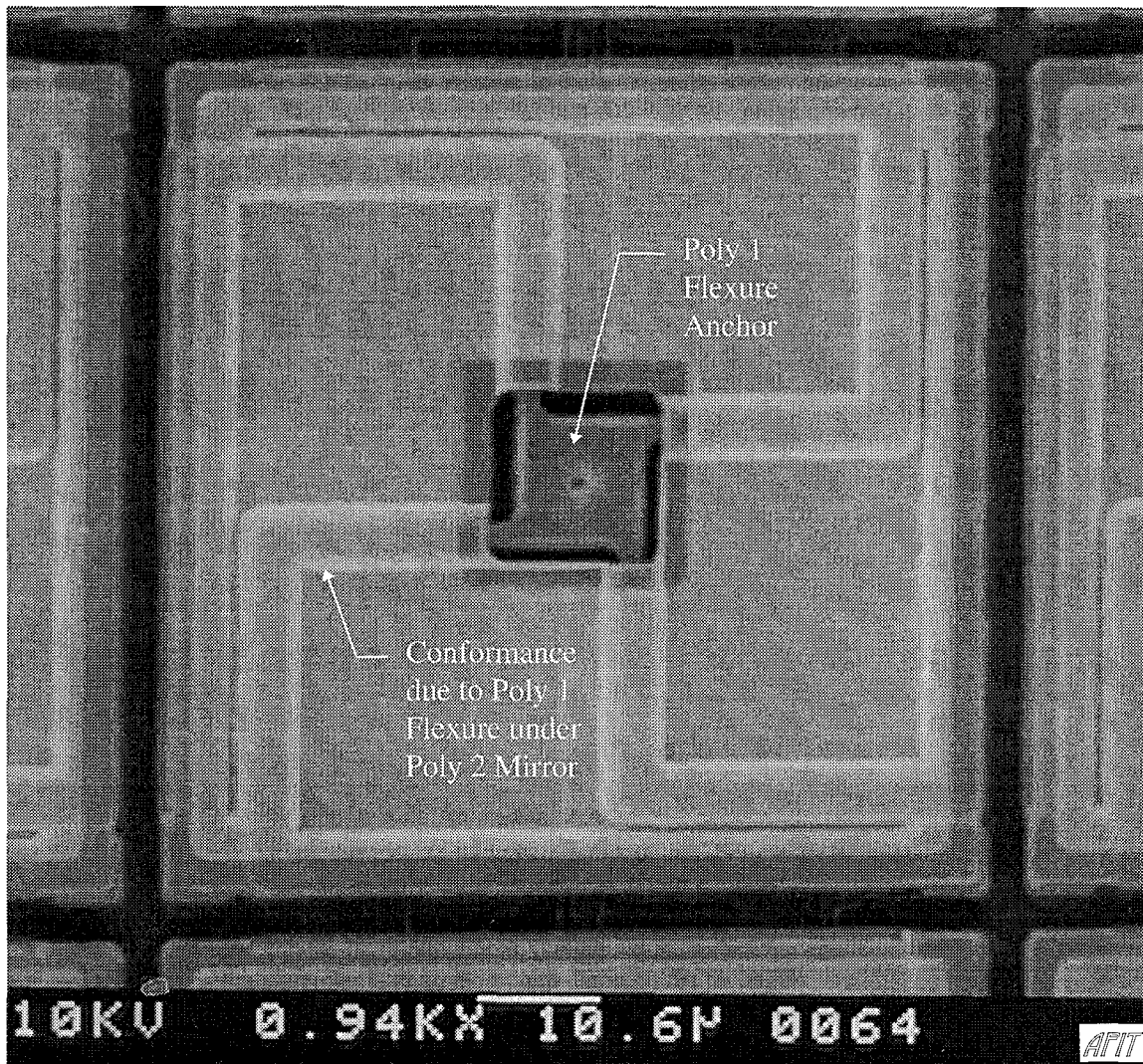


Figure 5-15. Scanning electron micrograph of ver. 2 (MUMPS 8) of the hidden hinge mirrors. Conformance of the top layer over the flexures is evident in the mirror surface.

5.6. Resonant Frequency Results

The use of the Spectrum analyzer to detect the resonance of FBMD structures proved to be the most accurate method for determining the spring constant of the devices tested. Since the spring constant can be determined from Eq. (3.51) for a known resonance frequency, there is no need to fit a curve to the data as in the case of the voltage

versus deflection curve obtained using the microscope-based laser probe interferometer. The fitting operation is more susceptible to error since the ideal FBMD model is not precise and the mathematical description is more involved.

Testing showed that resonance was not observable for pressures greater than ~ 100 Torr. Above this value, the fraction of critical damping (ζ) becomes large enough that the resonance is less than the noise of the test setup. Figure 5-16 shows how the resonance frequency shifts to the left as ζ increases. Furthermore, the resonance no longer exhibits a spike and the increase in mechanical energy of the mirror spans a larger frequency range.

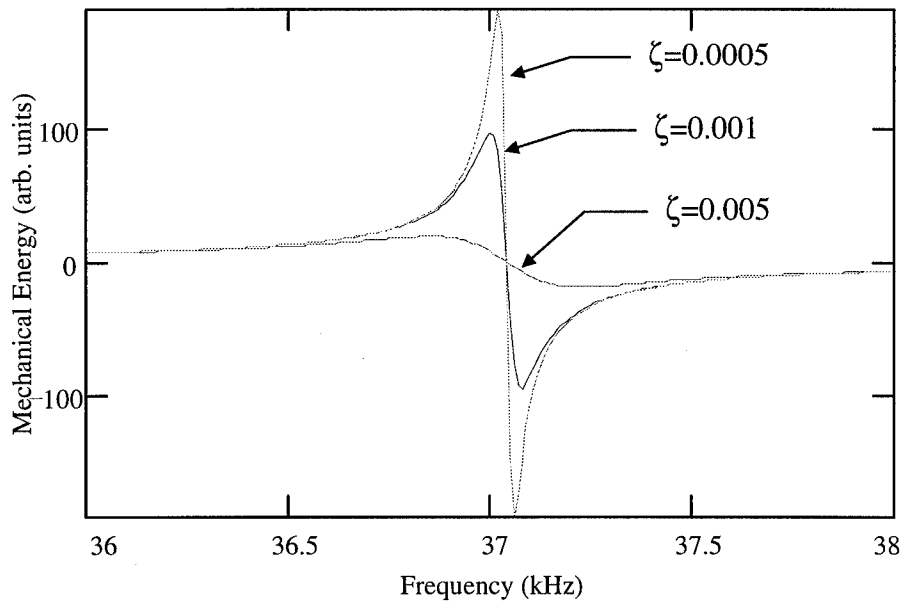


Figure 5-16. Transfer function plotted for three different values of the fraction of critical damping. Data used in the calculation (mass = 4.8×10^{-11} kg, spring constant = 2.6 N/m) was for a square, $65 \times 65 \mu\text{m}$, FBMD.

Data taken for the square FBMD at resonance was matched to the theoretical modeling equation by varying ζ (see Fig. 5-17). The best fit curve obtained by linear

regression yielded a value of $\zeta = 0.0001$ in which case the critical damping coefficient is found to be $c_c = 2.2E-9$ kg/s. This shows that the model matches the experimental data extremely well (within 0.1 %) and can be used to obtain the values of ζ and c_c for any FBMD.

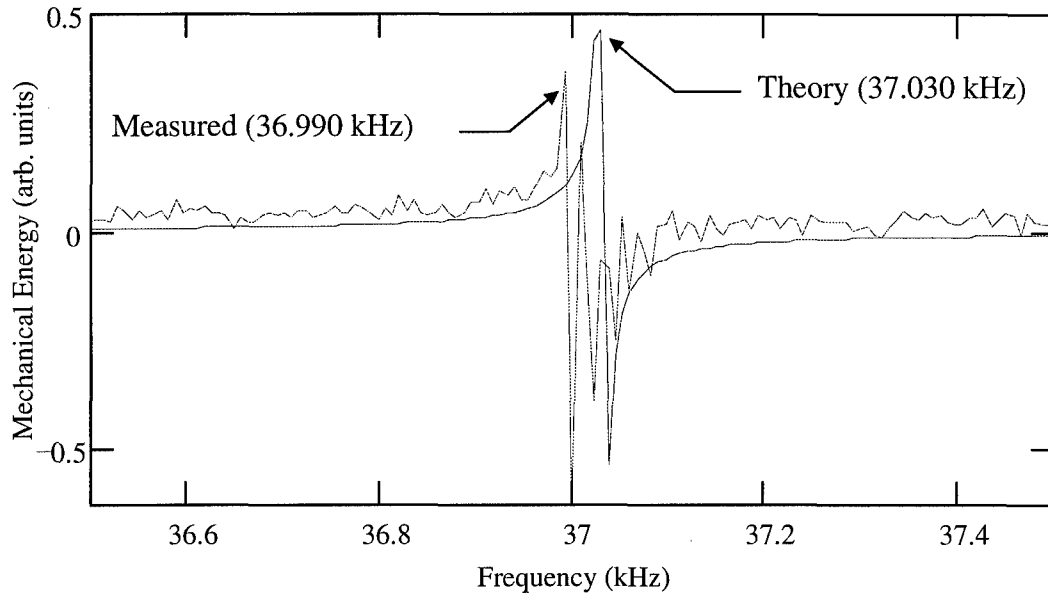


Figure 5-17. Experimental and theoretical resonant frequency curves for a square, $65 \times 65 \mu\text{m}$, FBMD. The resulting fraction of critical damping is $\zeta = 0.0001$.

A Fringe test array, as discussed in Section 4.4.3, was also tested for resonance. There are four arrays each containing the four different geometry's of fringe mirrors. Each array is separated by $988 \mu\text{m}$ across the surface of the die. By testing each array, in which case 36 mirrors (9 of each geometry) are all actuated at the same time, the resonance curve shown in Fig. 5-18 is obtained. The displacement of each primary peak is due to the different masses of each geometry along with the difference in the modulus of elasticity across the surface of the die. The first set of resonance spikes is larger in relative magnitude since it is the superposition of the resonance curve for two of the

geometry's. The three sets of resonance spikes each have multiple peaks since the nine mirrors of each geometry are spatially separated and therefore have different spring constants which yields different resonant frequencies. A complete match with the model is not possible from the data since the modulus as a function of position on the die can only be calculated in one direction (i.e. the direction of spatial displacement for the four fringe arrays). Shown in Fig. 5-19 is the model derived resonance curve for the fringe array with no adjustment for the spatial change in the modulus of elasticity across the die. The spatial separation of the four fringe arrays causes the entire resonance curve for each array to shift to the left due to the spatial change in the modulus of elasticity (see Fig. 5-20). From the spikes of each curve and the known spatial separation of the fringe arrays, the resonance frequency was found to change by $0.2 \text{ Hz}/\mu\text{m}$ on the particular MUMPS 7 die tested.

Other mirrors on the MUMPS 6 die were also tested for resonance at 290 K. No resonance was found for the paddle-cantilever style mirrors which would have been ideal for testing since the flexures contain no bends which introduce the torsional term into the spring constant equation. These devices are all wired together in big arrays which have a common ground. The resonance for the square FBMD was initially found using devices that are individually wired. The initial indication was that the multiple mirror connections may be too great of an electrical load for the small 1.26 V peak-to-peak signal of the spectrum analyzer. However, three other mirror devices that were wired on the die in an arrayed fashion were successfully tested for their resonance frequency values.

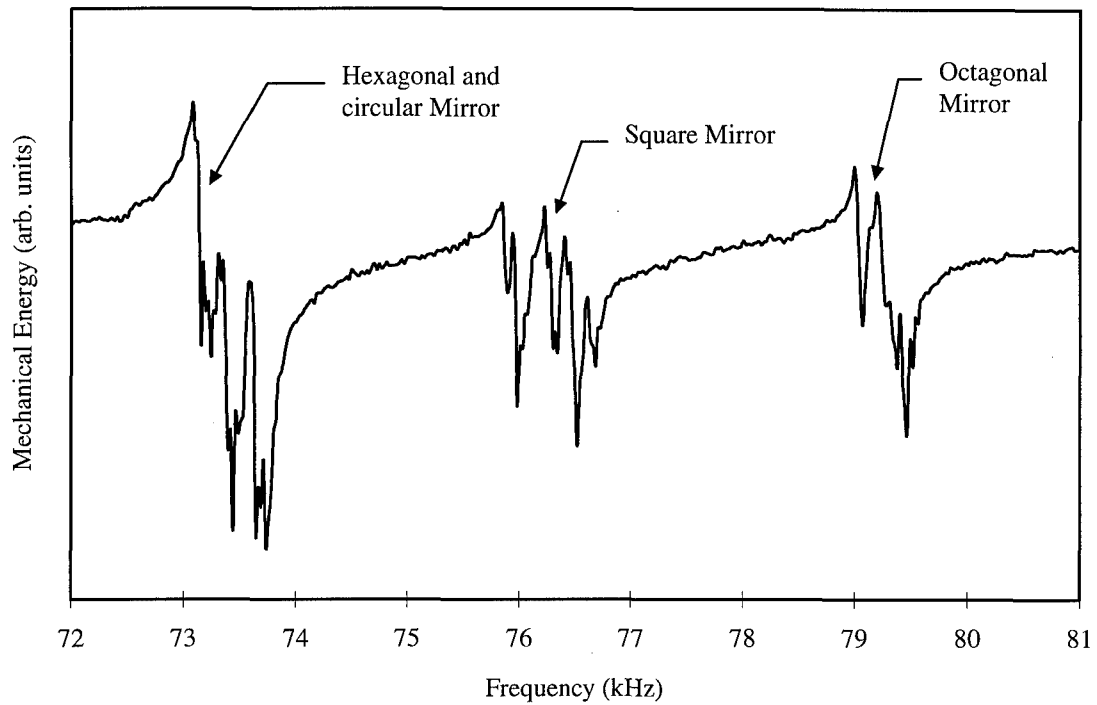


Figure 5-18. Resonance profile for a single fringe test array containing 36 mirrors with 4 different geometry's. Taken at a temperature of 290 K and a pressure of 20 mTorr.

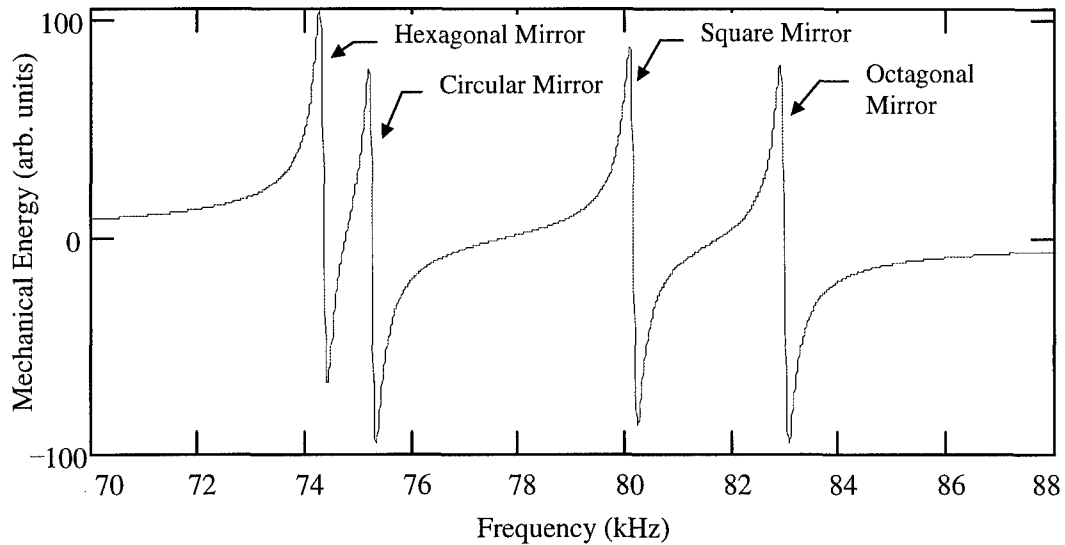


Figure 5-19. Theoretical frequency profile for a fringe test array. Data is not corrected for spatial change in modulus of elasticity.

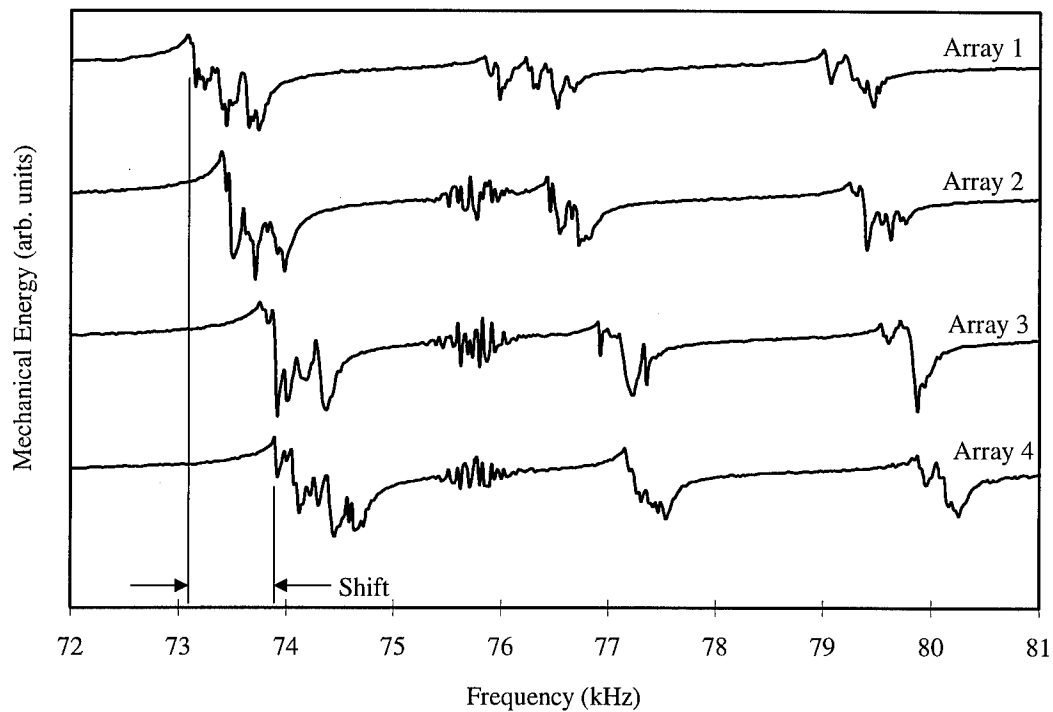


Figure 5-20. Experimentally obtained resonance profiles for all four of the fringe test arrays. Taken at a temperature of 290 K and a pressure of 20 mTorr.

5.7. Thermal Testing Results

5.7.1. Test Setup Difficulties

Time limitations and test equipment difficulties prevented the testing of devices for thermal effects as originally planned. The microscope-based laser probe interferometer was relocated to bldg. 640, room 61, from bldg. 194 and initially was tested in its original configuration before making the necessary adjustments to incorporate the LTMP.

The optical bench in room 61 requires a Nitrogen supply to fill the dampers and isolate the table from mechanical vibrations. A Nitrogen tank and regulator were acquired and connected to the table before operation of the test setup. The surrounding environment in bldg. 640 is significantly more noisy than bldg. 194 since the HVAC system for the building is located just across the hall and was constantly in operation over the summer months. The air table was a must for isolating the setup and minimizing the noise in the acquired traces from devices tested.

To fit the LTMP below the microscope required that the support post holding the microscope be retracted and elevated due to interference. An aluminum box with adjustable bolt holes was designed to provide the necessary extension. A holding fixture to clamp the LTMP to the translation stage was also required. The fixtures worked as designed and allowed for placement of the LTMP under the microscope without interference. The initial setup of the system was delayed by 6 weeks since the required jigs had to be manufactured at the AFIT machine shop.

The microscope objective was replaced with a longer focal length objective and a copper block was mounted on the refrigerator, as discussed in Chapter 4, to allow for

focusing of the device through the sapphire window of the LTMP. Furthermore, the focusing lens shown in Fig. 2-10 was repositioned to maintain the 4 μm spot size on the device. The reference mirror of the interferometer was repositioned to closely match the length of the object leg. This allows for the interference fringe size to be maximized at the detector. The interferometer was aligned using the beam splitter and reference mirror such that the center of the fringe pattern illuminated the optical detector. The aperture of the optical detector is close to ~ 1 mm to ensure only the center fringe is being evaluated.

Prior research at AFIT [68] indicated that die in the LTMP would exhibit moisture drops during low temperature operation. When testing conventional IC devices this moisture is not a factor since the die typically has a protective passivation layer which protects the devices. For MEMS device testing, the moisture is significantly detrimental since the structures are directly exposed to the environment and the high surface tension of water will cause stiction when the moisture evaporates. Furthermore, electrostatic devices require an air gap to operate and the entrapment of any water in the gap acts as a damper on the device and impedes the desired movement. Exhaustive efforts were made to reduce or eliminate the moisture in the vacuum chamber. MMR recommends baking out the chamber at just below 50°C for five days every time a new die is positioned in the chamber. This procedure was performed by placing a plate warmer, monitored by two thermocouples, around the LTMP. The vacuum chamber was pumped down and the temperature was found to stabilize at 45°C . After 5 days of baking out the chamber, the moisture was still present during cool down at approximately 260 K. The device temperature was returned to 290 K and an additional 5 day bake out was performed. The moisture was still present after this second attempt. Additional efforts were taken by

developing a desiccant filter for the backfill line and running the backfill into the chamber at 760 Torr for 1+ hours with the refrigerator removed to attempt to drive out the moisture. This was tried five times with no success. Furthermore, an additional 5 day bake out resulted in similar condensation on the die at 260 K.

Since removal of the moisture was unsuccessful, it was determined that all thermal measurements would have to be from room temperature (290 K) to the limit for the silicon conductive grease (450 K). The original plan was to test devices for thermal effects from 450 K down to 77 K.

5.7.2. Resonant Frequency Results

The resonance frequency test setup was used to obtain the flexure spring constant of a device as a function of temperature. Given the flexure spring constants, the modulus of elasticity can be calculated using Eq. (3.52) to obtain a change in modulus as a function of temperature. The results for one of the square FBMD mirrors as a function of temperature are shown in Fig. 5-21. As shown, the change in the modulus of elasticity is extremely linear over the range of temperatures tested.

The original intent was to also verify this change in the modulus of elasticity from data taken using the microscope-based laser probe interferometer. However, the change in the modulus of elasticity versus temperature from this technique was significantly greater (10-30 %) and yielded a larger amount of variability. The only plausible explanation for the change is that all of the voltage versus deflection measurements were taken prior to the resonance measurements. Since the same die was used for all measurements, there may have been some change in the material characteristics each time the die was thermally cycled. The resonance data yielded an average modulus as a

function of temperature for the three square FBMD mirrors tested (mirror area of 3,716 μm^2 and flexures that are 132 μm long) of:

$$E(T) = -0.041T + 173.99 \quad \text{GPa} \quad (5.1)$$

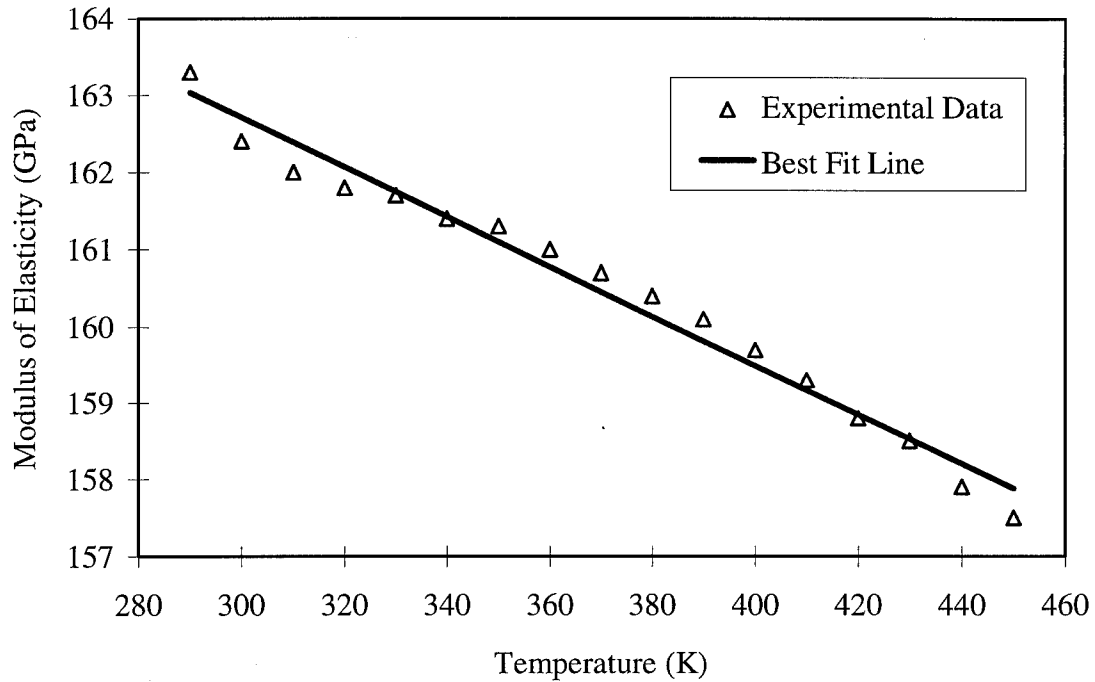


Figure 5-21. Results of thermal testing of a square FBMD from MUMPS 6. The modulus of elasticity for the Poly 2 (flexure material) was extracted from the spring constants obtained by detecting the resonant frequency. For this mirror, the best fit line yields: $E(T) = -0.032T + 172.39$.

5.7.3. Resistivity Results

The resistivity of each layer (Poly 0,1, and 2) was calculated using straight 180 μm long polysilicon lines terminated at each end with gold plated probe pads. The lines were all 15 μm wide and the MCNC reported thickness' were used to calculate the resistivity. Resistance measurements were taken at 10 K steps for each layer from 290 to 450 K and the temperature was allowed to stabilize for a minimum of 5 minutes before

measurement of the resistance. The resistivity of the layers was found to change linearly versus temperature with a slope of $1\text{E-}6$ to $2\text{E-}6 \text{ } \Omega\text{-cm/K}$ observed for all three layers (see Fig. 5-22).

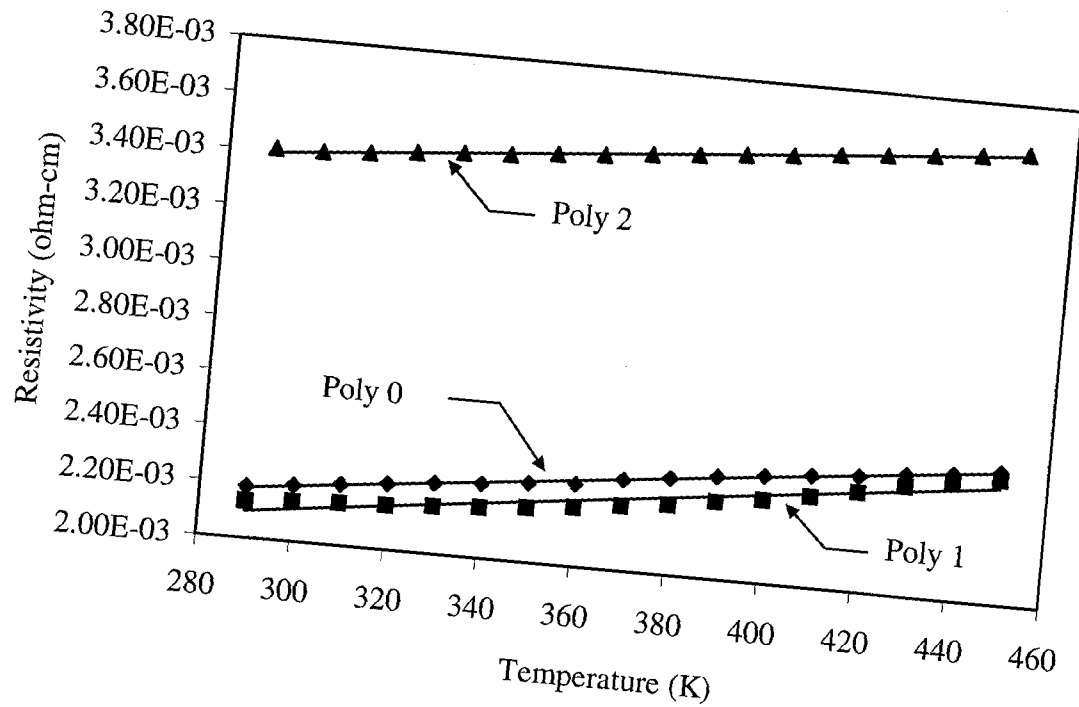


Figure 5-22. Results of resistivity versus temperature of the three polysilicon layers of the MUMPS process. Best fit lines from linear regression are shown with the points indicating the experimental data (Die from MUMPS 4).

5.8. Micro-Interferometer Results

The micro-interferometer requires the flip-up of four structures one of which is also attached to a center, DC blocking, plate on some versions. For the versions that do not have optical fiber interfaces, there are two additional flip-up mirrors of the design shown in Fig. 5-12 that must be elevated to 45 degree nominal angles. A micro-interferometer that is partially flipped-up is shown in Fig. 5-23. The systems are only partially flipped-up to facilitate observation of the structures. Using the flip-up techniques

described in Section 5.4, the structures were easily flipped-up into the operational configuration.

The device was designed for testing at 632.82 nm wavelength with the use of a Helium-Neon laser. At that wavelength, the table used to generate Fig. 2-1 indicates that the absorption of Silicon is $\sim 0.02 \text{ cm}^{-1}$. For a $2 \mu\text{m}$ thick layer the absorption reduces the field by only 0.0004 % which can be considered negligible. The grating used for beam splitting will therefore operate as phase-mostly diffraction gratings since the light at normal incidence on the incoming side will be reflected back at $\sim 35 \%$ and the remaining $\sim 65 \%$ will be transmitted into the diffracted orders. The phase difference between the light passing through the slits and the light that is transmitted through the polysilicon will therefore create a diffraction pattern due to constructive and destructive interference. The phase difference will be created by the index of refraction difference between the slits ($n_{\text{air}}=1$) and the polysilicon ($n_{\text{poly}} = 3.9 @ 632.82 \text{ nm}$).

The DC blocks performance is limited since the $\sim 65 \%$ of the light is still transmitted. The light that is reflected on the current designs feeds back into the system which is not desirable since it leads to multiple reflections which cause interference. To be more effective the DC block should have been turned at an angle to spectrally reflect the incident beam away from the first beam splitter.

The distance from the beam splitters to the mirrors must be greater than minimum distance for Fraunhofer diffraction since the mirrors are intended to reflect the $m = +/- 1$ order of the Fraunhofer diffraction pattern. The distance to the Fraunhofer region from the aperture has been defined in the literature [34] and can be written for a one-dimensional diffraction pattern as

$$z \gg \frac{ka^2}{2} \quad (5.2)$$

where $k = 2\pi/\lambda$, a is the maximum width of the slits and \gg is taken to be a factor of 10.

For a $2 \mu\text{m}$ gap and line grating, like the one used for the beam splitters of the micro interferometer, Eq. (5.1) yields a distance to the Fraunhofer region of $198.58 \mu\text{m}$ for $\lambda = 632.82 \text{ nm}$. The smallest interferometer designed is shown in Fig. 5-23 and has a beam splitter-to-mirror separation distance of $218 \mu\text{m}$ which is sufficient to satisfy the approximation given by Eq. (5.1).

Shown in Fig. 5-24 is a portion of a large interferometer that has been flipped-up. For both the small and large interferometers to work, the optical path length of the objective leg must be varied. The movable mirror that provides the modulation was tested for the small interferometer and yielded excellent results. After flipping-up the plate into the locked position, the pair of heat-drive actuators were easily driven to provide visible deflection of the mirror ($\sim 2\text{-}4 \mu\text{m}$) which is sufficient to yield modulation. The output of the interferometer as a function of the object mirror deflection distance can be calculated using Eq. (3.41) and is shown in Fig. 5-25. The plot indicates that ~ 20 cycles of optical modulation is achievable per $1 \mu\text{m}$ of deflection in the object mirror.

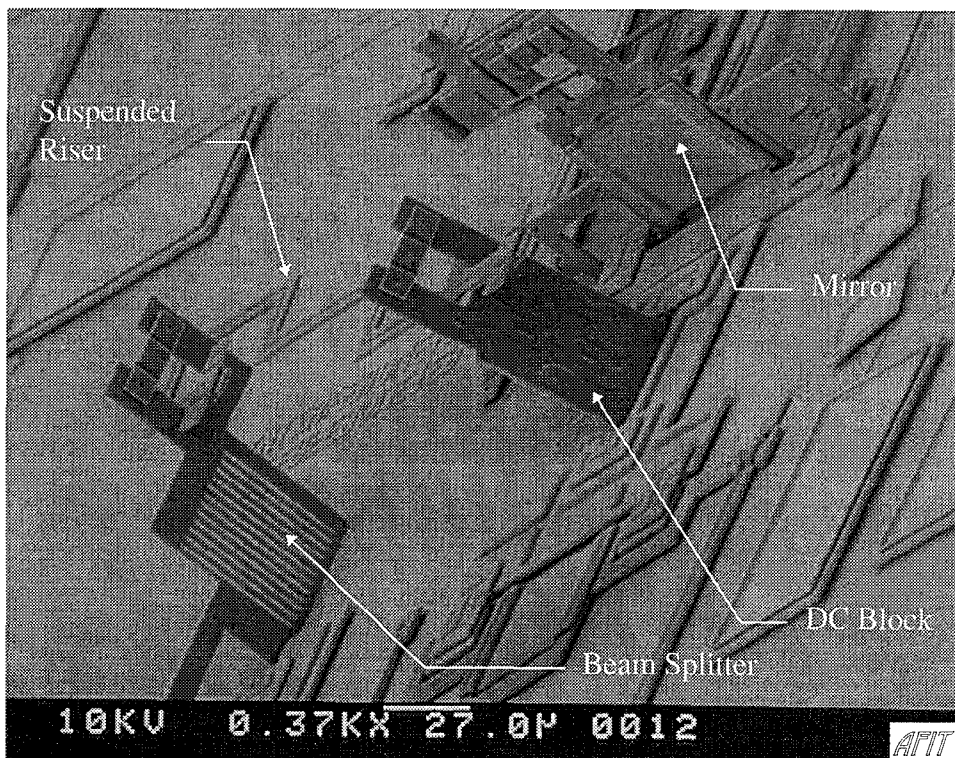
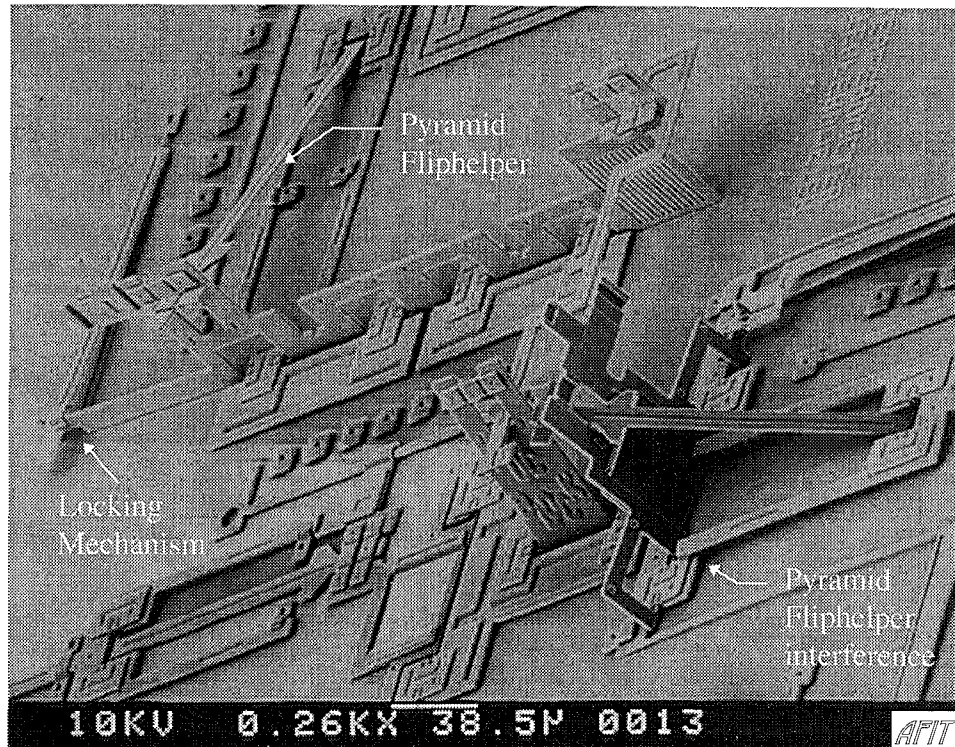


Figure 5-23. Scanning electron micrographs of a 172 x 400 μm small interferometer (MUMPS 9). Top micrograph shows how the fliphelper on the first beam splitter has been used to flip-up the DC blocking plate. Bottom micrograph is a closer shot of the two 50 x 50 μm flipped-up plates that are coupled together with the suspended riser.

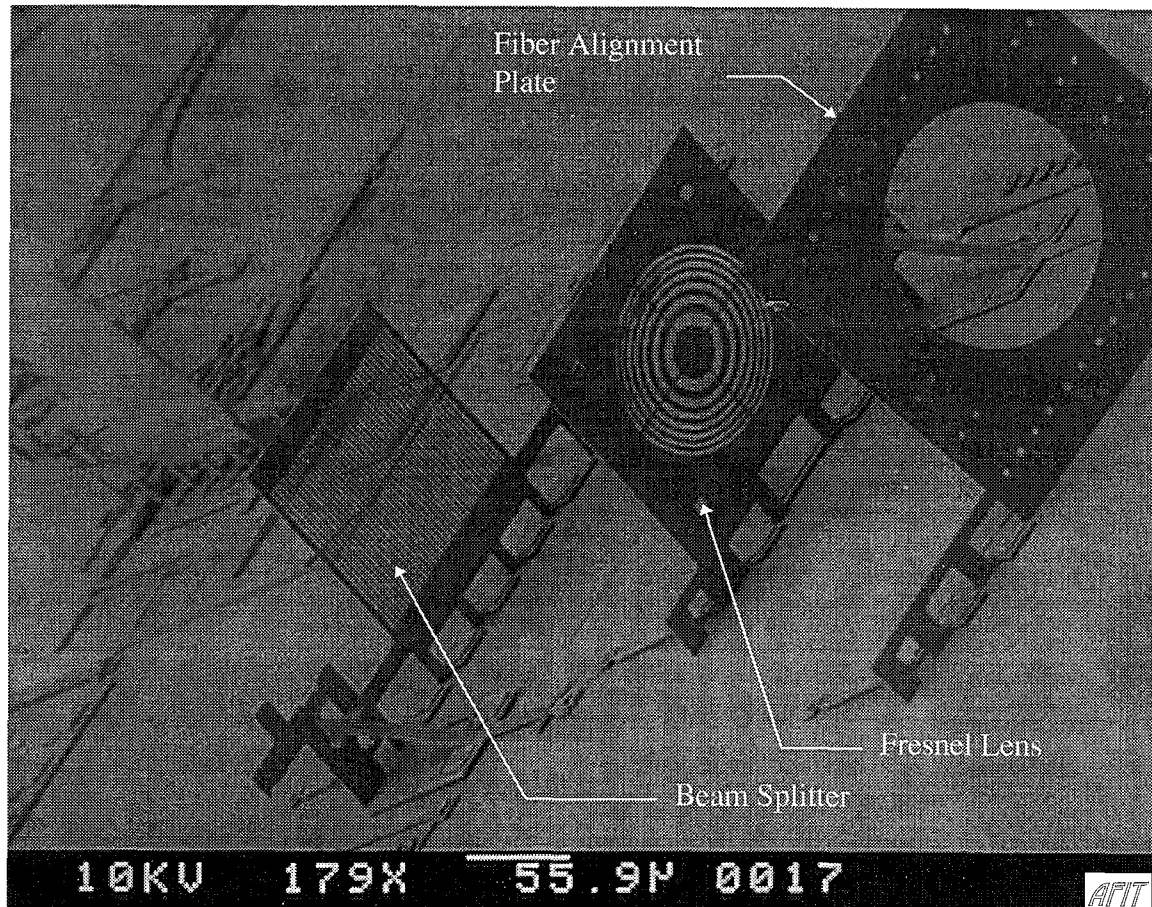


Figure 5-24. Scanning electron micrograph of 250 x 1500 μm large interferometer designed with optical fiber couplers for the input and output. First flip-up plate on right is for edge alignment of the optical fiber. Fresnel lens is designed for 632.82 nm light and acts as a collimator for the rapidly diverging beam from the fiber. Third flipped-up plate is the first beamsplitter of the interferometer and in the background is the flipped-up stationary mirror for the reference beam.

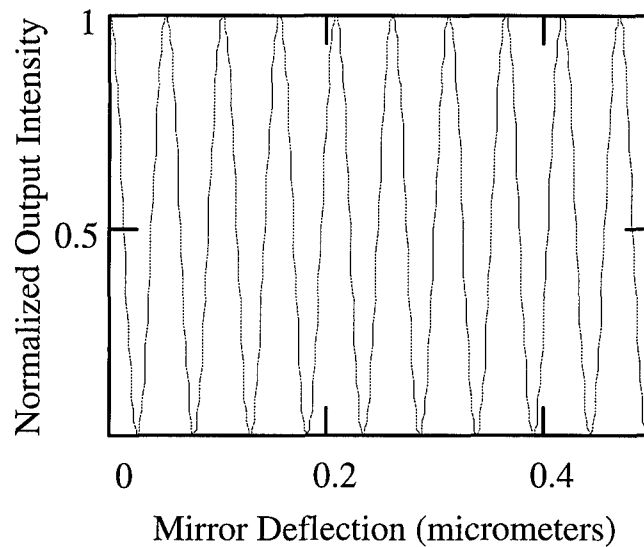


Figure 5-25. Optical modulation calculated for the micro-interferometer as a function of the object mirrors deflection distance.

5.9. Heat Actuator Results

The heat drive actuator design variations discussed in Chapter 4, Section 4.4.2, were tested on the micromanipulator probe station. All devices were on the same MUMPS 7 die released just prior to testing.

All three circular heat actuators design variations, from MUMPS 7, exhibited less than 1 μm of movement for an applied current up to the burn-out condition ($\sim 5.4 \text{ mA}$). At burn-out the thin sections of both legs of the actuators were glowing which indicates that the heat generated in the flexure section of the outer leg is not being dissipated into the thick section and anchor. Expansion of the inner leg is therefore impeded by the outer leg which is also expanding. Mechanical probing of each device at the end of the actuator was done to ensure that stiction was not preventing the device from expanding. These devices had thick sections on the outer leg that were approximately half its length. The

MUMPS 6 test array of linear actuators indicated that the flexure section of the outer leg should be ~ 10-15 % of the actuators length [phipps].

The vertical heat actuator test array (MUMPS 7) composed of a Poly 1 and Poly 2 leg connected with a via exhibited no observable movement. These devices were found to burn out at ~ 3.6 mA at which point the current would immediately drop to 0 mA. Probing of the legs after burn-out revealed that the Poly 1-2 via was no longer connected. The Poly 1-2 via on the devices was designed at 2 μm in diameter which yields a cross-section of 3.14 μm^2 . Since the thin section of the vertical heat actuator has a cross-section of 4 μm^2 , the Poly 1-2 via is found to be the current limiting spot in the device. Therefore the device fails were it should based on the design. Future designs need to incorporate a larger diameter Poly 1-2 via in order to prevent burn-out at that location and to allow the thin leg to heat-up and expand.

The other version of vertical heat actuator (MUMPS 7) was composed of two Poly 1 legs connected at the corner. At ~ 4.6 mA both legs of the device would glow and an outward movement of 1-2 μm was detected for the longest (105 μm) device. The intention was to use this device when connected to a poly 2 mirror as described in Chapter 4, Section 4.4.3. Since the corners weren't constrained by the mirror on this test array, it was expected that they would move outward versus upward when actuated. The resistance of these devices before actuation ranged from 347 Ω for the short device (51 μm) to 642 Ω for the long device (105 μm).

The vertical square mirror was tested next with the legs of one of the four connected vertical heat actuators glowing at 18.6 mA. The higher current is required since the four vertical heat actuators are connected in parallel. Each actuator burned-out

individually with the first one being the closest to the probe pads were the voltage source is connected. This occurs since the resistance of the Poly 0 routing wires is significant between the four vertical heat actuators. Movement of the mirror was not observed and it appeared that the vertical heat actuators buckled to allow for the thermal expansion.

5.10. Summary

This chapter has explained in detail the results obtained for the various experiments conducted. The results of testing one version of the variable grating were covered in detail. Explanations into the difficulties associated with testing MEMS at low temperature were revealed. Finally, the flip-up structures and associated techniques for successful elevation were discussed.

6. Conclusions and Recommendations

This chapter summarizes the main conclusions from this thesis research.

Recommendations for future work that extend the scope of this thesis are also discussed.

6.1. Conclusions

Numerous devices have been designed and evaluated for use in flip-up structures. The fabrication problems discussed in Chapter 4 prevented design iteration required to improve on the designs, but MUMPS 9 results have provided an initial verification of operation of key components of an optical system. A flip-up ratcheting mirror was shown to work exceptionally well and can be used in future optical system designs. A *fliphelper* and lock mechanism were developed and proven to work for flip-up structures that don't require probe adjustment after elevation. These devices only require minor design modifications to increase their effectiveness. A technique for performing multiple device flip-ups with a single fliphelper was also successful.

Methods for testing MEMS devices for material properties were developed. The LTMP was integrated into the previously existing microscope-based laser probe interferometer and a new drive signal generator was developed. This test setup allows for acquisition of the surface deflection versus voltage for any FBMD structure at a specified temperature. The current system exhibits moisture during low temperature operation which prevented evaluation of electrostatic devices below 260 K.

A test setup was developed to more accurately and readily determine the spring constant of a device. This technique utilizes the resonance frequency of the structure

which is known to match theory for a single degree of freedom system. It was found that resonance could be obtained for a number of FBMD structures when placed under vacuum (~ 20 mTorr). The resonance frequency can be used to back out the spring constant for a FBMD. Results for a square FBMD were found to compare favorably with the known spring constant from prior research [23]. From the spring constant, it was shown that the modulus of elasticity can be determined. The resonance frequency test setup was used to evaluate the effects of temperature on a square FBMD. The modulus of elasticity of Poly 2 on MUMPS 6 was found to decrease as a function of temperature by 0.03-0.05 GPa/K from 290 to 450 K. The resistivity of MUMPS layers on MUMPS 4 was found to increase at higher temperatures. All three polysilicon layers were tested for thermal changes in the resistivity from 290 to 450 K and yielded similar slopes of 1.4E-6 -to- 3.0E-6 Ω -cm/K.

A novel variable grating was designed and tested with excellent initial results. Variations in period dimensions can be achieved by deflecting a top grating plate relative to a lower grating plate. Different dimensions were evaluated and all designs matched the theoretical diffraction patterns from the developed model. The first and second diffracted orders of the variable grating ($\omega_1 = 6 \mu\text{m}$ and $\omega_2 = 2 \mu\text{m}$) were shown to swap energy with almost equal maximum intensities for 0 to 6 mA of applied current, while the specular reflection ($m=0$) reduced in intensity by only a small amount, ~14 %. This lends the device well toward multi-channel switching applications. Design improvements from the first generation of device yielded smoother operation due to the incorporation of a symmetrical actuator, top plate hold downs, and a clean fabrication without the sticking

discussed in Chapter 4. Modulation of 6.4 and 9.0 dB was observed for the first and second diffracted orders, respectively. The test method used to verify the operation of these devices was found to work extremely well. The evaluation of diffracted angles, intensities and modulation can all be determined from a single test station as shown in Chapter 4.

Design variants of the heat drive actuator were found to be ineffective. The use of vertical heat drive actuators to power vertical movement of a mirror was unsuccessful. Furthermore, circular heat drive actuators were found to have design deficiencies which prevented proper actuation and resulted in burn-out of the device. Modifications to the original design of a circular heat drive actuator have been made on the MUMPS 10 run to correct for the identified deficiencies.

6.2. Recommendations

6.2.1. Continued Thermal Testing

The acquisition of an optical dewar package from MMR was made during this research effort. This device should completely eliminate the presence of moisture from vacuum leaks since there is only four seals versus the fifteen on the LTMP. Furthermore, the dewar is considerably smaller than the LTMP since no probes are provided in the chamber. The refrigerator utilized in this dewar requires that the devices for testing be bonded out and electrical measurements made using the K-20 ribbon connector electrical interface. This dewar also has the advantage of a shorter distance between the optical windows and the device to be tested which should allow for a better interface with the microscope-based laser probe interferometer.

6.2.1.1. Material Parameter Measurements

It was found that the determination of material parameters was very sensitive to the device selected. In the case of the square FBMD, the flexure requires a complex equation in order to back out the modulus of elasticity as a function of temperature. In order to simplify this equation by eliminating the torsional term, an array of simple resonators has been developed for MUMPS 10 (see Fig. 6-1). Design variations for this device include three different widths for the flexure, three different lengths for the flexure and three different areas for the mass. Since the flexure is a straight member with no

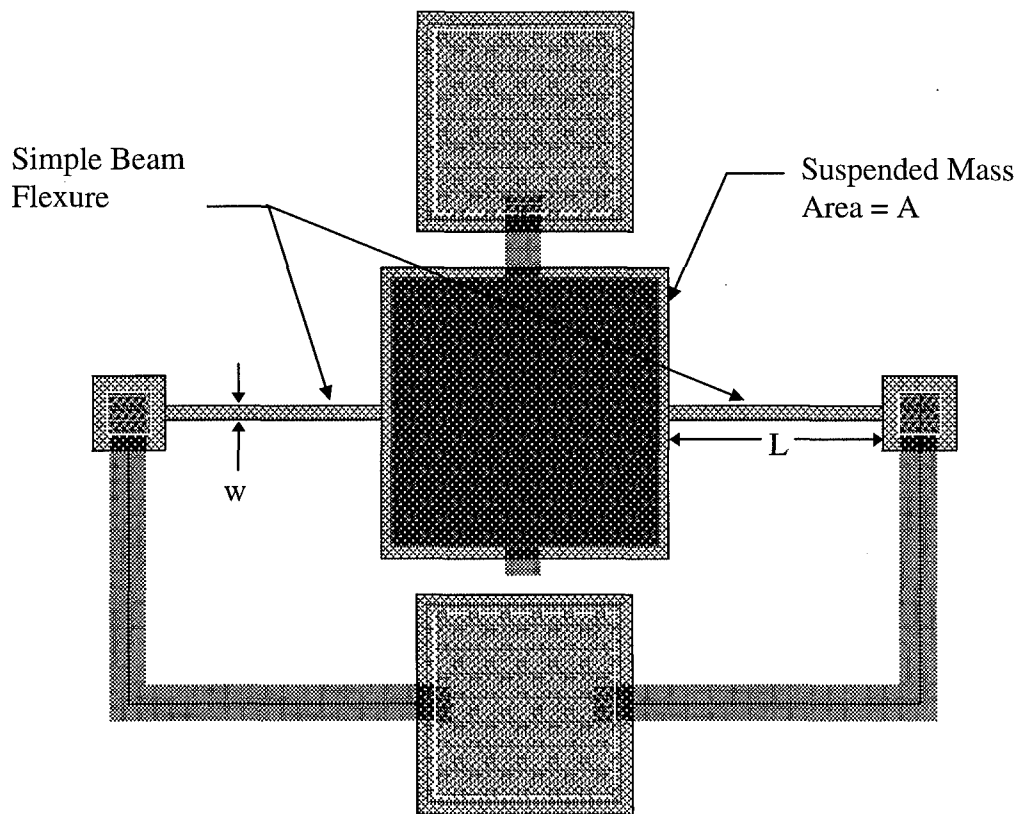


Figure 6-1. Cadence layout of simple resonator from array designed for fabrication on MUMPS 10. $L = 40, 50, 60 \mu\text{m}$; $w = 2, 4, 6 \mu\text{m}$; and $A = 3600, 6400, 10000 \mu\text{m}^2$.

bends, the only spring constants that must be considered are the lateral deflection and stress terms.

To more accurately calculate the resistivity of the MUMPS layers as a function of temperature, an array of Transfer Length Resistors (TLR) has been designed for MUMPS 10 (see Fig. 6-2). The TLR allows the resistivity to be calculated by knowing the current through the device and the resulting voltage drop across the resistor section. This is one of the techniques used by MCNC to calculate the resistivity and should yield comparable results at ambient temperature ($T=290$ K).

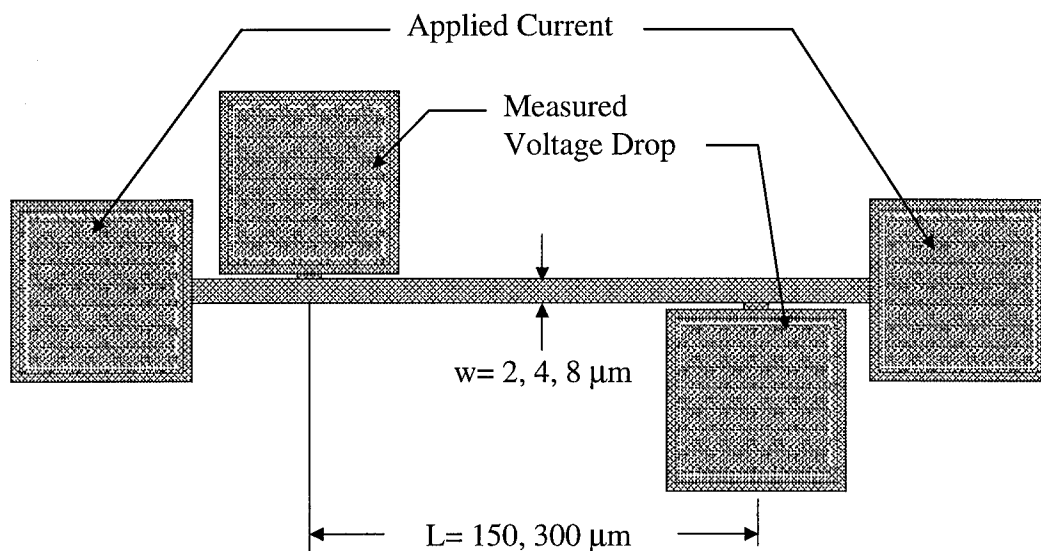


Figure 6-2. Cadence layout of a transfer length resistor from MUMPS 10. All variations are included for each of the polysilicon layers.

6.2.2. Variable Grating Testing

The design of the variable diffraction grating continues to be improved. The next generation, designed for fabrication on MUMPS 10, increases the active area in order to prevent overflow during testing (see Fig. 6-3). As mentioned in Chapter 5, the overflow was

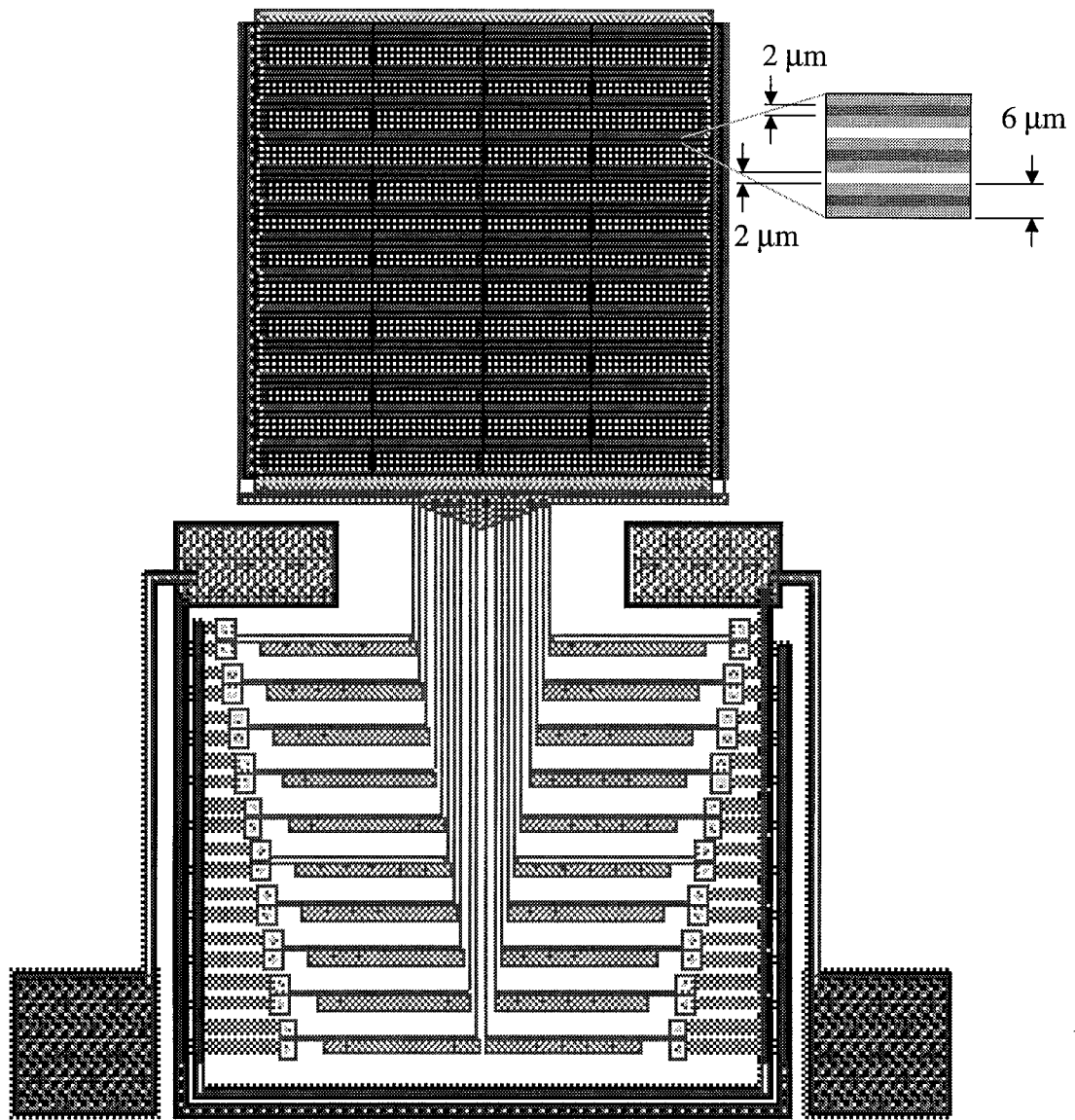


Figure 6-3. Cadence layout of large, 500x500 μm, variable diffraction grating designed for fabrication on MUMPS 10. Period dimensions are indicated in the blow-up of the grating.

initially required in order to keep the size of the device small to ensure successful actuation. The device designed for MUMPS 10 has an active area of 0.5 mm by 0.5 mm square and incorporates a gang of heat drive actuators. Each actuator is individually attached to a load bar which transfers the force to the grating plate. The individual attachments for the heat drive actuators can be broken with a probe to determine the number of actuators required to move the grating.

The diffraction grating model was built under the assumption that the wavelengths of light to be used during operation were either reflected or absorbed at the surfaces of the grating. It was found through this research that for the thin films the absorption is negligible and therefore transmission of light at wavelengths below 1.1 μm need to be included. The diffraction model needs to be improved to account for the transmission through the layers which results in multiple reflections. This can be done by performing a thin film analysis on each section of the grating which accounts for the total phase and reflected intensity for each interface of that section. For example, reflection from the Poly O surface needs to include the phase change and reflected intensity from the Si_3N_4 top and bottom surfaces.

6.2.3. *Fiber Optic Coupler Testing*

None of the fiber optic couplers were tested during this thesis research. The devices need to be evaluated for ability to lock and hold the optical fibers without breaking. Based on testing results, the shuttle mechanism works to drive the single fiber hold plate but it is unknown if it will be able to drive the plate with a fiber connected. The operation of this portion of the device also needs to be evaluated. The larger, 250

μm diameter optical fiber locks also need to be evaluated. For both sizes of fiber locks, it appears that the sections that go up around the fiber may be too thin. Additional design variations should be fabricated to evaluate a sufficient thickness for locking structures to allow the fiber to be held, but that prevents breakage during fiber installation.

6.2.4. *Optimized Flip-up Locking Mechanism*

The current flip-up locks appear to work extremely well but were not optimized due to the fabrication problem. With the fabrication process now back on-line, variations of the flip-up lock mechanism should be designed to determine the optimum design. Of primary interest is the height on the flip-up structure to position the lock. The flip-up structure will exhibit greater stability for locks that are higher on the structure, yet may not flip-up due to the increased force imparted on the elevating plate by the lock mechanism.

6.2.5. *Rotating Flip-up Structures*

These devices require significant design improvements. The incorporation of a ratcheting mechanism needs to include the latest design of heat drive actuators. Furthermore, larger ($\sim 10 \mu\text{m}$ in diameter) pivot anchors need to be used to prevent the structures from separating from the substrate. Design variations of the pyramid *fliphelper* need to be made that can be separated from the flip-up plate after elevation. This will allow the structure to be rotated after elevation by disconnecting the *fliphelper*.

APPENDIX A

Matlab Diffraction Grating M-files

This Matlab m-file is used to interactively determine the diffraction pattern for a grating designed using MUMPS. All process and design dependent variables are adjustable variables of the program with the exception of the layer widths (i.e. Poly 1 and Poly 2). Output includes a graphical representation of the pattern and the first three diffracted order angles (if all are real).

```

% this m-file Matlab Program creates an N length vector that
% represents the grating in 1-D.
%%%%%%%%%%%%%%%%%%%%%%%%%%%%%%%%%%%%%%%%%%%%%%%%%%%%%%%%%%%%%%%%%%%%%%%%
% variable declarations & initialization

clear;
nper=input('How many periods do you want to evaluate for?');
wave=input('What is the wavelength of interest (in nanometers)?');
stang1=input('What is the incidence angle of the light (in degrees)?');
fang0=floor(stang1);
sang0=floor(100*(stang1-fang0));
width0=input('What is the width of the poly0 layer (in microns)?');
fwid0=floor(width0);
swid0=floor(100*(width0-fwid0));
width1=input('What is the width of the poly1 layer (in microns)?');
fwid1=floor(width1);
swid1=floor(100*(width1-fwid1));
thicks1=input('what is the gap between poly0 and poly1 (in microns)?');
fthic1=floor(thicks1);
sthic1=floor(100*(thicks1-fthic1));
quest1=input('Is poly2 a part of the grating (y/n) ?','s');
if quest1=='y'
    width2=input('What is the width of the poly2 layer (in microns)?');
    thicks2=0.5;
    initpos2=input('What is the starting position for poly2 layer (in microns)?');
else
    width2=0;
    thicks2=0;
end;
fwid2=floor(width2);
swid2=floor(100*(width2-fwid2));
thickp1=2.0;
thickp2=1.5;
i=sqrt(-1);
lambda=wave/1000;    % lambda is the wavelength in microns
frac=1000;

%%%%%%%%%%%%%%%%%%%%%%%%%%%%%%%%%%%%%%%%%%%%%%%%%%%%%%%%%%%%%%%%%%%%%%%%
% each pixel(vector element) equals 1/frac th of a micron
% this procedure sets-up a single period, accounting for reflection
% from poly0, poly1, & poly2

perwidth=(width0+width1)*frac;
perid=ones(1,perwidth);
for x=1:(width0*frac),
    perid(x)=exp(i*(2*pi)*0);
end;
for x=(width0*frac)+1:((width0+width1)*frac),
    perid(x)=exp(i*(2*pi)*(2*(thicks1+thickp1)/lambda));
end;

```

```

if width2>0
    for x=((initposp2)*frac)+1:((initposp2+width2)*frac),
        perid(x)=exp(i*(2*pi)*(2*(thicks1+thickp1+thicks2+thickp2)/lambda));
    end;
end;

%%%%%%%%%%%%%%%%%%%%%%%%%%%%%%%%%%%%%%%%%%%%%%%%%%%%%%%%%%%%%%%%%%%%%%%%
% determine size for the vector. Make size a power of two (ie 2^N, where
% N is an integer). Size will be next power greater than nper*perwidth

minlngth=nper*perwidth;
pow=nextpow2(minlngth);
veclngth=2^pow;
spaces=(veclngth-minlngth)/2;

%%%%%%%%%%%%%%%%%%%%%%%%%%%%%%%%%%%%%%%%%%%%%%%%%%%%%%%%%%%%%%%%%%%%%%%%
% setup vector for normal incidence light

rawgrat=ones(1,veclngth);

numpix=length(rawgrat);
center=numpix/2+1;

for period=1:nper,
    rawgrat(spaces+1+(period-1)*perwidth):spaces+(period*perwidth)=perid;
end;

%%%%%%%%%%%%%%%%%%%%%%%%%%%%%%%%%%%%%%%%%%%%%%%%%%%%%%%%%%%%%%%%%%%%%%%%
% adjust raw vector for off angle light

gratmain=ones(1,numpix);
if stang1>0
    for x=1:center-1,
        gratmain(center-1+x)=rawgrat(center-1+x)*exp(i*2*pi*(sin(stang1*(pi/180))/lambda)*((x-1)/frac));
        gratmain(center-x)=rawgrat(center-x)*exp(i*2*pi*(sin(stang1*(pi/180))/lambda)*((-x)/frac));
    end;
else
    gratmain=rawgrat;      % if angle = 0 Degrees
end;

%%%%%%%%%%%%%%%%%%%%%%%%%%%%%%%%%%%%%%%%%%%%%%%%%%%%%%%%%%%%%%%%%%%%%%%%
% find the spectrum/diffraction pattern by taking the Fourier
% transform of gratmain

spect1=fftshift(fft(fftshift(gratmain)));

%%%%%%%%%%%%%%%%%%%%%%%%%%%%%%%%%%%%%%%%%%%%%%%%%%%%%%%%%%%%%%%%%%%%%%%%
% if off angle input light, find the shift in the DC value & set M value
% to 0 instead of 1

shiftv=find(spect1==max(spect1));
DCshift=shiftv-center
mval=1;
DCstep=0;
if DCshift>0

```

```

mval=0;
maxima(1)=DCshift+center;
DCstep=1;
end;

%% %% %% %% %% %% %% %% %% %% %% %% %% %% %% %% %% %% %% %% %% %% %% %% %% %% %% %% %%
% find the first 3 maximum in the spectra beyond the DC value

if nper>5

% METHOD 1 - No need to set magnitude req.
maxcount=0+DCstep;
scanspec=spect1(center+DCshift:numpix);
scanspec(1:6)=zeros(1,6);
for x=1:3,
    biggest=max(abs(scanspec));
    [loc]=find(abs(scanspec)==biggest);
    maxcount=maxcount+1;
    maxima(x+DCstep)=center-1+loc+DCshift;
    scanspec(loc-2:loc+2)=zeros(1,5);
end;

else

% METHOD 2 - No need to zero out part of the data
mincount=0;
maxcount=0;
x=1;
while x<center-10,
    while abs(spect1(center-1+x))>abs(spect1(center+x)),
        x=x+1;
    end;
    mincount=mincount+1;
    % minima(mincount)=center-1+x;
    while abs(spect1(center-1+x))<abs(spect1(center+x)),
        x=x+1;
    end;
    % screen out the noise with filter %
    if abs(spect1(center-1+x))>0.2*(abs(spect1(center)))
        maxcount=maxcount+1;
        maxima(maxcount)=center-1+x;
    end;
    x=x+1;
end;
end;

%% %% %% %% %% %% %% %% %% %% %% %% %% %% %% %% %% %% %% %% %% %% %% %% %% %% %% %% %%
% find the corresponding angles(in degrees) for the maxima

for x=1:maxcount,
    lightang(x)=(180/pi)*asin(wave*(maxima(x)-center)*(frac/1000)/veclngth);
end;
lightang(1:maxcount)          % print angles to screen

ang1=lightang(1);

```

```

frst2a1=floor(ang1);
ang2=(ang1-frst2a1)*1000;
secn2a1=floor(ang2);

if maxcount>1
  ang1=lightang(2);
  frst2a2=floor(ang1);
  ang2=(ang1-frst2a2)*1000;
  secn2a2=floor(ang2);
end;

if maxcount>2
  ang1=lightang(3);
  frst2a3=floor(ang1);
  ang2=(ang1-frst2a3)*1000;
  secn2a3=floor(ang2);
end;

%%%%%%%%%%%%%%%%%%%%%%%%%%%%%%%%%%%%%%%%%%%%%%%%%%%%%%%%%%%%%%%%%%%%%%%%
% plot the output

pnum=input('what figure number do you want to plot?');
figure(pnum);
stplot=(center-(maxima(3)-center)-10);
enplot=(center+(maxima(3+DCstep)-center)+10);
numplot=enplot-stplot;
for x=1:numplot+1,
  xax(x)=stplot-center-1+x;
end;
plot(xax,abs(spect1(stplot:enplot))/abs(spect1(center+DCshift)));
tlabel(['Normalized Output Spectrum']);
title(tlabel);
px1=xax(1)+2;
px2=2;
text(px1,0.95,['Wavelength= ',int2str(wave),' nm']);
text(px1,0.90,['Number of Periods= ',int2str(nper)]);
text(px1,0.85,['Incident Angle= ',int2str(fang0),' ',int2str(sang0),' deg']);
text(px1,0.80,['Angles= ']);
text(px1,0.75,['m= ',int2str(mval),' ',int2str(frst2a1),' ',int2str(secn2a1),' deg']);
if maxcount>1
  text(px1,0.70,['m= ',int2str(mval+1),' ',int2str(frst2a2),' ',int2str(secn2a2),' deg']);
end;
if maxcount>2
  text(px1,0.65,['m= ',int2str(mval+2),' ',int2str(frst2a3),' ',int2str(secn2a3),' deg']);
end;
text(px2,0.95,['width0= ',int2str(fwid0),' ',int2str(swid0),' microns']);
text(px2,0.90,['space 1-2= ',int2str(fthic1),' ',int2str(sthic1),' microns']);
text(px2,0.85,['width1= ',int2str(fwid1),' ',int2str(swid1),' microns']);
text(px2,0.80,['width2= ',int2str(fwid2),' ',int2str(swid2),' microns']);
axis([xax(1) xax(numplot+1) 0 1]);

%%%%%%%%%%%%%%%%%%%%%%%%%%%%%%%%%%%%%%%%%%%%%%%%%%%%%%%%%%%%%%%%%%%%%%%%
% save the figure to a postscript file

width0

```

```

width1
width2
filerec=input('what is storage value for this run ?');
pfilename=['gpsfiles/gt',int2str(nper),'_',int2str(wave),'_',int2str(filerec)];
eval(['print ' pfilename]);

```

The following Matlab m-file is a representative procedure which calls the m-file function gratfunc1 repetitively to generate a table of data for export to a spreadsheet. This and similar procedures were used to analyze the operation of designed gratings as a function of different variables.

```

%%%%%%%%%%%%%%%%%%%%%%%%%%%%%%%%%%%%%%%%%%%%%%%%%%%%%%%%%%
% this m-file runs the function gratfunc1.m by varying the position of poly 2
% grating over the poly 1 grating
% will find the angle of the first 3 orders

%%%%%%%%%%%%%%%%%%%%%%%%%%%%%%%%%%%%%%%%%%%%%%%%%%%%%%%%%%
% Initialize
clear;
nper=10;
wave=input('What wavelength do you want to run program for ?');
stang1=0;
width0=2;
width1=input('What is the width of the poly 1 runners ?');
thicks1=2;
width2=2;
thicks2=0;
initposp2=0;
rangemp2=width0+width1-2;

varmovp2=zeros(10,7);
for x=1:10
    initposp2=rangemp2*(x/10);
    filerec=['77',int2str(x)];           % file storage code will be 77 + number of the run
    [lightang,htm]=gratfunc1(nper,wave,stang1,width0,width1,thicks1,width2,thicks2,initposp2,filerec);
    varthick(x,1)=x;
    for step=1:3,
        varthick(x,2*step)=lightang(step);
        varthick(x,1+2*step)=htm(step);
    end;
end;
varthick

```

The following Matlab m-file is a representative function called by the procedure shown above. This function is similar to the gratings.m m-file shown above with the exception that all variable are supplied by the procedure.

```

% this m-file Matlab Program creates a n length vector that
% represents the grating in 1-D.           3:41PM 7/26/95

%%%%%%%%%%%%%%%%%%%%%%%%%%%%%%%%%%%%%%%%%%%%%%%%%%%%%%%%%%
% initiate function

function

```

```
[spect1,center]=gratfunspec(nper,wave,stang1,width0,width1,thicks1,width2,thicks2,initposp2,filerec);
```

```
%%%%%%%%%%  
% variable declarations & initialization
```

```
fang0=floor(stang1);  
sang0=floor(100*(stang1-fang0));  
fwid0=floor(width0);  
swid0=floor(100*(width0-fwid0));  
fwid1=floor(width1);  
swid1=floor(100*(width1-fwid1));  
fthic1=floor(thicks1);  
sthic1=floor(100*(thicks1-fthic1));  
fwid2=floor(width2);  
swid2=floor(100*(width2-fwid2));  
i=sqrt(-1);  
thickp1=2.0;  
thickp2=1.5;  
lambda=wave/1000;    % lambda is the wavelength in microns  
frac=1000;
```

```
%%%%%%%%%%  
% each pixel(vector element) equals 1/frac th of a micron  
% this procedure sets-up a single period, accounting for reflection  
% from poly0, poly1, & poly2
```

```
perwidth=(width0+width1)*frac;  
perid=ones(1,perwidth);  
for x=1:(width0*frac),  
    perid(x)=exp(i*(2*pi)*0);  
end;  
for x=(width0*frac)+1:((width0+width1)*frac),  
    perid(x)=exp(i*(2*pi)*(2*(thicks1+thickp1)/lambda));  
end;  
if width2>0  
    for x=((initposp2)*frac)+1:((initposp2+width2)*frac),  
        perid(x)=exp(i*(2*pi)*(2*(thicks1+thickp1+thicks2+thickp2)/lambda));  
    end;  
end;
```

```
%%%%%%%%%%  
% determine size for the vector. Make size a power of two (ie 2^N, where  
% N is an integer. Size will be next power greater than nper*perwidth
```

```
minlngth=nper*perwidth;  
pow=nextpow2(minlngth);  
veclngth=2^pow;  
spaces=(veclngth-minlngth)/2;
```

```
%%%%%%%%%%  
% setup vector for normal incidence light
```

```
rawgrat=ones(1,veclngth);
```

```
numpix=length(rawgrat);
```

```

center=numpix/2+1;

for period=1:nper,
    rawgrat(spaces+1+((period-1)*perwidth):spaces+(period*perwidth))=perid;
end;

%%%%%%%%%%%%%%%%%%%%%%%%%%%%%%%%%%%%%%%%%%%%%%%%%%%%%%%%%%%%%%%%%%%%%%%%
% adjust raw vector for off angle light

gratmain=ones(1,numpix);
if stang1>0
    for x=1:center-1
        gratmain(center-1+x)=rawgrat(center-1+x)*exp(i*2*pi*(sin(stang1*(pi/180))/lambda)*((x-1)/frac));
        gratmain(center-x)=rawgrat(center-x)*exp(i*2*pi*(sin(stang1*(pi/180))/lambda)*((-x)/frac));
    end;
else
    gratmain=rawgrat;      % if angle = 0 Degrees
end;

%%%%%%%%%%%%%%%%%%%%%%%%%%%%%%%%%%%%%%%%%%%%%%%%%%%%%%%%%%%%%%%%%%%%%%%%
% find the spectrum/diffraction pattern by taking the Fourier
% transform of gratmain

spect1=fftshift(fft(fftshift(gratmain)));

%%%%%%%%%%%%%%%%%%%%%%%%%%%%%%%%%%%%%%%%%%%%%%%%%%%%%%%%%%%%%%%%%%%%%%%%

```

APPENDIX B

MUMPS Die Layouts from Cadence

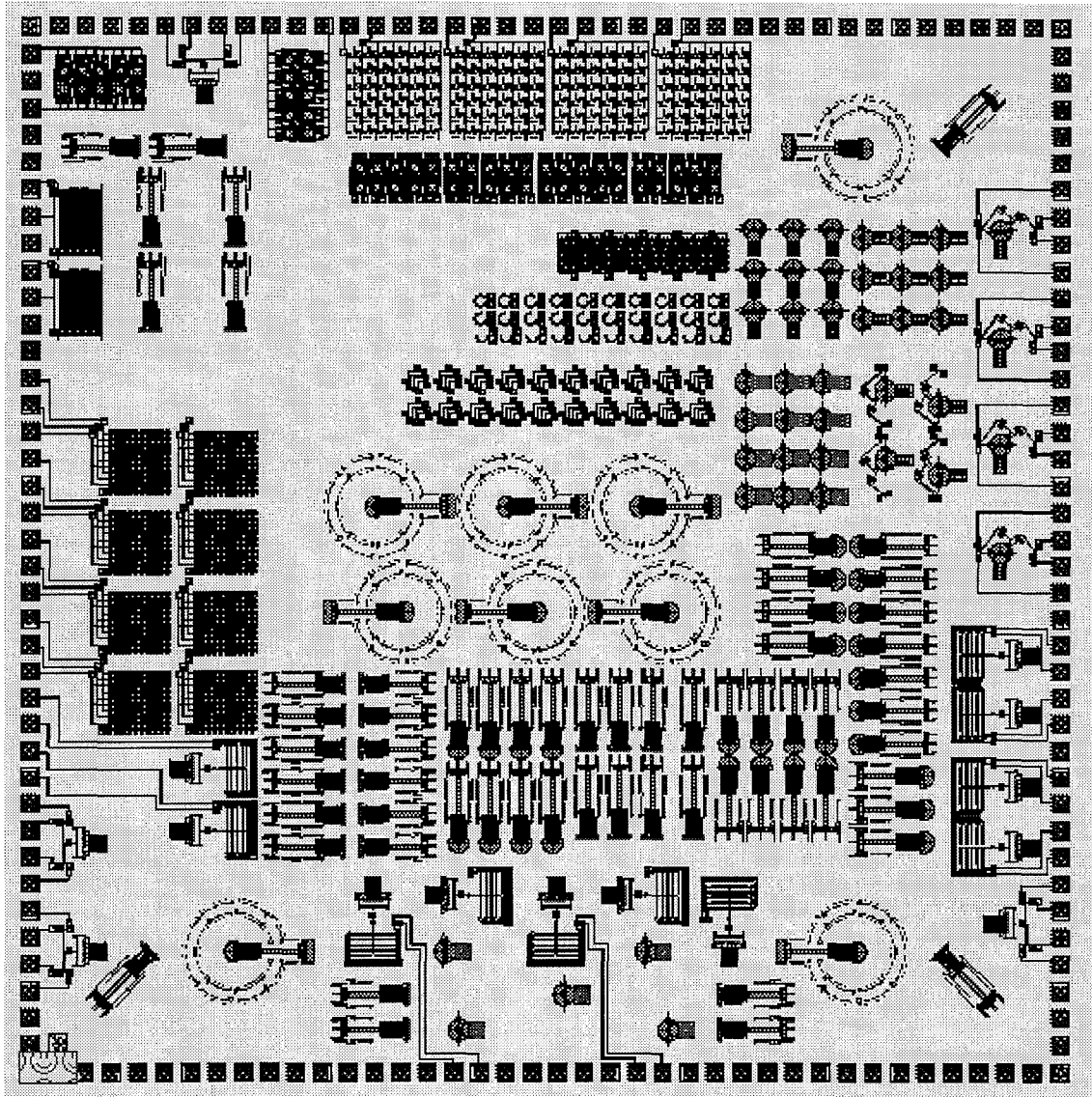


Figure 1. MUMPS 7 Chip Layout. Contains initial flip-up device designs including: mirrors, gratings and Fresnel lenses. Surface structures include fringe test mirrors, circular heat actuators and gratings.

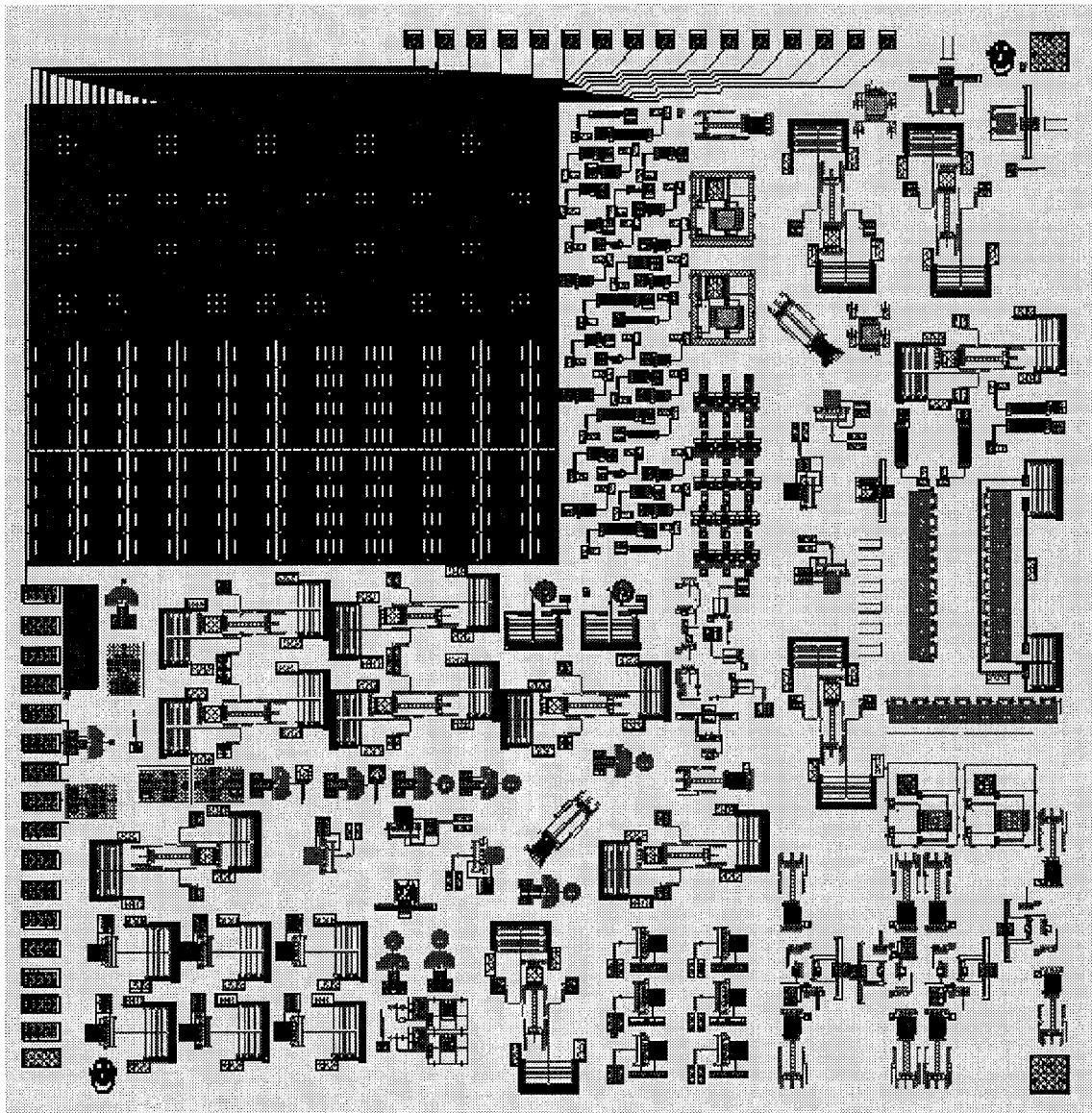


Figure 2. MUMPS 8 Chip Layout. Contains first generation of variable gratings. Also contains heat actuated flip-up structures, including Fresnel lens arrays and parallel to the plane of the substrate flip-up plates with Fresnel lenses.

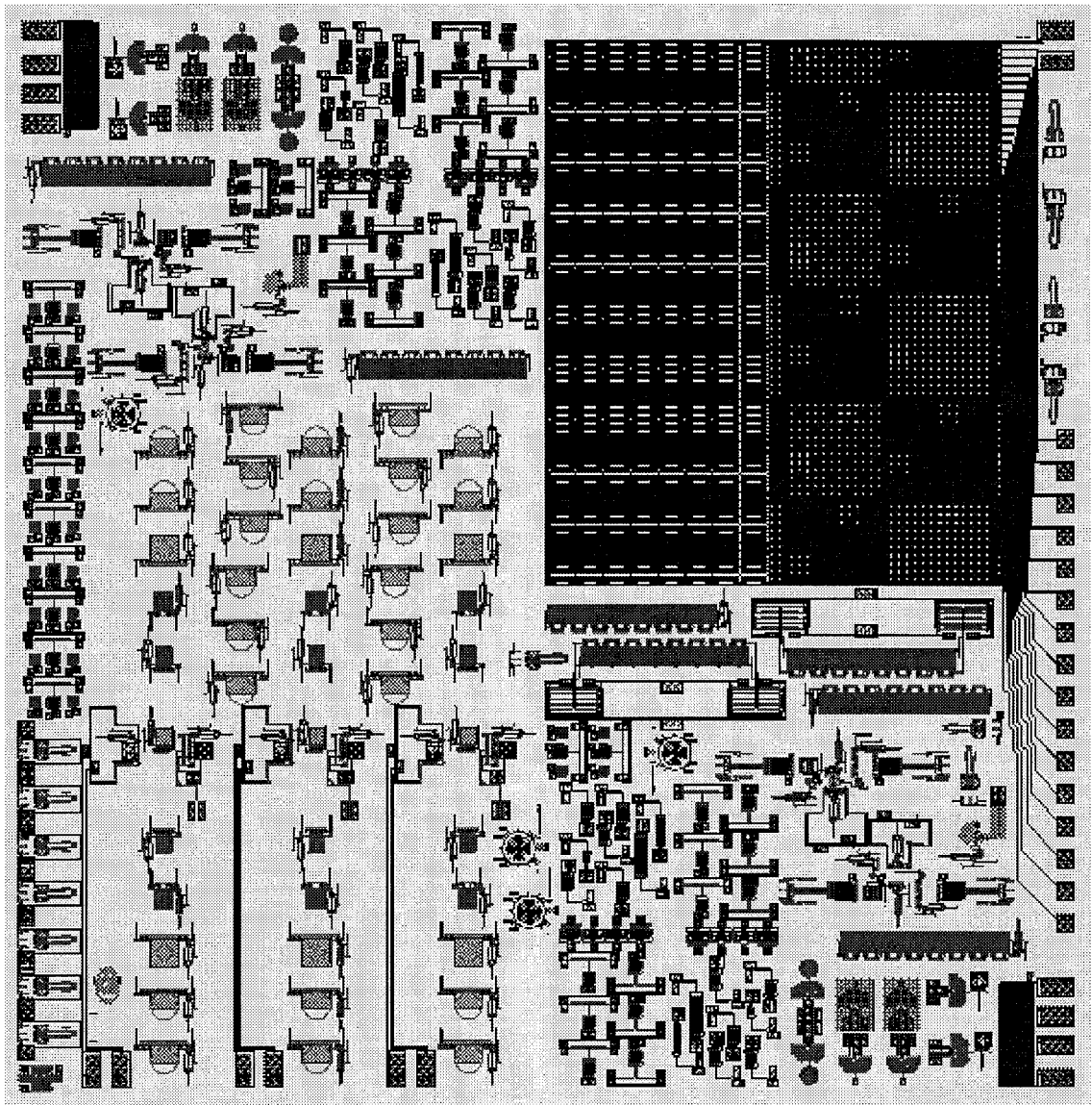


Figure 3. MUMPS 8 Redo Chip Layout for submission on MUMPS 9 run. Includes second generation variable gratings and copies of the first generation gratings. Also contains the fiber coupled version of the micro interferometer and Fresnel lens arrays.

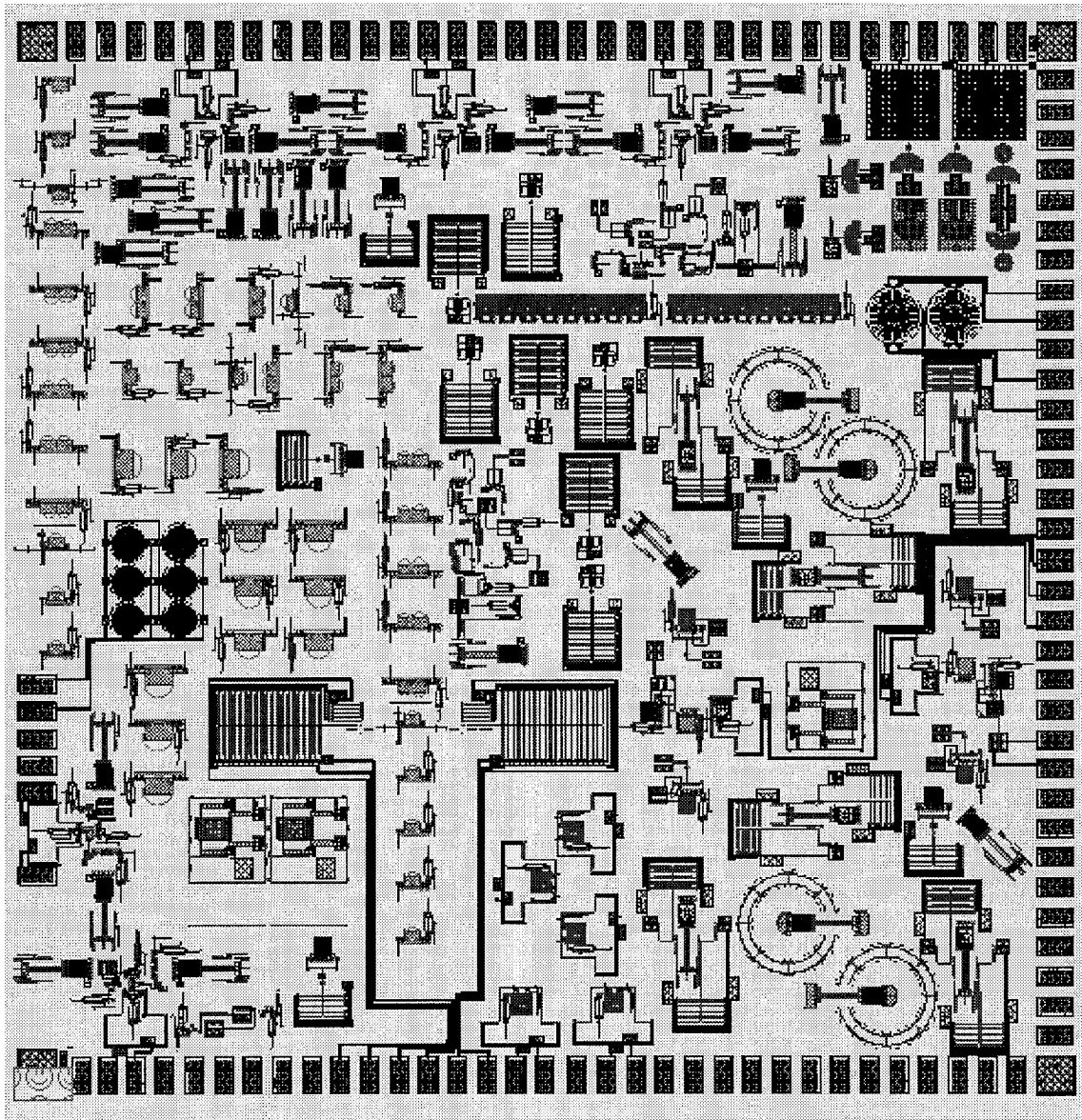
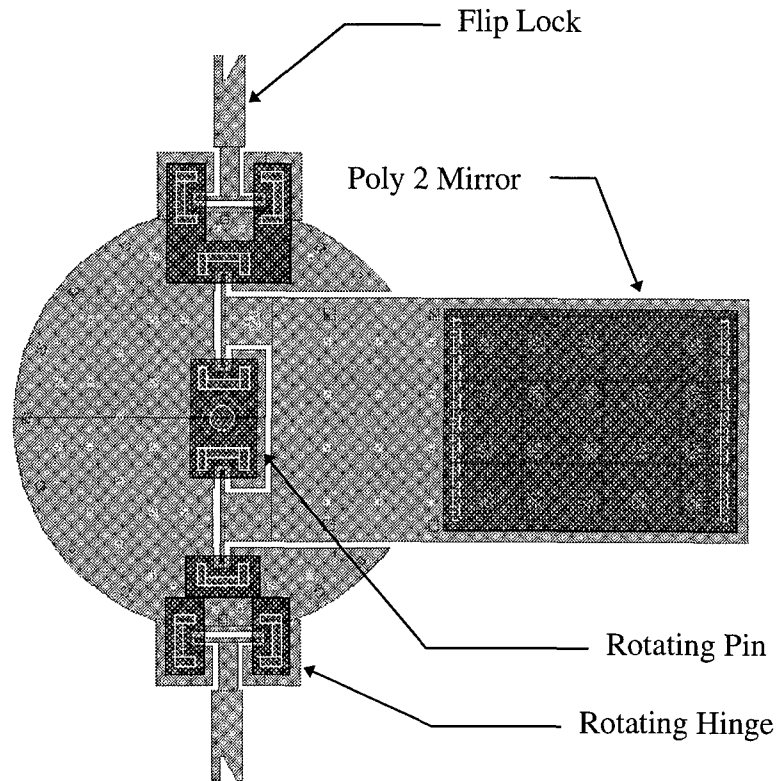


Figure 4. MUMPS 9 Chip Layout. Contains electrostatically actuated lenses, large and small interferometers and heavily actuated variable gratings.

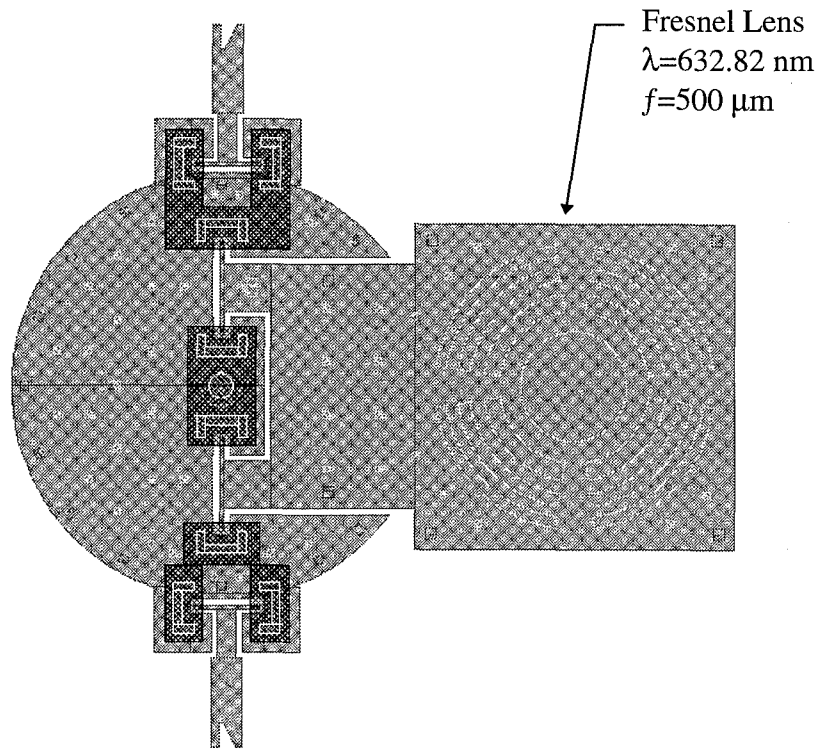
APPENDIX C

Cadence Layouts not shown in Chapter 4

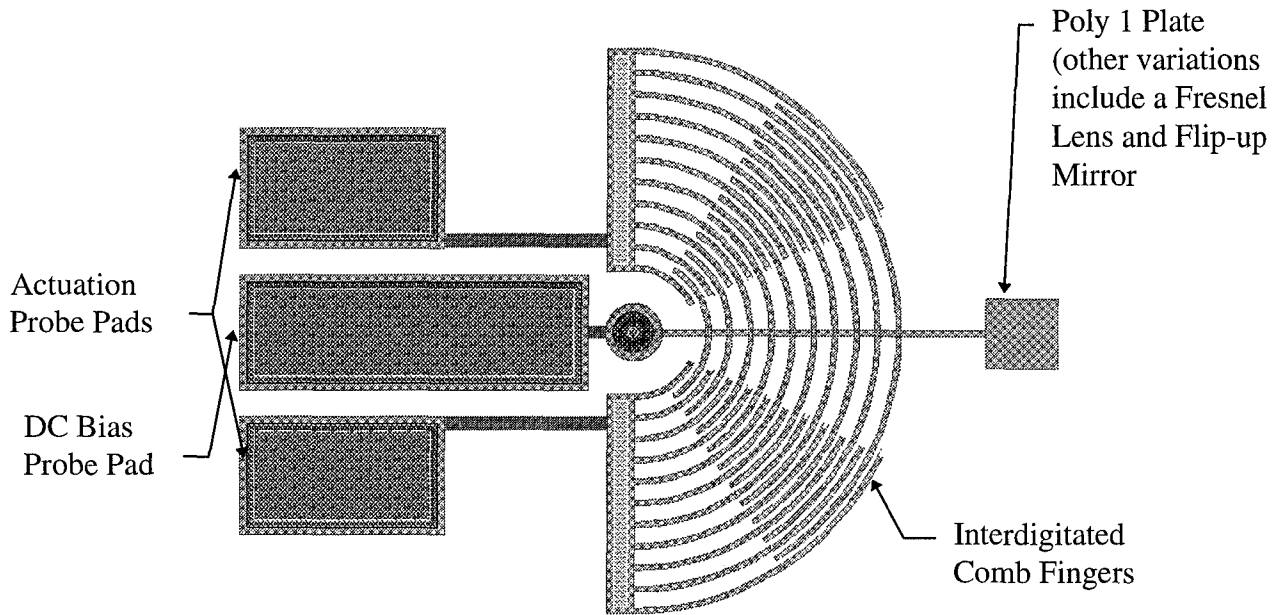
Device Name: Flip-up Rotating Mirror, ver. 3
Actuation Method: Mechanical



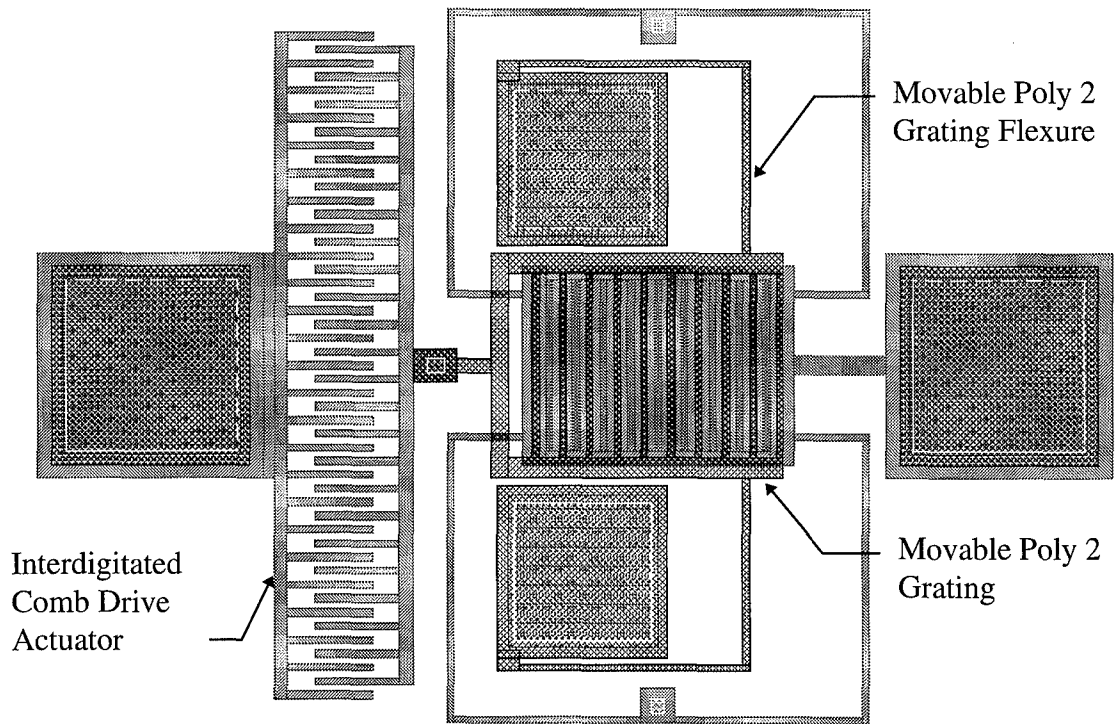
Device Name: Flip-up Rotating Fresnel Lens, ver. 1
Actuation Method: Mechanical



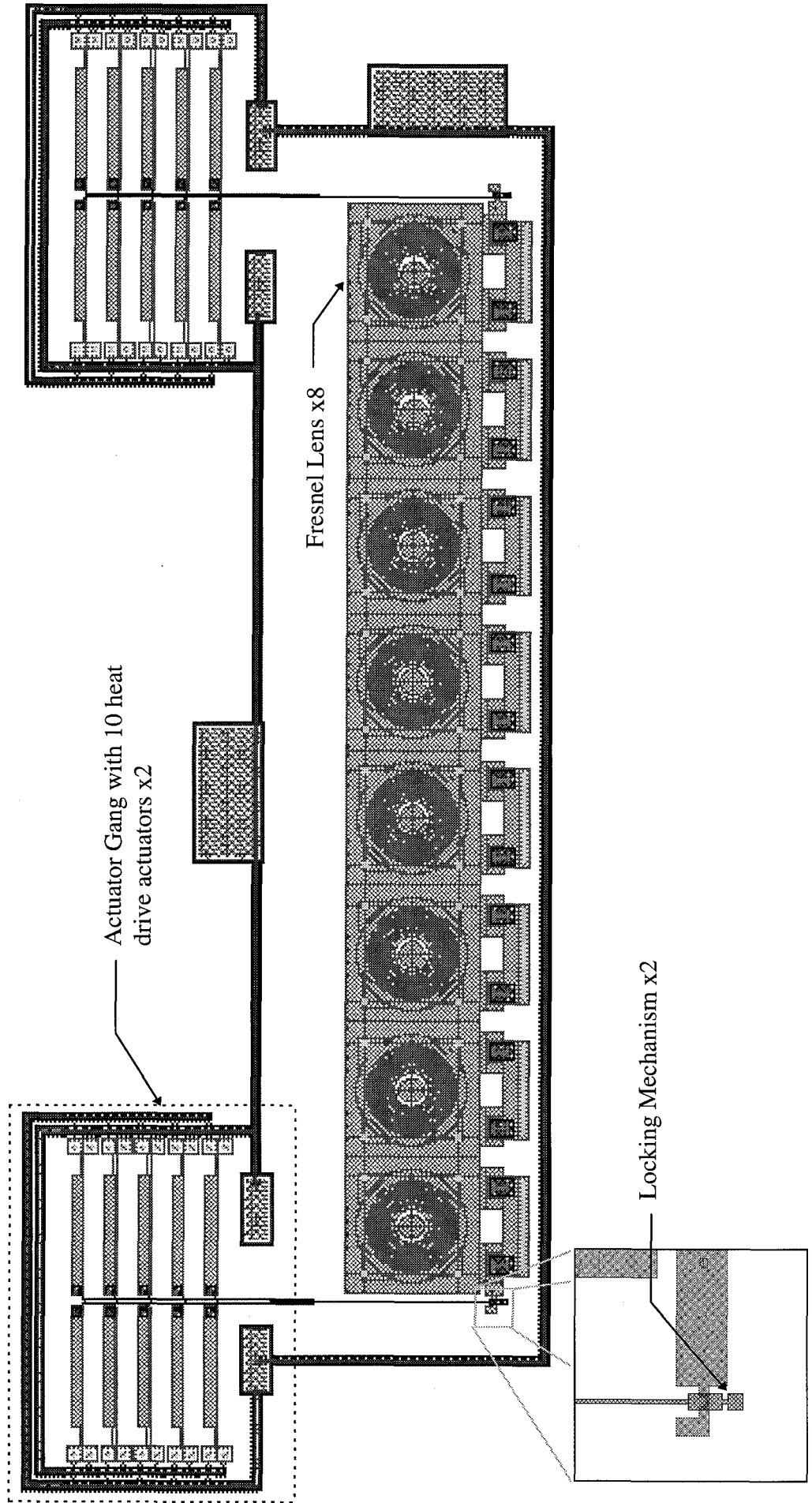
Device Name: Rotating +/- 30 Degree Poly 1 Plate
Actuation Method: Comb Drive Actuator



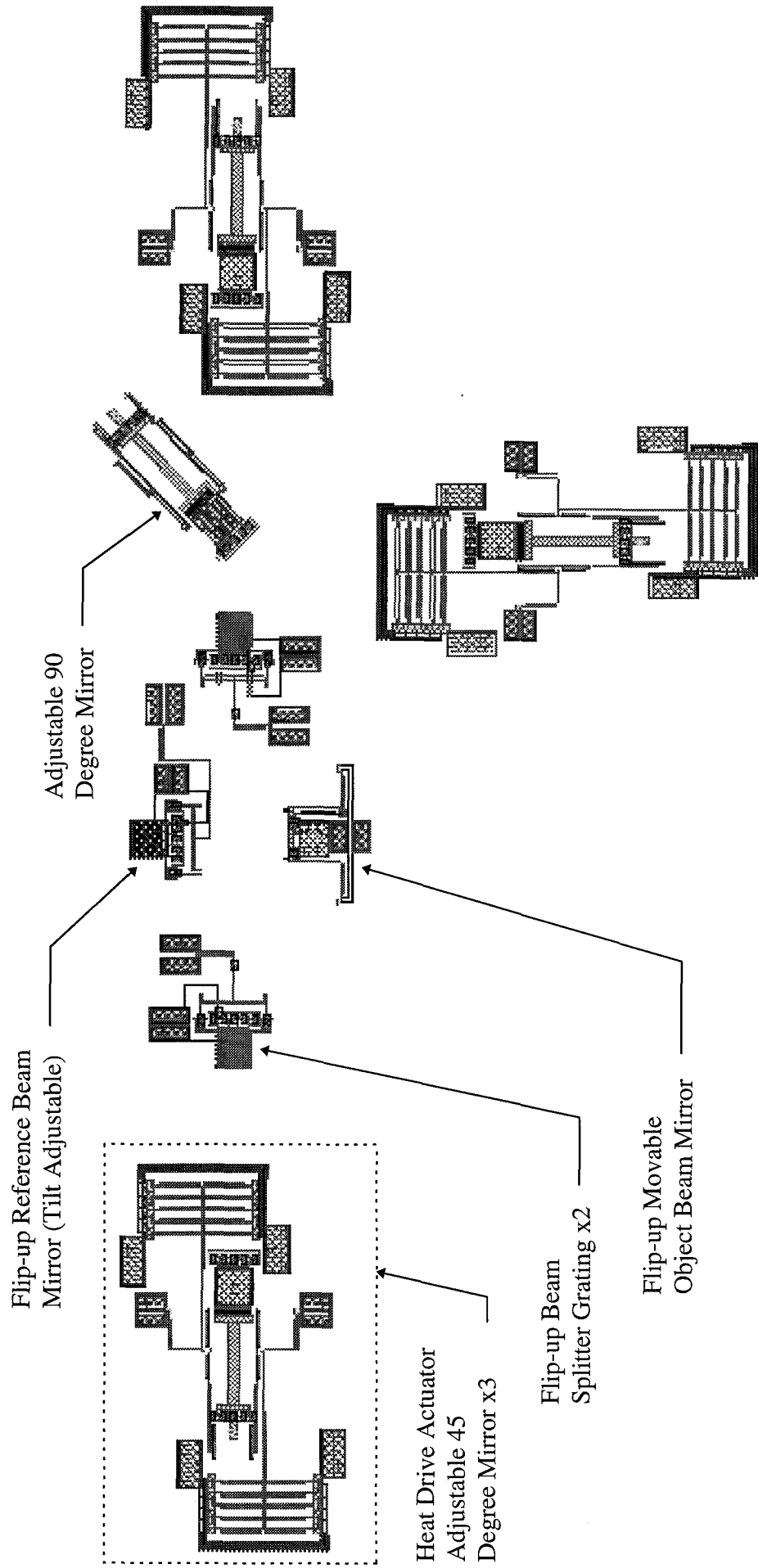
Device Name: Variable Grating, ver. 3
Actuation Method: Comb Drive Actuator



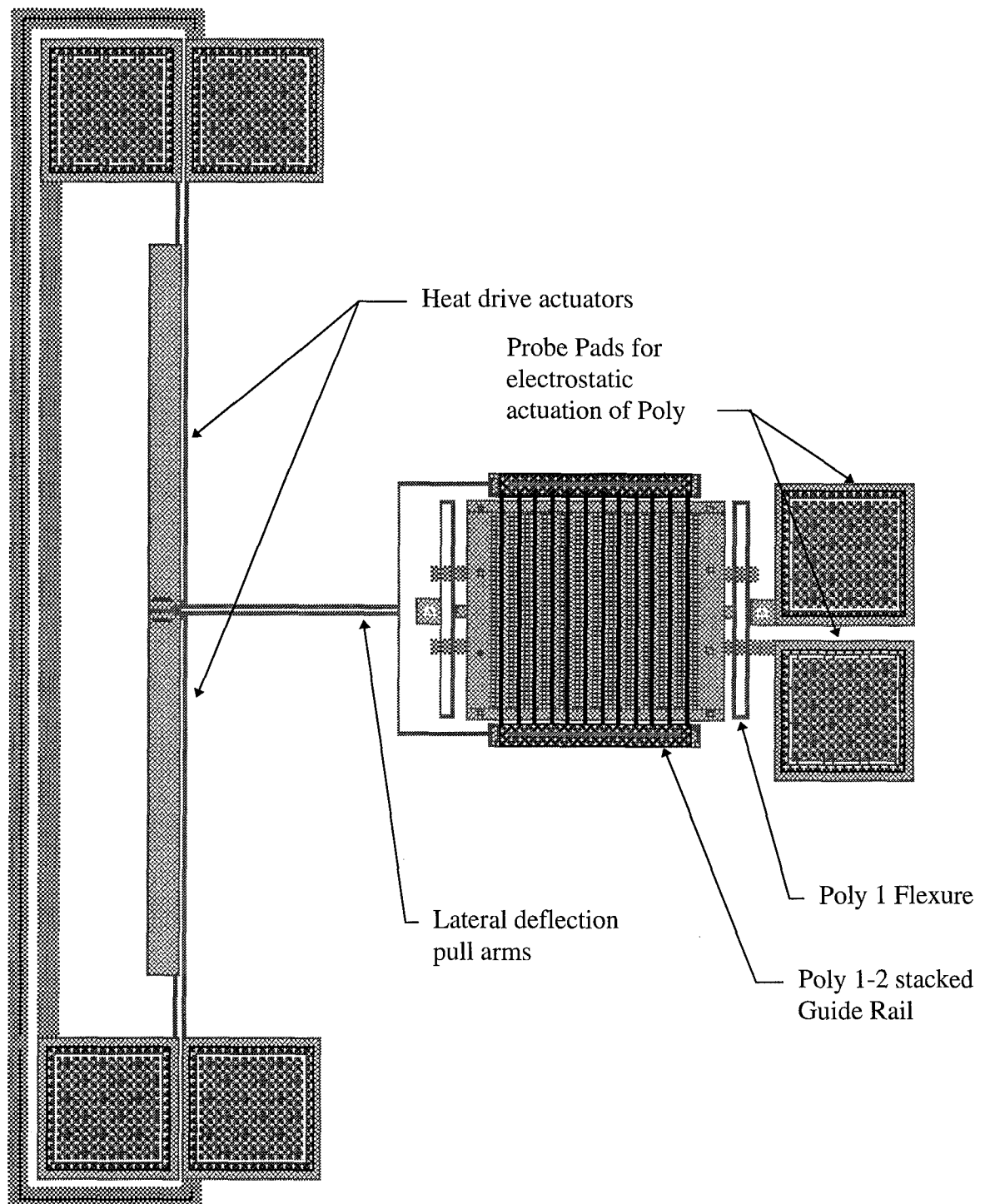
Device Name: Fresnel Lens Array with Heat Drive Actuator Angle Adjustment
Actuation Method: Heat Drive Actuator



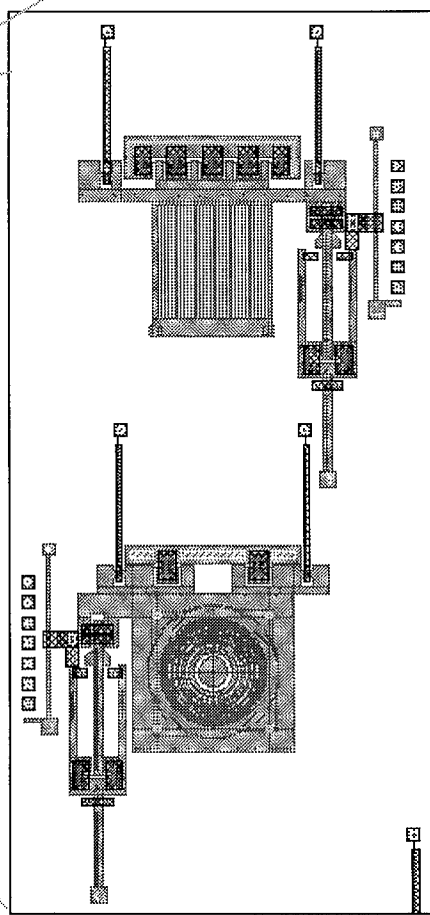
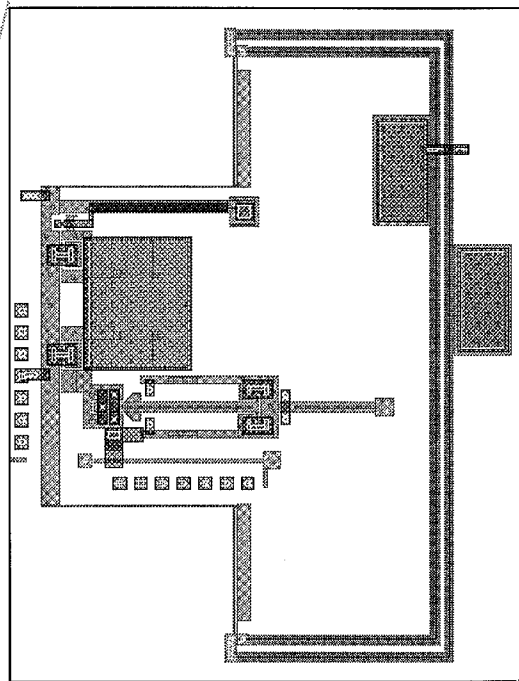
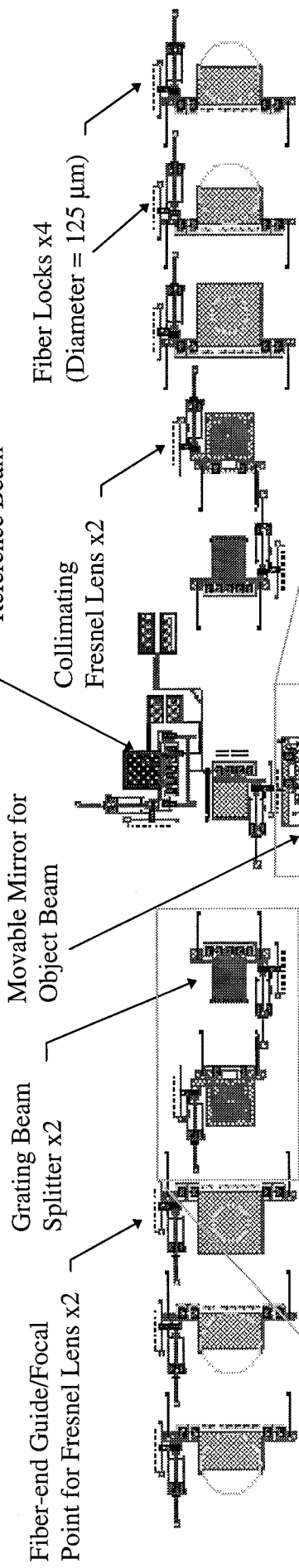
Device Name: Large Interferometer, ver. 2
Actuation Method: Heat Drive Actuator



Device Name: Variable Heat Actuator, ver. 8
Actuation Method: Heat Drive Actuator



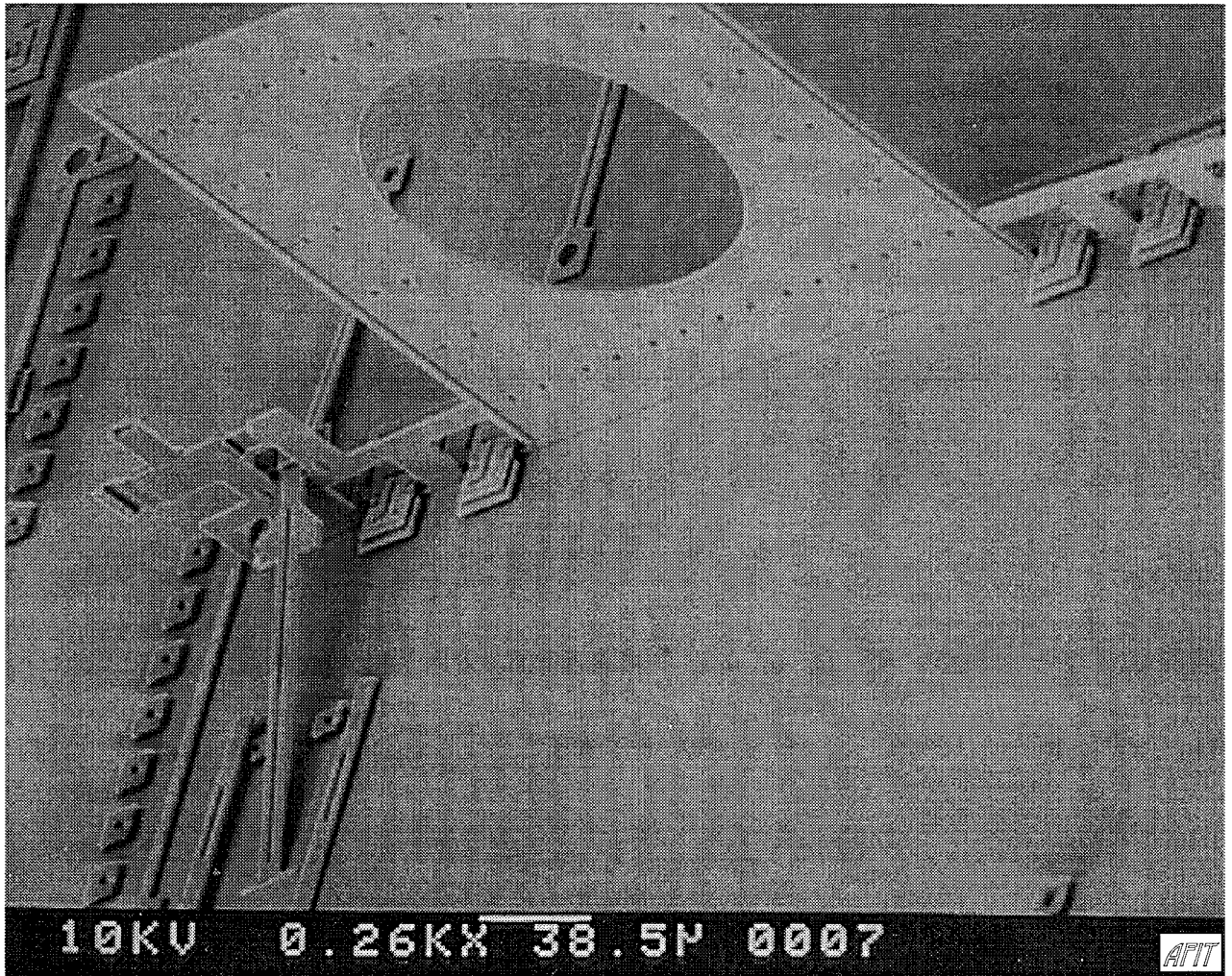
Device Name: Large Interferometer with Fiber Locks
Actuation Method: Mechanical and Heat Drive Actuator



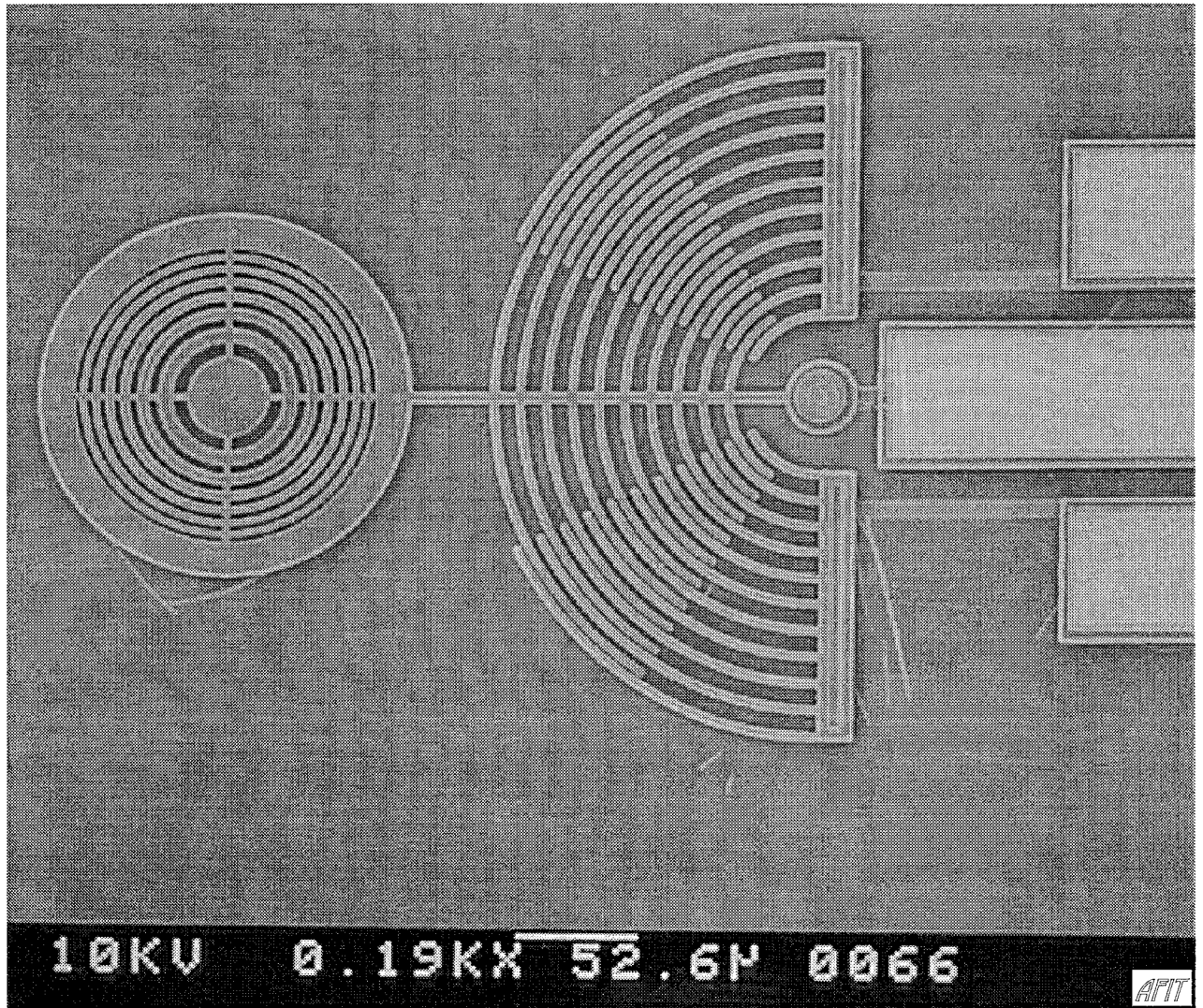
APPENDIX D

Scanning Electron Micrographs not shown in Chapters 4 or 5

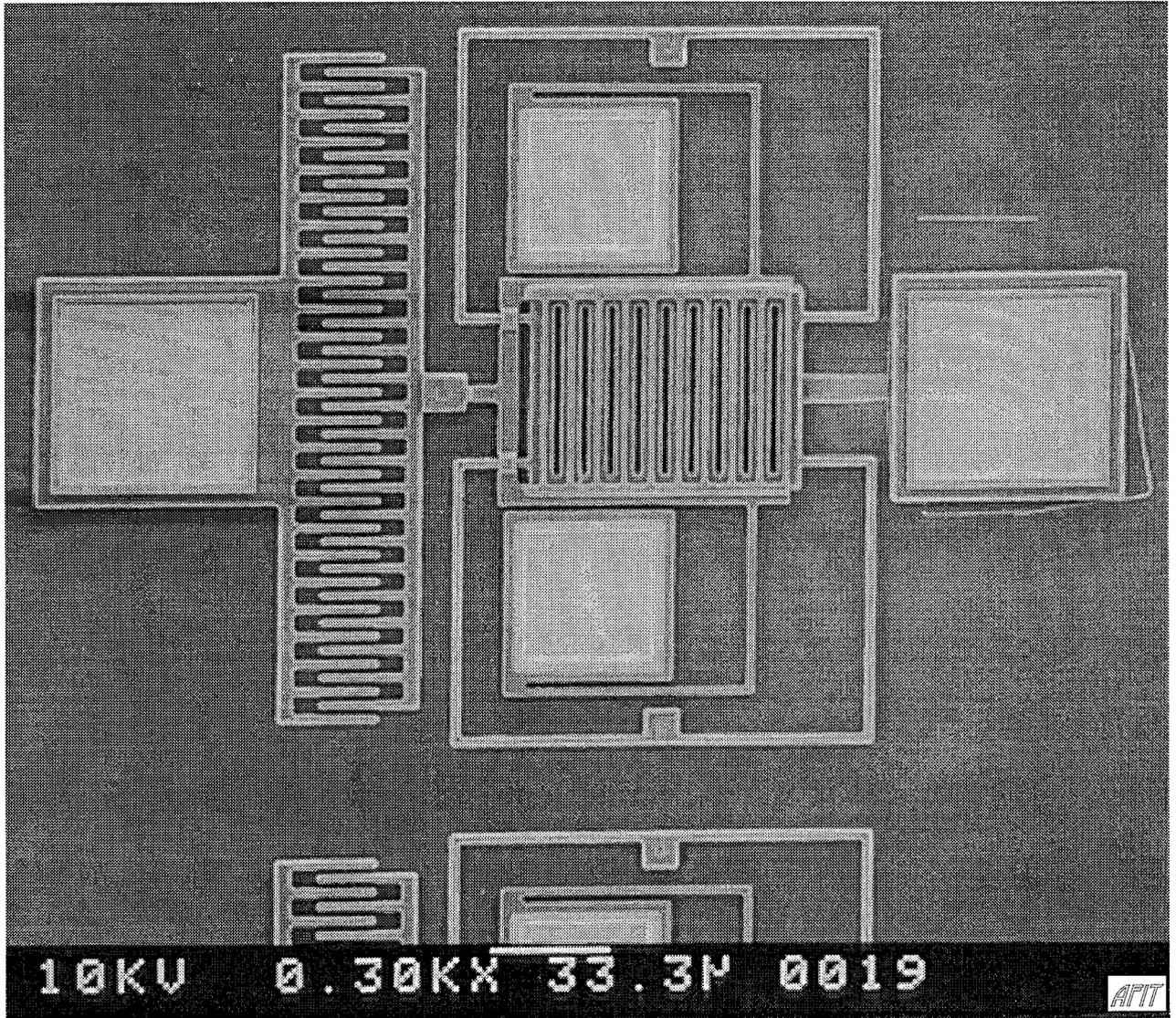
Device Name: Fiber Alignment Aperture from Large Fiber Coupled Interferometer
Actuation Method: Mechanical



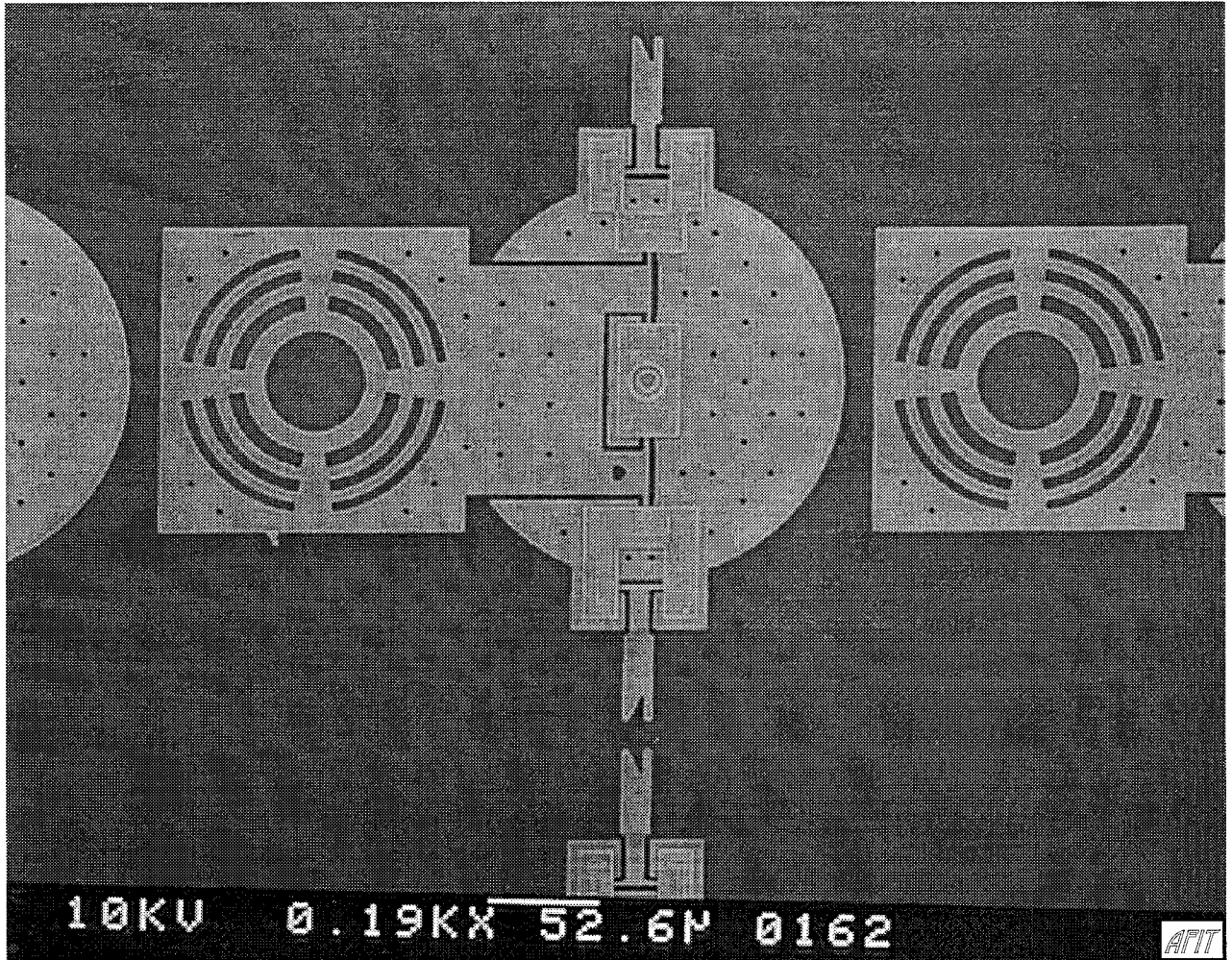
Device Name: Rotating +/- 30 Degree Poly 1 Fresnel Lens
Actuation Method: Comb Drive Actuator



Device Name: Variable Grating, ver. 3
Actuation Method: Comb Drive Actuator



Device Name: Flip-up Rotating Fresnel Lens
Actuation Method: Mechanical



Bibliography

- [1] J. T. Verdeyen, Laser Electronics, 3rd ed., Prentice-Hall, Inc., 1995.
- [2] T. A. Brunn, Optical Characterization of a Flexure Beam Micromirror Device, AFIT thesis, March, 1995.
- [3] J. M. Younse, "Mirrors on a chip," *IEEE Spectrum*, pp. 27-31, November 1993.
- [4] J. Younse, "Projection display systems based on the digital micromirror deviceTM (DMDTM)," *SPIE*, Vol. 2641, pp. 64-75, October 1995.
- [5] K. E. Peterson, "Silicon as a mechanical material," *Proceedings IEEE*, Vol. 70, No. 5, pp. 420-457, May 1982.
- [6] R. Nass, "Tiny accelerometer IC reaches high sensitivity," *Electronic Design*, pp. 170-172, September 1988.
- [7] R. P. Feynman, "There's plenty of room at the bottom," *Journal of Microelectromechanical Systems*, Vol. 1, No. 1, pp. 60-66, March 1992.
- [8] R. P. Feynman, "Infinitesimal machinery," *Journal of Microelectromechanical Systems*, Vol. 2, No. 1, pp. 4-14, March 1993.
- [9] M. E. Motamedi, "Micro-opto-electro-mechanical systems," *Optical Engineering*, Vol. 33, No. 11, pp. 3505-3517, November 1994.
- [10] M. W. Phipps, Design and Development of Microswitches for Micro-Electro-Mechanical Relay Matrices, AFIT thesis, June, 1995.
- [11] J. Comtois, V. Bright, and M. Phipps, "Thermal microactuators for surface-micromachining processes," *SPIE*, Vol. 2642, pp. 10-21, October 1995.
- [12] M. C. Wu, L. Y. Lin, & S. S. Lee, "Micromachined free-space integrated optics," *SPIE*, Vol. 2291, pp. 40-51, July 1994.
- [13] Cadence Layout Editor, Ver. 9201, Cadence Design Systems, San Jose, CA.
- [14] D. A. Koester, R. Mahadevan, & K.W. Markus, Multi-User MEMS Processes (MUMPS): Introduction and Design Rules, Rev. 3, MEMS Technology Application Center, October 1994.
- [15] L.P. Boivin, "Thin-film laser-to-fiber coupler," *Applied Optics*, Vol. 13, p. 391, 1974.

- [16] E. Hecht with contributions by A. Zajac, Optics, 2nd ed., Addison-Wesley Publishing Co., Inc., 1987.
- [17] D. A. Koester, "Testing of MUMPS6 fabrication," private e-mail correspondence, 20 Feb 1995.
- [18] M. T. Ching, R. A. Brennan, and R. M. White, "Microfabricated optical chopper," *Optical Engineering*, Vol. 33, pp. 3634-3642, November 1994.
- [19] S. M. Sze, Physics of Semiconductor Devices, 2nd ed., John Wiley & Sons, Inc., 1981.
- [20] O. Madelung, editor, Data in Science & Technology: Semiconductors, Group IV elements & III-V compounds, Springer-Verlag Berlin Heidelberg, 1991.
- [21] Y. Uenishi, H. Tanaka, and H. Ukita, "AlGaAs/GaAs micromachining for monolithic integration of optical and mechanical components," *SPIE*, Vol. 2291, pp. 82-91, July 1994.
- [22] J. Bryzek, K. Peterson, & W. McCulley, "Micromachines on the march," *IEEE Spectrum*, pp. 20-31, May 1994.
- [23] M. A. Michalick, Design, Fabrication, Modeling, and Testing of Surface-Micromachined Micromirror Devices, AFIT thesis, June, 1995.
- [24] L. J. Ristic editor, Sensor Technology and Devices, Chapter 4: Surface Micromachining Technology, pp. 95-155, Artech House, Inc., 1994.
- [25] R. B. Apte, F. S. A. Sandejas, W. C. Banyai, & D. M. Bloom, "Deformable grating light valves for high resolution displays," *Solid State Sensor and Actuator Workshop*, Hilton Head, South Carolina, pp. 1-6, June 1994.
- [26] K. S. Pister, M. W. Judy, S. R. Burgett, and R. S. Fearing, "Microfabricated hinges," *Sensors and Actuators*, Vol. 33, pp. 249-256, 1992.
- [27] L. S. Fan, Y. C. Tai, R. S. Muller, "Integrated movable micromechanical structures for sensors and actuators," *IEEE Trans. Electronic Devices*, Vol. 35, pp. 724-730, June 1988.
- [28] P. B. Chu, P. R. Nelson, M. L. Tachiki, and K. S. J. Pister, "Dynamics of polysilicon parallel-plate electrostatic actuators," *The 8th International Conference on Solid State Sensors and Actuators*, Vol. 2, pp. 356-359, June 1995.

- [29] S. R. Burgett, K. S. Pister, and R. S. Fearing, "Three dimensional structures made with microfabricated hinges," ASME winter annual meeting, Dynamic Systems and Control, Micromechanical Systems, Vol. 40, pp. 1-11, November 8-13, 1992.
- [30] R. Yeh, E. J. J. Kruglick, K. S. J. Pister, "Microelectromechanical components for articulated microrobots," The 8th International Conference on Solid State Sensors and Actuators, Vol. 2, pp. 346-349, June 1995.
- [31] K. Markus, D. Koester, A. Cowen, R. Mahadevan, V. Dhuler, D. Roberson and L. Smith, "MEMS infrastructure: the multi-user MEMS Processes (MUMPS)," *SPIE*, Vol. 2639, pp. 54-63, October 1995.
- [32] Richard C. Jaeger, Introduction to Microelectronic Fabrication, Modular Series on Solid State Devices, Vol. 5, (G.W. Neudeck & R.F. Pierret, eds.), Addison Wesley, 1988.
- [33] P. Van Zant, Microchip Fabrication: A Practical Guide to Semiconductor Processing, 2nd ed., McGraw-Hill Publishing Company, 1990.
- [34] J. W. Goodman, Introduction to Fourier Optics, McGraw-Hill Book Co., Inc., 1968.
- [35] J. Comtois and V. Bright, "Design techniques for surface-micromachining MEMS processes," *SPIE*, Vol. 2639, pp. 211-222, October 1995.
- [36] T. A. Rhoadarmer, V. M. Bright, B. M. Welsh, S. C. Gustafson, and T. H. Lin, "Interferometric characterization of the flexure-beam micromirror device," *SPIE*, Vol. 2291, pp. 13-23, July 1994.
- [37] T. H. Lin, "Implementation and characterization of a flexure-beam micromechanical spatial light modulator," *Optical Engineering*, Vol. 33, No. 11, pp. 3643-3648.
- [38] R. M. Boyssel, T. G. McDonald, G. A. Magel, G. C. Smith, and J. L. Leonard, "Integration of deformable mirror devices with optical fibers and waveguides," *SPIE*, Vol. 1793, pp. 34-39, September 1992.
- [39] P. Hsiang, A. Garcia-Valenzuela, M. A. Neifeld, and M. Tabib-Azar, "Micromachined 50 μ m x 250 μ m silicon torsional mirror arrays for optical signal processing," *SPIE*, Vol. 1793, pp. 190-198, September 1992.
- [40] J. Comtois, V. Bright, S. Gustafson, and M. A. Michalick, "Implementation of hexagonal micromirror arrays as phase-mostly spatial light modulators," *SPIE*, Vol. 2641, pp. 76-87, October 1995.

- [41] H. Toshiyoshi and H. Fujita, "An electrostatically operated torsion mirror for optical switching device," The 8th International Conference on Solid State Sensors and Actuators, Vol. 1, pp. 297-300, June 1995.
- [42] W. Ehrfeld, et al., "LIGA process: Sensor construction techniques via x-ray lithography," *Record of the IEEE Solid State Sensor and Actuator Workshop*, pp. 1-4, 1988.
- [43] M. E. Motamedi, A. P. Andrews, W. J. Gunning, M. Khoshnevisan, "Miniaturized micro-optical scanners," *Optical Engineering*, Vol. 33, No. 11, November 1994.
- [44] C. T. Troy, "Adjustable micromirrors aid laser fiber coupling," *Photonics Spectra*, pp. 26-28, February 1995.
- [45] L. A. Field, D. L. Burriesci, P. R. Robrish, and R. C. Ruby, "Micromachined 1x2 optical fiber switch," The 8th International Conference on Solid State Sensors and Actuators, Vol. 1, pp. 344-347, June 1995.
- [46] N. C. Tien, O. Solgaard, M-H. Kiang, M. Daneman, K. Y. Lau, and R. S. Muller, "Surface micromachined mirrors for laser-beam positioning," The 8th International Conference on Solid State Sensors and Actuators, Vol. 2, pp. 352-355, June 1995.
- [47] S. Lee, L. Lin, and M. Wu, "Realization of FDDI optical bypass switches using surface micromachining technology," *SPIE*, Vol. 2641, pp. 41-48, October 1995.
- [48] L. Lin, J. Shen, S. Lee, and M. Wu, "Micromachined three-dimensional tunable Fabry-Perot etalons," *SPIE*, Vol. 2641, pp. 20-27, October 1995.
- [49] C. Marxer, M. A. Gretillat, V. P. Jaecklin, R. Baettig, O. Anthamatten, P. Vogel, N.F. de Rooij, "MHz opto-mechanical modulator," The 8th International Conference on Solid State Sensors and Actuators, Vol. 1, pp. 289-292, June 1995.
- [50] Matlab High Performance Numeric Computation and Visualization Software, Ver. 4.0, The MathWorks, Inc., Natick, MA.
- [51] Mathcad, Ver 5.0, MathSoft, Inc., Cambridge, MA.
- [52] N. N. Rao, Elements of Engineering Electromagnetics, 2nd ed., Prentice-Hall, Inc., NJ, 1987.

- [53] C. M. Harris, Shock & Vibration Handbook, 3rd ed., McGraw-Hill Book Company, Inc., NY, 1988.
- [54] J. Gaskill, Linear Systems, Fourier Transforms and Optics, Wiley & Sons, Inc., 1978.
- [55] M. C. Hutley, Diffraction Gratings, Academic Press, NY, 1982.
- [56] N. P. Chironis, editor, Spring Design and Application, McGraw-Hill Book Company, Inc., NY, 1961.
- [57] M. R. Lindeburg, EIT Reference Manual, 7th ed., Professional Publications, Inc., CA, 1990.
- [58] N. E. Dowling, Mechanical Behavior of Materials - Engineering Methods for Deformation, Fracture, and Fatigue, Prentice Hall, NJ, 1993.
- [59] G. Feddler and K. Clark, "Modelling and simulation of microresonators with meander suspensions," Simulation and Design of Microsystems and Microstructures, pp. 175-183, Computational Mechanics Publications, Boston, MA, 1995.
- [60] Data Translation, Image-ProTM Interactive Image Processing System, Ver. 1.6, with DT2851 High resolution Frame Grabber and DT2858 Auxiliary Frame Processor, Marlborough, MA.
- [61] LeCroy 7200 Oscilloscope, PC Connect Software, LeCroy, Inc., Kansas City, MO.
- [62] SPICE Simulation Software, Ver. H92, Meta-Software, Inc., Cambell, CA.
- [63] Low Temperature Micro Probe User's Manual, MMR Technologies, Inc., Mountain View, CA, July 1985.
- [64] Accessory Kit for MMR Refrigerators: Part Number C1810/C1812, MMR Technologies, Inc., Mountain View, CA, July 1992.
- [65] Vacuum Accessory Kit: Model #C1805 and C1806, MMR Technologies, Inc., Mountain View, CA, July 1989.
- [66] User Instructions for Operating MMR Joule-Thomson Refrigerators, MMR Technologies, Inc., Mountain View, CA, July 1989.
- [67] Model K-20 Programmable Temperature Controller User's Manual, MMR Technologies, Inc., Mountain View, CA, October 1984.

- [68] K. G. Merkel, Ohmic Contact to Ion Implanted Gallium Arsenide Antimonide for Application to Indium Aluminum Arsenide/Gallium Arsenide Antimonide Heterostructure Insulated-Gate Field Effect Transistors, AFIT dissertation, September, 1995.
- [69] North Hills Electronics, Inc., Glen Cove, NY, 11542.

Vita

Captain Darren E. Sene [REDACTED]. After graduating from Sherwood High School, Sherwood, OR, in May of 1986 he went to Portland Community College for two years and then on to the University of Portland on an AFROTC scholarship, both schools in Portland, Oregon. In December 1990 he graduated with a Bachelor of Science degree in Electrical Engineering and was commissioned a Second Lieutenant in the United States Air Force. Following graduation he spent 9 months working for a private company in the Portland area before being called to active duty. His first assignment was at the Ballistic Missile Organization (BMO), Norton AFB, California where he was a Project Officer for the Titan IV System Program Office, Solid Rocket Motor Division. Later, while at BMO, he was assigned to the Rocket Systems Launch Program as Project Manager for Booster Engineering and guided the control system modification of the SR-19 (Minuteman II, Stage II) for the Theater Missile Defense program. While in southern California he obtained a Masters of Science degree in Human Resource Management from Chapman University, Orange, California. Following assignment at Norton AFB, he moved to Wright-Patterson AFB, Ohio where he was assigned to the Air Force Institute of Technology to pursue a Masters of Science degree in Electrical Engineering through the electro-optics program. After graduating on 19 December 1995, he was assigned to the National Aerospace Intelligence Center at Wright-Patterson AFB, Ohio.

Permanent Address: [REDACTED]
[REDACTED]

REPORT DOCUMENTATION PAGE

Form Approved
OMB No. 0704-0188

Public reporting burden for this collection of information is estimated to average 1 hour per response, including the time for reviewing instructions, searching existing data sources, gathering and maintaining the data needed, and completing and reviewing the collection of information. Send comments regarding this burden estimate or any other aspect of this collection of information, including suggestions for reducing this burden, to Washington Headquarters Services, Directorate for Information Operations and Reports, 1215 Jefferson Davis Highway, Suite 1204, Arlington, VA 22202-4302, and to the Office of Management and Budget, Paperwork Reduction Project (0704-0188), Washington, DC 20503.

1. AGENCY USE ONLY (Leave blank)		2. REPORT DATE December 1995	3. REPORT TYPE AND DATES COVERED Master's Thesis	
4. TITLE AND SUBTITLE DESIGN, FABRICATION AND CHARACTERIZATION OF MICRO OPTO-ELECTRO-MECHANICAL SYSTEMS			5. FUNDING NUMBERS	
6. AUTHOR(S) Darren E. Sene, Captain, USAF				
7. PERFORMING ORGANIZATION NAME(S) AND ADDRESS(ES) Air Force Institute of Technology, WPAFB OH 45433-6583			8. PERFORMING ORGANIZATION REPORT NUMBER AFIT/GEO/ENG/95D-03	
9. SPONSORING / MONITORING AGENCY NAME(S) AND ADDRESS(ES) Captain James Lyke, Phillips Laboratory (PL/VTEE) 3550 Aberdeen Ave. SE, Kirtland AFB, NM 87117-5776			10. SPONSORING / MONITORING AGENCY REPORT NUMBER	
11. SUPPLEMENTARY NOTES				
12a. DISTRIBUTION / AVAILABILITY STATEMENT Distribution Unlimited			12b. DISTRIBUTION CODE	
13. ABSTRACT (Maximum 200 words) Several micro-opto-electro-mechanical structures were designed using the Multi-User MEMS Process (MUMPS). Specific design techniques were investigated for improving the capabilities of elevating flip-up structures. The integration of several flip-up micro-optical structures into a micro-optical system was explored with emphasis on the development of a micro-interferometer. The thermal effects on the Modulus of Elasticity were determined by detecting the resonant frequency for a square Flexure Beam Micromirror Device. The resonance of the device was found to match theory to within 0.1 % and the Modulus of Elasticity was found to decrease by 0.041 GPa/K from 290 to 450 K. Thermal testing on each of the polysilicon MUMPS layers yielded a linear increase in resistivity of 1×10^{-6} to $2 \times 10^{-6} \Omega\text{-cm/K}$ from 290 to 450 K. Several designs of a surface micro-optical structure known as a variable grating were developed and characterized. The device yielded modulation intensities of up to 6.4 and 9.0 dB for the first two diffracted orders, respectively. The devices utilize heat drive actuator(s) to deflect a Poly 2 grating laterally, up to 4 μm , over a Poly 1 stationary grating which changes the period dimensions of the composite grating. This device can be effectively used for multi-channel optical switching.				
14. SUBJECT TERMS flip-up structures, interferometer, micro-interferometer, micromechanical, micromirror devices, micro-optics, MEM, MEMS, MUMPS, optical modulation, optical switching, thermal testing			15. NUMBER OF PAGES 213	
			16. PRICE CODE	
17. SECURITY CLASSIFICATION OF REPORT UNCLASSIFIED	18. SECURITY CLASSIFICATION OF THIS PAGE UNCLASSIFIED	19. SECURITY CLASSIFICATION OF ABSTRACT UNCLASSIFIED	20. LIMITATION OF ABSTRACT UL	

GENERAL INSTRUCTIONS FOR COMPLETING SF 298

The Report Documentation Page (RDP) is used in announcing and cataloging reports. It is important that this information be consistent with the rest of the report, particularly the cover and title page. Instructions for filling in each block of the form follow. It is important to *stay within the lines* to meet *optical scanning requirements*.

Block 1. Agency Use Only (Leave blank).

Block 2. Report Date. Full publication date including day, month, and year, if available (e.g. 1 Jan 88). Must cite at least the year.

Block 3. Type of Report and Dates Covered. State whether report is interim, final, etc. If applicable, enter inclusive report dates (e.g. 10 Jun 87 - 30 Jun 88).

Block 4. Title and Subtitle. A title is taken from the part of the report that provides the most meaningful and complete information. When a report is prepared in more than one volume, repeat the primary title, add volume number, and include subtitle for the specific volume. On classified documents enter the title classification in parentheses.

Block 5. Funding Numbers. To include contract and grant numbers; may include program element number(s), project number(s), task number(s), and work unit number(s). Use the following labels:

C - Contract	PR - Project
G - Grant	TA - Task
PE - Program Element	WU - Work Unit Accession No.

Block 6. Author(s). Name(s) of person(s) responsible for writing the report, performing the research, or credited with the content of the report. If editor or compiler, this should follow the name(s).

Block 7. Performing Organization Name(s) and Address(es). Self-explanatory.

Block 8. Performing Organization Report Number. Enter the unique alphanumeric report number(s) assigned by the organization performing the report.

Block 9. Sponsoring/Monitoring Agency Name(s) and Address(es). Self-explanatory.

Block 10. Sponsoring/Monitoring Agency Report Number. (If known)

Block 11. Supplementary Notes. Enter information not included elsewhere such as: Prepared in cooperation with...; Trans. of...; To be published in.... When a report is revised, include a statement whether the new report supersedes or supplements the older report.

Block 12a. Distribution/Availability Statement. Denotes public availability or limitations. Cite any availability to the public. Enter additional limitations or special markings in all capitals (e.g. NOFORN, REL, ITAR).

DOD - See DoDD 5230.24, "Distribution Statements on Technical Documents."

DOE - See authorities.

NASA - See Handbook NHB 2200.2.

NTIS - Leave blank.

Block 12b. Distribution Code.

DOD - Leave blank.

DOE - Enter DOE distribution categories from the Standard Distribution for Unclassified Scientific and Technical Reports.

NASA - Leave blank.

NTIS - Leave blank.

Block 13. Abstract. Include a brief (*Maximum 200 words*) factual summary of the most significant information contained in the report.

Block 14. Subject Terms. Keywords or phrases identifying major subjects in the report.

Block 15. Number of Pages. Enter the total number of pages.

Block 16. Price Code. Enter appropriate price code (*NTIS only*).

Blocks 17. - 19. Security Classifications. Self-explanatory. Enter U.S. Security Classification in accordance with U.S. Security Regulations (i.e., UNCLASSIFIED). If form contains classified information, stamp classification on the top and bottom of the page.

Block 20. Limitation of Abstract. This block must be completed to assign a limitation to the abstract. Enter either UL (unlimited) or SAR (same as report). An entry in this block is necessary if the abstract is to be limited. If blank, the abstract is assumed to be unlimited.